Monte Carlo Characterisation of Proton Minibeams

James Thomas Eagle

School of Physical and Chemical Sciences
College of Science
University of Canterbury

Abstract

Proton therapy has been shown to offer clinical advantages over standard photon based external beam modalities. Additionally, there is evidence from small animal experiments showing that the recovery of healthy tissue is improved with the use of spatially modulated beams, referred to as microbeams or minibeams which consist of an array of parallel narrow beamlets. Using Monte Carlo modelling, this thesis explores the potentially powerful combination of minibeams and proton therapy by characterising the physical and biological dose when generating proton minibeam by means of a collimator.

It is known that patient motion has the potential to spread dose to regions between the minibeams thereby, reducing or removing the spatial modulation. A thorough characterisation of the impact of such motion on lateral spread of dose was performed for a wide range of motion amplitudes, relevant for small animal irradiation (60 μm to 10 mm). Clinical beams appropriate for human therapy were also investigated to determine the impact motion has on proton minibeams. Motion was shown to detrimentally impact all proton minibeam dose distributions. However, simulations for irradiating a brain undergoing pulsations of up to 300 μm an array of a 0.3 mm wide beamlets, (centre to centre (CTC) spacing of 1 mm), showed that the dose between the beamlets, known as the valley region, only increased by a maximum of 2% for both mouse and human treatments. It was further found that increasing the CTC spacings up to 10.77 mm reduced the impact of motion on the valley region, for motions up to as high as 1.1 mm. Increasing the width of the beamlet reduced the effect of motion on dose delivered within the

beamlet tracks, however it increased dose in the valley regions, and therefore it is not recommended.

Having established motion does not negate the usefulness of proton minibeam therapy, a comprehensive Monte Carlo framework was developed in Tool for particle simulation (TOPAS) to simulate the University of Washington's preclinical proton radiation platform, which is currently the only existing preclinical proton minibeam beamline. A detailed and novel analysis of the impact each beamline component has on the resulting dose distribution was performed. Unknowns in the physical dimensions of beamline components were identified and estimated by adjusting physical dimensions in the simulated beam transport system. The final beamline model was experimentally verified against measurements with an ion chamber and diamond detector to have a Bragg peak depth consistent with an energy of 44.95 MeV (a depth of 18.1 mm). The decrease in energy from the nominal 50.5 MeV (depth of 22.3 mm) was shown to be due to proton interactions with the graphite degrader, Kapton exit window, and the monitoring ion chamber. It was further shown that these components reduced the Bragg peak depth by 2.0 mm, 0.3 mm, and 2.0 mm, respectively. Other components were also investigated and found to have minimal impact on the beam energy.

At the University of Washington proton minibeams are currently produced by means of a physical collimator designed and manufactured during this thesis. A comprehensive analysis and characterisation of collimator material and physical dimensions was carried out with the aim of defining the ideal proton minibeam collimator designed for this beamline, i.e. one that maximises spatial modulation and limits scattered dose. Results indicated that there exists an optimum

collimator thickness and a 20 – 25 mm thick collimator was found to be ideal. Increasing the thickness of the collimator beyond this was undesirable, as the collimator would then reduce the number of primary protons whilst maintaining the same number of scattered protons. It was shown of the 50.5 MeV proton beam with a nickel collimator that the first 15 mm of the collimator was responsible for producing the most neutrons, electrons, and photons. The ideal width of the collimator slot width for the UW proton beam was found to be between 0.3 – 0.4 mm as it produced beamlets with a high spatial modulation, commonly characterised as the peak to valley dose ratio (PVDR), whilst only reducing dose at the Bragg peak by approximately 60% of an open (non-collimated) beam. It was also shown that although a high-density collimator should be used to maximise the PVDR, care needs to be taken to reduce neutron production. Of the 78 materials investigated, Group 4 transition metals, particularly nickel, provided the highest PVDR. Nickel was also found to result in the lowest neutron yield, 2.7 times less than that of tungsten, making it an ideal material for minibeam collimators.

To fully understand the therapeutic benefit of collimated proton beamlets requires knowledge of the Relative Biological Effectiveness (RBE) and the resulting RBE weighted dose (RWD), of all primary and scattered particles emanating from the proton minibeam collimator. These were investigated for four previously identified materials. While at 50.5 MeV the neutron dose from the different materials varied by a factor of 3.2, overall, it was an insignificant component of the total RWD. The RBE of protons was shown to increase by up to a value of three on the distal edge of the Bragg peak, shifting the Bragg peak depth deeper by 0.1 mm. The RBE in the valleys was found to be up to a value of 1.5 at the surface. This has the consequence of reducing the effective normal superficial tissue sparing from proton minibeams.

Summarising the main results from this thesis, it has been shown that proton minibeams for small animal irradiation are feasible even when the target is undergoing internal motion. Having accurately simulated the preclinical proton radiation platform (PPRP) beamline at the University of Washington it was identified that the most suitable design for a physical collimator for 50.5 MeV protons is to construct from either nickel, stainless steel, copper, and brass. The thickness of the collimator should be 25 mm to sufficiently block protons without introducing any additional scatter. This thesis also provides evidence for supporting an increase in the commonly used value for proton RBE as a function of depth in tissue. This result is imperative for planning treatment and therefore should be implemented when considering dose effects for any animal and ultimately human therapies.

Acknowledgements

I would like to thank the following people for helping with this thesis:

My supervisor's Dr Juergen Meyer and Dr Steven Marsh for all their support, guidance, and patience throughout my thesis. I will miss our weekly meetings in the future. The University of Washington Medical Centre, Radiation Oncology Medical Physics department for their contribution. The University of Canterbury school of Physical and Chemical Sciences for their support and funding. I would like to thank the cancer society of New Zealand for their funding. Finally, I would like to thank Mariann Brennan for being there and supporting me throughout my thesis. I would also like to thank my parents for their support.

Table of Contents

List of Figures

Abbreviations

BP	Bragg peak
CTC	Centre to centre
DSB	Double-strand break
FWHM	Full width half maximum
GEANT	Geometry and tracking
IMRT	Intensity-modulated radiation therapy
LET	Linear energy transfer
MATLAB	Matrix laboratory
MRT	Microbeam radiation therapy
PBS	Pencil beam scanning
PDD	Percentage depth dose
PMRT	Proton minibeam radiation therapy
PPRP	Preclinical proton radiation platform
PVDR	Peak to valley dose radio
RBE	Relative biological effectiveness
RWD	RBE weighted dose
SBRT	Stereotactic body radiation therapy
SRIM	Stopping and range of ions in matter
TOPAS	Tool for particle simulation
UW	University of Washington
VMAT	Volumetric modulated arc therapy

Chapter 1

Introduction

1.1. Background

Radiation therapy kills or slows the growth of cancerous tissue by delivering a lethal dose of radiation, whilst simultaneously delivering a minimal dose to normal tissue [1, 2]. Various clinical treatment techniques aim to improve normal tissue sparing, and thus reduce treatment complications. Some techniques achieve this by delivering a large number of small radiation fields from multiple beam directions to precisely sculpt the dose to the tumour. Examples of this are intensity-modulated radiation therapy (IMRT) and volumetric modulated arc therapy (VMAT). Both of these techniques have been shown to reduce toxicity compared to more traditional and less conformal techniques [2-4]. Stereotactic body radiation therapy (SBRT) is a hypo-fractionated treatment regime showing further improvements for some cancers [2, 5]. Both IMRT and VMAT are delivered with photons and are utilised clinically around the world. Proton therapy is less common and more costly than photon therapy with benefits in terms of how the radiation is deposited. This can lead to further reduction of toxicity in normal tissue, which is beneficial especially for paediatric patients [6, 7]. Currently there are 93 proton therapy treatment centres worldwide, compared to several thousand

linear accelerators used for photon treatments, with a growing interest in this treatment modality [8, 9].

Reduction of toxicity in normal tissue when using protons is due to an intrinsic dosimetric advantage they have over photons. Protons deliver dose to the surrounding medium proportional to the ionisation per millimetre of path, with the maximum dose delivered at the end of the proton's range, referred to as the Bragg peak [10]. The depth of this Bragg peak depends on the initial energy of the proton; thus, manipulation of the initial energy allows the Bragg peak to coincide with the tumour at depth. The tumour will consequently receive a large dose, whilst normal tissue near the surface receives a low dose, and there is virtually no dose beyond the Bragg peak.

Preclinical research with spatially fractionated beams referred to as microbeams, has indicated that they may be advantageous compared to uniform beams, due to the considerably reduced normal tissue toxicity that has been observed in cell and small animal experiments [11-13]. This normal tissue sparing effect was first discovered in the 1950's by Curtis *et al.* using synchrotron generated radiation, whilst studying the effects of cosmic radiation on mice [12]. The radiation resistance of the mouse brain tissue was discovered to be inversely related to the width of the beam. The use of small beams on the micro scale was later established by Slatkin *et al.* at the European Synchrotron Radiation Facility [13]. This research used microscopically narrow, synchrotron generated photon beams for treatments on the central nervous system of vertebrates and was the first implementation of microbeam radiation therapy (MRT). Further research by the National Synchrotron Light Source, Brookhaven National Laboratory and European

Synchrotron Radiation in the 1990s demonstrated that use of MRT on rat physiology exhibited the same tissue sparing effect [14]. This reduction of toxicity could be of notable benefit to children with brain tumours as it will reduce damage to their developing nervous system [15]. If this sparing effect is demonstrated to be applicable for treatment of human oncology patients, then normal tissue complications could be reduced whilst simultaneously maintaining or increasing local tumour control.

The unique dose distribution of protons combined with spatial fractionation has the potential to improve upon traditional synchrotron generated photon microbeams. By designing appropriate spatial modulation of proton beams, it is possible to produce a beam which can deliver a nearly uniform dose to the cancerous tissue whilst maintaining spatial modulation of dose near the surface and normal tissues. A typical proton MRT dose distribution is displayed in Figure 1.1.

Methods of producing this type of dose distribution require either; a physical collimator, which blocks portions of a uniform beam, or a temporarily varying collimator, such as a scanning pencil beam, which moves a small beam over a region in a pattern designed to result in a spatially modulated dose [16]. The degree of dose modulation may be described by the ratio between the peak and the valley dose and is referred to as the peak to valley dose radio (PVDR) [16]. This is used to describe the beam modulation relative to a uniform beam. The widths of these spatially modulated beams can either be in the order of micrometres or millimetres and are referred to as microbeams and minibeams, respectively. The combination of proton therapy and minibeams, which is known as proton minibeam radiation

therapy (proton MRT), could drastically reduce normal tissue toxicity, whilst maintaining dose to cancerous tissue[16].

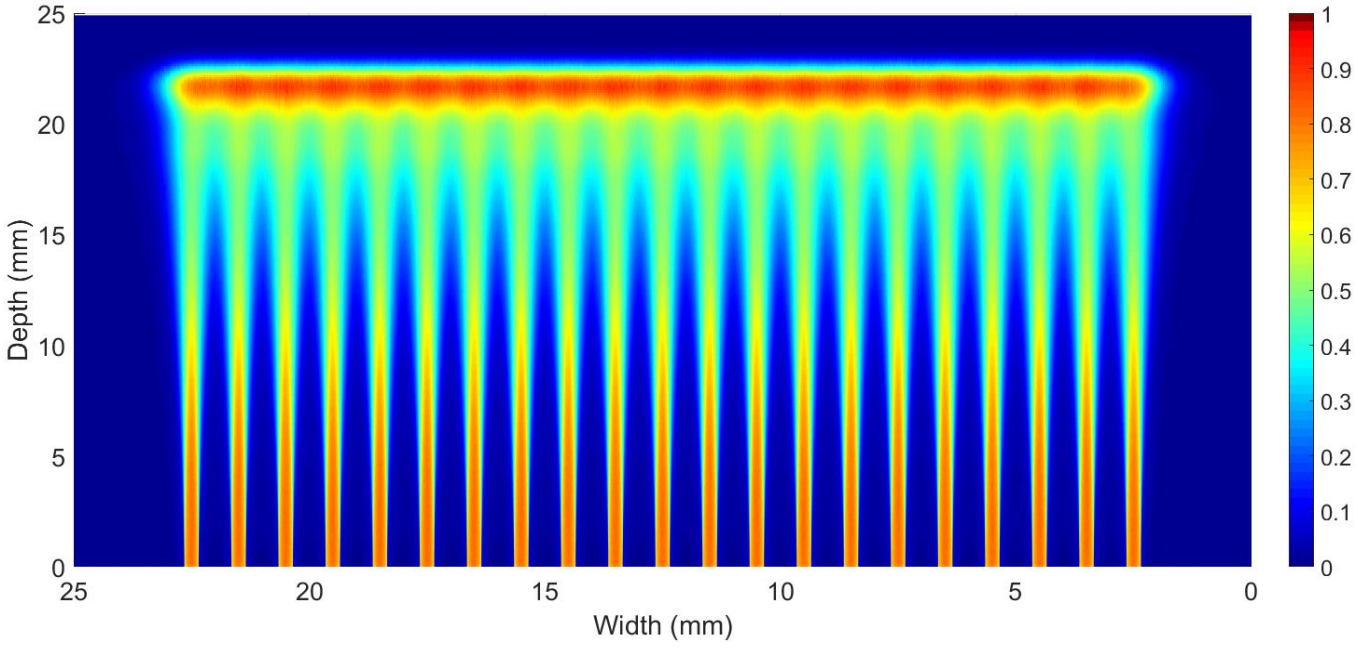

Figure 1.1: Simulation of a 50.5 MeV proton minibeam dose distribution in water phantom. Beam is obtained from below. The minibeam peak regions are the high dose regions at the entrance surface shown in red. The valley regions are in between the peak regions and are regions of low dose shown in blue. Dose is scaled to a value of 1.0 at the Bragg peak.

1.2. Aims

This work was in collaboration with the University of Washington and focused on small animal irradiation for use in preclinical research into proton minibeams. While the work presented is generalised for a range of proton energies, there is a focus on the 50.5 MeV PPRP at the (UW) in Seattle, USA [17, 18].

The thesis has the following primary aims:

1. Investigate the effects of motion on proton MRT dose distributions.
2. Produce and experimentally verify a TOPAS model of the 50.5 MeV PPRP beamline and use this model to produce an understanding of how beamline components reduce the energy spectrum of the proton beam.
3. Consider various materials for use in proton minibeam collimators to reduce secondary radiation production and maintain sharp beam profiles. And to optimise the geometry of proton minibeam collimators to maximise the PVDR and reduce the minibeam valley dose.
4. Model the RBE effects of proton MRT caused by different collimator materials.

The first aim of investigating the effect of motion is to address a key limitation of proton MRT. This limitation arises as spatially modulated dose distributions are vulnerable to motion, which blurs their sharply defined peak and valley profiles, resulting in unwanted dose in the valley regions. Spatially modulated proton minibeams generated by the PPRP have a comparatively low dose rate, in the order of 8.4 Gy/min relative to the traditional synchrotron generated X-ray microbeams with dose rates of several thousand Gy/s [18, 19]. This results in longer treatment

times on the PPRP. Consequently, the proton minibeam dose distributions may be more susceptible to organ motion. Work by Manchado de Sola *et al.* demonstrated that even very high dose rate synchrotron generated microbeams can be impacted by small brain pulsations [19]. This highlights the need for research to be applied to proton minibeams as motion has the potential to fully destroy any spatial modulation of the dose distribution removing any potential benefit of proton MRT over uniform proton treatments. Characterising the effects of motion on the spatially modulated proton dose distributions and determining if there are methods to limit the impact of motion is therefore the first aim of this thesis.

The second aim of this thesis is to produce and experimentally verify a working model of the 50.5 MeV PPRP in TOPAS and use this to produce an understanding of how the beamline components reduce the energy spectrum of the proton beam. Production of the model requires modelling all components that the beam will come into contact with before delivering dose to a target. Verifying this model requires the simulated dose from the model to match physical measurements taken from the PPRP at the University of Washington. An in-depth investigation to explain how the energy and particle spectrum of the beam is modified by beamline components will be performed with this model. This information on the PPRP can then be directly applied to further research throughout this work and for future biological experiments.

The third aim is to investigate how the dose distribution of proton minibeams is affected by different design components of physical collimators. Proton MRT dose distributions can be produced with either pencil beam scanning or a physical collimator, each of which have their advantages and disadvantages for clinical

applications. This thesis focuses on physical collimators for the following reasons. This work is in collaboration with UW's PPRP, which does not have pencil beam scanning capability currently. Also, the majority of current pencil beam scanning systems have spot sizes that are a magnitude too large to produce minibeam dose distributions [20]. There are two areas of research into the design of physical collimators that will be focused on in this thesis. The unwanted secondary radiation produced due to interactions between the incoming proton beam and the physical collimator. This scatted radiation is unwanted and increases the surface dose, as well as blurring the sharp beam profiles, reducing the PVDR thereby reducing the effectiveness of the treatment. Collimator material has been shown to have a considerable impact on the secondary dose produced from the collimator and the neutron production is of particular concern [21, 22]. Therefore, the first area of research in collimator design aims to determine an optimal collimator material for use in proton minibeams which reduces the secondary dose, particularly dose from neutrons, whilst maximising the PVDR throughout the dose distribution. The secondary area of research is the optimisation of the geometry, as this directly controls the shape of the resultant dose distribution. Minimising the dose delivered to the valley regions whilst increasing the PVDR will increase the sparing effect thus reducing biological damage to normal tissue. This work builds on previous research by Lee *et al.* and aims to provide an in-depth analysis on how the collimator geometry controls the final dose distribution [23].

The fourth aim of this thesis is to investigate how collimator material can impact the RBE of the proton minibeams. The RBE is the ratio of biological damage between two different types of radiation for the same physical dose. For this research, the RBE for photons, electrons, neutrons, and protons generated by

minibeam collimator is considered. The RBE of protons varies with energy and depth in the target. Protons that interact with a collimator will lose energy and thus their dose and RBE is affected. Collimator material influences the variation caused by this and therefore how these two factors interact is an important area of this research. The RBE of neutrons produced by the collimator is another important factor. Although the number of neutrons exiting the collimator is a small component of the total number of particles, they can have a remarkably high RBE and potentially deliver an undesirable high biological dose to normal tissue.

1.3. Outline

This thesis is comprised of seven chapters. Chapter 2 contains an overview of background material in radiation therapy, proton therapy, microbeams and Monte Carlo modelling relevant to this thesis. Chapter 3 investigates the effects that motion has on proton MRT dose distributions for 50 MeV – 250 MeV proton beams using Monte Carlo modelling. Chapter 4 introduces the design of a Monte Carlo model of the proton beamline at the University of Washington Medical Centre. This model was generated to match the actual preclinical beamline and was used to investigate how components of the beamline interact and impact the beam energy and the final dose distribution. The accuracy of the model was verified experimentally to match the Monte Carlo model. Chapter 5 discusses collimator design parameters and limitations. An in-depth analysis of how geometric designs and materials impact the resulting dose distributions and output from the collimator was carried out. Chapter 6 covers RBE modelling of proton and neutrons exiting various proton MRT collimators. The origin and impact of these particles have on the dose distribution is investigated. Chapter 7 contains concluding remarks and a discussion of possible future areas of work.

Chapter 2

Background Material

This section starts with a brief overview of radiation therapy covering the need and the objectives that radiation therapy aims to achieve when treating cancer. Proton therapy is then discussed and the difference to traditional photon treatments highlighted. The physics behind proton therapy is covered to provide the reader with a background in these concepts which will be discussed later in the thesis. Background on how beams are shaped is included as this is important background information when dealing with collimators to produce proton MRT beams. The differences between proton beams and photon beams can in some part be explained by the differences in linear energy transfer (LET) and RBE, so a brief background is provided to introduce the reader to these topics. An introduction to spatially fractionated treatments is provided covering their history and current use. This is expanded upon in a section on proton microbeams, which are a subset of spatially fractionated treatments that use protons rather than synchrotron generated photons. Proton minibeams are a main component of this thesis and the background and history of this treatment modality is introduced. The last section in is on Monte Carlo modelling providing important background on the methods used for investigating proton MRT beams throughout this thesis.

2.1. Radiation Therapy

Cancer was responsible for 9.6 million deaths worldwide in 2018, with new cases estimated to rise by around 70% over the next 20 years [24]. Current treatment of cancer is achieved with one or a combination of: radiotherapy, chemotherapy, or surgery. Radiotherapy has been shown to be beneficial to at least half of cancer patients [1].

Radiation therapy aims to use ionising radiation to deliver sufficient dose to kill all tumour cells whilst sparing normal cells. Ionising radiation is defined as radiation with sufficient energy to free an electron when interacting with an atom, resulting in the atom becoming ionised. There are two main types of ionising radiation; directly ionising, which consists of charged particles such as protons, electrons, positrons, and heavier ions, and indirectly ionising radiation which has no charge such as high energy photons and neutrons. Charged particles can directly ionise atoms through the Coulomb force, where non-charged particles do not interact strongly with matter and therefore ionise atoms through secondary interactions, such as the photoelectric effect. Ionisation occurs along the path of ionising radiation, ionising both normal and cancerous tissues indiscriminately, leading to cell death of both.

Ionising radiation kills cells by damaging the DNA molecule in a cell, causing the cell to die. DNA is made up from base nucleotides that form a sugar phosphate backbone forming a single polynucleotide strand, which is bonded with another complementary stand using hydrogen bonds. Damage to the DNA occurs either directly in the DNA when an atom in the molecule is ionised by radiation, or

indirectly when a free radical interacts with a DNA atom. Free radicals are often a result of the ionisation of water in the cell, in close proximity to the DNA molecule [25]. The various types of DNA lesions that can occur from ionising radiation is shown in Figure 2.1 [26]. Base damage occurs when part of a single nucleotide is ionised. Single strand breaks occur when an ionisation occurs in the sugar phosphate backbone resulting in a break. If two of these breaks occur on opposite sides of two strands in proximity this can fully break the DNA molecule in a double-strand break. Of these DNA lesions, the most damaging type is the double-strand break, which has a high correlation of cell death [25].

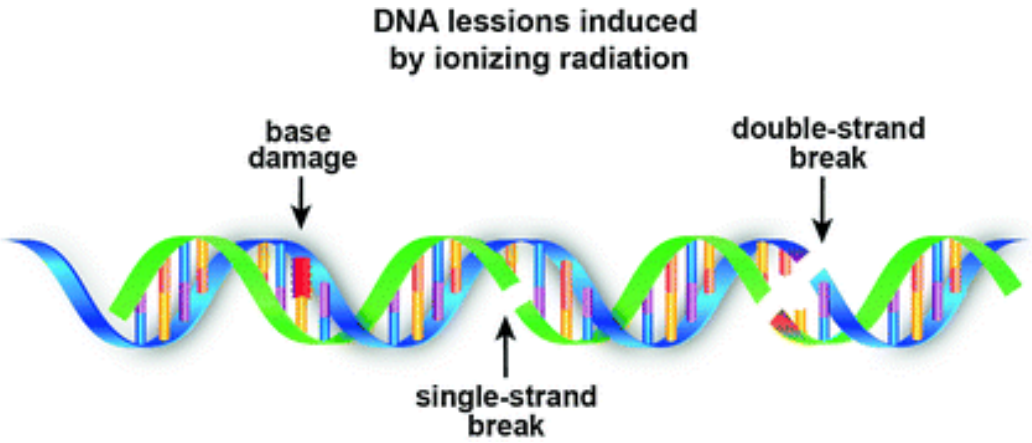

Figure 2.1: Various types of damage that can occur from interactions between radiation and DNA. Showing the differences between base damage, single strand breaks and double strand breaks. Obtained from Iliakis G. (2018) [26]

2.2. Proton Therapy

The use of protons in radiation therapy was first proposed by Wilson in 1946 [10]. The advancement of new accelerators enabled production of protons with energy higher than 125 MeV. These protons have a penetration depth of around 11 cm enabling use in human treatments [10]. Wilson proposed the use of protons over the traditional photons due to their unique dose distributions. The first human treatments were carried out at the Berkeley Radiation Laboratory in 1954 and in Uppsala, Sweden in 1957 [27, 28].

Protons are charged particles, when they travel though matter, they will primarily interact with the matter through Coulomb interactions. They also interact infrequently with an atom's nuclei via nuclear reactions resulting in various nuclear decays to occur, or, with electric fields to produce photons known as Bremsstrahlung. The most common of these interactions are illustrated in Figure 2.2 [29]. Inelastic Coulomb interactions with electrons are the most common interactions where the positively charged proton interacts with a negatively charged electron, resulting in kinetic energy being transferred from the proton to the electron. This collision will have little impact on the momentum of the proton as it has a rest mass of nearly 2000 times that of an electron, resulting in the protons path being roughly linear throughout the interaction. Most of the energy from the proton beam is lost in this manner, thus, the resultant path of a proton beam is roughly linear, with a slight increase in the spread with depth.

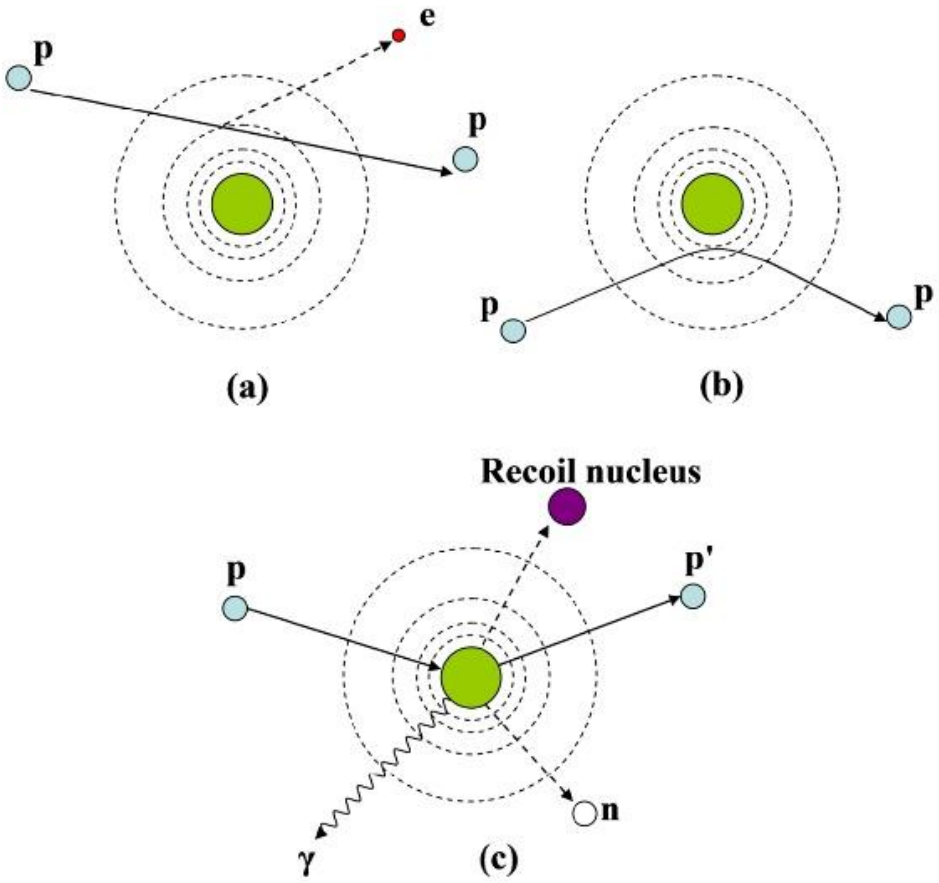

Figure 2.2: Diagram of proton interactions (a) Inelastic Coulomb interactions with electrons, (b) Repulsive Coulomb interactions with nucleuses, and (c) non-elastic nuclear interactions. Retrieved from Newhauser et al [29].

When a proton interacts with a nucleus repulsive Coulomb interaction occur. However, this this type of interaction occurs infrequently, as the relative size of the nucleus is significantly smaller than that of the electron orbitals. The kinetic energy is transferred from the proton to the nucleus in this interaction. As the proton has less mass than the nucleus, there is a large change in momentum for the proton, deflecting it from its original path. This effect causes a small amount of spread in the proton beam, which increases with depth, thus decreasing the penumbral sharpness.

Non-elastic nuclear interactions occur when a proton directly collides with a nucleus, which results in the nucleus emitting secondary particles either: a proton, a neutron, a gamma ray, or a heavier ion. If the secondary particle is a proton or heavier ion, then they will have a short range and deposit dose nearby. However, the gamma ray and neutrons can deliver secondary dose over a large range. As the cross-sectional area of a nucleus is quite small, nuclear interactions occur infrequently. Nuclear interactions are the primary reason for the decrease in beam fluence, and unwanted secondary radiation.

The energy lost in matter from these interactions was described by Bethe in 1932, and describes the energy loss for fast moving charged particles travelling through matter [30].

$$-\left(\frac{dE}{dx}\right) = \frac{4\pi}{m_r c^2} \cdot \frac{nz^2}{\beta^2} \cdot \left(\frac{e^2}{4\pi\varepsilon_0}\right)^2 \cdot \left[ln\left(\frac{2m_r c^2 \beta^2}{I \cdot (1-\beta^2)}\right) - \beta^2\right] \quad [1]$$

The energy lost per distance travelled (dE/dx) is inversely proportional to the electron number density (n) in the medium, z the particle charge in multiples of the electron charge, the mean excitation potential I, the relativistic velocity β=v/c, and m_r the rest mass. Where ε_0 is the permittivity of free space and c is the speed of light in a vacuum. This results in the energy lost being approximately inversely proportional to the velocity of the particle squared, particularly for protons with $\beta << 1$. This relationship results in a unique dose distribution for protons. The depth that a proton will travel in matter is dependent on the initial energy of the proton [10]. Energy lost per distance travelled increases with depth, resulting in protons depositing the majority of their dose near the distal end of the path. This high dose

region at the end of a proton path is known as the Bragg peak (BP) [10]. The Bragg peak as a percentage of depth dose is illustrated in Figure 2.3 in red as the pristine peak, showing the low surface dose, which increases to a maximum at the Bragg peak with a small trailing dose.

The depth of the Bragg peak, or range of a proton beam is defined as the depth when half of the protons have come to a rest state [29]. The depth is dependent on the initial energy of the proton beam. This means that the beam can be manipulated to coincide with a tumour at any depth. Figure 2.3 shows a comparison between the proton beam and two x-ray (photons) beams, highlighting the large difference in the depth of the peak. This gives protons a dosimetric

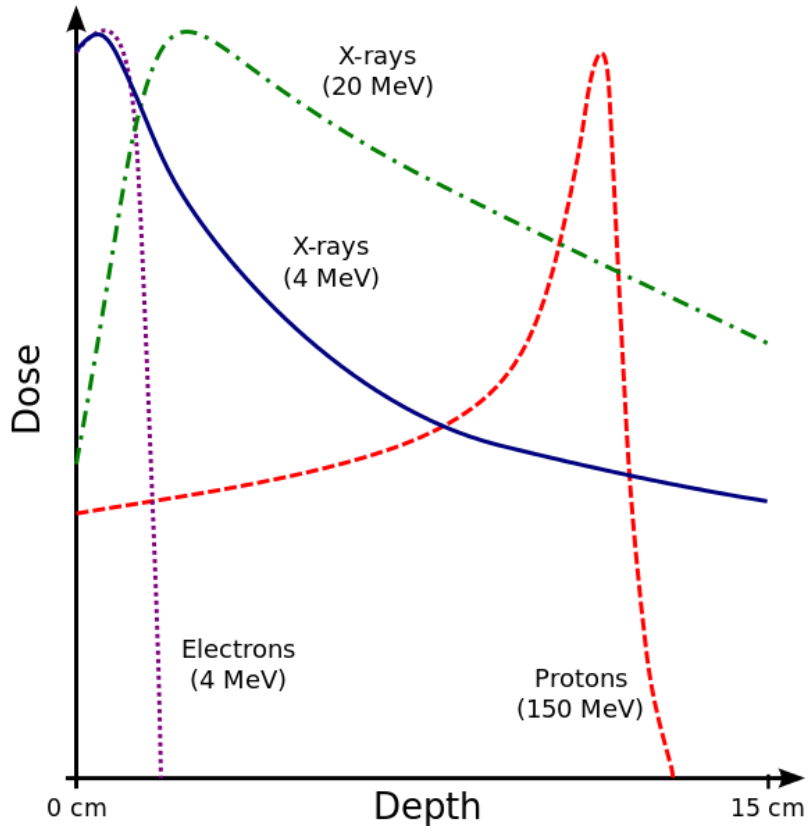

Figure 2.3: Depth dose curve for various particles types highlighting their differences. 150 MeV Protons shown in red displaying a Bragg peak at depth. 20 MeV and 4 MeV X-ray (Photon) beams shown in green and blue, respectively. Demonstrating that higher energy photons have their peak at a greater depth. 4 MeV electrons shown in purple, showing that electrons are not very penetrating. Adapted from wikicommons by Cepheiden

advantage over photon treatments when using a single fixed beam. However, modern photon treatments use multiple beams from different angles, which all converge on the tumour to overcome this problem. This leads to some debate on the overall advantages of proton therapy for many applications, however, there has been some evidence that it is superior for paediatric central nervous system malignancies [7, 31].

2.2.1. Linear Energy Transfer

LET is defined as the amount of energy deposited by ionising radiation per unit length into local medium. LET is dependent on radiation type, energy, and local medium. Protons deliver a large amount of energy over shorter distances because they are charged particles and readily interact with matter. Protons are therefore classified as having a high LET, with an LET greater than 100 MeV/mm at the Bragg peak [32]. There is a relationship between the LET and the biological response of the radiated tissue [33]. This allows LET to provide some insight into why different types of radiation cause disproportionate biological responses with the same amount of absorbed dose. The relationship between LET and biological response can be modelled dependant on several factors, such as the alpha and beta ratios for specific tissues, and are often built on empirical models [34, 35].

When protons travel through a medium they lose energy and their rate of dose deposition increases thus the LET increases with depth until it peaks on the distal edge of the Bragg peak [36]. The high LET on the distal edge of the Bragg peak comes with a corresponding high biological response. Quantifying the magnitude of this effect is an important area of research as the distal edge of the Bragg peak

can be placed near heathy tissue and an increase in biological damage in this region is a concern.

2.2.2. Relative Biological Effectiveness

The damage to biological tissue which results from two equal doses of radiation may differ if the two sources are of different radiation type. This is known as the RBE and is dependent on cell type and biological response to radiation, making it difficult to simulate and measure. Low LET radiation such as ^{60}Co is used as reference radiation and therefore has an RBE of one. An RBE of 1.1 has been used clinically in the past for proton beam therapy [37-40]. This average RBE of 1.1 for clinical proton was confirmed to be a reasonable estimate of the average RBE in the spread out Bragg peak, with a range between 0.9 and 2.1 observed by Paganetti *et al* [37]. However, further results for a large range of proton beams from preclinical energy to clinical energy beams was summarised in 2014 by Paganetti *et al* demonstrating that the RBE varies between 1.1 for the entrance region and 1.7 for the distal edge clearly showing that using an averaged RBE may be inadequate [9]. Results from these studies showed that the RBE of protons varied based on energy, biological endpoint and LET [9]. The RBE of protons also increases on the distal edge of the Bragg peak, and therefore increases the biological response at this point [36]. The high biological response at the distal edge of the Bragg peak is of great concern as this is often placed near critical structures and normal tissue and increasing the biological damage may lead to unwanted complications.

Neutrons have a higher RBE than that of photons, with an RBE of up to 20 for neutrons with one MeV of energy [41]. This is significantly higher than that of

protons, resulting in increased biological damage from neutrons for the same amount of energy deposited. Production of proton microbeams by means of a metal collimator has the side effect of producing a small number of unwanted neutrons. Neutrons are not charged particles and will not readily interact with matter. This results in the energy, which is deposited being spread throughout the patient, potentially causing increased biological damage to normal tissue. While the energy deposited from neutrons is typically a small component of the total energy deposited from the proton MRT beam, the higher RBE is a concern as it disproportionately increases the biological damage caused by neutrons.

2.3. Spatially Fractionated Treatments

Initial work on spatially fractionated treatments was performed by Kohler in 1909, where a mesh of wire was used to block sections of the incoming kilovoltage x-ray beam, this was known as grid therapy [42]. The idea behind this was to reduce dose to the skin and allow higher doses to treat difficult large, bulky tumours. Further work by Liberson in 1933 used lead to shield regions on the skin enabling these regions to act as areas of regrowth healing areas of skin around them damaged by treatment fields [43]. The development of megavoltage x-ray treatments which have increased depth dose and skin sparing properties led to the decline in use of grid therapy. This difference is illustrated in Figure 2.3. Recently there has been research into using megavoltage beams for grid therapy, using multi-leaf collimators or fixed collimators to produce dose grids. Recent studies have demonstrated some benefit for bulky tumours [16, 44-46]. This improvement over uniform beams is often attributed to the bystander effect [47]. The bystander effect occurs when an unirradiated cell behaves as if it has been irradiated as a result of

signals from nearby irradiated cells [48]. Some initial work implementing grid therapy for clinical use with proton therapy was done by Geo *et al.* for use in a single fraction treatment of large tumours to improve the treatment of these difficult to treat tumours, this is illustrated in Figure 2.4 [49].

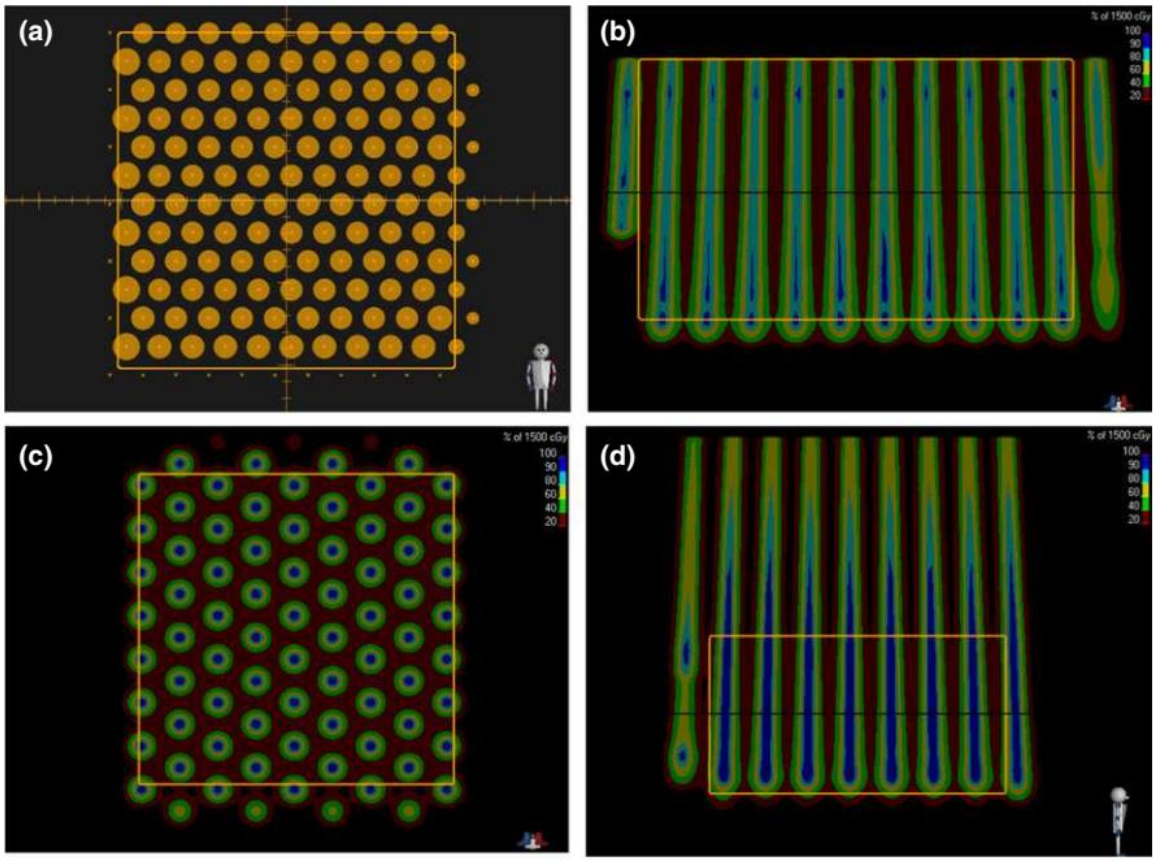

Figure 2.4: Geo's proton grid treatment plan. Showing the array of parallel beams that are used to treat a target centred at 6 cm depth (a, b) or 14 cm depth (c, d). Target is outlined by the orange box. Figure obtained by Geo et al. [49]

2.4. Microbeams

Microbeams are a subset of spatially fractionated treatments modulated on the scale of microns. Initial work on microbeams was first done by Zeman and Curtis at the Brookhaven National Laboratory in an experiment with a deuteron microbeam [11, 12]. This experiment simulated the biological effect of heavy cosmic-ray particles to determine the impact on manned spaceflight. Their research investigated the effect of a 25, 100 and 1000 μm deuteron beam on mice brains. Results indicated that to produce a histological lesion, a dose of 250, 750 and 10,000 Gy was required for each of the beams, respectively. This initial research demonstrated that microbeams had extraordinary normal tissue sparing properties, with resistance of the mouse brain tissue to the radiation being inversely proportional to the beam size [12].

Slakin proposed the idea of MRT for use in treatment of brain lesions in rats in 1992, with initial work at Brookhaven National Laboratory and further work at the European Synchrotron Radiation Facility [13, 50-54]. Slakin proposed the use of synchrotron generated x-rays with a sub-beam width ranging between 7- 75 μm and a CTC separation between sub-beams of 50-400 μm for treatment [14]. These beams produce regions of low dose and regions of high dose that remain parallel and constant with depth. A diagram of a minibeam dose distribution is shown in Figure 2.5, highlighting differences in the peaks and valley doses at the surface and illustrating the naming convention used throughout this thesis, note this figure shows the illustration with minibeams rather than microbeams for clarity.

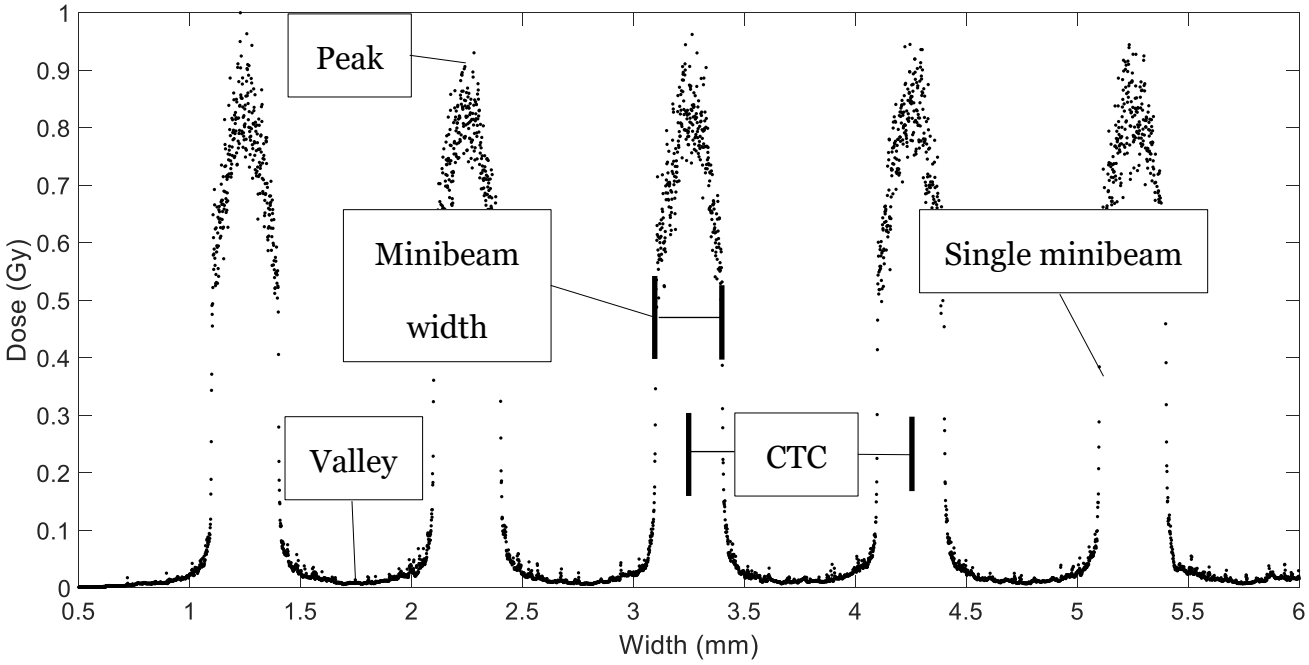

Figure 2.5: Surface dose profile of a 50.5 MeV proton minibeam dose distribution, displaying: The minibeam peak dose which occurs at the maximum dose in the minibeam path and the valley dose which occurs at the minimum dose between two peaks. Also displayed is a single minibeam that is part of the dose distribution, the centre to centre spacing between the minibeams, and the width of the minibeam. This terminology will be the naming convention used throughout this work.

Microbeams allow tissue sparing beyond just the skin surface, maintaining sparing throughout the beam's depth. This offers an improvement over that of grid therapy. The sparing effect was demonstrated to reduce damage to the developing nervous systems of young rats [50]. Thus, this particular treatment method is ideally suited for paediatric brain tumours due to the decreased normal tissue damage and decreased risk for developing nervous systems [53]. MRT also demonstrated palliative and curative effects on rat cerebral tumours whilst maintaining tissue sparing effects [51, 55, 56].

Spatially fractionated treatments with large sub-beam widths of up to 0.67 mm and CTC separation of up to 1.2 mm have been shown to preserve this extraordinary normal tissue sparing, these larger beams are known a minibeams [57].

2.4.1. Proton Minibeams

As discussed in Section 2.2, protons offer intrinsic dosimetric advantages over photons. These advantages have the potential to be improved on when the proton beams are spatially fractionated on either a micrometre scale (microbeams) or a millimetre scale (minibeams). Initial Monte Carlo modelling by Prezado *et al.* demonstrated the proof of this concept [16]. As discussed previously protons lose energy inversely proportional to the square of the velocity. This results in most of the dose being delivered at the Bragg peak. The dose at the Bragg peak will have a greater spread in all directions than the surface due to Coulomb interactions. This results in proton micro/minibeams having a spatially modulated dose region at the surface with well-defined regions of high and low dose. These region's definition blurs with depth, resulting in a semi-uniform high dose region at the Bragg peak. Figure 2.6 shows a 50.5 MeV proton minibeam dose distribution, demonstrating the modulated dose at the surface and the uniform dose at the Bragg peak. This figure also shows the relatively high maximum dose delivered at the surface and the dose delivered at the Bragg peak. The lateral spread of the proton beam is a function of initial energy. The uniformity of the dose distribution at the Bragg peak is therefore controlled by the initial energy and the spacing between micro/minibeams. While it is possible to produce a uniform dose distribution with photon synchrotron generated microbeams, there is a requirement for at least two interlaced beams. This results in a more error prone complex setup [58].

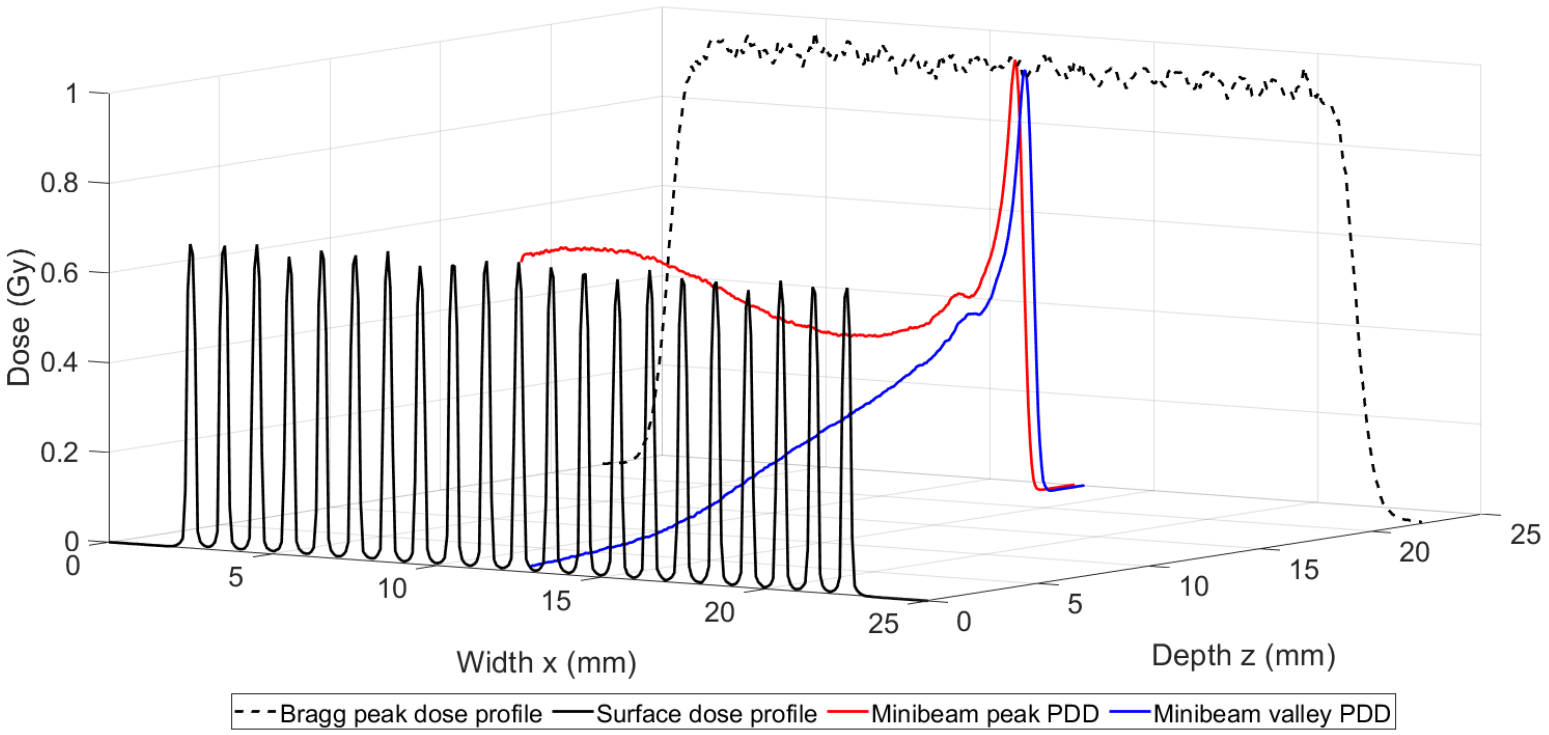

Figure 2.6: Dose distribution for a 50.5 MeV proton minibeam. Showing the spatially modulated dose profile at the surface (black line) and the semi uniform dose profile at the Bragg peak depth (black dashed line). Displaying the minibeam peak dose PDD (red) and the minibeam valley PDD (blue). Dose results have been scaled to the Bragg peak dose.

The quality of a spatially fractionated dose distribution is often measured by the ratio, between the peak dose and the valley dose. The peak dose, not to be confused with the Bragg peak, is the maximum dose across the width of the microbeam and the valley dose is the minimum dose located between the spatially fractionated beams. This is shown in Figure 2.5, displaying the profile for a 50.5 MeV proton minibeam at the surface. The PVDR is roughly consistent for synchrotron generated beams throughout their depth. Spatially fractionated proton beams diverge with depth, resulting in PVDR decreasing with depth.

Spatially fractionated proton beams can either be generated with a physical collimator blocking a designated portion of a uniform beam or they can be produced temporarily with a scanning pencil beam. Pencil beams have the

advantage of producing no secondary particles which can affects the dose distribution. However, scanning pencil beams has the disadvantage of a lower dose rate, requiring a typically longer treatment time. A second major limitation of pencil beam scanning is current treatment spot sizes generated on clinical beams are considerably larger than the required sub-millimetre size [20, 59, 60]. A physical collimator overcomes these two limitations and is significantly less complex and expensive to implement.

The use of a physical collimator has the drawback of introducing secondary scatter into the dose distribution. These scattered particles primarily consist of lower energy proton, neutron, electrons, and photons. Scattered particles increase the surface dose, the valley dose, and the dose post Bragg peak. Scatter also blurs the peaks and the valleys of the minibeams. The physical collimator also reduces the dose rate that can be delivered to the Bragg peak as it blocks a portion of the beam.

Proton therapy is typically delivered at a dose rate of around 20 Gy/min compared to that of synchrotron generated photon beams at 10,000 Gy/s. This results in proton micro/minibeam therapy having a non-instant delivery and thus the dose distribution is susceptible to motion artefacts that might compromise the skin sparing effects. Work on the impact that motion has on proton minibeams is discussed in Chapter 3.

The PVDR is impacted by secondary radiation generated from the collimator. The position of the collimator has been shown to have a strong effect. Research from Meyer *et al*, showed that moving a minibeam collimator from being adjacent to a water phantom to a distance of 2 cm resulted in a PVDR decrease by a factor of ten

from 37 to 3.7 [18]. This decrease in the PVDR is a result of scatter from the collimator. Scattered particles generated by the minibeam collimator have a greater divergence than protons that pass through the collimator without interacting with it This scatter consists of mostly protons that have undergone Coulomb interactions and some particles that have been generated through interactions between protons and the collimator. These scattered particles will have a higher angular divergence than the proton beam due to deflection and transference of momentum. This effect increases the minibeam peak dose at the surface when the collimator is placed close to the water phantom. Placing the collimator further away will spread the scattered dose into regions of low dose decreasing the peak dose and increasing the valley dose. As the proton's energy determines its path length when depositing dose, these secondary protons contribute significantly to the surface dose and their impact decreases with depth. This is the inverse of an ideal treatment, as the skin is at the surface with a tumour located at the Bragg peaks depth. Therefore, increasing the primary dose and decreasing the secondary dose is important to maintain the Bragg peak ratio. This effect is outlined in research by Hong *et al.* with work on pencil beams [61].

2.5. Monte Carlo Modelling

The Monte Carlo method is a well-known mathematical algorithm which uses repeated random measurements to estimate results [62]. The idea behind this is that computing the exact interactions of all particles involved in an experiment would be unfeasible, therefore an approximation is required.

The Monte Carlo method estimates an unknown quantity using inferential statistics [62]. Inferential statistics assumes that a random sample of the population has the same properties as the whole population. An estimation of the true properties of the population can therefore be determined with repeated random sampling. The variation in the mean of each random sample gives an underlying uncertainty in the overall mean value of the population. Increasing the number of samples will cause the sampled mean to trend towards the population mean.

Monte Carlo modelling in physics uses physical cross sections of atoms to compute probability. Each type of interaction has its own probability for a range of energy and a range of atoms. For example, a photon interacting with an electron can undergo: the photoelectric effect, Compton scattering or pair production. Therefore, each of these processes have an independent likelihood of occurrence. Cross sections for an interaction occurring per length of matter for a particle passing through, is determined by the density of atoms in the material, the probability each atom has to interact, and the probability of each type of interaction.

Monte Carlo modelling models transport of a single particle at a time, usually known as a history. Variations between each history are randomised based on the initial design of the simulations. The particle is tracked until it exits the simulation boundary or loses all its energy through interactions. Secondary particles can be produced through some interactions and these particles are also tracked. Researches are usually only interested in measuring a single quantity in a single part of the beam, such as the dose in a water phantom. Only this information would be recorded and carried over between each history. Multiple measurements can be performed at the same time if necessary, although this can impact the time it takes for the simulation to run.

Chapter 3

Effect of Motion on Proton Minibeam Dose Distributions

A primary concern of proton minibeams is the comparatively low dose rate, in the order of 20 Gy/min, compared to that of synchrotron generated x-ray beams, with dose rates of 1000 Gy/s or higher [63]. As a result, treatment times for proton minibeams are, depending on the dose to be delivered, in the order of minutes, rather than sub-second for synchrotron generated x-ray beams. Consequently, spatially modulated proton minibeam dose distribution is more susceptible to motion artefacts that occur over this longer time period. Motion blurs the sharply defined spatial modulation of the dose distribution. If there is sufficient motion, then the spatial modulation can be entirely removed leaving only a uniform dose distribution. Work by Manchado de Sola *et al.* investigated the impact of cardio-synchronous brain pulsations on microbeams for synchrotron radiation [19]. This work demonstrated that even with the extremely high dose rates generated by synchrotrons, spatially modulated dose distributions were still blurred by motion. This indicates the need for research into this area as proton microbeams will be impacted to a greater degree by motion due to their greater amount of time to deliver the same dose.

Motion in patients can originate from internal organs, or from skeletal muscle movements. Skeletal muscle movements, which are commonly up to 10 mm or larger, can be reduced or removed fully through utilising immobilisation devices and/or anaesthesia [64-66]. Internal organ motion, for example lung tumour movement as a result of breathing, was reported by Seppenwoolde *et al.* in one study to have an average amplitude of 12 ± 2 mm [67]. The impact breathing motion has on the dose distribution to a lung tumour can be reduced through the use of gating and breath hold techniques. However these techniques do not fully remove the effect of this motion, and is a current area of research [66, 68]. Breathing motion is likely to negatively impact the spatially modulated dose distribution from proton minibeam if used to treat lung tumours. A second example of organ motion is small brain movements caused by cardiovascular pulsations, these can be up to 0.3 mm [69]. The amplitude of these movements is small and is typically inconsequential for typical radiotherapy treatment modalities, yet is potentially still problematic for proton MRT, as these motions are similar in size to the small beams used and can potentially blur the modulated dose distribution. These movements are complex and non-rigid and exist throughout the body. In addition, various sections of the body experience different amplitudes of motion over brief time periods [67, 69].

Research in this thesis is particularly interested in motions that occur in small animals, which can impact treatments on the PPRP at UW. The magnitudes of these movements in small animals are smaller than in humans, for example rats have a maximum displacement of 60 μm in sections of their brain, compared to 300 μm for humans [69, 70]. While the maximum displacement of these

movements is small, they still potentially reduce the modulation of the dose distribution and thus reduce the sparing effect.

When motion is applied to a dose distribution, the sharp peaks are smoothed into the valleys. Figure 3.1 displays and illustrates a profile of a simplified 300 μm wide proton minibeam distribution at the surface of a water phantom and what occurs to this dose distribution after different amplitudes of motion are applied. Motion is applied in single direction with linear motion having a constant velocity and Gaussian motion having in a variable velocity. This shows that when motion is applied, the profile broadens, and the penumbra sharpness decreases. Further broadening as a result of 400 μm of motion also decreases the height of the peak, this occurs after the amplitude of the motion is greater than the width of the minibeam.

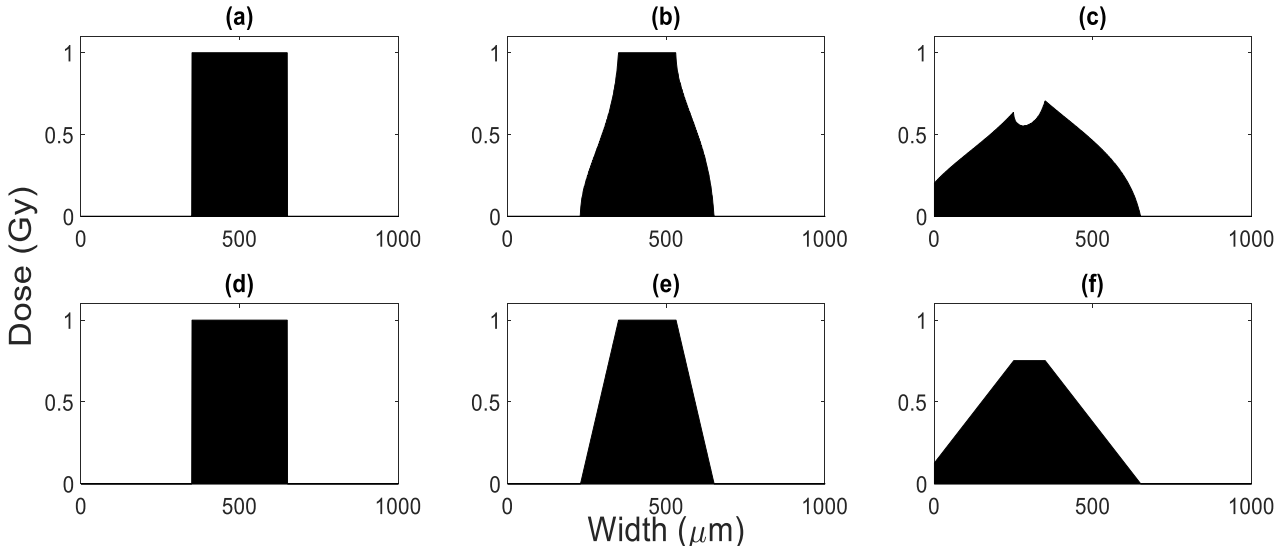

Figure 3.1: Illustration of surface dose from proton beam illustrated with a simple step function with motion modelled in MATLAB. (a) displaying no motion 300 μm minibeam width. (b) 120 μm of gaussian motion simulated. (c) 400 μm of gaussian motion simulated. (d) no motion. (e) 120 μm of linear motion simulated in MATLAB. (f) 400 μm of linear motion simulated in MATLAB.

The difference between linear and Gaussian movement is also displayed, highlighting the maximum width of the minibeam is increased by the same amount for each type of movement, and the shape of the profile varies with the different types of movement. Increasing the width of the micro/minibeam has been shown to decrease the sparing effect for photons [12]. While this relationship has not been fully verified for protons it is assumed to behave similarly. The increase in the width of the micro/minibeam from motion thus reduces the normal tissue sparing, negatively impacting the treatment. Figure 3.1 implies that the valley dose between the minibeam peaks is zero, in a realistic micro/minibeam dose distribution the valley dose is low but non-zero. It can be hypothesised that low valley dose is the determining factor for normal tissue tolerance [71, 72]. Internal organ motion is able to increase this valley dose by spreading dose from the micro/minibeam peaks in the valleys. These two factors are the primary way that motion negatively impacts a micro/minibeam dose distribution and reduce the normal tissue tolerance.

A diagram of a proton beam with a collimator and a water phantom is shown in Figure 3.2, illustrating the naming conventions and orientations used for this work. In this design arrangement, proton minibeams are most susceptible to motion in width direction as a result of the dose modulation being in this direction. Motion which is less than 10 mm in the height (y) or z (direction) do not directly impact the spatial modulation of the beam, as the beam in these directions behaves similar to a uniform beam.

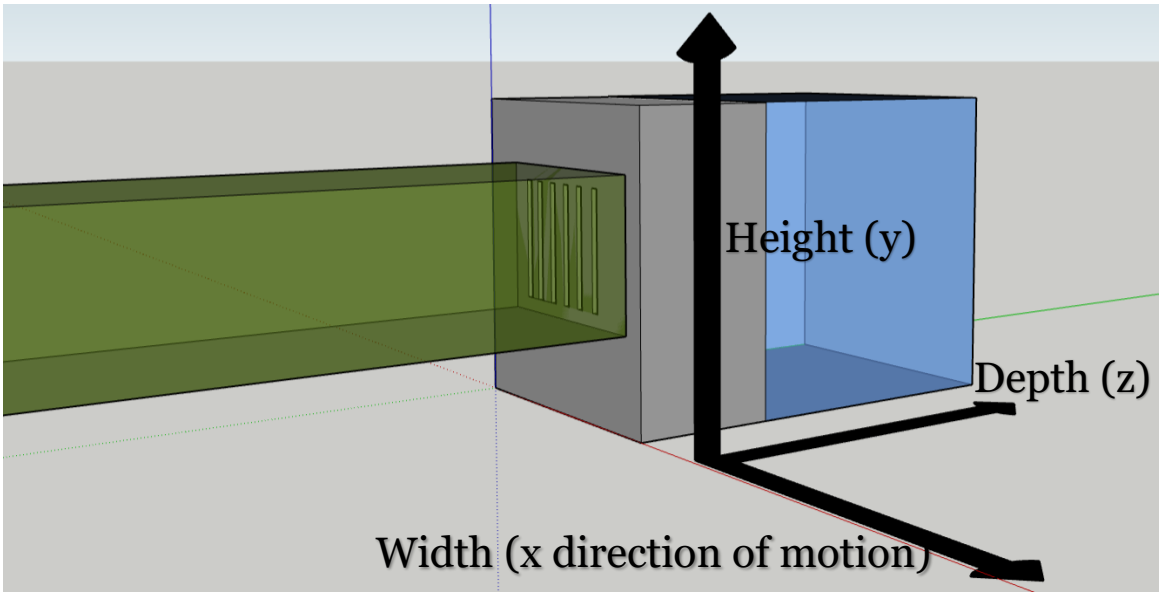

Figure 3.2: Diagram of simulation setup and directions. Showing the proton beam in green, the minibeam collimator with vertical slits (fewer are shown for clarity) in grey and the water phantom in blue

This work is primarily concerned with the overall impact motion will have on a dose distribution. The treatment time of a proton minibeam treatment is on the order of minutes, which is significantly longer than the timescale of most motions particular brain pulsations [69]. We therefore aim to model motion as the sum of a large number of combined single movements that impact the total dose delivered to a target.

Synchrotron generated kV photon micro/minibeam widths remain roughly constant when penetrating a water phantom. Proton micro/minibeams on the other hand have an intrinsic divergence with depth, due to increased lateral scatter with slowing down. It is this property of protons that can be used to generate the uniform profile at the Bragg peak. This contrasts with the photon minibeams discussed by Manchado de Sola *et al.* where motion had a similar impact on all depths of a photon micro/minibeam dose distribution [19]. Investigating how

motion effects proton minibeam dose distribution as depth increases is an area of research that is currently lacking.

The work presented in this chapter aims to model and characterise the effects of motion, from smaller respiratory and cardiovascular pulsations (60-300 μm) to larger motions with amplitudes of up to 10 mm, on proton minibeam dose distributions.

This chapter investigates two areas regarding motion and the impact it has on dose distribution from proton MRT beams generated from a physical collimator. The first area of investigation is how the spacing of the minibeams can be used to minimise the impact of motion, particularly on the valley regions. The spacing between the minibeams is dependent on the spread of the protons at the Bragg peak and the desired uniformity. The magnitude of the spread of the protons at the Bragg peak is a function of energy, therefore we decided to investigate a range of proton energies. The second are that was investigated was how the width of the minibeam can be changed to reduce the impact of motion.

3.1. Methods to Model Motion Effects

Modelling the effects of motion on a proton minibeam dose distribution was divided into two steps. The first step was to simulate high resolution proton minibeam dose distribution in TOPAS. The second step, motion was simulated in MATLAB. Modelling the motion in MATLAB allowed greater flexibility and a wider range of parameters to be investigated, and this greater volume of data to be produced. This methodology is similar to that used by Manchado de Sola *et al* [19].

The TOPAS simulation was designed to produce a realistic proton minibeam dose distribution from a physical collimator. The particles exiting the collimator enter at a water phantom in which particle interactions will result in the deposition of dose. The interaction of the proton beam with the collimator generates secondary particles that impact the dose distribution. Water was used as it has similar properties to human tissue, which allows findings to be applied to a wide range of tissues.

Motion was simulated in MATLAB by making copies of the original dose distribution and shifting each copy in the width direction by an incremental amount of 1 μm. Each copy is then weighted based on a motion function and then combined to form a dose distribution that has undergone motion. For linear based motion, each step would be weighted evenly. Further details can be found in the MATLAB modelling section (Section 3.1.4). The high resolution of both the TOPAS simulation and the small steps of the MATLAB modelling enables exceedingly small motions on the micron scale to be analysed. This work assumes that all motion is non-deforming translational motion for two reasons. First, that this

translational motion in the width direction has the greatest negative impact on the dose distribution. Secondly, the type of translation is dependent on the location in the body and tissue type. This requires specific motion types to be modelled for individual organs and is therefore more complex to model and less applicable to a range of situations. Motion was modelled primarily in the direction that minibeam dose distribution is most vulnerable, shown previously in Figure 3.2. Motion which is in the depth or height directions will not have a substantial impact on the dose distribution.

3.1.1. Monte Carlo Modelling of Proton Minibeams

Monte Carlo simulations were performed using TOPAS version 3.0.1, TOPAS is a wrapper for Geometry and Tracking (GEANT) 4, a well-known Monte Carlo particle simulation toolkit [73-75]. These simulations used the default physics parameters built into TOPAS, which are optimised for proton therapy, and have been experimentally validated for a range of proton facilities [76-80]. The simulations modelled a pristine beam with no beamline. This keeps the results general so they can be applied to wide range of proton beamlines. As discussed in previous sections, the generation of a proton minibeam dose distribution currently requires a physical collimator, and it was decided to model the collimator so as to include the scatter generated from it in the dose distribution.

The simulation modelled a vacuum world with a water phantom located at its centre, a brass minibeam collimator was placed adjacent to the water phantom. Brass was chosen for the collimator material as it is frequently used for collimating

proton beams [22, 81]. A detailed analysis of different collimator materials can be found in Chapter 5. The proton beam was modelled as a rectangular source with a fixed height of 25 mm and a variable width to ensure it covered the required minibeam spacing, this is given later in Table 3.1. The proton beam was simulated with a Gaussian energy spread of 1.15% and a Gaussian angular distribution with a standard deviation of 0.15 degrees. This angular and energy spread is to produce a more realistic result and is based off previous work [23]. The beam simulated 100 million histories for each energy to reduce statistical variation of individual histories and results in a maximum uncertainty of 0.5% in the peak and valley regions for final results. The proton beam traverses 100 mm in the vacuum world and then is collimated into minibeams when passing through the collimator. A diagram of the setup was shown previously in Figure 3.2. Full details on the collimator variables are provided in Section 3.1.2 and 3.1.3.

The simulations were split into two sets of collimator variables. The first simulation modelled different minibeam CTC spacing between each sub-beam, collimator variables are shown in Figure 3.3. The amount of lateral spread of a proton beam

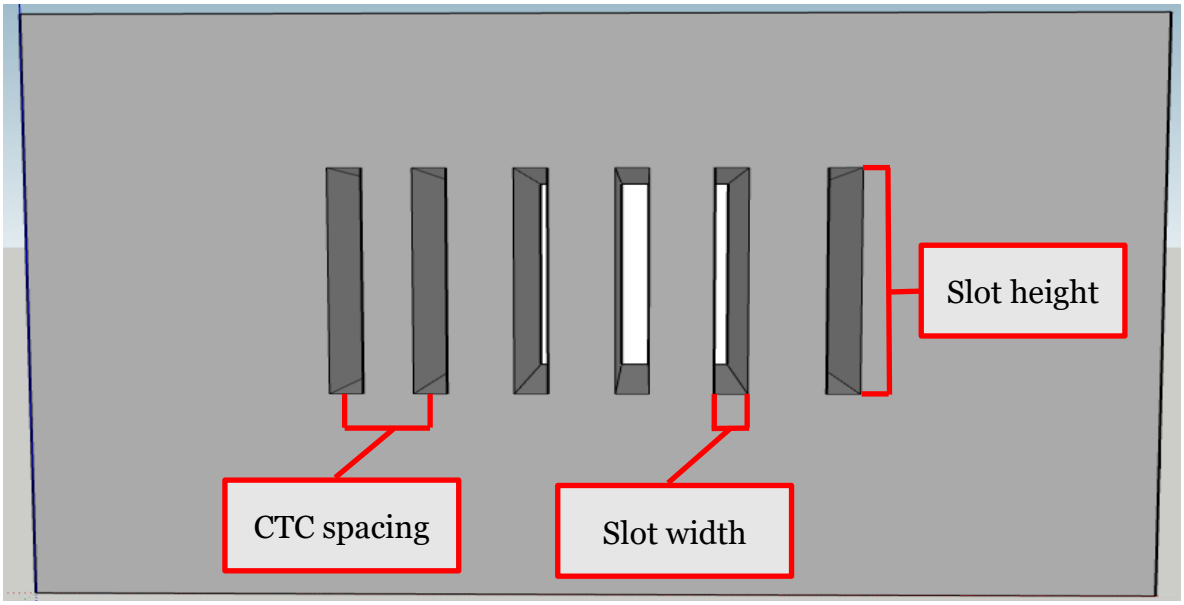

Figure 3.3: Beams eye view of the collimator. Showing the collimator slots and variables used in TOPAS simulations. Note size and number of slots has been changed for clarity.

is energy dependent, therefore the amount of spacing between minibeams to produce the same level of uniformity at the Bragg peak is also energy dependant. While it is possible to use a fixed energy proton beam and change the spacing of the minibeam to highlight the impact the spacing has on how minibeams can affect motion, this method will not produce a uniform dose at the Bragg peak as the protons only have a set amount of lateral spread.

This results in the minibeam peaks combining at a shallower depth or not combining at all. The merging of the minibeams with depth is a key component of proton minibeams as discussed previously, and, if not utilised then protons are not being used to their full potential. To illustrate this, Figure 3.4 shows how the width of a 300 μm wide minibeam increases with depth for various proton minibeam energies used in this thesis. It can be observed that at a certain depth the minibeams merge and produce a uniform dose distribution, at this point the width of the minibeam is shown as a constant width, which is equal to the CTC spacing. Four different energies, 50, 100,150 and 200 MeV were modelled. This range was selected to be appropriate for application to a range of applications, from preclinical research beams operating at lower energy to high energy clinical beams.

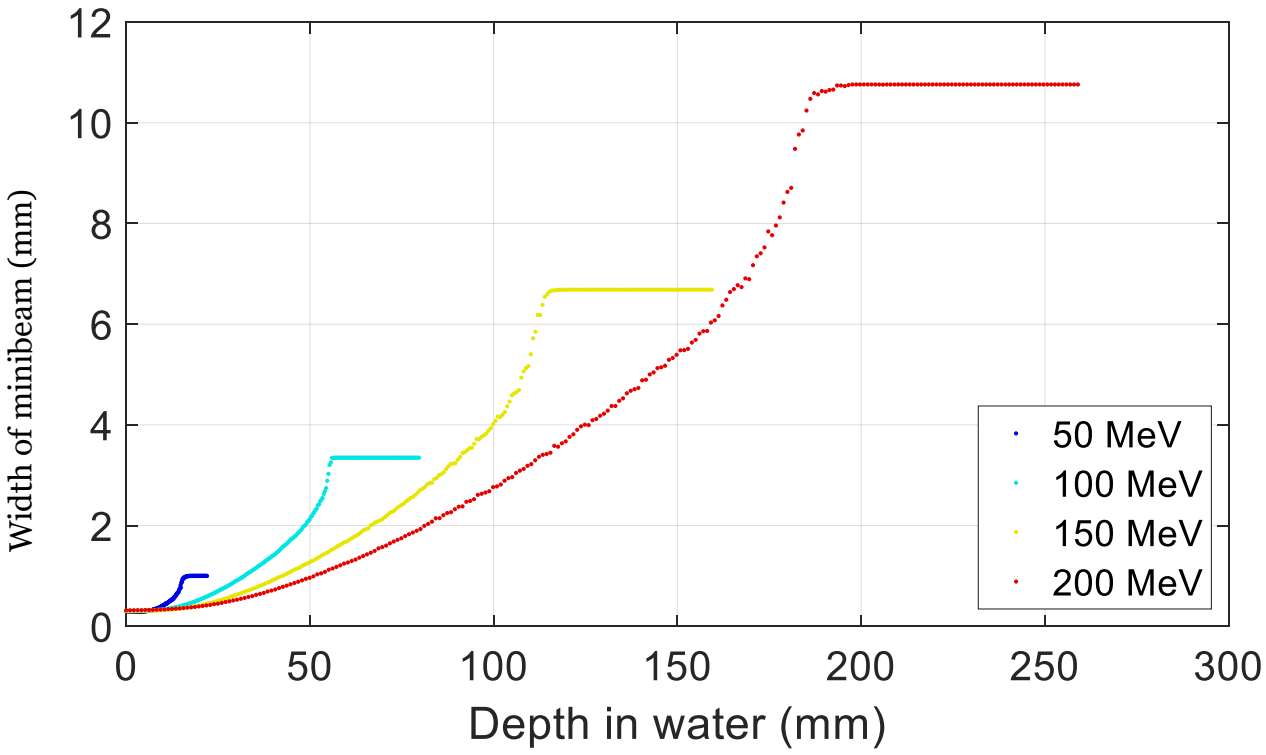

Figure 3.4: Diagram displaying how the width of the minibeam increases with depth until it becomes uniform near the depth of the Bragg peak for various proton minibeam energies. Width is measured as the full width half maximum of the peak.

The second set of simulations varied the width of the minibeams from 100 to 700 µm. The aim of this simulation was to determine if modifying the width of the minibeam can be used reduce the effects of motion on the dose distribution. The range between 100 and 700 µm was simulated as this covers the full range of minibeams, up to the point where the spatially modulated sparing effect has been observed. This simulation used only a single proton beam energy of 50 MeV, so the energy of the beam would not be a factor of the comparison.

3.1.2. CTC Spacing and Motion

As discusses previously, having the ideal CTC spacing between the minibeams allows for a spatially modulated dose at the surface and uniform dose at the Bragg peak. Each of the proton beam energies has a different lateral spread and depth of Bragg peak. Using this lateral spread of the protons the CTC spacing was set to produce uniform dose where the minimum dose was 85% of the maximum dose at the Bragg peak. This level of uniformity was chosen based on previous research by Lee *et al*. Decreasing the CTC spacing would increase the level of uniformity at the Bragg peak if this was desired [23]. The required spacing was calculated by maintaining a constant ratio between the lateral spread of the beam and the CTC spacing. The lateral spread of the proton beam was obtained from the stopping and range of ions in matter (SRIM) 2013 [82]. The calculated CTC for each energy is show in Table 3.1 along with all parameters for the collimator.

Each proton beam energy has a different range in brass and water, therefore the thickness of the collimator and water phantom required adjustment to ensure all particles were fully absorbed in the respective media. As the CTC spacing increased to maintain the same number of slots in the collimator, the incoming uniform beams width was increased as well as the total width of the collimator and water phantom. The collimator and water phantom have a fixed height of 50 mm and 30 mm, respectively.

Table 3.1: Proton minibeam collimator and water phantom parameters used in Monte Carlo model

Incoming uniform proton beam initial energy (MeV)	50	100	150	200
Incoming uniform beam width (x) (mm)	25	75	145	230
Total collimator width (x) (mm)	50	100	200	300
Total collimator thickness (z) (mm)	25	80	160	260
Water phantom width (x) (mm)	25	75	150	250
Water phantom thickness (z) (mm)	25	80	160	260
Bragg peak depth in water (z) (mm)	21.9	76.0	155.6	256.2
Distance between collimator and water phantom (mm)	0	0	0	0
CTC spacing (x) (mm)	1.00	3.35	6.69	10.77
Slot width (x) (mm)	0.3	0.3	0.3	0.3
Slot height (y) (mm)	10	10	10	10
Slot depth (z) (mm)	25	80	160	260
Septa between slots (mm)	0.7	3.05	6.39	10.47

Dose was measured in the water phantom, which was divided into 25000 voxels in the direction of motion (x) and 250 voxels in the height (y) and direction of the beam (z) directions. The higher number of voxels in the direction of motion increases the resolution in this direction and allows the simulation of small motions to be observed and maintains overall voxel limitations and trade-offs.

3.1.3. Minibeam Width and Motion

To model how the width of the minibeam is affected by motion, a simulation was developed for a 50 MeV proton beam, defined using the same parameters as per the minibeam CTC spacing simulation in section 3.1.2 for the 50 MeV beam. The primary modification was varying the width of the slots in the collimator, to produce minibeams of various widths. The width of the collimator slots was varied between 0.1 – 0.7 mm, the CTC spacing remained constant at 1000 μm. This resulted in the material between the slots varying between 0.9 – 0.3 mm, respectively. This allows the width of the minibeam to be decoupled from most other variables and its effect to be investigated independently.

3.1.4. Motion Simulations

As discussed previously, there are several advantages to the approach taken in this thesis with regards to the simulation of phantom motion. The Monte Carlo simulations produce a dose distribution without applying motion to the phantom; instead, this motion is simulated further down the processing chain using MATLAB. For this section we modelled motion as a Gaussian motion to represent the true motion of any part of the body which is based off the motion of brain from MRI studies [69]. The difference in how linear motion and Gaussian motion impact minibeams was displayed previously in Figure 3.1. The MATLAB motion simulation was achieved by making copies of the original dose distribution and shifting each copy in the width direction by an incremental amount of 1 μm. Each copy is then weighted based on a motion function, in this case a Gaussian, and then combined to form a dose distribution that has undergone motion.

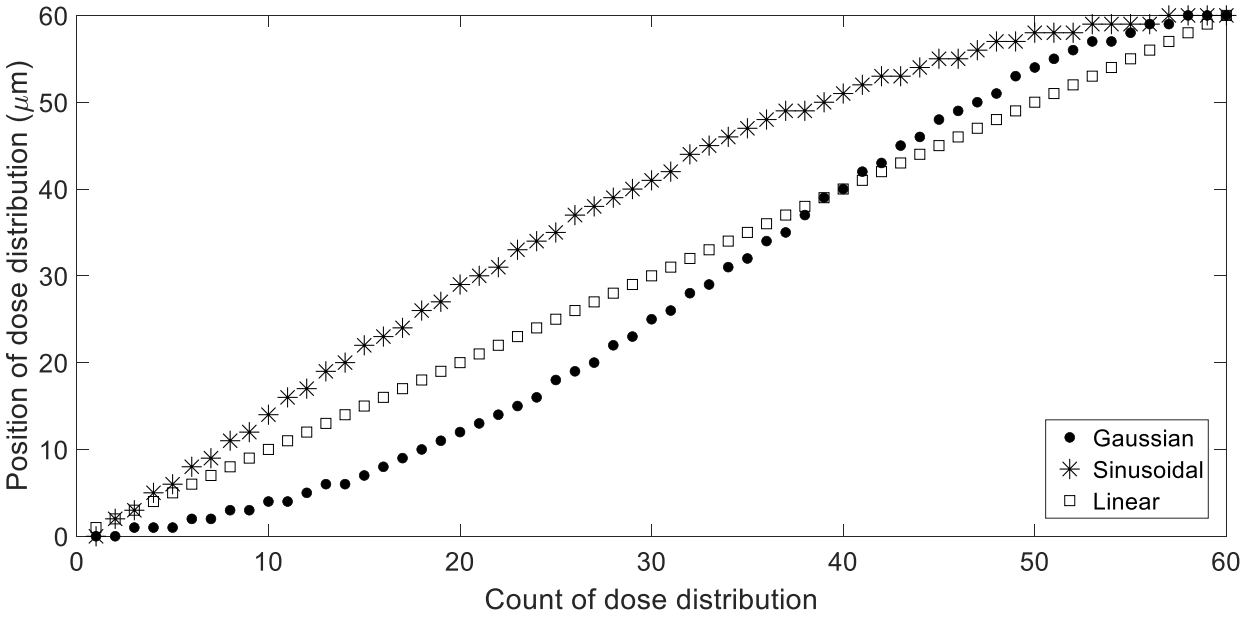

Figure 3.5: Position of dose distributions used to build a final dose that has undergone 60 μm of motion.

This, in effect, weights each position by the percentage of time the dose distribution is located at that position. This is shown for 60 μm of motion in Figure 3.5 for Gaussian, sinusoidal and linear motion. It can be observed that as the dose distributions are only moved in 1 μm voxel steps, and that this results in discrete steps rather than a continuous distribution. This should not pose any problem especially for larger motions. A range of different magnitudes of motion was simulated from 60 to 9500 μm, in steps of 60 μm. This large range covers from small motions from animals, 60 μm, and human brains, 300 μm, up to larger cardio induced and breathing motions [69].

3.2. Results

This section contains the results from the previously discussed simulations and first starts with an introduction to the dose distribution from a static proton minibeam with no motion, which will be used as a standard to compare all other results.

The 50 MeV proton minibeam simulation has eleven 0.3 mm wide minibeams which deposits dose in the water phantom. The dose distribution from the 50 MeV simulation before any motion is applied in MATLAB is shown in Figure 3.6 as a reference. This shows the spatially modulated dose distribution at depth = 0 mm. The minibeams then broaden with depth to produce a near uniform dose distribution at the Bragg peak at depth of 21.9 mm. In the valley regions at the surface there is a dose of approximately 10^{-3} Gy, this small dose is a originates from scatter which is discussed further in Chapter 4.

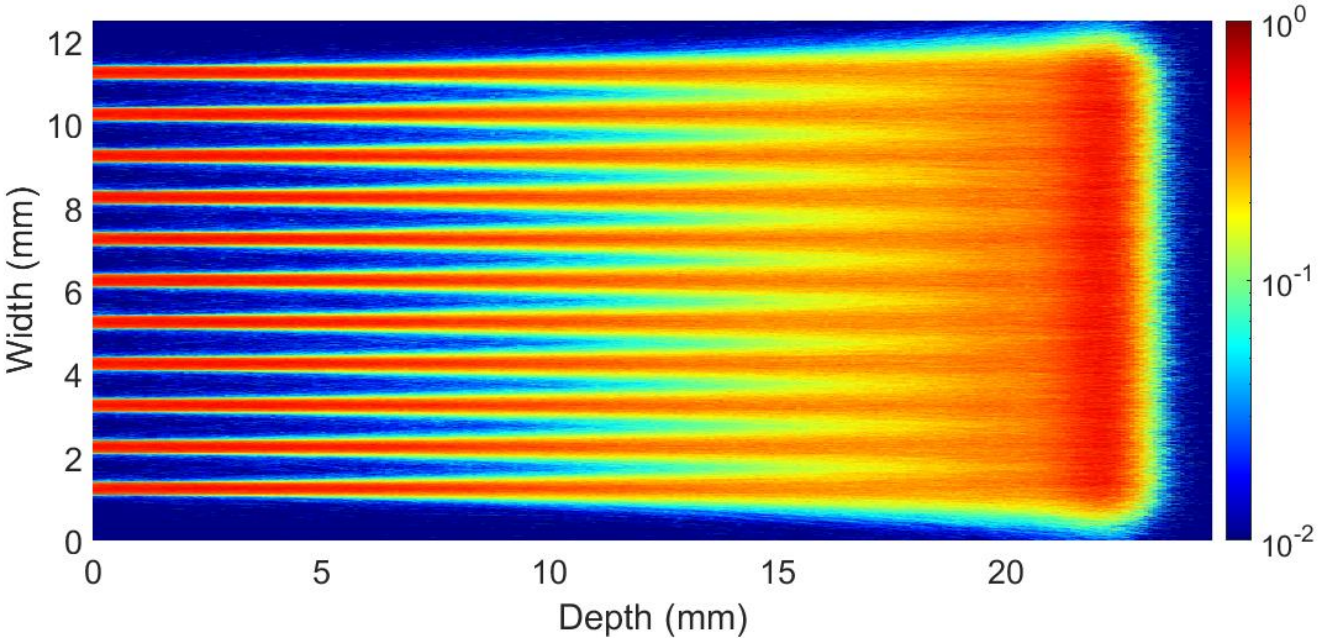

Figure 3.6: 50MeV Proton minibeam dose distribution in water phantom with no motion applied. Normalised to the entrance dose.

A percentage depth dose (PDD) of the peak and valley regions for all proton energies used in this section is displayed in Figure 3.7. The depth scale of this graphic was modified to illustrate difference between different energies. The PDD was also normalised to the entrance dose. It can be observed that the ratio between the surface dose and the Bragg peak dose increases with energy between 50 MeV and 200 MeV. This was caused by the separation of the minibeams and the width of the minibeam resulting in a lack of in-scatter with depth [83]. Proton beams diverge with depth, as discussed in Chapter 2. As the beams are spaced further apart energy from the beam is spread over a larger volume resulting in lower dose at the Bragg peak. The large surface dose is produced by scatter from the collimator, which is investigated further in Chapter 4. The scatter consists of mostly lower energy protons that have interacted with the collimator and lost energy thought Coulomb interactions. These low energy protons deposit their energy at a shallow depth in the water phantom.

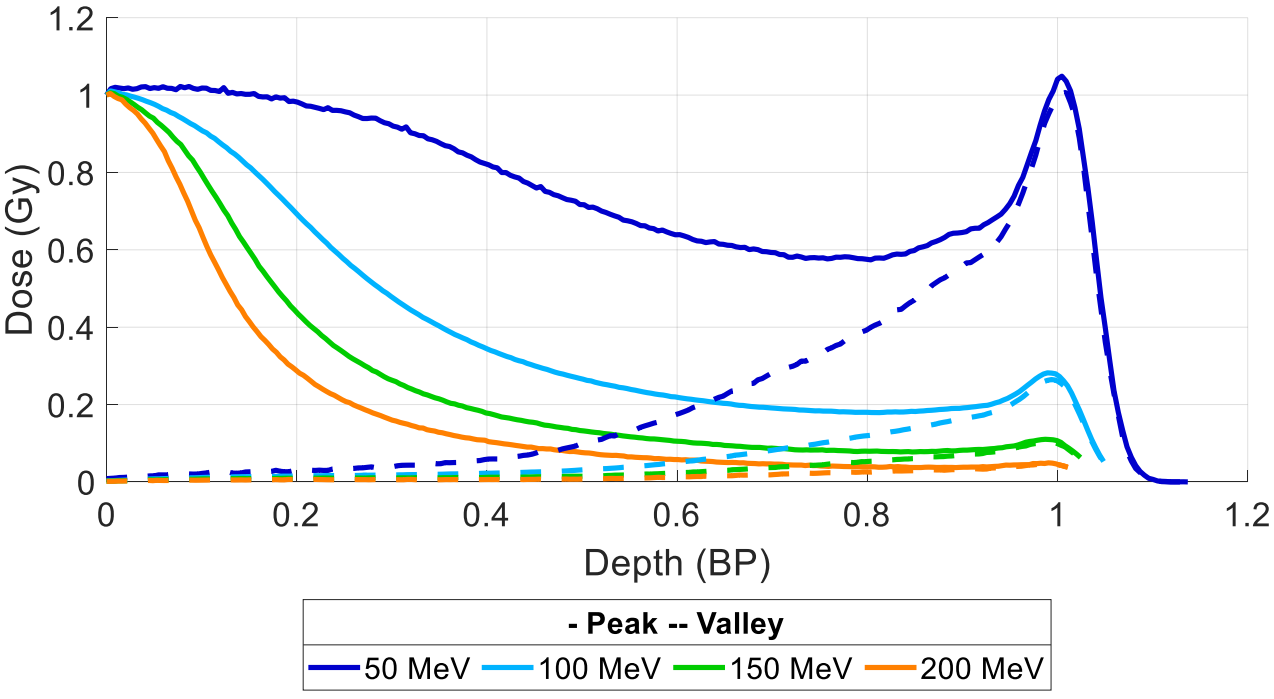

Figure 3.7:PDD for peak and valley for various proton minibeam energies. Dose is scaled to the entrance dose. Depth is normalised to the Bragg peak.

While this high surface dose is a concern with a uniform dose distribution, due to increased damage delivered to normal tissue. This is likely to not have a negative effect on proton minibeam dose distributions as normal tissue tolerance is believed to correspond to the valley dose. The rest of the results section is split into how the minibeam CTC spacing and width are impacted by motion.

3.2.1. CTC Spacing

A minibeam dose distribution was generated for each motion range from 0 – 10000 μm and was analysed using the method described below. For clarity, only a small number of the motion simulations are shown, The range chosen was 0, 60, 90, 150, 240, 400, 660, 1100, 1800, 3000, 4900, 8100 μm, these are on an exponential curve so the range could be covered evenly.

A depth dose curve was generated for each dose distribution for the peak region and the valley region. Rather than generate the depth dose curve from a single voxel at each depth a small width and height, 100 μm, was averaged, this reduced noise in the data. The peak curve is generated from the central voxels of the beamlet 100 μm in the width and height directions. Of the eleven beamlets, the two edge were ignored for this section of work, as they had lower dose at the Bragg peak, due to less dose being spread from one adjacent, instead of two adjacent beamlets. The remaining nine beamlets were averaged together to reduce fluctuations from individual histories, thus reducing noise. The valley curve is generated from the 100 μm wide central voxels that are evenly spaced between the peaks. The valley curve is processed with the same method to how the peak curve is generated. With

the peak and valley curves generated the PVDR can be calculated as the ratio between the two. This is often used as a metric in spatially modulated dose distributions, as discussed in Chapter 2. The width of the minibeam is measured from the 50% of the maximum dose of the peak of the minibeam profile for all depths, for values when the minimum dose is greater than 50% of the maximum dose the beam width is then equal to the CTC spacing, or the dose is uniform. This threshold of 50% of the maximum dose was selected as a usual standard of full width half maximum is used to measure with width of Gaussians and provides an adequate estimate of the area which the minibeam covers.

The four metrics described above, peak dose, valley dose, PVDR and beam width were calculated for each motion magnitude and are used to produce Figure 3.8 – 3.11 for the 50 MeV to 200 MeV proton minibeam distributions, respectively. The peak and valley dose have been normalised to the Bragg peak of the zero-motion result. Results only display motions which were less than the CTC spacing for each energy, as in motions larger than this the dose distribution becomes uniform.

The peak dose shown in Figure 3.8 – 3.11 demonstrates that all energies follow a similar trend, where motion has a large impact at the surface and this impact decreases with depth. Increasing the energy of the minibeams does not appear to change the relationship between motion and the peak dose. Which implies that increasing the CTC spacing does not have an influence on this as beam energy is linked to CTC spacing for this setup. It can be observed that the peak dose at the Bragg peak will sometimes exceed a dose of one Gy as large motions cause some overlap in the minibeam peaks resulting in increased dose. A discontinuity in the peak dose data can be observed in the Figures 3.8 – 3.11, between the 240 and 400

µm motions, where the peak dose only decreases by 10 – 15% before the discontinuity, and after by 37 – 44%. Occurring when the motion exceeds the width of the minibeam in this case 300 µm, this is investigated further in the next section of results. For the 60 µm motion scenario the peak dose at the surface only has a 1% drop, demonstrating a minimal impact for small mouse motions.

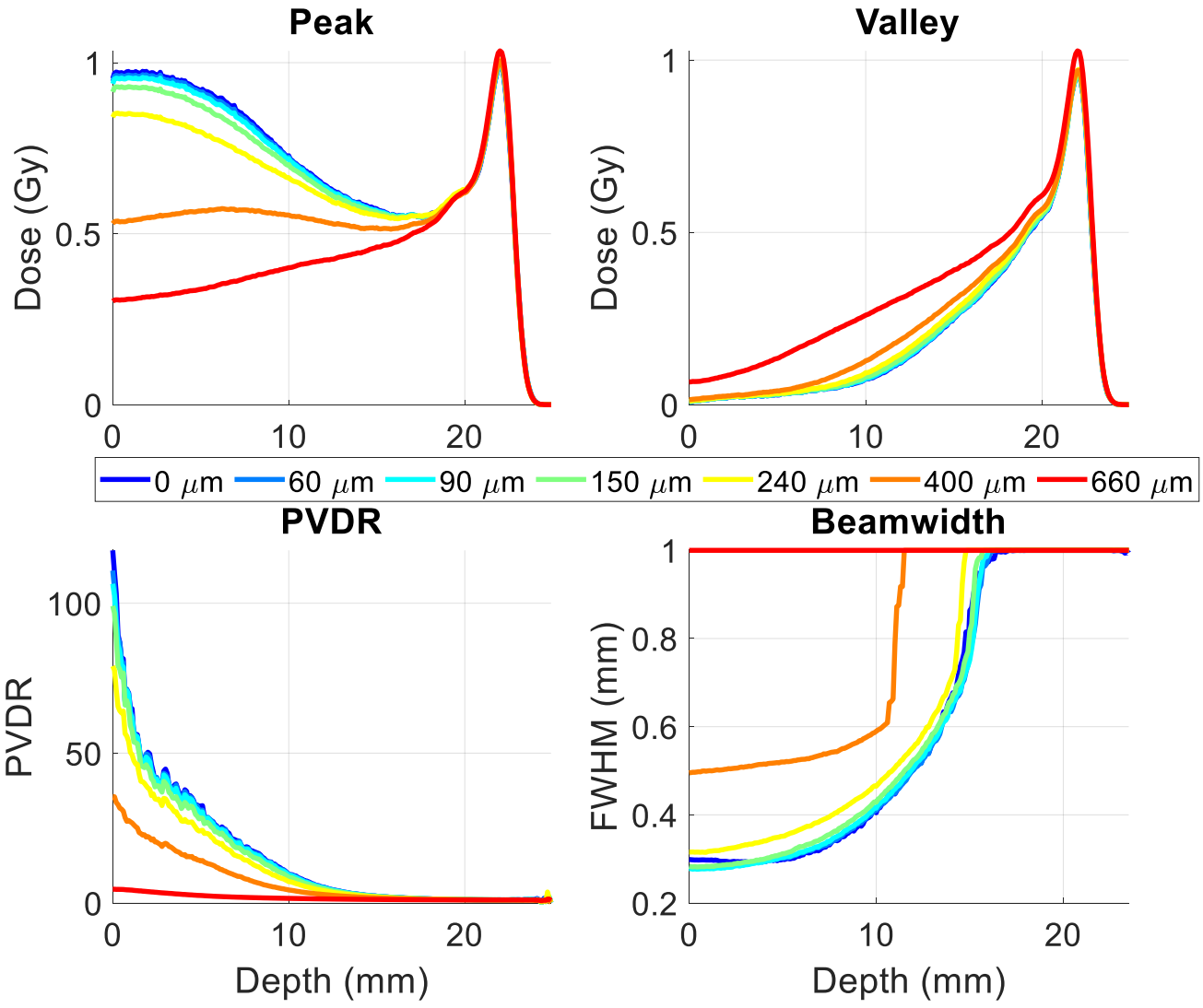

Figure 3.8:Impact of motion on the peak, valley PVDR and beam width for a 50 MeV proton minibeam dose distribution

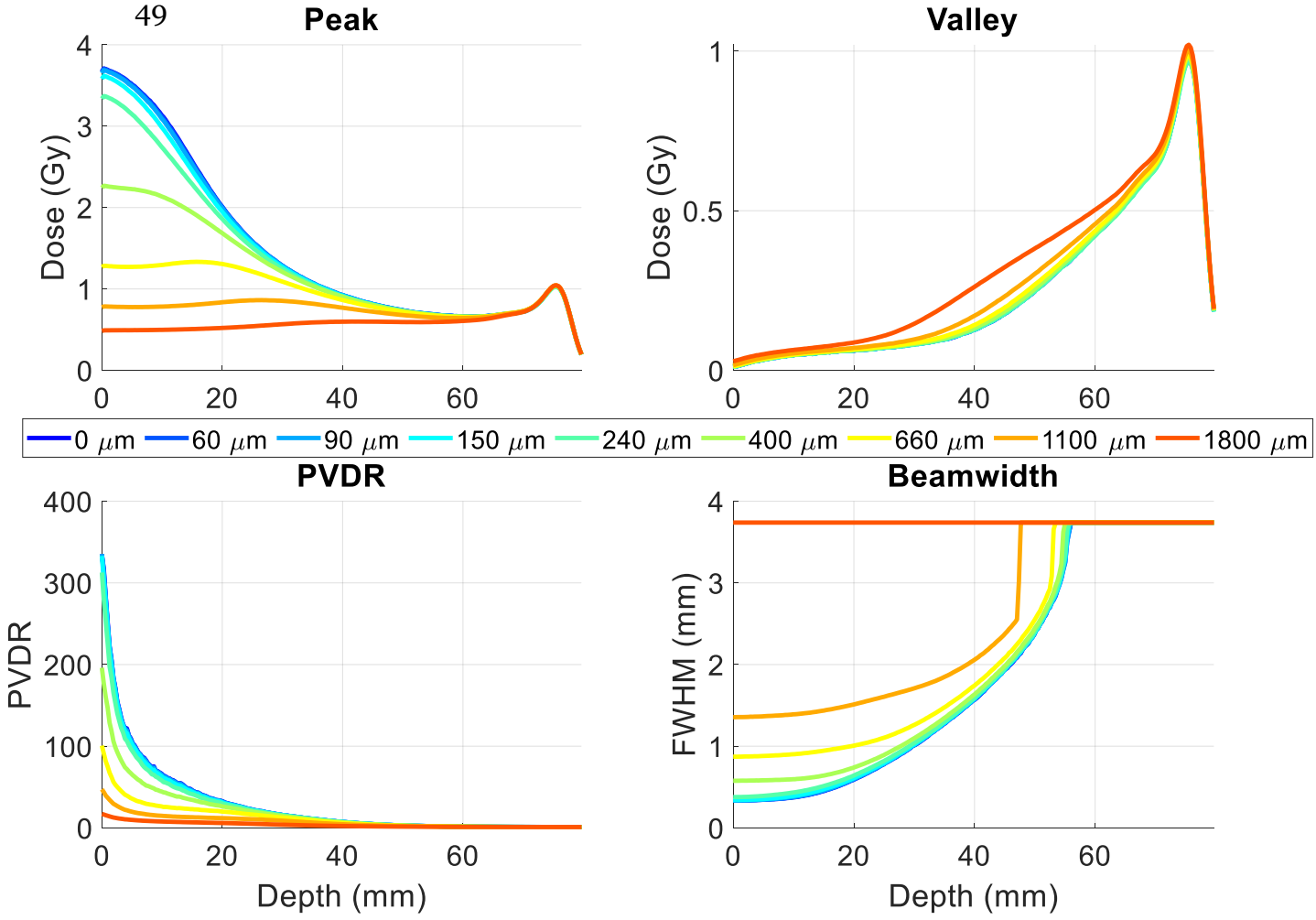

Figure 3.9:Impact of motion on the peak, valley PVDR and beam width for a 100 MeV proton minibeam dose distribution

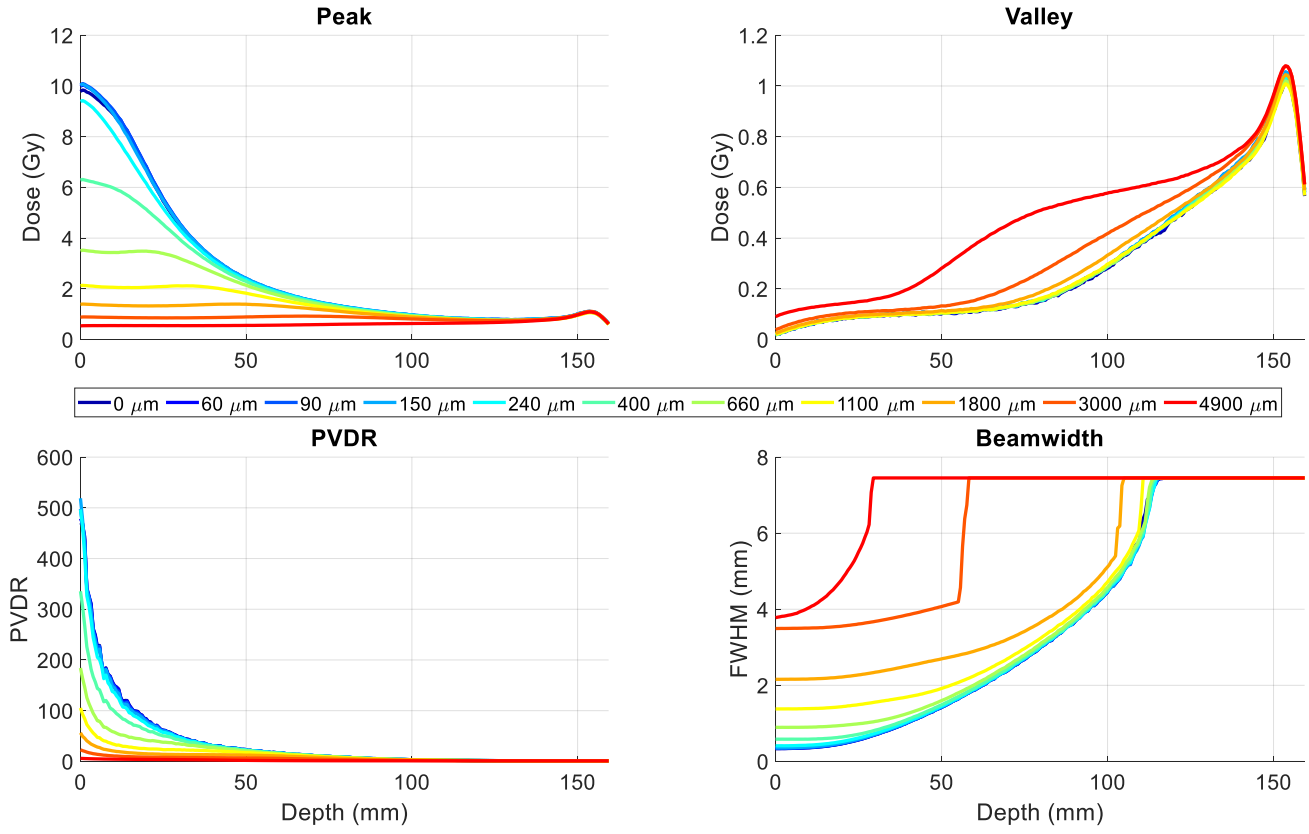

Figure 3.10:Impact of motion on the peak, valley PVDR and beam width for a 150 MeV proton minibeam dose distribution

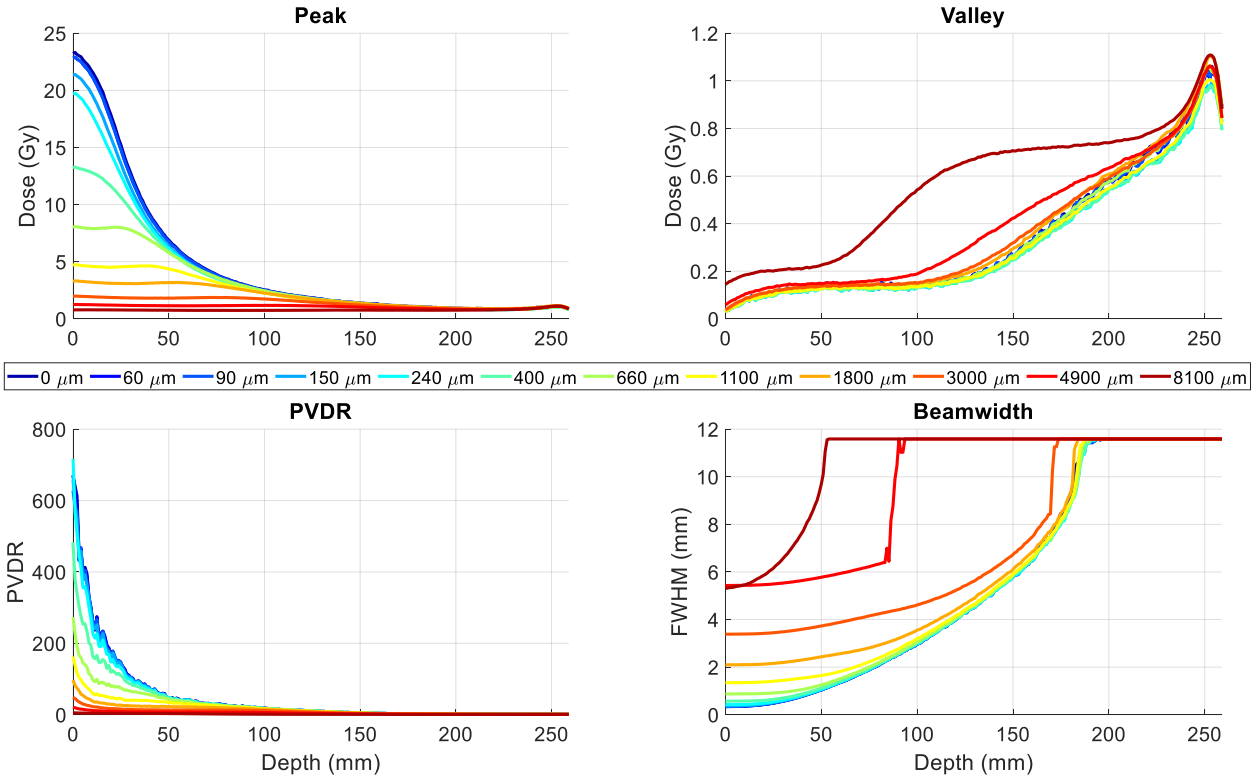

Figure 3.11:Impact of motion on the peak, valley PVDR and beam width for a 200 MeV proton minibeam dose distribution

The valley dose shows similar trends in Figures 3.8 – 3.11, where motion has a minimal impact at both the surface and the Bragg peak, but affecting a region part way between them. For the valley dose to be increased, dose from the minibeam peak regions needs to be spread into the valleys. This occurs when the minibeams are broadened to a width nearing the CTC spacing. Minibeams have been shown to broaden with depth, however, motion also broadens the minibeams causing a compounding effect, which results in an increase in the valley dose. This demonstrates that the ratio between motion and the CTC spacing is important in maintaining a low dose in the central valley regions. For the 60 µm motion scenario the valley dose at the surface only has a 2% increase, demonstrating a minimal impact for small mouse motions. As motion increases the depth where the valley

dose is impacted decreases, this is further shown in the beam width results in Figures 3.8 – 3.11.

The PVDR results follow similar trends for all energies, being greatest at the surface and decreases with depth. The impact of motion is greatest at the surface, decreasing the PVDR by the largest amount. The impact motion has on the PVDR depends more on the large decrease in the peak dose rather than the small increase in the valley dose, due to the high spatial modulation at the surface.

Results from the beam width demonstrate that the full width half maximum (FWHM) of the beam increases with depth until it becomes uniform slightly before the Bragg peak. Motion increases the width of the minibeam at all depths. It is typically expected that the width of the minibeam plus the motion would equal the measured FWHM at the surface, this does not occur as the FWHM measures the width at the halfway point so the overall width at the base of the minibeam has increased but the width halfway up might not have change by the same factor. This can also lead to some artefacts where motion appears to reduce the width of the minibeam. Motion has a secondary effect where it reduces the depth where the minibeams merge into a uniform beam, this occurs rapidly before the Bragg peak and appears as a sharp increase in the width of the minibeam. Increasing the spacing between the minibeams allows a reduction in the amount of dose that can be spread into the centre of the valleys.

Overall, it can be observed that motion has the greatest impact on the peak dose, decreasing by a similar magnitude for all energies at the surface. The decrease in the peak dose is dependent on the width of the minibeam. This is explored further

in the next section. When the width of the beam increases with depth, motion is able to spreads dose from the peak regions into the centre of the valley. This makes the central valley region vulnerable to motion at a depth between 25 – 75% of the depth of the Bragg peak.

3.2.2. Minibeam Width.

This section of results investigates how the dose for different slot widths is impacted by motion. The peak dose, valley dose, PVDR and beam width were all produced with the same method as the previous section. A motion range of 0 – 660 mm was chosen to cover a wide range up to where the minibeams start to merge into a uniform dose distribution. In the following, only four representative sets of data are shown for clarity, displaying minibeams with widths of 100, 300, 500 and 700 μm. Each setup has a CTC spacing of 1 mm between the minibeams. The results are shown in Figure 3.12 – 3.15, respectively. Results have been normalised to the Bragg peak for the zero-motion result. Some results have a higher Bragg peak than one due to motion merging the minibeams at the Bragg peak.

Results of the peak dose in Figures 3.12 – 3.15, demonstrate that the peak dose is only reduced by up to 15% for motions less than the width of the minibeam beamlet. It would be expected that the peak dose would not decrease for motions less than the width of minibeam beamlet. However, the minibeams are not flat so a small decrease is observed in the peak. For motion larger than the width of the minibeam beamlet the peak dose rapidly reduces in height.

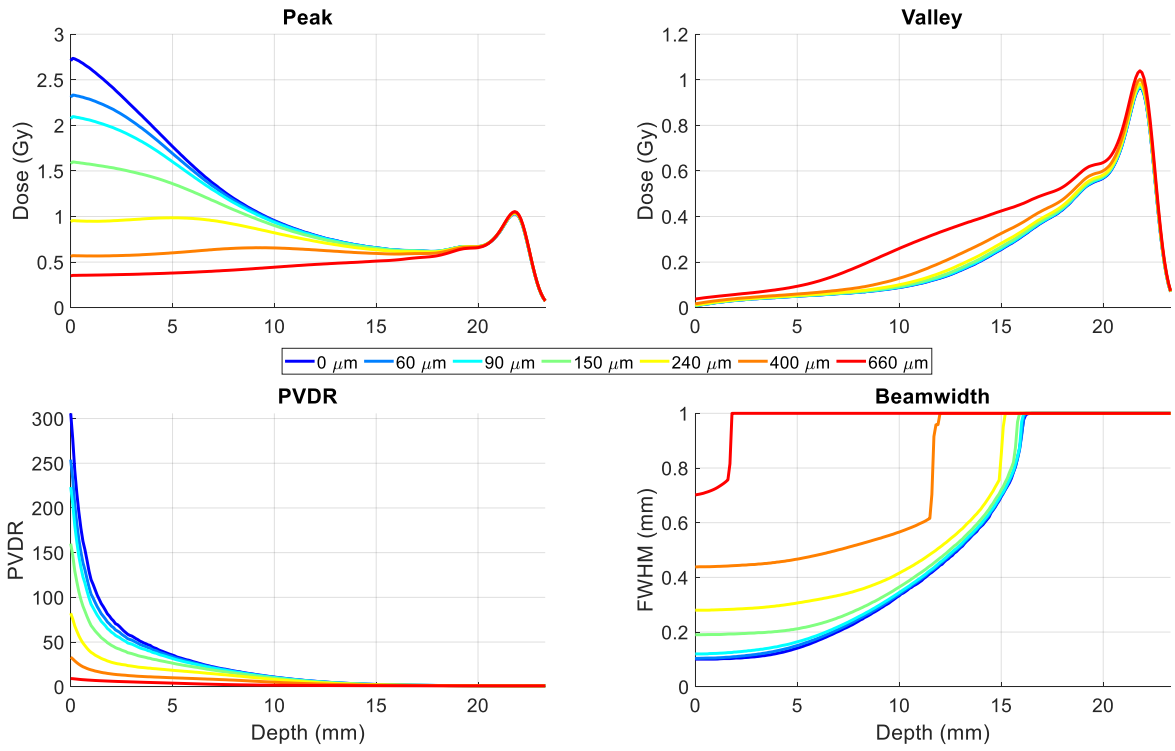

Figure 3.12: Impact of motion on the peak, valley PVDR and beam width for a 100 µm wide 50 MeV proton minibeam dose distribution

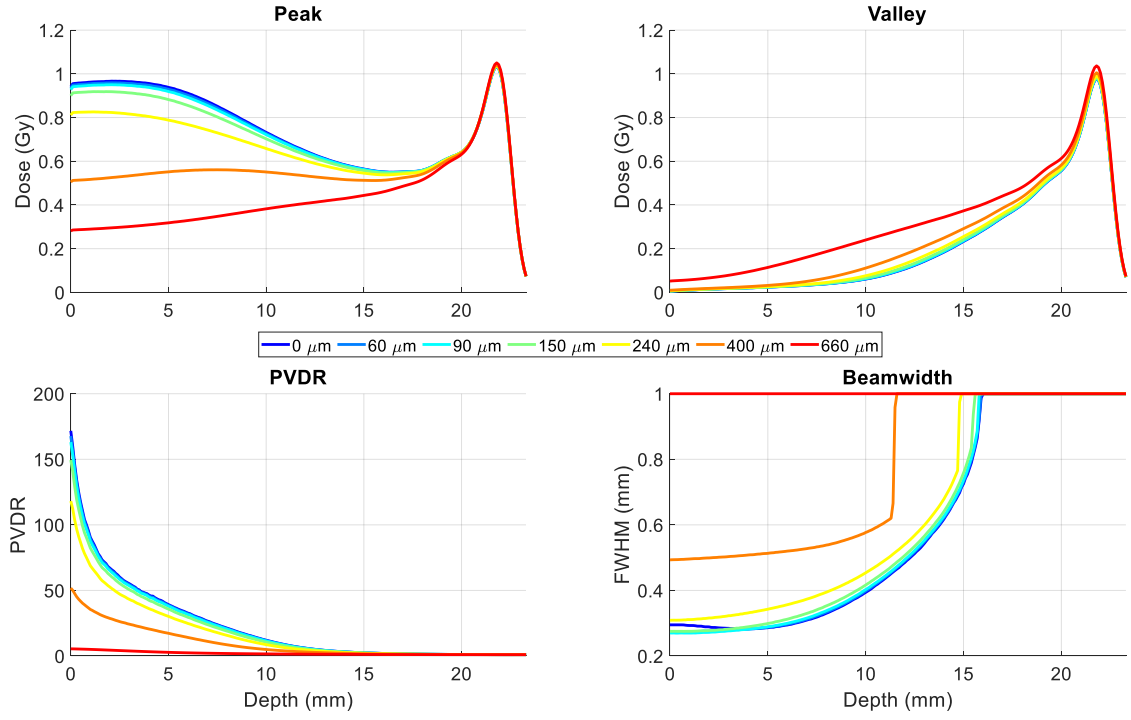

Figure 3.13: Impact of motion on the peak, valley PVDR and beam width for a 300 µm wide 50 MeV proton minibeam dose distribution

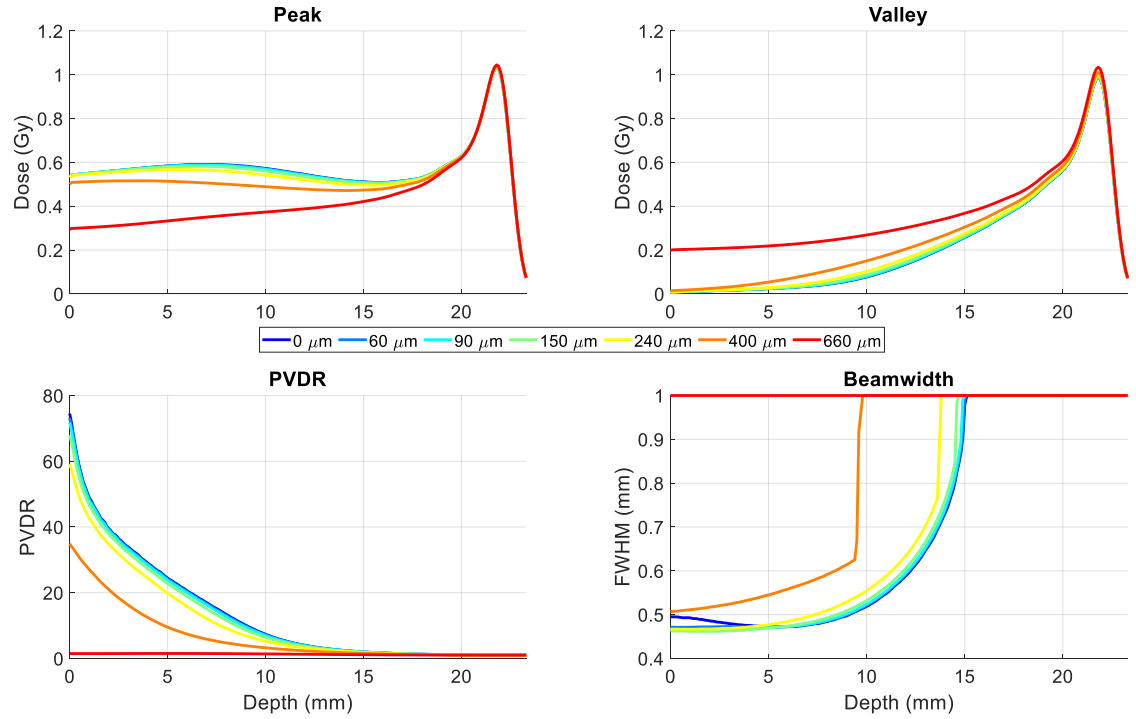

Figure 3.14: Impact of motion on the peak, valley PVDR and beam width for a 500 μm wide 50 MeV proton minibeam dose distribution

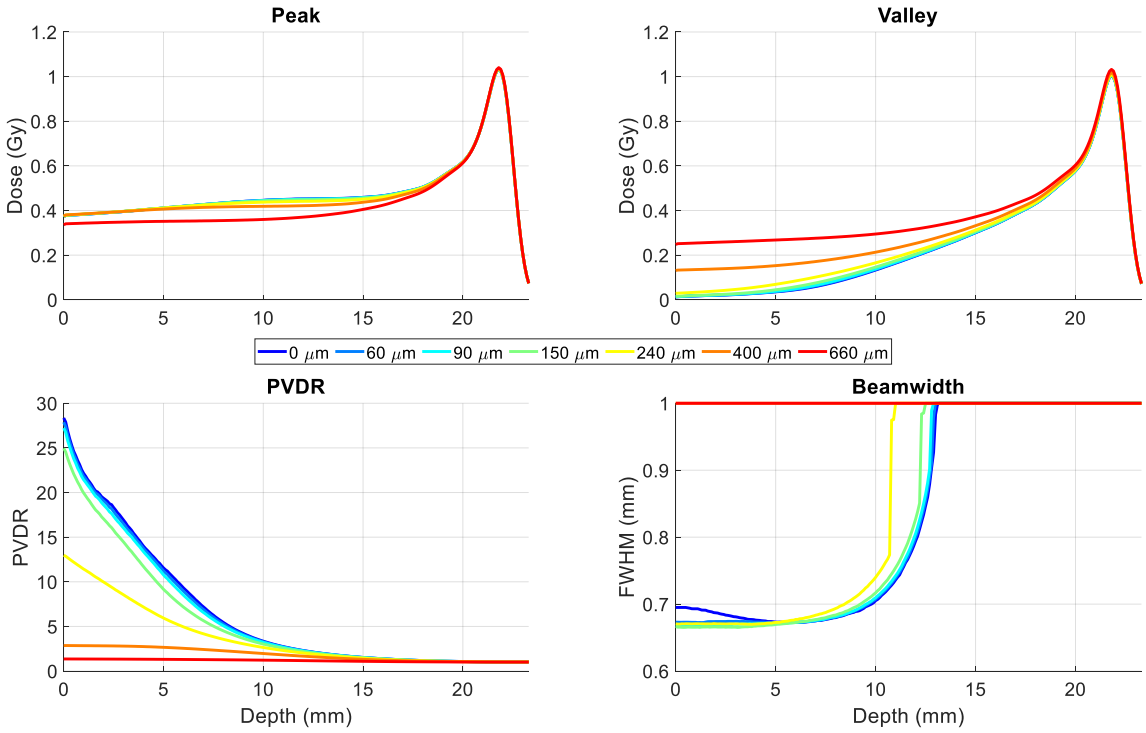

Figure 3.15:Impact of motion on the peak, valley PVDR and beam width for a 700 μm wide 50 MeV proton minibeam dose distribution

The valley results show that increasing the width of the minibeams, whilst maintaining a constant CTC spacing, results in more dose spread into the valleys. This makes the valleys more susceptible to motion. The valley results show that there is a depth where they are most susceptible to motion, this depth is located partway between the surface and the Bragg peak and depends on the magnitude of motion applied and the width of the minibeam.

The PVDR results agree with the previous results showing that the reduction in the PVDR primarily depends upon the reduction in the peak dose. Therefore, as the width of the minibeams is increased, and the peak dose is less susceptible to motion, the PVDR is also less susceptible to motion. This does have the drawback that the overall PVDR is less with wider minibeams.

The increased width of the beam results in a decrease in the depth where the beam becomes uniform. Overall, the width of the minibeams show similar effects of motion with the primary difference being the initial starting width of the minibeam and the depth where the minibeams merge into a uniform dose distribution. The results from this section clearly show that increasing the width of the minibeams is beneficial at reducing the impact motion has on the peak dose but it does increase the dose delivered to the valley, reduce the PVDR and decrease the depth where the minibeams merge into a uniform beam.

3.3. Discussion

This discussion is divided into three parts. Firstly, the results of the impact motion have on the minibeam peak dose distribution. This region delivers high dose tracks through normal tissue and maintaining high peaks means that less dose is spread into the valley regions. Secondly, the impact on the valley dose distribution. The valley region is a key region in proton minibeams, as normal tissue damage in this region is believed to be correlated to the valley dose. Maintaining a low valley dose reduces normal damage to this tissue. The last section discusses the overall impact motion has on proton minibeams and combines the results from the previous discussions.

3.3.1. Impact of Motion on Peak Dose

When motion is applied it has been shown to widen the minibeam and spread dose from the peaks into the valley regions, which reduces the PVDR. The high surface dose in the peak regions may been seen as a concern, however, previous research has indicated that these regions are likely to be repaired by the surrounding normal tissue [53, 72, 84]. It is therefore vital to maintain the height of these peaks, so dose is not spread into the valleys and any reduction in the peak dose is subsequently added to dose in the valley regions.

The results from the CTC spacing simulations demonstrate that increasing the spacing between the minibeams does not an impact on the peak dose or limit the impact motion has on it. Differences observed in the results can be attributed to the different energies used in the simulations, which produce various magnitudes

and types of scatter with a range of energies. The peak dose is less impacted by motions that are less than the beamlet width. Larger motions will rapidly decrease the peak dose. This creates a plateau effect for motions smaller than the width of the beamlet. Which occurs as a product of the geometric design of the collimator and minibeams. For a beamlet with a flat profile it is expected that there should be no decrease in maximum dose when the amplitude of the motion is less than width of the minibeam. However, some differences are observed this indicates the profile of the minibeam is not flat.

3.3.2. Impact of Motion on Valley Dose

It is critical to maintain a low valley dose to minimise biological damage to surface and normal tissue [53, 72, 84]. Results from the CTC spacing simulations (see Figures 3.8 – 3.11) demonstrate that there is a relationship that increasing the spacing between the minibeams reduces the effects motion on the dose distribution. This occurs as increasing the spacing decreases the amount of dose that can be delivered to the central region of the valleys. If the spacing between the minibeams is greater than the width of the minibeam plus motion, then minimal dose from the peak can reach the centre of the valleys. This allows higher energy beams to less impacted by motions with larger amplitudes, this is beneficial for scaling from small animals to human size motions as human treatments will use a higher energy with increased CTC spacing.

Increasing the width of the minibeam has been shown to reduce the threshold for motion to spread dose from the peak regions into the valley regions. Increasing the

CTC spacing is shown to counteract this problem by increasing the width of the valleys between the minibeams.

The broadening of minibeams with both depth and motion has been shown to have a threshold at a depth between the surface and the Bragg peak where the valley dose is rapidly increased. This occurs when the motion plus the width of the minibeam at depth approaches the CTC spacing between the minibeams, thus spreading dose into the low dose regions. Any motion will impact the valley dose at some depth as the spacing between the minibeams trends towards zero when they merge at the Bragg peak. Therefore, motion decreases the depth where the peaks merge into a uniform dose. This problem is limited by modulation of the dose distribution decreasing with depth.

3.3.3. Impacts of Motion on Proton Minibeams

The combined results of the PVDR showed a strong relationship between the decrease in the peak dose caused by motion and the decrease in the PVDR at the surface of the water phantom. The PVDR is often used in the literature to gauge the spatially fractionation of a modulated dose distribution, and therefore is used to gauge the quality [63, 71]. Results showed that increasing the width of the beamlet did help to limit the impact of motion, however this did reduce the PVDR and the width of the beamlet has been shown in photons to be inversely related to the normal tissue sparing [11-13]. The microbeam sparing effect has also been observed in x-ray synchrotron generated beam with widths of up to 0.68 mm [57]. Assuming this minibeam width is applicable to proton minibeam, this creates an upper bound for the beam width. This is an important consideration as proton beams broaden with depth. Avoiding this potential limit will help maintain normal tissue sparing. Therefore, it is not recommended to increase the width of the beamlet whilst trying to reduce the impact of motion. Further investigation into the width of the minibeam is investigated in Chapter 5.

Healthy tissue sparing is also believed to depend on the valley dose [63]. The key method investigated, which helped in reducing the valley dose in the presence of motion was increasing the CTC spacing between the minibeams. The ability to increase the CTC spacing is limited without increasing the energy of the proton beam without reducing uniformity in the dose distribution at the Bragg peak. Human brain motion has a been observed to have a maximum motion of 300 μm, therefore using a minibeam of equal width will have reduce the impact from this motion [69]. For small animal studies a maximum motion of 60 μm was observed

in a rat brain [85]. Based on the simulations in this chapter, this small motion should have very minimal effect on the overall dose distribution and allows the use of small minibeams in treatment without compromising the minibeam maximum dose. The results from this research indicate that motion less than 300 μm only has a minimal impact on the valley dose. Therefore, the effect of motion on normal tissue should be minimal. The impact of motion on the valley dose primarily depends on the minibeam CTC distances. Therefore, if the distances are significantly greater than any applied motion then the effect of motion will remain minimal.

Motion has been shown to decrease the depth where the Bragg peak dose becomes uniform. This could potentially be used to improve the uniformity at the Bragg peak. If the motion is regular and repetitive narrower beams with greater CTC spacings could be used to produce a dose distribution that is still uniform at the Bragg peak. For example, for the simplified scenario modelled here, if the mean amplitude of motion in a particular human brain is 120 μm then the CTC spacing could be increased by this same magnitude and the minibeam width could be decreased by the same amount. Care should be taken with this as most motions will not be fully predictable and repetitive and the profile of the dose distribution will be less sharp than an equivalent distribution with no movement.

It should be noted that this work does look at a worst-case model for motion in terms of motions being perpendicular to the slots. This leads to the results potentially over exaggerating the impact of motion for a given motion value. To correct for this a smaller amount of motion would be used if the direction of motion were at an angle to the direction of motion modelled. The overall motion could be

reduced to just the component that matches the direction modelled. Another limitation of this work is this model uses a monoenergetic beam that produces little scatter, future work should verify these results on a more realistic beam that can generate a spread out Bragg peak.

3.4. Conclusion

This chapter investigated and characterised the effects of motion on the dose distribution for various proton minibeam collimator designs, providing insight into a critical area of research that currently is currently unexplored. This work is novel and covers a wide range of motion relevant for small animal irradiation, but also extends to clinical beams and as such is easily translatable to a range of proton minibeam geometries.

It was demonstrated that whilst motion can be problematic for proton minibeam dose distributions, by spreading dose from the peak regions into the valley regions, there are solutions to mitigate this effect. These include maximising the CTC spacing to reduce the ability of motion to reach the centre of the valleys and minimising the widths of the minibeams in order to reduce collateral damage from them. This work also demonstrates that for an expected motion of 60 μm in mice brains, the impact minimal for all minibeam width investigated, with a drop of less than 1% in the peak dose and an increase of 2% for the valley dose. For proton energies and geometries relevant for human patients, the results show that a greater CTC spacing allows the valley dose to be unaffected with motions smaller than 1000 μm.

The effect of motion has been shown to have minor impact on the peak minibeam dose for motions less than the beam width of the minibeam. The decrease in peak minibeam dose caused by motion is greatest at the surface and decreases with depth, this effect is primarily dependant on depth and not energy/spacing. It was determined that the area between the surface and the Bragg peak is the most affect

by motion due to the diverging beamlets. Human scale motions on the order of 300 μm have minimal to no effect on the valley dose for 100 MeV proton beams and above. This is a result of the valley dose being dependant on the CTC spacing between each of the minibeams. Control of the CTC spacing is determined by the beam's initial energy, to produce a uniform dose distribution a collimator with a specific CTC measurement is required. The effect of motion on the valley dose is therefore dependant on beam energy, with higher beam energies being less impacted by motion due to the larger CTC spacing.

This work primary investigated monoenergetic beams. However, the results should be easily translatable to a wide range of multi-energy proton beams as the primary difference would be the depth where the beamlets merge into a uniform distribution. An assumption made during this research was that the treatment time would be much longer than the motion that would occur, so the effect of motion would be the sum of all small motions that occurred during a treatment. If the patient was shifted during treatment or the treatment time was shorter than a period of motion, then some of these results might not fully apply to that situation. It was also assumed that motion would not deform the shape or the density of the target, this would modify the resulting dose distribution in ways that are not fully modelled with this setup. However, these results should provide a baseline and provide a good initial approximation for most cases.

A critical area of future work is determining the full extent of the relationship between the width of minibeams, and their sparing effect. This is of importance for proton minibeams that diverge and increase their width with depth. This would require biological experiments and is beyond the scope of this thesis. This

biological experimental information is also key to complete the motion work and give a complete guide to how minibeams can be designed to reduce the impacts of motion. While high dose proton beams are possible in the future there will still always be some degree of motion present that reduces the spatial modulation by some degree and should be considered.

Chapter 4

Monte Carlo Modelling of the Preclinical Proton Beam

This chapter introduces modelling of the Precision Proton Radiotherapy Platform proton beamline at the University of Washington. A detailed Monte Carlo model was developed, including all beamline components, which was used in later chapters of the thesis. The model output was compared and verified against measurements from the real output of the proton beam. A novel in-depth analysis was then performed on the impact of each of the beamline components, to determine the scatter contribution from each component and the impact they have on the final dose distribution. This chapter has been published in part in Meyer *et al.* [18].

4.1. Introduction

The University of Washington Clinical Cyclotron was installed in 1983 and primarily used to treat patients with fast neutrons produced by bombarding a beryllium target with protons [86]. Currently a second neutron treatment room is setup as a proton research facility, referred to as the Precision Proton Radiotherapy Platform (PPRP). The PPRP outputs a proton beam of up to 50.5 MeV and is shown in Figure 4.1. The relatively low proton beam energy, compared to clinical proton

beams with a maximum energy of typically around 230 MeV, is ideal for biological studies on small animals, such as mice due to the shallow depth of the Bragg peak of approximately 20 mm in water. It is possible to conduct biological studies on a clinical proton beam, however, in order to do so the beam energy would need to be degraded. This requires the use of a degrader or range modulator, which absorbs energy from the protons. Which has the side effect of introducing scattered radiation, thus reducing the quality of the beam from near monoenergetic with a pristine Bragg peak to a poly-energetic beam with a lower dose rate, and a flattened Bragg peak. The aim of this chapter was to develop a full and accurate model of the proton beamline in TOPAS, with the intention to use it for current and future biological proton beam experiments.

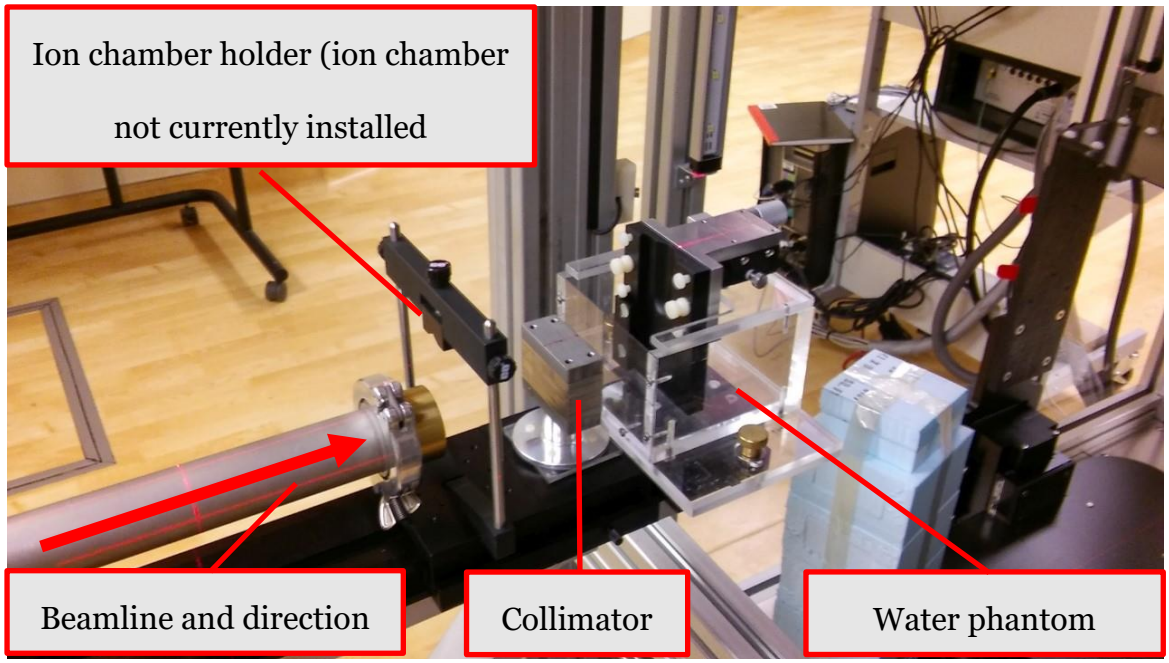

Figure 4.1: Image of PPRP beamline with minibeam collimator and water phantom. Note the ion chamber is currently not in place in the picture.

The cyclotron beamline has been in operation for over 35 years, and whilst for most parts of the beamline detailed documentation was available, it was found that some changes to the original beamline have not been recorded or detailed records could not be found. It is currently impractical to disassemble the entire beamline to catalogue all components. Therefore, there was some uncertainty in the materials and intricate details of the design of some components.

The goal was to model known components accurately and estimate unknown details to the best available knowledge before refining and analysing the model through physical measurements of the current beam. Interactions between the beam and each component in the beamline as simulated in the model was examined to identify where energy or particles are lost and determine any impact the secondary radiation produced had on the final dose delivered. Future proton minibeams radiobiological experiments will make use of the model and forms a real-world grounding for much of this work.

4.2. Methods

TOPAS 3.0.1 was used for modelling with the default physics lists, remaining consistent with the previous chapter in this thesis. The output from the model was then processed in MATLAB version R2016a. The following method used in the chapter is divided into four sections. The first discusses the initial design of the model produced in TOPAS and the various components modelled. The following section explains methods used in measuring the physical dose delivered to a water phantom from the 50.5 MeV beam at the University of Washington. These physical measurements are used to verify the TOPAS model of the beamline. The third section covers the modelling of scatter from beamline components, and how each component degrades the energy of the proton beam. The final section explains the methods used to model how each component of the proton beamline affects the final dose distribution delivered to the water phantom.

4.2.1. Producing a Model of the PPRP Beamline in TOPAS

A TOPAS model was produced which contains of all components of the 50.5 MeV proton beamline at the University of Washington that are downstream from the cyclotron. The cyclotron was excluded from the model as the output from it is a monoenergetic 50.5 MeV proton beam, and majority of the degradation of the beam occurs downstream, this assumption is based off previous work [23].

TOPAS simulations start with what is defined as the ‘world’ box which contains all other components. For the simulations used throughout this chapter the world is defined to be composed of air to simulate realistic degradation of the beam in

getting to the target. All other components are then added to the world. It should be noted that whilst the world is air-filled, some components can still contain vacuum inside them to match the physical beamline, as necessary. Figure 4.2 is a diagram displaying the various components of the beam, which are modelled in the simulation. This next section will work through each of the components in the beamline in the order in which the beam traverses them.

First the near monoenergetic proton beam from the cyclotron encounters a beam degrader. This is located upstream to the left of the diagram and is not shown for clarity due to the long length of the large beampipe. The degrader consists of a 1.23 mm sheet of graphite that is the entire width of the beampipe.

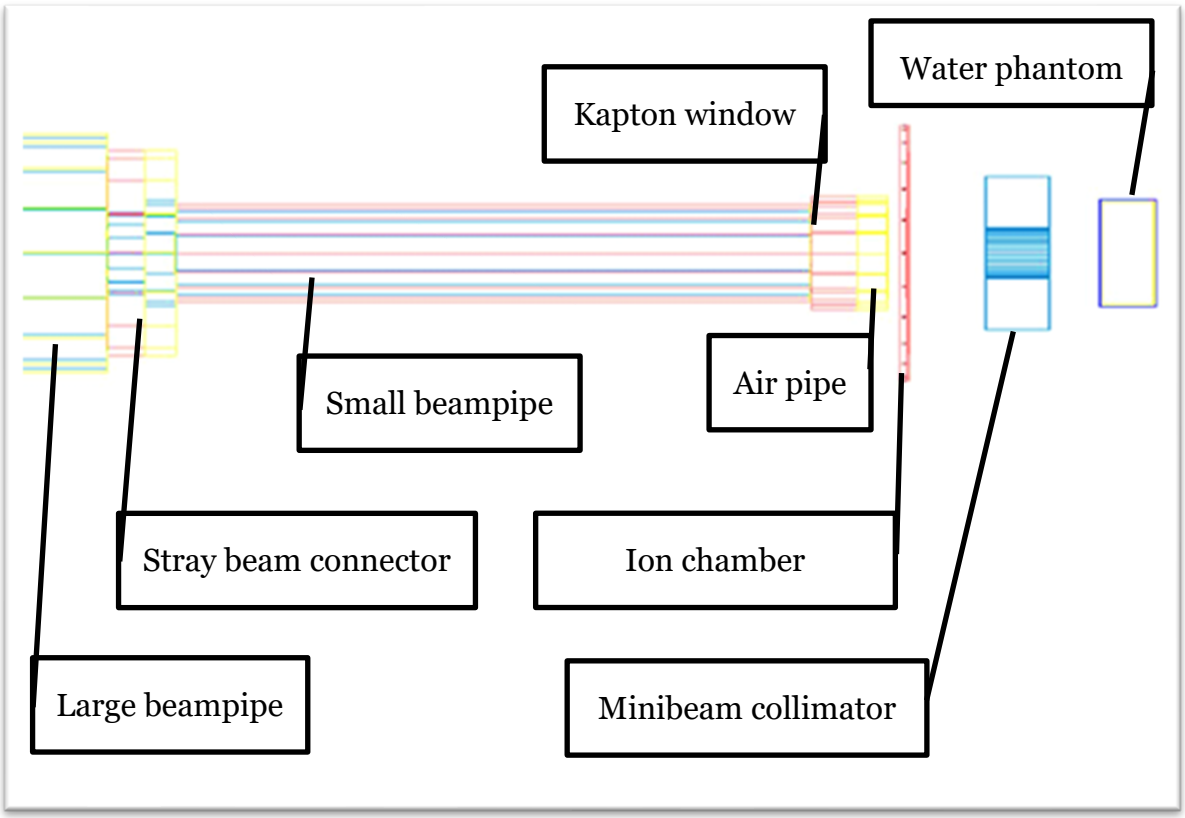

Figure 4.2: Diagram of the components in the TOPAS model of the PPRP. The proton beam enters the large beampipe from the left. The beam degrader is not shown for clarity.

The degrader has two functions, first to spread out the narrow pencil beam coming from the cyclotron in to produce a wider beam on the beam exit side. The second is to decrease the ultra-high dose rate of the beam to dose rates comparable to that of clinical photon and proton beams. As a consequence, the peak energy of the beam is reduced, and scattered radiation is produced as the protons pass through it. This is explored later in this chapter.

The beam then travels down a large stainless steel beam pipe, 4.158 m long with an internal radius of 30 mm and a thickness of 1.75 mm. Vacuum is maintained in the large beam pipe, stray beam connector and small beampipe, ensuring that the beam does not interact with any particles on its path which would degrade it as it travels. The large beampipe then connects with a 26 mm long graphite and stainless steel stray beam connector which is used to reduce the diameter of the beam and connect it to a smaller stainless steel beam pipe. The radius of the beam is reduced from 30 mm to 16 mm when passing through the stray beam connector.

The beam then travels down the small beam pipe with an internal radius of 19 mm and an outer thickness of 1.5 mm and a length of 255 mm. Upon exiting the small beam pipe, the beam passes through a 0.15 mm long Kapton window into an air-filled room. The Kapton window maintains a vacuum inside the beampipes and is designed to reduce the energy of the beam by a minimal amount. The beam passes through an air-filled pipe, no interactions between the beam and the pipe occur due to its larger internal diameter. Once in the air-filled room, the beam passes through a pancake ion chamber, used for monitoring the amount of dose delivered. For minibeam experiments the beam is passed through a 25 mm long stainless steel collimator, reshaping the uniform beam into spatially modulated minibeams.

The collimator was designed as part of this thesis and was based using results obtained in Chapter 5. The collimator contains 31 individual 0.3 x 30 mm air-filled slots cut out of it, each slot is spaced 1 mm CTC, creating a 30 x 30 mm minibeam field. During some simulations and setups, the minibeam collimator is omitted to allow a uniform beam to deposit dose in the water phantom. After exiting the collimator, the beam travels 23 mm before depositing dose into a water phantom. A cube with sides of 4 cm, which is surrounded by 1 mm of Lexan. The simulated water phantom is smaller on the distal side than the physical water phantom. As the beam only deposits dose to a small volume of the phantom and simulating the remainder of the phantom would have only increased computational complexity with no additional benefit. This covers all components of the beamline that were simulated in this chapter. The next sections of the methods will cover any changes to this model and any other methods used.

4.2.2. Verification of PPRP Model

For this section, simulated dose delivered to the water phantom is verified against physical measurements on the PPRP at the University of Washington. The minibeam collimator was removed from both the TOPAS model and the real beamline, enabling an open field comparison to be performed, with the goal of matching the PDD from TOPAS to the measured PDD on the beamline.

The TOPAS model used in this section is based on the model described in Section 4.2.1, with a few small modifications. First the minibeam collimator is removed from the model as explained previously. Then the exterior of the water box was removed, enabling an easier comparison between the measurements and modelled

values. This was done because the water equivalent depth of the material on the surface of the water box was included in the measured values. The modelled water phantom was divided into 100 μm voxels in the depth direction, no divisions were made in the other directions. Ensuring high resolution for producing depth dose curves to compare to the measured results and reduces statistical variation from individual histories in the Monte Carlo simulation. The simulation calculated 100 million histories for this section.

The physical dose measurements were performed with an Exradin Spokas A11 parallel plate ion chamber with a collecting volume of 0.62 cc (Standard Imaging, Middleton, WI, USA) and a micro-Diamond detector (Type 60019, PTW-Freiburg, Germany) with a nominally sensitive volume of 0.004 mm^3. The detectors were able to be precisely positioned in the water phantom with a motion stage with the ion chamber positioned in 1 mm steps in the build-up region of the Bragg peak and 100 μm steps close to the Bragg peak. Higher spatial resolution was used around the Bragg peak as this region has a much higher dose gradient. The micro-Diamond detector was moved in steps of 500 μm.

4.2.3. Modelling Beamline Components Scatter in TOPAS

This section aims to gain and understanding of how each component interacts with the beam and how the beam was degraded from the initial 50.5 MeV beam. The entire beamline is simulated including the minibeam collimator. The large beam pipe's radius was modified from 30 to 45 mm as per results explored later in Section 4.3.1. This was to be done to better match the TOPAS model to measured values. This change will be used throughout the remainder of the thesis. How each

component alters these particles as they pass through is of particular interest. As the beam predominately interacts via Coulomb interactions with the components along the path of the beam the particles will lose energy and produce secondary particles. To collect particle information phase space filters were placed on the front and rear surface of each component orthogonal to the beam. The filter counted every particle passing through it and measured their position, direction, angular cosine, energy, and particle type. This naturally generates a large amount of data and analysis of this data provides an in-depth picture and valuable insight of where particles are produced and absorbed throughout the beamline.

Ten million histories were simulated for this investigation. The number of histories is smaller than the other simulations performed throughout this thesis. Recording all the details to all particles is very diskspace dependent and total useable RAM puts constraints on the maximum number of histories. As this method collects particles over the entire surface of each component the number of histories required to reduce statistical variation in the mean is lower.

4.2.4. Quantifying Contributions Beamline Components Have on the Dose Distribution

This section explores how the proton beam interacts with each component along the beamline and resulting impaction of the final dose distribution. The primarily interest of this work is any secondary radiation from interactions between the proton beam and components of the beamline. The simulation was designed based on the TOPAS model discussed previously in Section 4.2.1. A simulation with all components was first performed to establish a baseline of dose delivered to the

water phantom. Components were then removed one at a time, firstly from the exterior of the beam in the following order: Lexan exterior of the water box, minibeam collimator, ion monitoring chamber, small air-filled pipe and the Kapton exit window on the end of the small beam pipe. The air in the world was then removed and changed to vacuum, to determine the impact of the beam travelling through a short distance of air. Changing the world to vacuum is also useful are components upstream from this point are vacuum filled. Each component of the beamline was then removed in the following order: small beam pipe, stay beam connector, large beam pipe and the graphite beam degrader. The final simulation was just the pure beam from the cyclotron and the water phantom, with no exterior box, collecting dose. The order used here allows the beam exiting each component to be compared and the cumulative effects of the components to be investigated.

In each of the simulations the water phantom was divided into 40 x 40 x 400 voxels in the x, y, z directions, resulting in voxel sizes of 1 mm x 1 mm x 0.01 mm, respectively. The arrangement of voxels was chosen to increase resolution in the depth direction and decrease the resolution in the other directions, since we are primarily interested in PDDs rather than lateral profiles in this section. Simulation time was reduced and the average number of histories per voxel was increased by reducing the number of voxels in the x and y directions. Results from these simulations were processed in MATLAB. The following section contains results from all of these experiments.

4.3. Results

The results from the models are split into four sections. The first section considers the dose modelling and experimental verification of the model by comparing the physical measured results to the TOPAS model. The second section explores particle energy results from the scatter modelling, displaying the various particles passing through each component of the beam and their energy. The third section containing the beam positional distribution and angular deviation distribution results from the scatter modelling, showing the divergence, and spreading of the beam as it passes through various components. The final section displays results from how the beamline components impact the dose distribution.

4.3.1. Verification of the PPRP

When comparing the results from the dose modelling a comparison of the PDD is used to match the results from TOPAS to the measured results obtained from the ion chamber and the diamond detector. The PDD was selected from the central voxels (along central axis) in the x and y directions and every voxel in the depth direction. PDDs presented within are scaled to have a dose of one at a depth of 5 mm in the water phantom. Results from the ion chamber and diamond detector were obtained in collaboration with the University of Washington. The ion chamber and diamond detector were cross calibrated with a clinical ion chamber from the Seattle Proton Therapy Centre, which is traceable to a primary standard. These results also include a depth calibration to consider the water equivalent thickness of the water tank and the material the beam passes through. The two water tanks used for these measurements were made from Perspex and had a

physical thickness of 1 mm for the ion chamber set up and 1.5 mm for diamond detector set up. The water equivalent thickness of 1 cm of the Perspex is 1.158 cm for a 50 MeV beam [87]. Therefore 1.2 mm and 1.7 mm have been added to all measurement results. These depth measurement results have a 0.5 mm positional zero uncertainty attached to them. The ion chamber and diamond detector have had an additional 0.3 mm added to their depth measurement to allow the depth of their Bragg peak to agree with the Bragg peak depth from the TOPAS model. This offset of 0.3 mm between these results is likely a minor setup error and is within the positional uncertainty.

Figure 4.3 shows the initial results, illustrating that that the ion chamber and diamond detector are both in agreement, but there is some disagreement between the TOPAS model and the physical measurements.

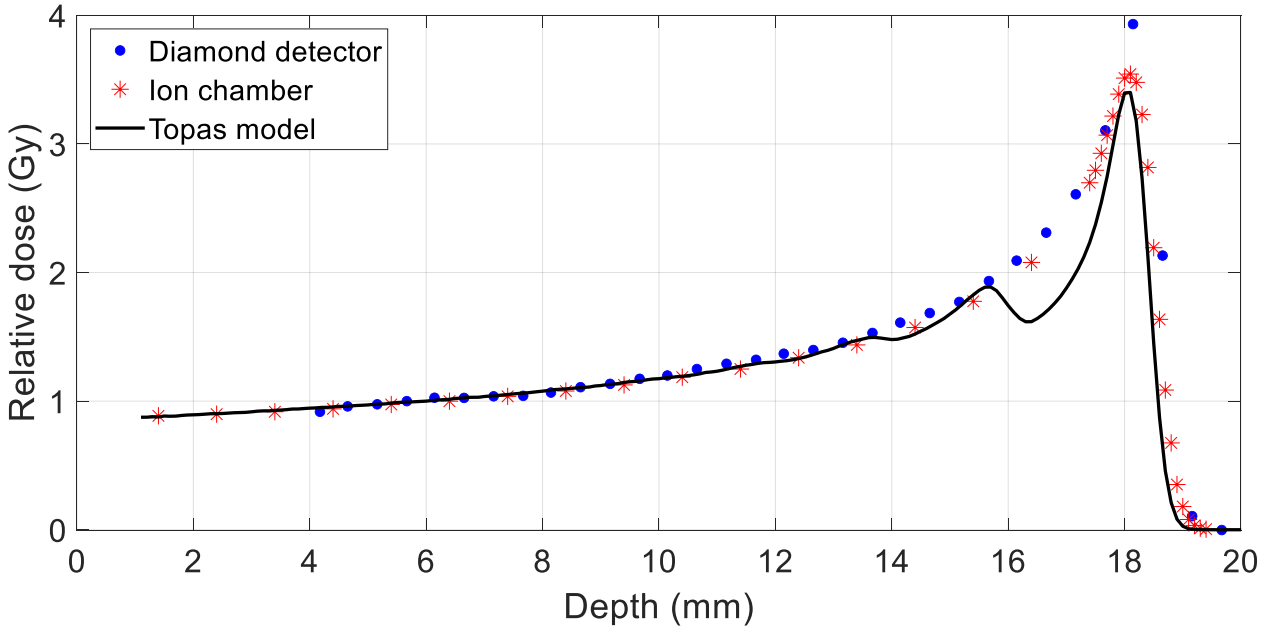

Figure 4.3: Comparison of PDD measured with TOPAS, ion chamber and diamond detector. Dose normalised at a depth of 5 mm.

The Bragg peak is sharper in the TOPAS model than in the experimental results, possibly an artefact of the physical detectors having lower resolution, resulting in volume averaging, than that of the TOPAS simulation. The physical results have also been shifted by a depth of 0.3 mm for the Bragg peak to align, to allow the shape of the PDD curves to be compared. A secondary peak can be observed at a depth of 15.6 mm with a considerable dip before the Bragg peak in the TOPAS model. The profile of the PDD from both the ion chamber and diamond detector agree, indicating that any difference between the TOPAS model and physical measurements is unlikely to be due to measurement error. Testing of the various components modelled in TOPAS revealed that this secondary peak was caused by the beam interacting with the sides of the large beam pipe and introducing secondary scatter into the beam.

The amount of secondary scatter is not present in the real measurements from either the ion chamber or the diamond detector. This disagreement between the model and the measurement is most likely not an issue in TOPAS physics or the measurements, but an inaccuracy in the geometry and inputted components put into TOPAS not matching the real components. As the beamline was built in 1983 and has undergone some undocumented changes throughout its history, current drawings and technical diagrams may be out of date. While external dimensions can be measured it was not feasible to disassemble the entire beamline to catalogue the internal geometry and materials of all components, leaving some inaccuracy in the components modelled. To address this problem, the model was modified so the scatter contribution was removed from the large beam pipe, by modifying the radius of the large beam pipe. As the proton beam travels down the beam pipe the beam broadens with depth, if the radius of the large beam pipe is large enough then

the beam will not interact with the large beam pipe due to the fixed length of the beam pipe. The model was simulated with the same components as the previous simulation except the large beam pipe's internal radius was changed to 30, 45 and 60 mm to determine which of these would best match the measurements. The thickness, length and material remained unchanged. These results are shown in Figure 4.4.

The results obtained with the beam pipe with a radius of 45 mm closely matches the measurement values. The secondary peak was removed, and the surface value closely match. The 60 mm simulation is approximately equal to the 45 mm simulation.

It can also be observed that the relative peak dose at the Bragg peak has increased, this is likely caused by volume averaging affects and is the expected outcome. The modification to the beam pipe will be used throughout the remainder of the thesis.

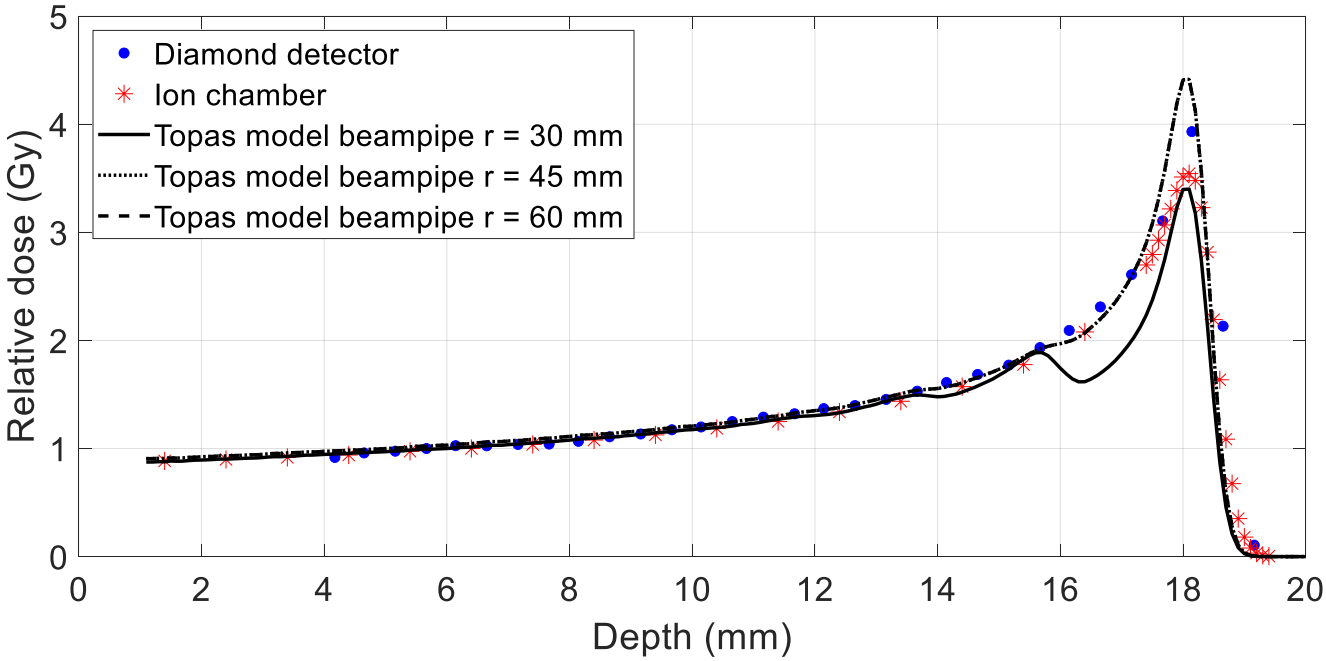

Figure 4.4: Results from multiple TOPAS simulations compared to physical measurements, demonstrating impact of the large beampipe's radius. Aligned to Bragg peak dose and depth of Bragg peak.

4.3.2. Scattered Particles Energy Distributions

Histograms of the energy distribution results from modelling scattered particles in the beam are shown in this section. They are split into following the types of particles: protons, electrons, photons, and neutrons, and are displayed in order. Starting at the cyclotron and progressing down the beamline through each component that has an impact on the spectrum of the beam, some components do not have a noticeable impact, these results will not be shown for clarity.

The beam first exits the cyclotron as a near monoenergetic pencil beam with a radius of 1.5 mm. It then impinges on a graphite degrader which is placed in the beam to reduce the dose rate and broaden the beam. Figure 4.5 displays spectra for particles on the entrance side of the graphite degrader. It can be observed that the beam consists of primarily 50.5 MeV protons. A small number of low energy electrons, photons and neutrons are also shown to exist in the beam, these are a result from backscatter from the graphite beam degrader and are all travelling in the opposing direction to the beam.

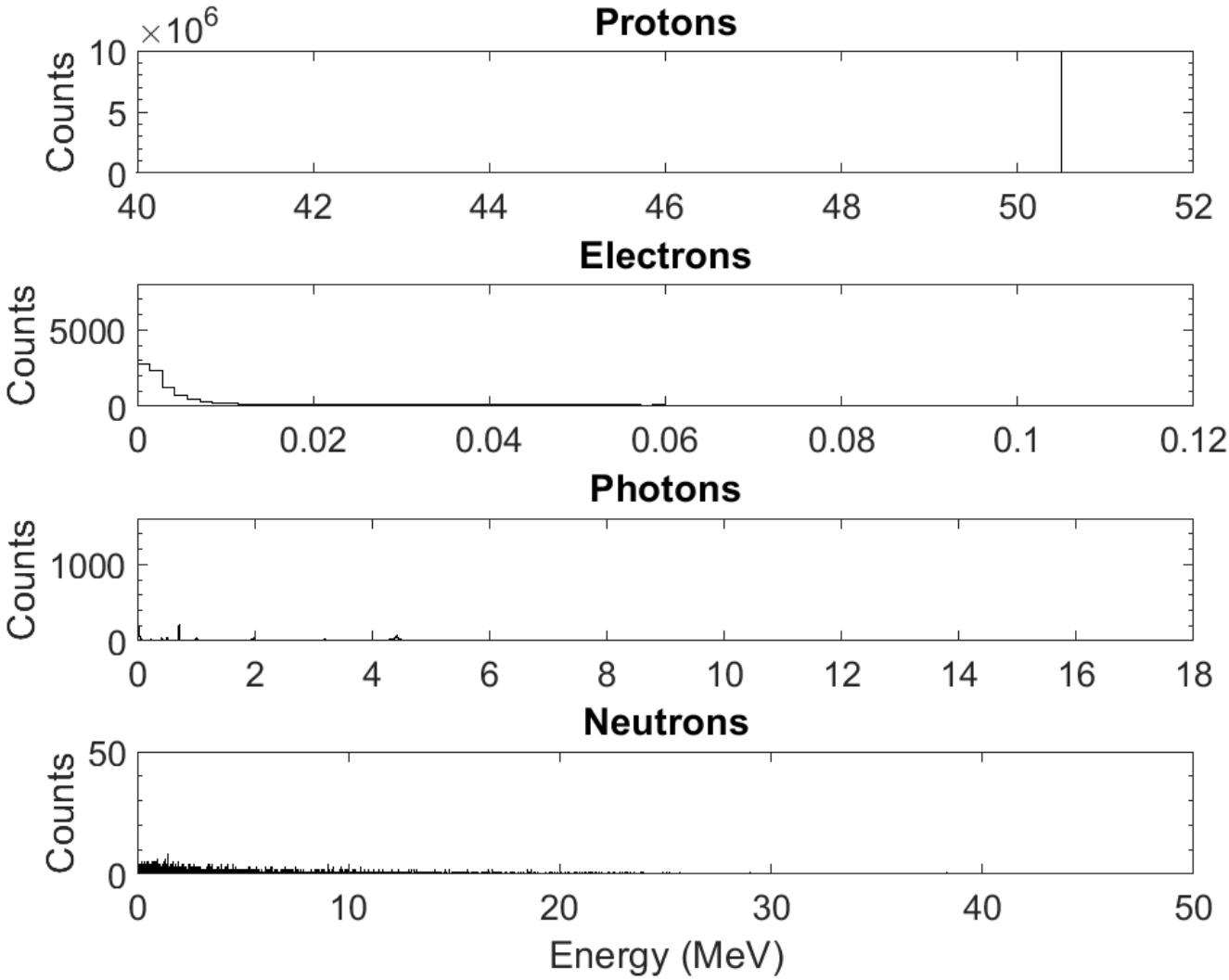

Figure 4.5: Spectrum of particles on the entrance surface of the graphite degrader before passing through

As the beam passes through the 1.23 mm thick sheet of graphite it interacts via Coulomb interactions and loses energy. The result of these interactions on the beam energy spectrum is shown in Figure 4.6, showing the particles on the exit side of the graphite degrader. The beam now primarily consists of protons which have lost energy to the degrader. The mean energy of exiting protons has decreased by 2.51 MeV, to 47.99 MeV. The standard deviation of energy of the protons in the beam increased to 1.22 MeV.

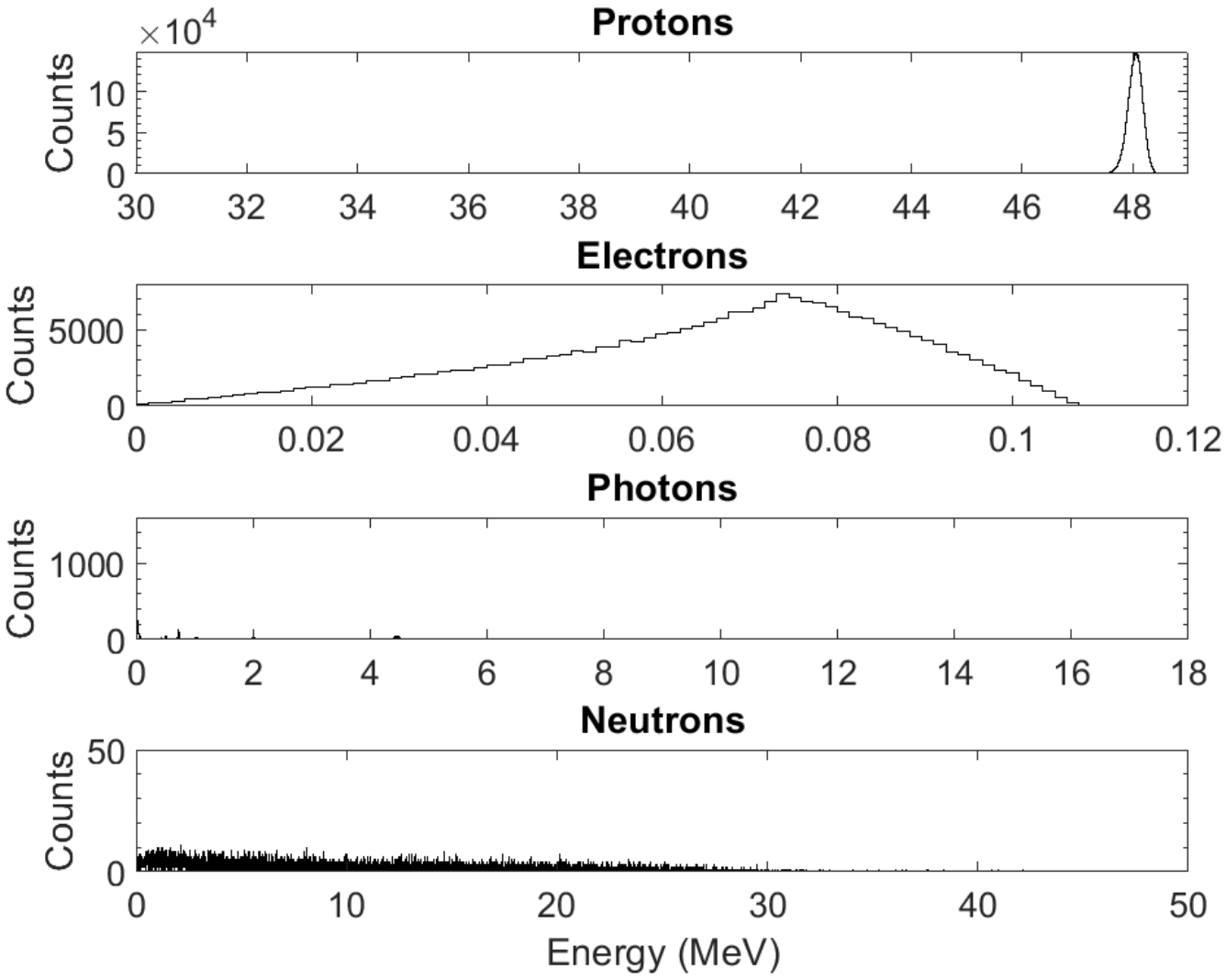

Figure 4.6: Spectrum of particles on the exit surface of the graphite degrader after passing through the degrader

The number of electrons present in the beam has increased by a factor of 17 representing 2.4% of the total number of particles in the beam. The mean energy of these electrons is 67.75 KeV with a standard deviation of 116.83 KeV. A small number of photons and neutrons are produced as a result of the interactions of the beam with the graphite degrader. These particles are less than 0.1% of the total number of particles in the beam.

The beam exits the graphite degrader and enters the vacuum of the large beam pipe. The front surface of the beam pipe is adjacent to the rear surface of the graphite degrader, so the particle distributions are unchanged. The beam then travels down the large beam pipe a total distance of 4.158 metres. As it does so it broadens. Broadening of the beam enables the edge of the beam to interact with the wall of the beam pipe. The spectrum for particles exiting the large beam pipe is displayed in Figure 4.7.

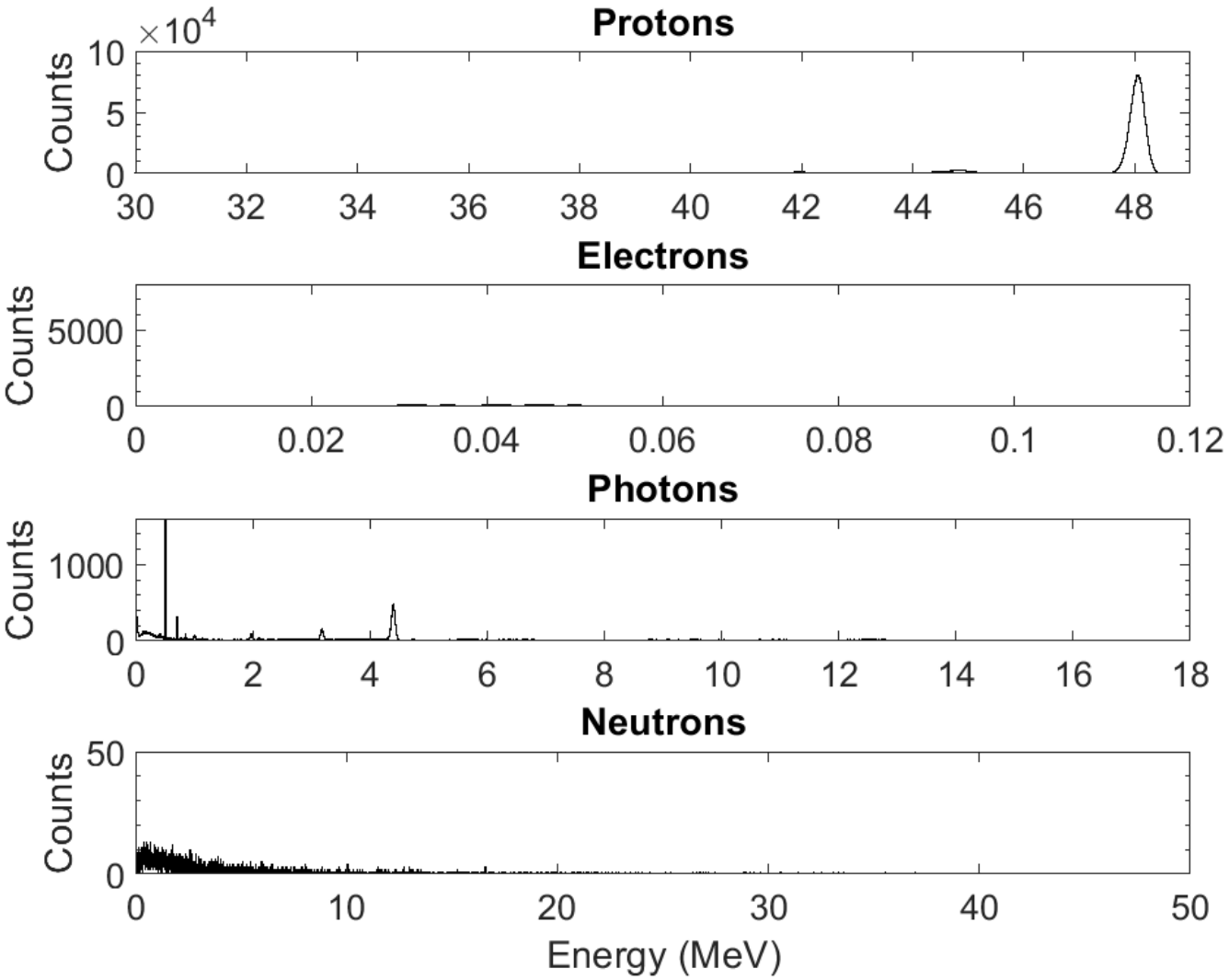

Figure 4.7: Spectrum of particles on the exit surface of the large beam pipe after traveling down it.

The majority of protons in the beam remain unchanged as they have travelled through vacuum, with a small number of them having impacted the side of the beam pipe, consequently losing energy, shown as a small peak at approximately 45 MeV. An analysis of these scattered protons is shown in Figure 4.8. The number of electrons in the beam has been reduced as a result of the high angular divergence they have when exiting the graphite degrader causing them to collide with the large beam pipe walls which absorbs them. Low energy photons can be observed in the energy spectrum of the beam as it exits the large beam pipe, these photons are produced when the beam interacted with the large beam pipe and, make up 1.5% of the total number of particles in the beam. They have peaks at 0.02, 017, 0.55, 0.71, 1.01, 1.98, 3.15 and 4.47 MeV. Both neutrons and electrons are a minor component of the beam representing less than 0.1% of the total number of particles in the beam.

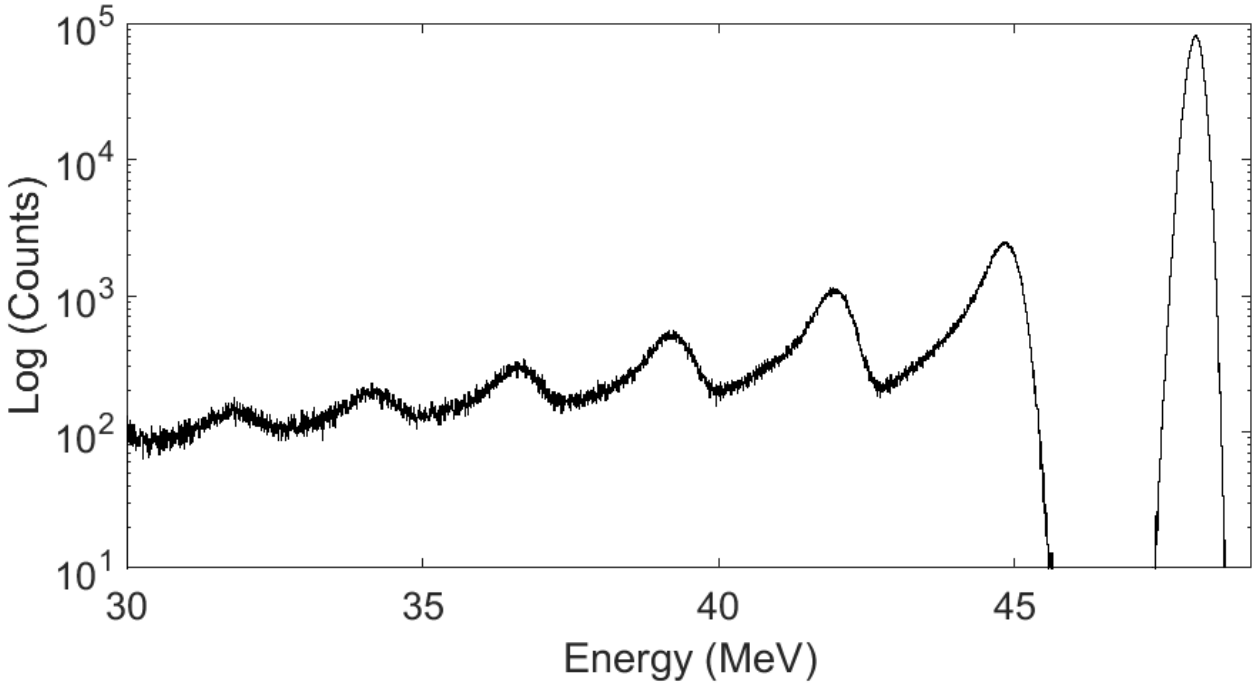

Figure 4.8: Spectrum of protons on exit surface of the large beam pipe, shown with a log scale

Protons that have interacted with the side of the large beam pipe can be observed as a small number of lower energy peaks, this is shown Figure 4.8 with a log scale to highlight the differences, but it should be noted that it will exaggerate the size of the small peaks. These lower energy peaks have a mean energy in decreasing amplitude of 44.8, 41.9, 39.2, 36.7, 34.0 and, 31.8 MeV. The largest secondary peak is 44.8 MeV and each further peak decreases by approximately a factor of two. Each peak is a result of a higher order scatter off the walls of the collimator. The first order scatter at 44.8 MeV has a high number of particles as particles that contribute to it. They originate from the original 47.99 MeV peak, whereas the second order scatter peak only originates from the first order particles and so on. Scattered protons represent 25% of the total number of protons that exit the large beampipe and thus are a significant proportion of the beam. Ten million protons enter the large beam pipe and only 6.83 million protons exit, resulting in a 31.7% drop in the total number of protons in the beam.

The beam's radius is then reduced from 45 to 16 mm when passing from the large beam pipe to the small beam pipe, with the use of a stray beam connector. How the reduction of the radius impacts on the beam spectra is shown in Figure 4.9. The figure illustrates, the spectra of particles on the front surface of the stray beam connector, demonstrating that the reduction of radius does not impact the proton energy spectrum apart from reducing the total number of protons by 85% (6.83 million down to 1.07 million) in the beam. It can also be observed that secondary photons and neutrons are removed from the beam, most of these particles are on the edge of the beam and have a high angular divergence, this is further investigated in the next section.

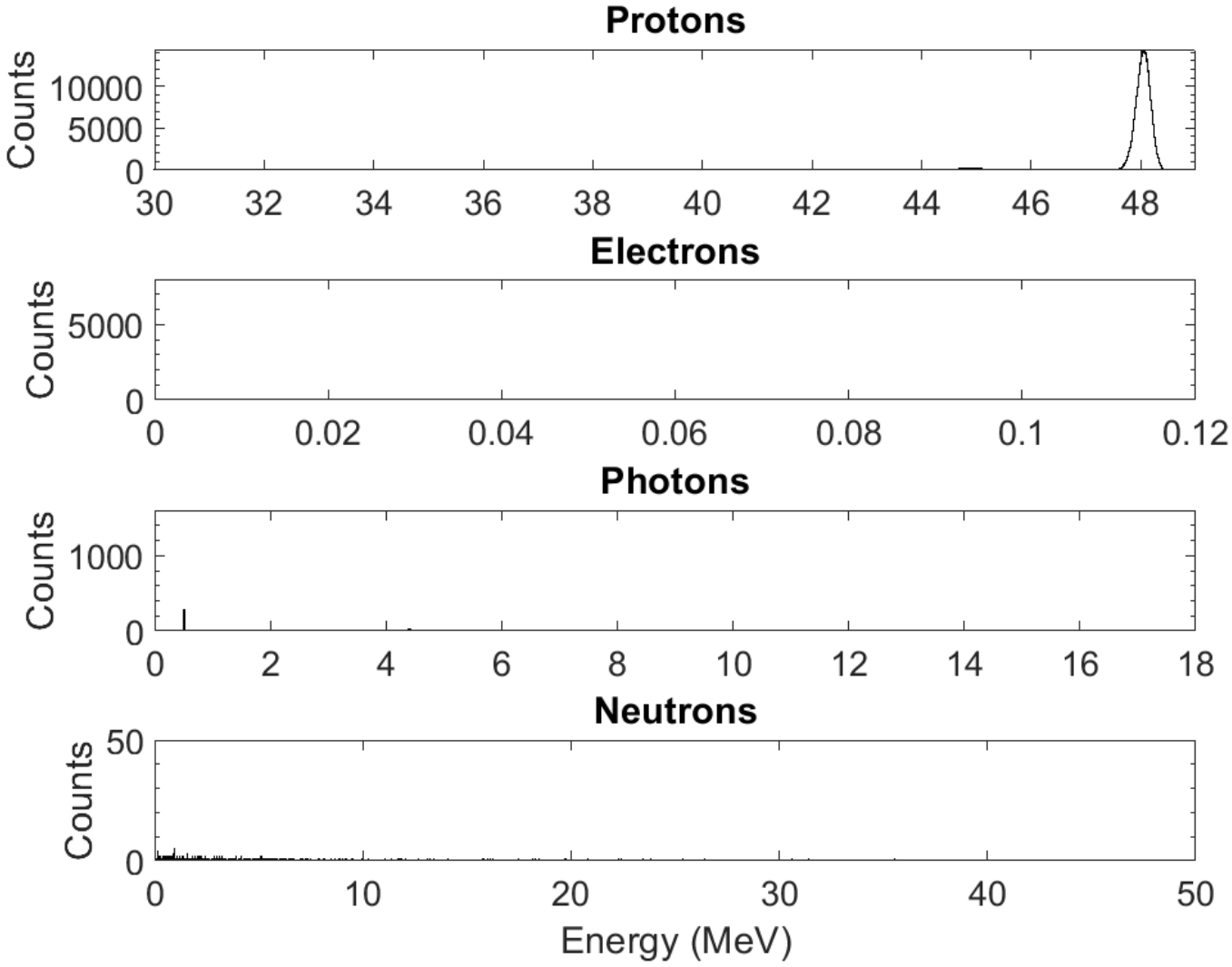

Figure 4.9: Spectrum of particles on the front surface of the stray beam connector

Passing through the vacuum filled stray beam connector, the radius increases from 16 mm to 20.5 mm at the midpoint. This has no impact on the beam as the total length of the stray beam connector is 2.4 cm which is not long enough for the divergence of the beam to impact the sides of the beam connector. Results for the beam exiting the stray beam connector are not shown, as no major changes to the beam occurs.

The beam then enters the small beam pipe which has a radius of 17.5 mm, the beam travels a total distance of 250 mm through the pipe. The beam broadens to a radius of 17 mm over the length of the pipe, which will be discussed in the next section. The increased radius is not sufficient enough for the beam to impact with the side of the beam pipe, resulting in no change to the proton spectrum, shown in Figure 4.10. It can also be observed that the number of photons and neutrons in the beam has been drastically reduced resulting in the beam consisting primary of protons. The reduction is a result of two factors, the beam not producing any scattered particles and the scattered particles already present in the beam having a high angular deviation and being absorbed by the small beam pipe.

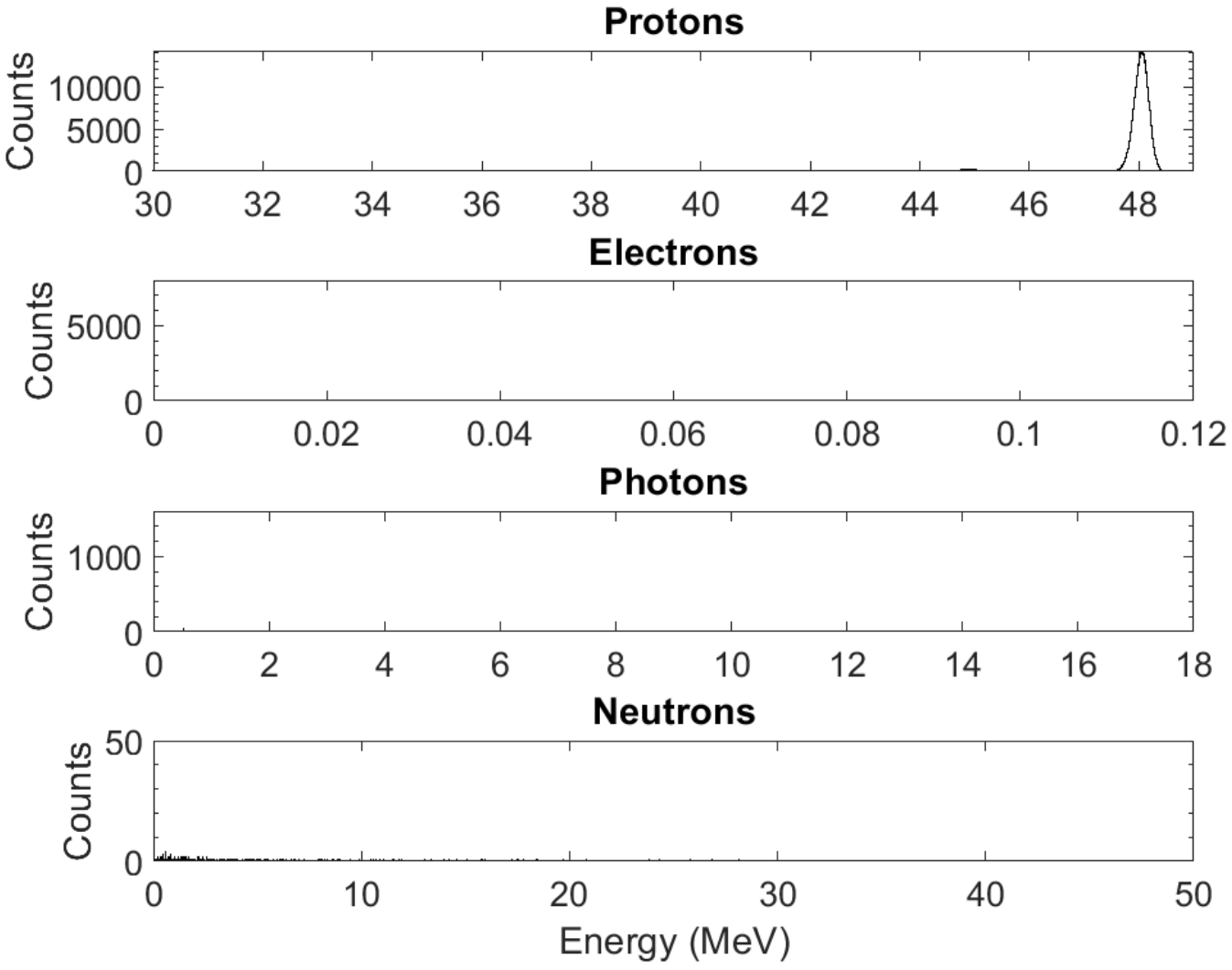

Figure 4.10: Spectrum of particles on the exit surface of the small beam pipe

The beam then exits the beam pipe and the internal vacuum into air through a 0.15 mm thick Kapton window. Figure 4.11 displays the spectrum of the beam exiting the Kapton window. Low energy electrons are produced when passing through the exit window. These electrons have two peaks at 1.5 KeV and 67 KeV and represent 3.6% of the total number of particles. The energy of the proton peak also has a slight reduction of 0.20 MeV which is observed for all proton's peaks in the beam as a result of Coulomb interactions between the beam and the Kapton material.

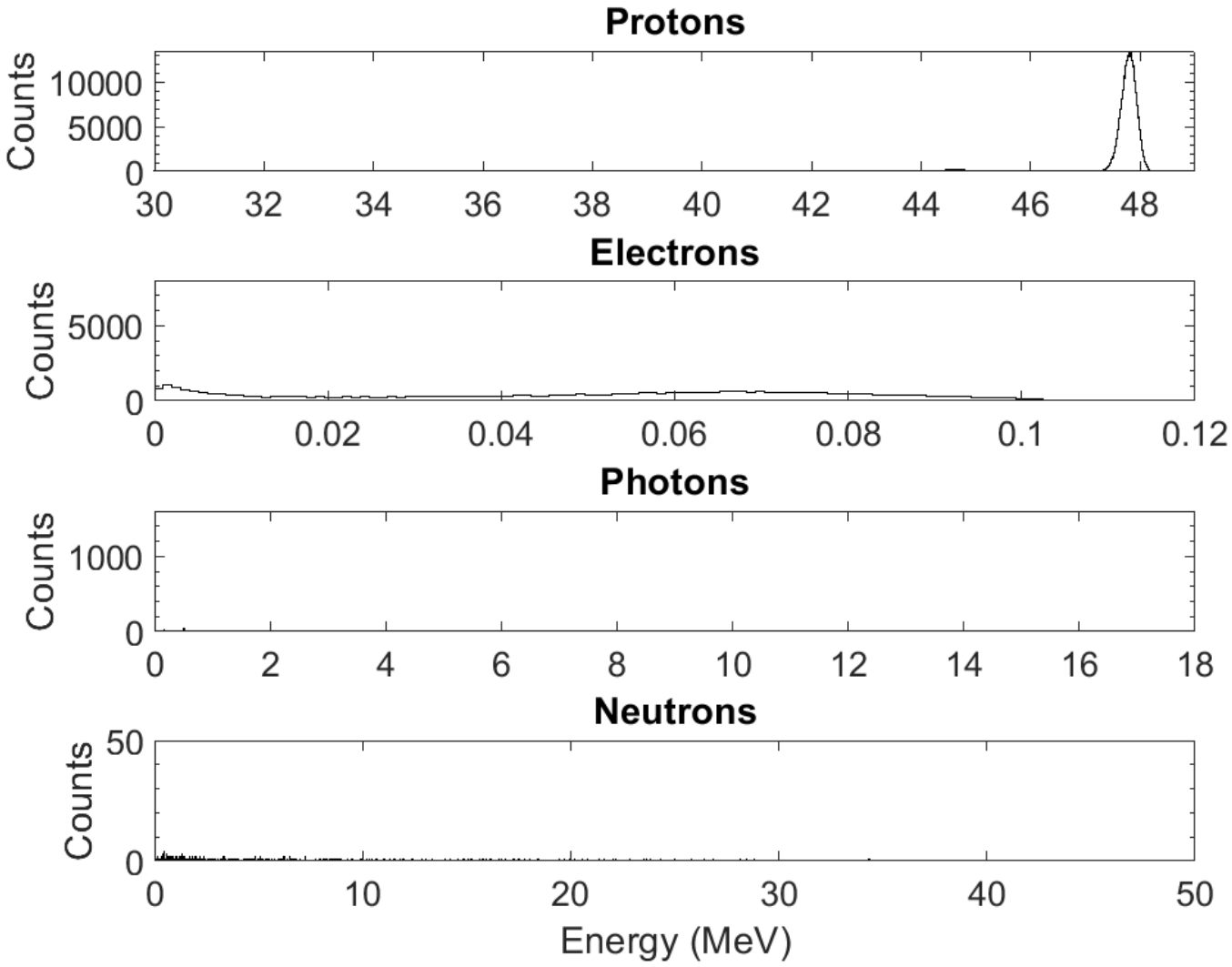

Figure 4.11: Spectrum of particles on the exit surface of the Kapton exit window

After the Kapton exit window, the beam travels through a 30 mm long air-filled beam pipe with a radius of 19.75 mm, increasing to 20.5 mm for the final 12 mm of length. The beam does not interact with the air beam pipe due to its larger radius. Upon exiting the air beam pipe, the beam travels another 4.85 mm in air before impacting on an ion chamber. Figure 4.12 displays this spectrum, highlighting the effect air has on the beam. The mean energy of the protons in the primary peak has been slightly reduced from 47.79 to 47.74 MeV. The number of electrons has increased to 6.7% of the particles in the beam and has a peak at 2.1 KeV.

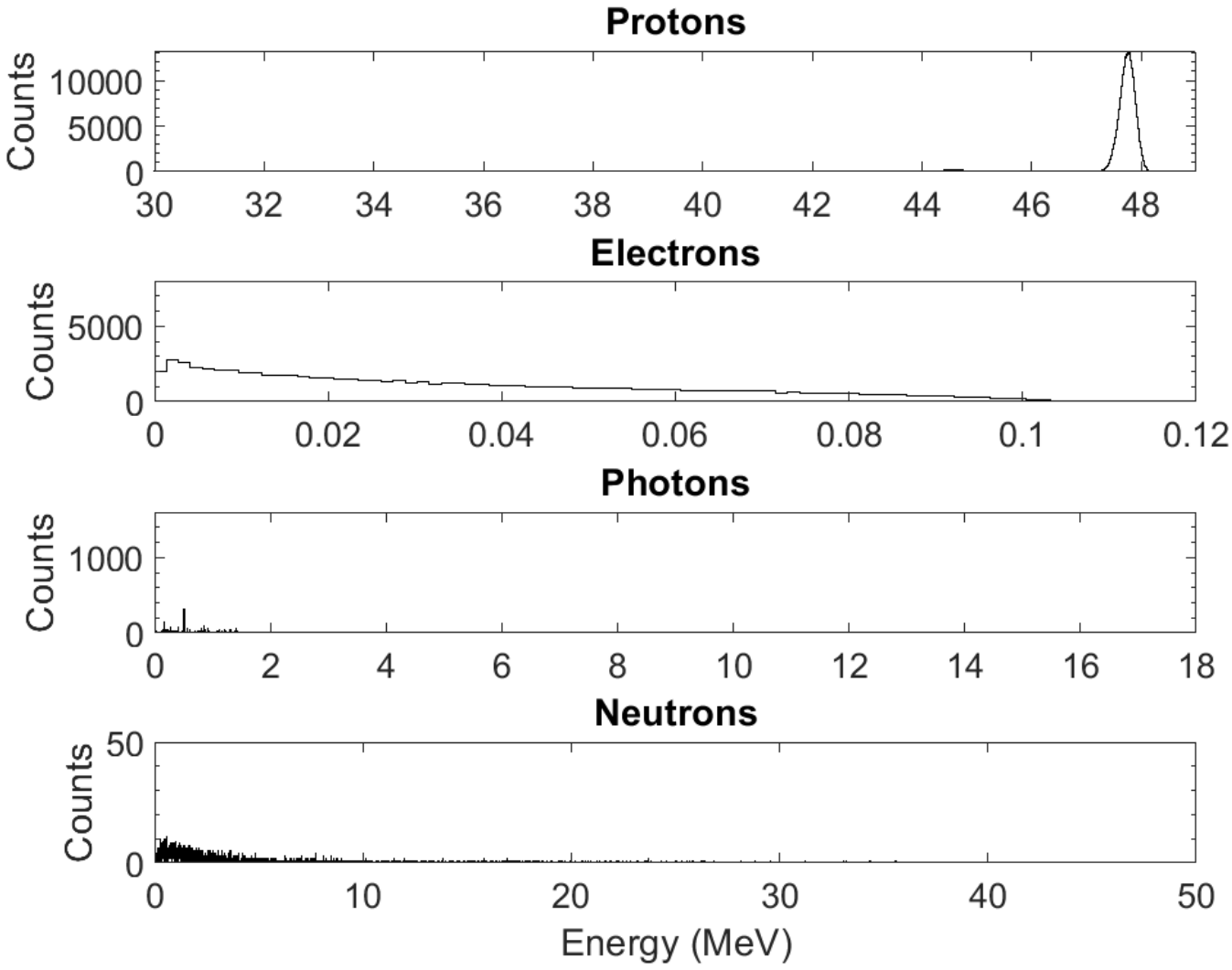

Figure 4.12: Spectrum of particles on the entrance surface of the Ion chamber

Some of these electrons were produced by the Kapton window but the majority of these have been produced due to backscatter from the ion chamber and are travelling in the opposite direction to the beam. Low energy neutrons are only 0.3% of the beam with a peak at 0.5 MeV, they are produced due to proton interactions with air.

The beam then passes through the ion chamber which consists of three acrylic layers, three graphite layers in-between the acrylic layers, and an air-filled layer. The total thickness of these layers is 1.7, 0.08 and of 2 mm, respectively. Figure 4.13 displays the spectrum of the particles in the beam exiting the ion chamber after they have passed through it. The primary proton peak has reduced in energy by 2.79 MeV. Secondary peaks that resulted from interactions between the large beam pipe and the beam are still present in the proton distribution with peaks at 41.60, 38.50, 35.50 and 32.8 MeV. Electrons are now 3.9% of the total number of particles in the beam and with a peak at 2 and 60 KeV. The number of neutrons increases to 0.4% of the particles in the beam as a result of interactions with the ion chamber.

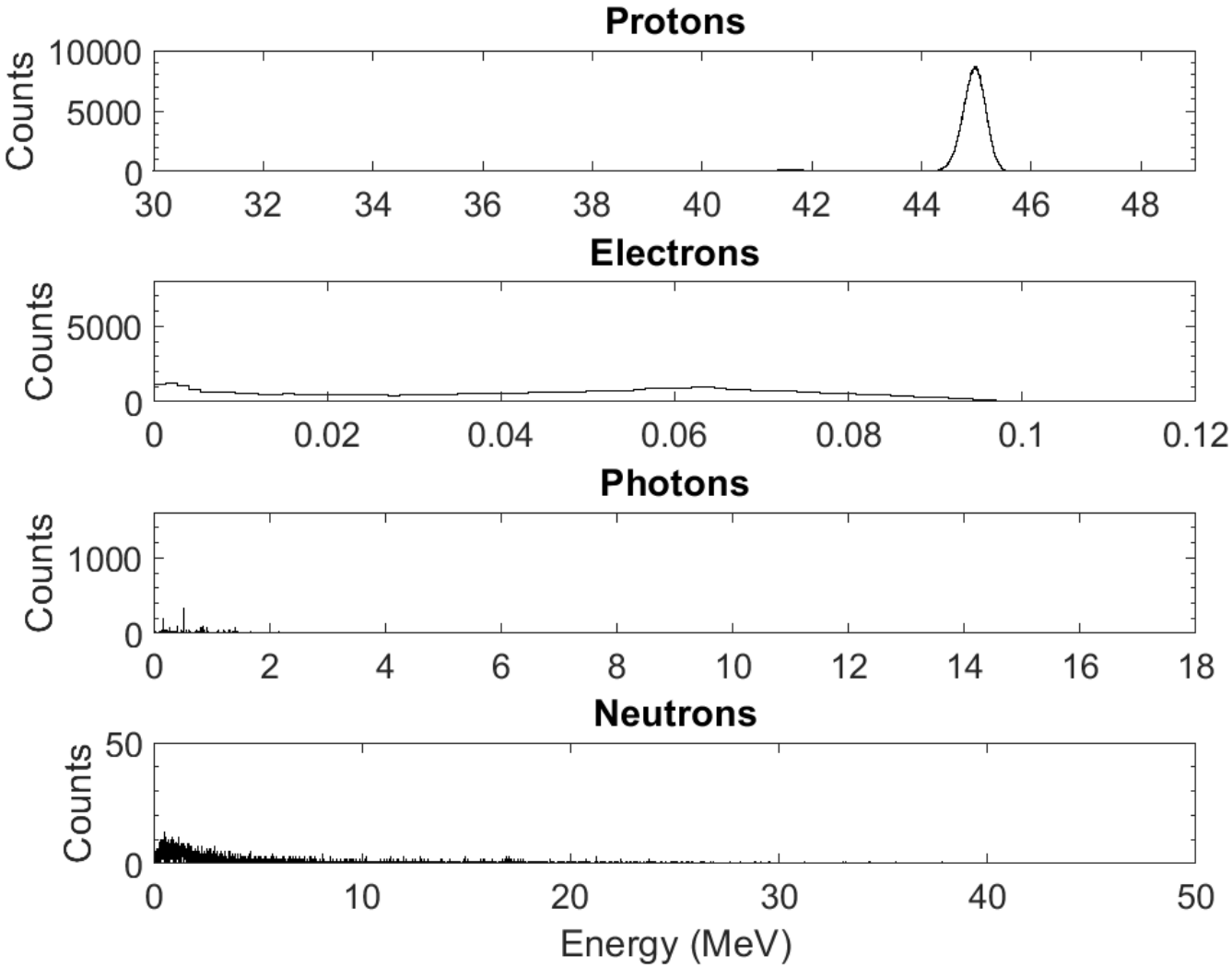

Figure 4.13: Spectrum of particles on the exit surface of the Ion chamber

The beam then travels 100 mm through air before being collimated by the minibeam collimator. Figure 4.14 displays the spectrum of particles exiting the minibeam collimator, displaying the impact the collimator has on the beam. The energy of the primary peak decreases to 44.85 MeV. The majority of the protons pass through the collimator without interacting with the stainless steel, thus only loose energy to the air they pass through.

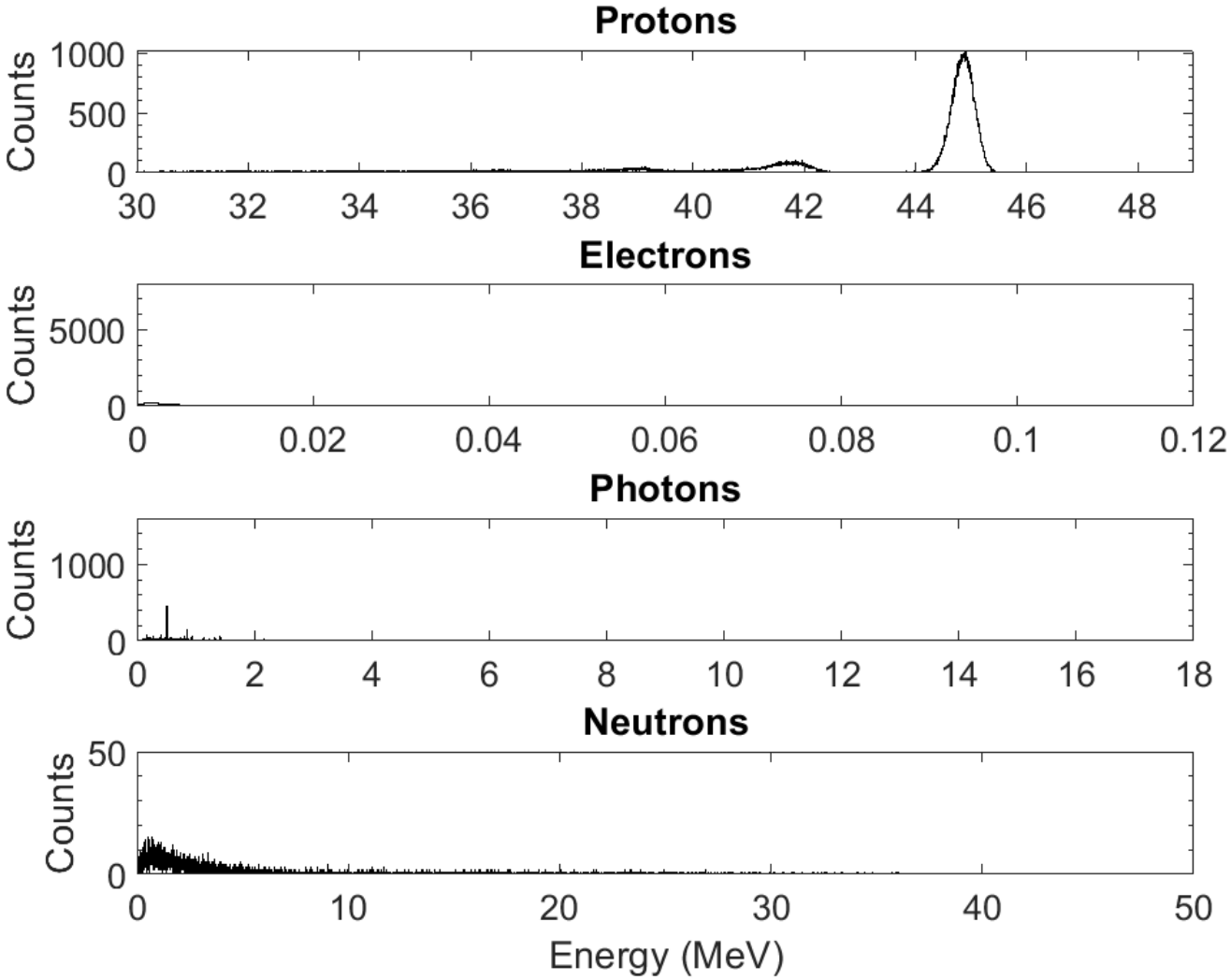

Figure 4.14:Spectrum of particles on the exit surface of the minibeam collimator

The secondary proton peaks are observed to be increased as a result from both impacts of protons with the collimator and the secondary peaks from the large beam pipe with a sizeable peak at 41.8 MeV and a smaller peak at 39.0 MeV. The spectrum is the final output of the beam before hitting a target, in this case a water phantom.

The final beam largest energy peak primarily consists of protons with a peak energy of 44.85 MeV. This peak energy has a standard deviation of 0.21 MeV and consists of 62% of all protons in the beam. The number of neutrons in the beam has increased to 3% of particles in the beam and peaks at 0.6 MeV as a result of interactions with the collimator. A more detailed analysis of the impact of these neutrons is covered in chapters five and six. A peak of photons is visible at 0.5 MeV, the total number of photons is 9.9% of the total number of particles.

4.3.3. Beam Positional and Angular Distribution

This section displays the positional distribution and angular distribution results from the scatter modelling of the particles in the beam. A diagram of the geometry and orientations of this setup is shown in Figure 4.15. Angular deviation is shown in width (X) and height (Y) direction cosines.

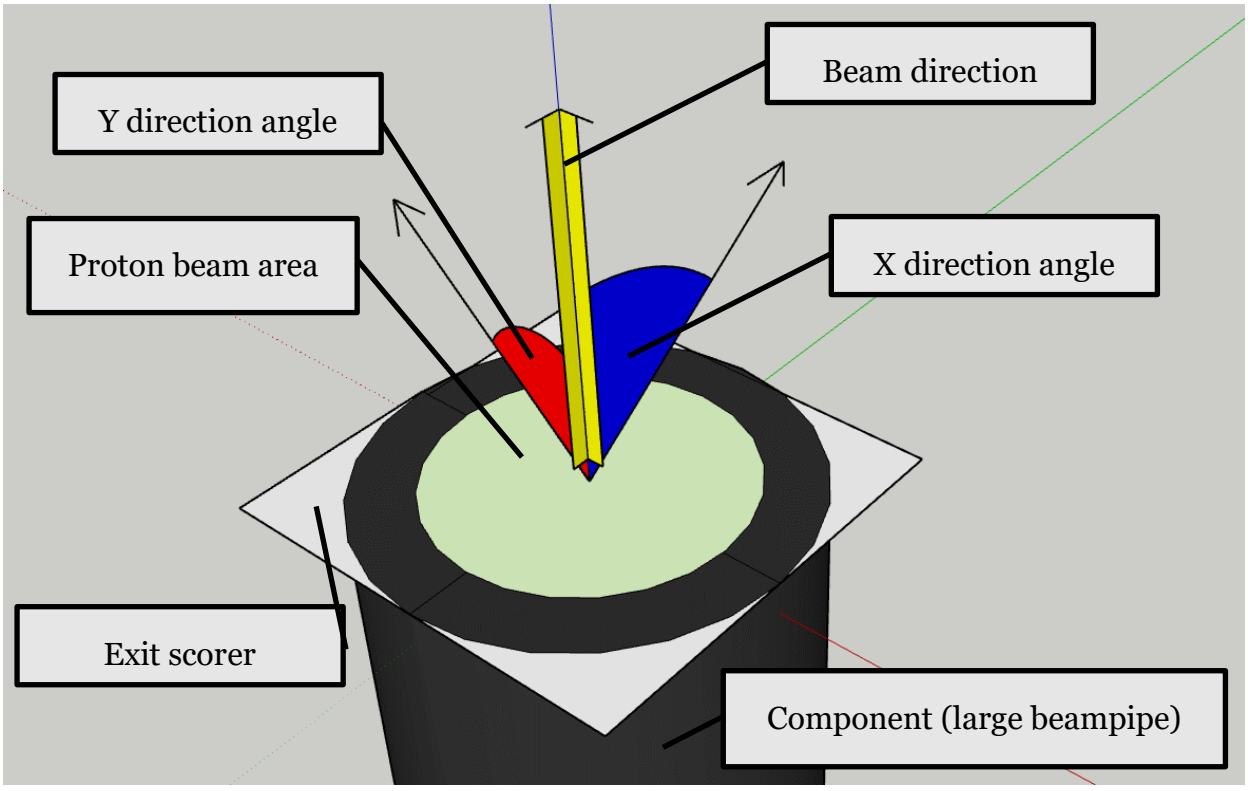

Figure 4.15: Diagram of phase space scorer for the large beampipe and the various components and directions that are investigated.

A direction cosine is the cosine of the angle between particle direction vector and the Z direction, a X cosine of one represents the particle travelling in the positive X direction 90 degrees to Z direction. In a parallel beam this should be zero, i.e. a beam with no angular divergence. The modelled beam has some initial divergence modelled to match the beam outputted from the cyclotron. The positional information displays particle density in a cross-section of the beam, demonstrating the distribution of particles in the beam.

A pure uniform beam with no divergence would appear in the results as a fixed radius circle throughout the length of the beampipes. Both the positional and angular results display particle density. Shown as a colour map with a logarithmic scale. Regions that have low particle density indicated in blue and regions that have high particle density shown in red. A flat beam with no penumbra beam would be shown as a sharp uniform red circle with the remainder of the cross-section in blue.

Figure 4.16 displays the position (left) and angular deviation (right) of particles in the beam prior to entering the graphite degrader. The beam is highly parallel with a diameter of 3 mm. Shown as a small red spot on the position figure and small Gaussian spot on the cosine figure with a standard deviation of 0.0087. This is a very pure beam with extraordinarily small divergence and serves as a reference for further results. As the beam interacts with materials along the beamline it will degrade from this.

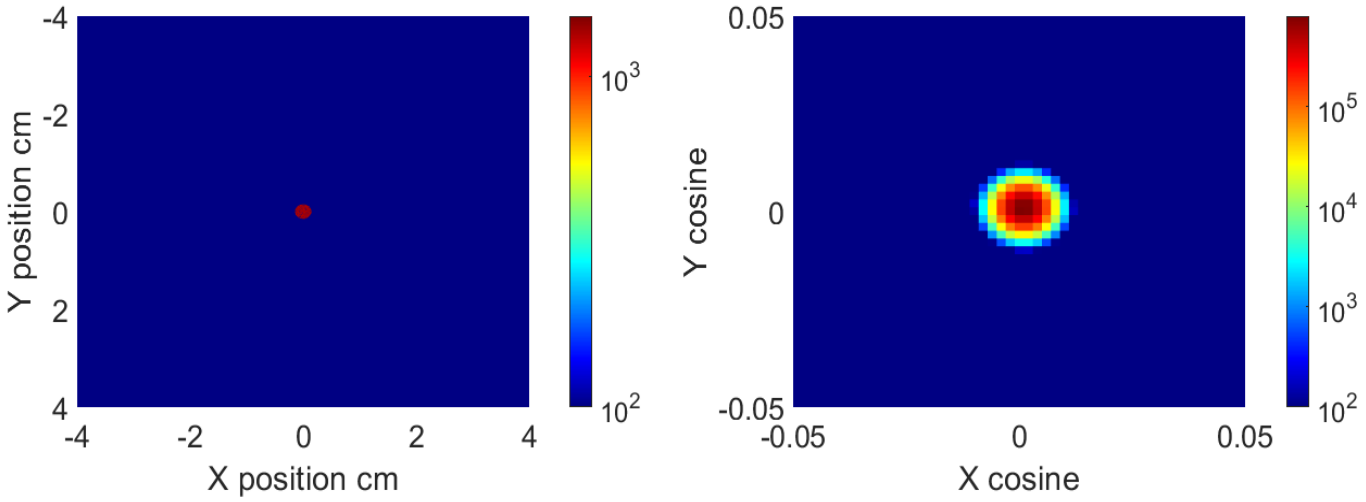

Figure 4.16: Position and direction cosine distributions for particles on the front surface of the graphite degrader prior to passing through. Colour scale represents number of particles.

The beam then passes through the graphite degrader, which is designed to decrease the dose rate and broaden the beam. Figure 4.17 displays the results for the entrance to the large beam pipe this can be compared to the previous figure to demonstrate the impact the graphite degrade has on the beam. The position results show the 3 mm wide beam has not immediately broadened with interactions with the graphite degrader. It can also be observed that the entrance beam is significantly smaller than the total radius of the large beam pipe. The cosines have both increased from 0.0087 to 0.0280 an increase of more than 300%. This increase in the angular deviation of the particles will cause the beam to broaden with distance as it travels down the beampipes.

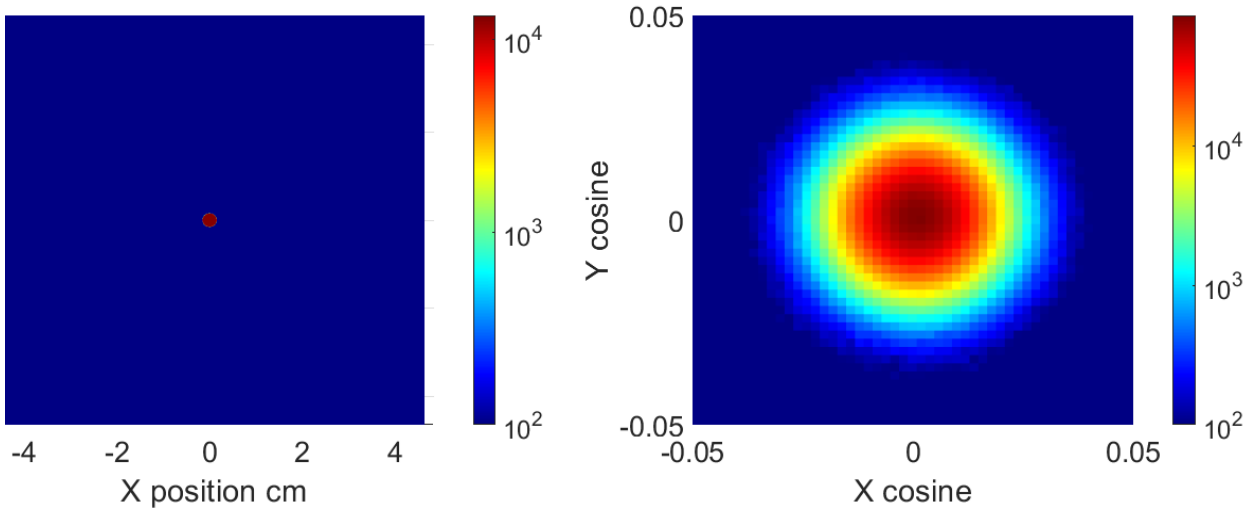

Figure 4.17: Position and direction cosine distributions for particles on exit surface of the graphite degrader after passing through it. Colour scale represents number of particles.

The beam then travels down the large beam pipe. Figure 4.18 shows the results from the beam on the exit surface of the beam pipe. The positional figure shows that the beam has expanded to the entire radius of the beam pipe as it has travelled down the beam pipe. The density of the positional figure displays the beam is uniform over the whole width of the beam. The beam has a mostly uniform distribution at this point as shown by the uniform colour. The angular distribution is remarkably like the distribution from the entrance surface to the large beam pipe, however particles with the most extreme angular deviations have been removed. Figure 4.18 (right) illustrates that the outer edge of the position cosine has a sharp change, showing no light blue. This is caused by particles impacting the walls of the large beam pipe. In turn, this is responsible for a slight collimation of the beam as it travels down the beam pipe and results in a standard deviation in the angular distribution of 0.209 which is slightly less than the previous result of 0.280.

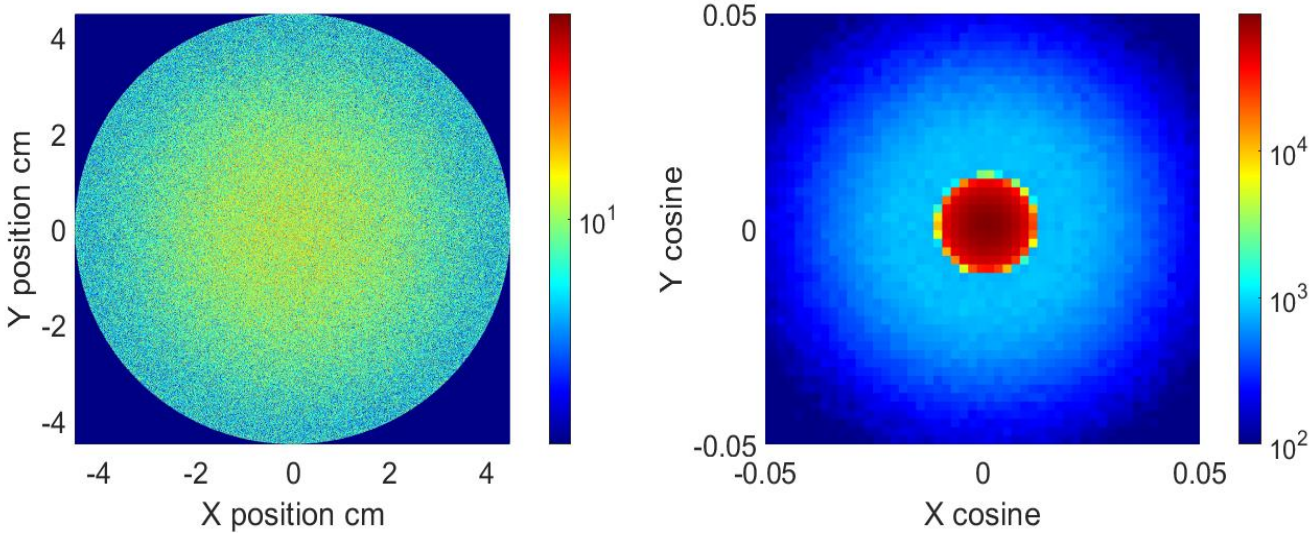

Figure 4.19: Position and direction cosine distributions for particles on exit surface of the large beam pipe after passing through it. Colour scale represents number of particles.

The beam then passes into the stray beam connector, made of graphite which reduces the radius of the beam, shown in Figure 4.19. The primary impact of the beam connector is to reduce the beam from a radius of 45 mm to a radius of 15 mm. The angular deviation is also reduced from 0.0208 to 0.0158. The large reduction in particles, discussed earlier, can also be observed at this point as there are only 10% of particles from the initial beam reaming.

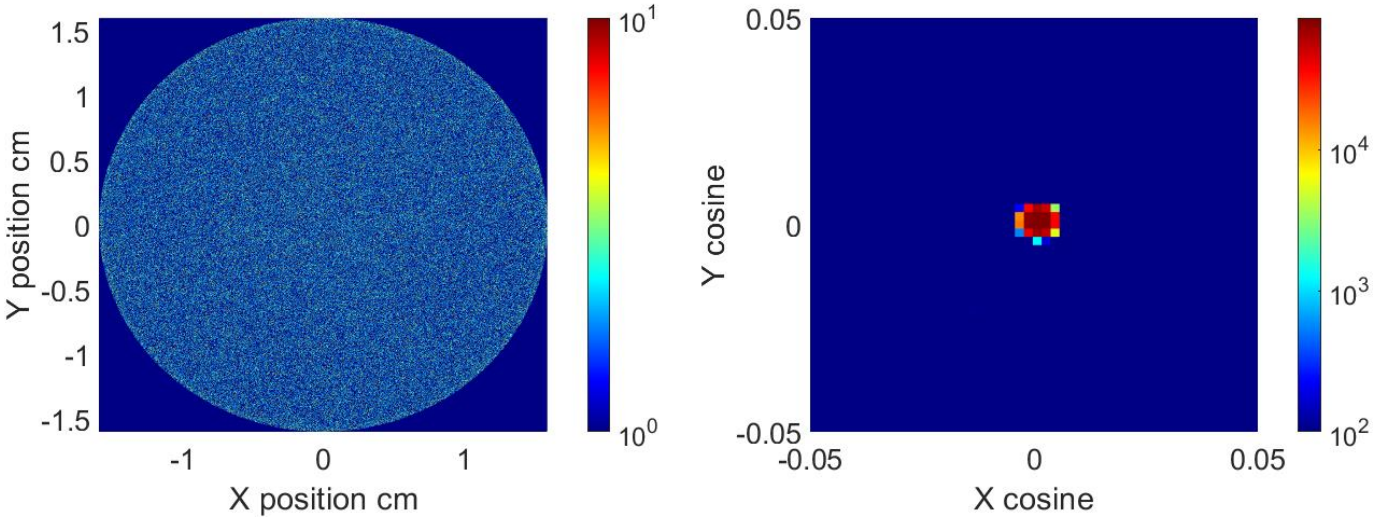

Figure 4.18: Position and direction cosine distributions for particles on exit surface of the stray beam connector prior to passing through it. Colour scale represents number of particles.

As the beam travels through the stray beam connector, the small beam pipe then exits through a Kapton window. The beam has very little interactions with the stray beam connector and small beam pipe, so only the results for the beam exiting the Kapton window are shown in Figure 4.20. The beam's positional information shows that the radius of the beam increases from 15 mm to 17 mm as it travels the length of the stray beam connector and small beam pipe. The angular divergence appears larger as it has a full Gaussian shape after exiting the Kapton window, however its standard deviation has decreased to 0.0151.

The beam exits the Kapton window, leaving the vacuum of the beampipe and travelling through air before passing through the ion chamber. Passing through the ion chamber has the primary effect of increasing the angular divergence of the beam from 0.0151 to 0.0327 as shown in Figure 4.21.

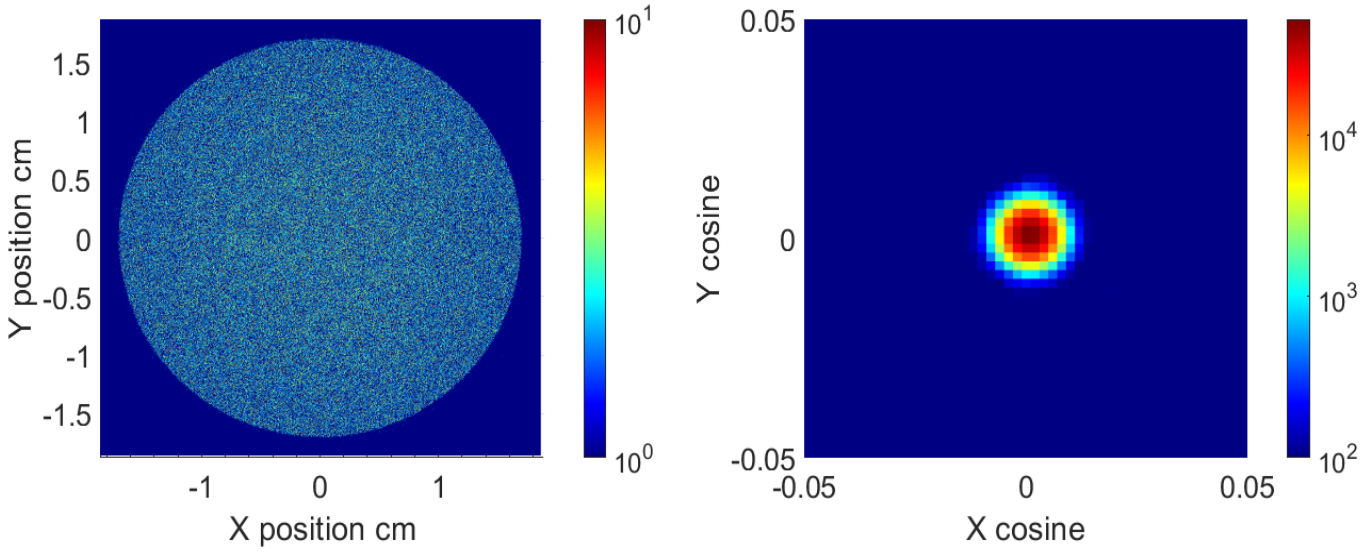

Figure 4.20: Position and direction cosine distributions for particles on exit surface of the Kapton window after passing through it. Colour scale represents number of particles.

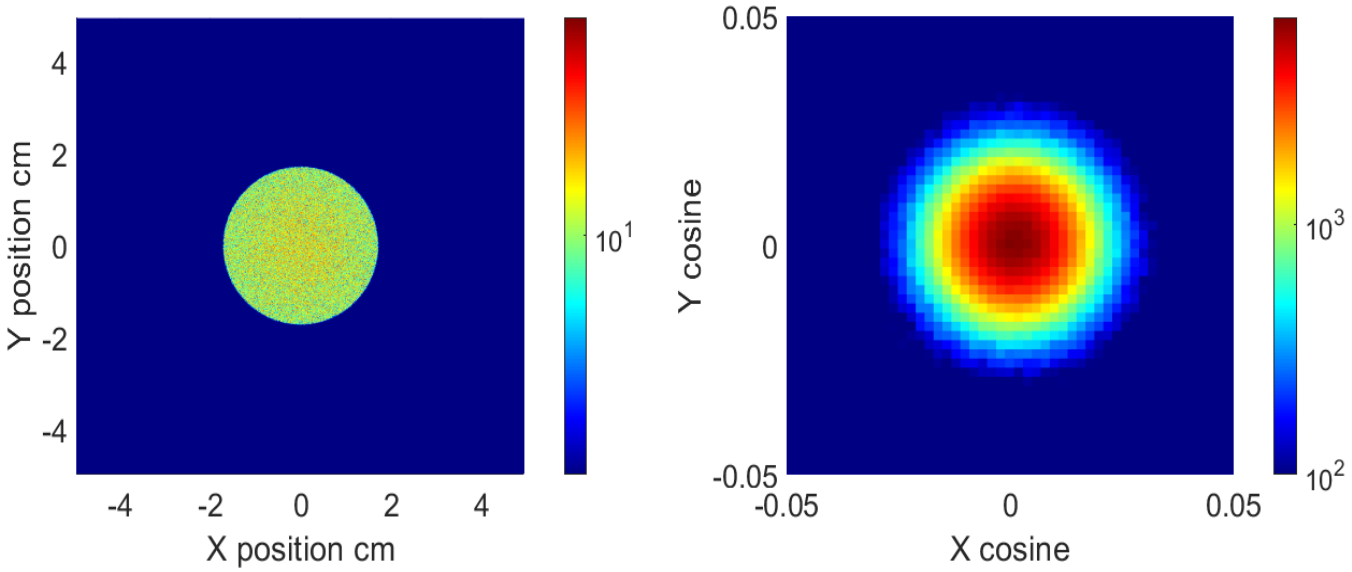

Figure 4.21: Position and direction cosine distributions for particles on exit surface of the ion chamber after passing through it. Colour scale represents number of particles.

This is a result of passing through the many layers inside the ion chamber thereby losing energy via Coulomb interactions as it interacts with the material. The positional information for the beam shows that the radius of the beam remains unchanged and uniform over its radius of 17 mm. Note that although the density of particles appears higher, this is an artefact of it covering a smaller area in the figure, it does in fact have the same density of particles.

The beam then travels a short distance through air before passing through the minibeam collimator. Figure 4.22 displays the positional distribution of the beam as it exits the collimator. The beam is reshaped into 31 vertical slits over a 30 x 30 mm area. As the beam is circular the corners of the beam remain curved. The angular distribution is also displayed showing the beam has been collimated in the vertical direction, making the cosine result not symmetrical. The standard deviation of the cosine in the x direction has decreased to 0.0301, whilst the standard deviation on the y direction has increased to 0.0391. The collimator has a "polarisation" effect on the beam. From this point the beam then impacts the dose target, usually a water phantom to deliver a minibeam dose.

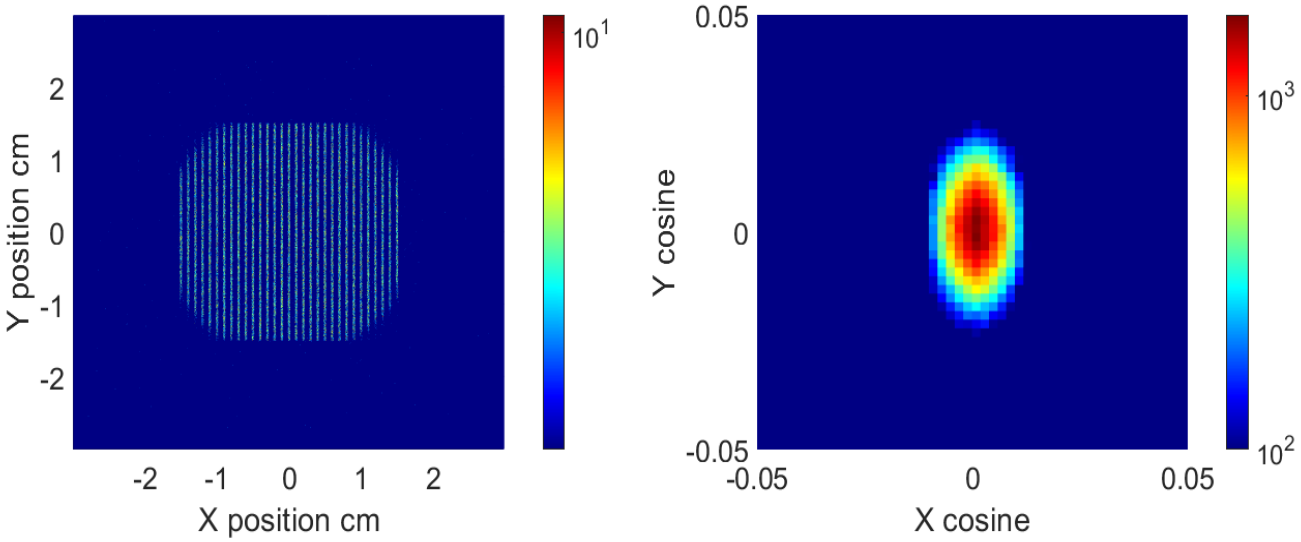

Figure 4.22: Position and direction cosine distributions for particles on exit surface of the minibeam collimator after passing through it. Colour scale represents number of particles.

4.3.4. Beamline Components Dose Contribution

This section displays results from modelling how each component impacts the final dose distribution. Results are displayed as a PDD of the central axis of the beam. These results were processed in MATLAB plotting a column of dose along the central axis. A 20 by 20 voxel area around the central axis was averaged to obtain a mean dose at each 0.1 mm depth to produce the PDD. Each PDD is scaled relative to their maximum dose, which occurs at the Bragg peak. All depth results have an origin on the surface of the water in the water phantom, unlike standard measurements where the origin is the exterior surface of the Lexan on the outside of the water phantom. In order to determine the impact of the Lexan exterior of the water phantom. Figure 4.23 displays the PDD results for the various components in the model.

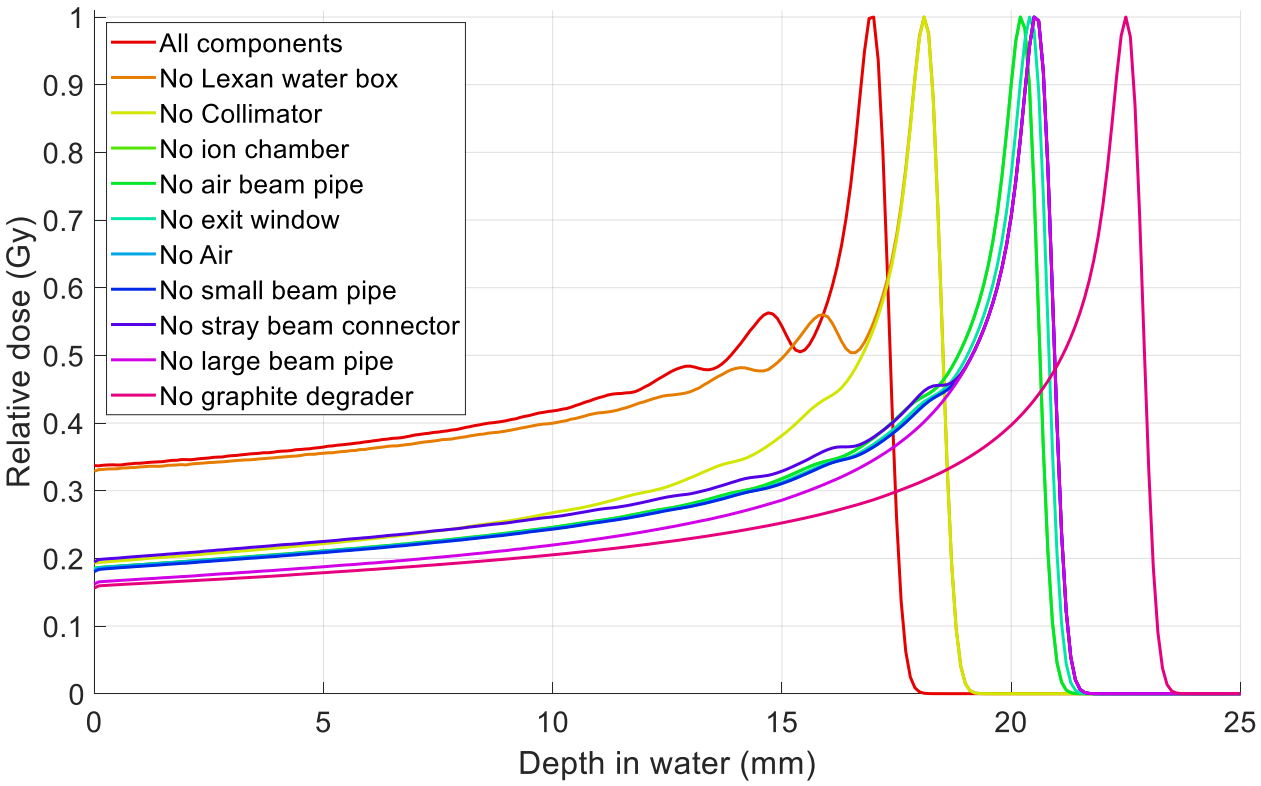

Figure 4.23:PDDs of beam exiting each component in the beamline

In the following section, results are described following the path of the beam, adding one component at a time, starting with the beam from the cyclotron without any additional components. This way the effects of each component has on the PDD can be investigated. Starting with the PDD on the right of the figure and moving left. The initial Bragg peak from the cyclotron exhibits a pristine peak at a depth of 22.5 mm with a low surface dose of 0.156 Gy. This is expected, as the beam is a monoenergetic 50.5 MeV proton beam.

The next PDD includes the graphite degrader, reducing the depth of the Bragg peak depth to 20.5 mm and increases the surface dose to 0.162 Gy a 3.8% increase. This is due to the fact that all protons in the beam lose energy to the graphite degrader and produce scatter in these collisions, as discussed previously. The third PDD shows that adding the large beam pipe has no impact on the depth of the Bragg peak. Interestingly it does have a large impact on the surface dose and the shape of the curve leading up to the Bragg peak. The surface dose is increased by 3.6%, demonstrating that scatter from the large beam pipe can travel through all components and impact the final dose distribution. The secondary proton peaks, that were observed in the previous section, can be seen here as the small peaks before the Bragg peak. The fourth PDD shows that adding the stray beam connector does not impact the depth of the Bragg peak, however it does decrease the surface dose by 1.5%, due to it blocking scattered radiation generated from the large beam pipe. This in turn decreases the height of the smaller peaks leading up to the Bragg peak.

Air (113.78 mm) between the small beam pipe and the water phantom is then added. The air only has a minor impact on the depth of the Bragg peak, decreasing it by 0.1 mm to 20.4 mm. Adding the exit window decreases the Bragg peak depth by a small amount of 0.3 mm to a depth of 20.1 mm. The surface dose was increased by 0.7% due to increased scatter as discussed previously. The Kapton window was designed to be very thin so it will only have a minor impact on the beam. Adding the air beam pipe has no impact on the PDD or dose distribution, as the beam does not interact with this component, or pass through it, so the PDD is identical to the previous one corresponding to the stray beam connector.

The ion chamber decreases the depth of the Bragg peak from a depth of 20.1 mm to 18.1 mm. The large decrease in depth is primarily due to Coulomb interactions between the protons in the beam and the various materials in the ion chamber, resulting in decreasing the energy of the particles. The ion chamber increases surface dose slightly from 19% to 20% of the maximum dose.

Adding the minibeam collimator does not shift the Bragg peak depth, as a portion of the beam is able to pass through the collimator without interacting with it. A portion of the beam will interact with the collimator and these protons are responsible for an increase in the surface dose from 20% to 34% of the maximum dose. Secondary peaks can also be observed before the Bragg peak because of interactions between protons and the minibeam collimator. The large increase in the surface dose demonstrates that most secondary dose at the surface is caused by beam interactions with the collimator. Results in the previous section showed these particles to be lower energy protons. Methods of reducing this will be discussed in later chapters.

The final PDD is shown in red, containing all components of the beamline with a Bragg peak at 17 mm depth. The Bragg peak in this PDD has decreased in depth by 1.1 mm and the secondary peaks have also been shifted by the same amount due to interactions with the Lexan material of the water phantom. This indicates that the correction factor of 1 cm of Lexan is 1.158 cm water equivalent depth that used in previous section agrees with the TOPAS model. The PDD has the same surface dose as the previous PDD without Lexan. The secondary peaks from the collimator and large beam pipes can be observed at depths of 14.8 mm and 12.9 mm.

Overall, the Bragg peaks depth is decreased by 2 mm by both the graphite degrader and the ion chamber, 1.1 mm by the Lexan material and 0.3 mm by the Kapton exit window. The large beam pipe adds scattered lower energy protons which increase the surface dose by 3.6% and, add secondary peaks. A portion of these scattered protons are collimated by the stray beam connector. The collimator itself also adds scattered protons increasing secondary peaks and the surface dose by 14%.

4.4. Discussion

The discussion summarises the impact of all beamline components simulated in the TOPAS model. The more important beamline components are first discussed and how they impact the final dose distribution before moving on to discuss the validation and modification of the TOPAS model.

4.4.1. Impact of Components in the Beam

A novel strategy has been presented to thoroughly investigate the impact of beam components in the proton beamline in terms of dose and angular spread. By doing so, a comprehensive understanding of the relative contribution each component has on delivered dose has been gained.

This section of the discussion steps through each major component in the beamline starting with the graphite degrader. The graphite degrader is shown to lower the mean output energy of the protons in the beam to 47.99 MeV and increases their spread (standard deviation) to 1.21 MeV. The divergence of the beam is greatly impacted, with the standard deviation of the angular cosines increasing to a maximum of 0.0280 from 0.0087. Secondary electrons are produced from interactions with the degrader, however, they do not impact the final dose distribution as they have large angular divergence, and, as such are absorbed by other components in the beamline. The purpose of the graphite degrader is to broaden the beam without degrading significantly. While it does broaden the beam by increasing the angular divergence it possibly increases the divergence by too much, this results in 90% of the beam's particles being lost by the end of the

beamline. A reduction in the thickness of the degrader could potentially fix this problem and would have the added benefit of having less impact on the energy of the protons and the spread of energy. The simulation helps to explain what is happening with this component and its impact on the final dose distribution[1].

The large beam pipe is a critical component in the beamline as it impacts the final dose distribution. The increased divergence from the graphite degrader results in the proton beam impacting the beam pipe part way down the pipe, causing a decrease in energy of protons and production of low energy electrons. Only part of the beam impacts with the sides of the beam pipe producing multiple energy peaks in the proton energy distribution; a primary peak of protons that have not interacted with the beam pipe and multiple smaller secondary peaks at a lower energy. These secondary protons increase the surface dose of the beam and introduce additional shallower Bragg peaks. The additional Bragg peaks were not observed in measured results, leading to some disagreement between the model and the physical beamline. It is postulated that the cause of this disagreement is due to our model producing too much scatter in the large beam pipe, for which there are two possible causes. First there could be inaccuracies in the historic drawing of the beamline resulting in an issue with the material or dimensions of the large beampipe that causes increased scatter. Or second there could be an issue with the divergence of the proton beam from the graphite degrader.

[1] A thinner degrader was physically installed in July 2020

An analysis of this disagreement led to modifications of the Monte Carlo model, in particular the radius of the large beam was increased from 30 mm to 45 mm, which decreased the number of lower energy protons produced as the beam travels further before impacting the large beam pipe.

The next components of the beam; the stray beam connector, the small beam pipe and Kapton window do not have a large impact on the beam or the final dose distribution, only a slight decrease in the energy of the proton beam when passing through the Kapton window and a decrease of the radius of the beam from the stray beam connector.

The ion chamber in the beamline is used to measure the number of monitor units delivered to the target, and thus gives a running approximation of the dose delivered to the target. In passing through the ion chamber there is an observed decrease in mean energy of proton in the beam of 2.79 MeV bringing the beam energy down to 44.95 MeV. This decrease in energy causes the depth of the Bragg peak to decrease from 20.2 mm to 18.1 mm. The divergence is also increased as a result of interactions between the beam and the ion chamber, increasing its directional cosines from 0.0151 to 0.0327. Although the ion chamber has a significant influence on the beam characteristics, it is essential component as it ensures the prescribed dose is delivered and thus must remain part of the beamline.

The collimator modifies the beam from being uniform in the x and y direction into 30 0.3 mm wide minibeams in the x direction, with a CTC spacing of 1 mm in the x direction. This results in the collimator blocking approximately 70% of the

incoming beam. Of the portion of the beam that passes through the collimator, some of it will interact with the sides of the collimator as a result of the beam's angular divergence and the beam broadening with depth. When protons interact with the collimator, they lose energy through Coulomb interactions, resulting in a small number of lower energy protons. These low energy protons cause an increase in surface dose, increasing it from 20% to 34% of the maximum dose. The low resolution in the x direction, which is same direction as the spatial modulation, results in the spatial differences between the peaks and valleys being averaged together. Meaning that the minibeam peak dose has a very high surface dose, the implication of which are discussed in Chapter five.

4.4.2. Validation and Modification of TOPAS Model

The Bragg peak was measured with the diamond detector and ion chamber to be 17.8 ± 0.5 mm in section 4.3.1. The depth agrees with the value from our TOPAS model of the beamline of 18.1 ± 0.1 mm within the experimental uncertainties. In order for the modelled PDD curves to closely match the measured data, the model was modified, and the large beam pipe's internal radius was increased from 30 mm to 45 mm. The change removed some scatter that the beam pipe was causing, which occurs when the beam broadens as it travels through the large beam pipe. After a certain distance, the beam will interact with the outside of the beam pipe and produce secondary scatter. This can be removed either by expanding the width of the beam pipe, shortening the length of the beam pipe, or reducing the divergence of the incoming beam. Each method has disadvantages and requires that we diverge from the current best estimates of the beamline dimensions. Expanding the width of the beam pipe is straight-forward to implement. Changing the length of

the large beam pipe was also investigated, however it was deemed to be less realistic. The divergence of the incoming proton beam before it impacts the graphite degrader was modified in some tests. This did not have a large impact on the dose distribution, or the secondary scatter produced from the large beam pipe. Since the graphite degrader is primarily responsible for the divergence in the beam as it enters the large beam pipe. Thickness of the graphite degrader could be modified to correct the spread in the large beam pipe; however, this would modify the output energy of the beam. The depth of the Bragg peak has been shown experimentally to match the TOPAS model, there was a small offset between the model and physical measurement that was within uncertainty a very small change to the degrader could resolve. However, initial work on did not demonstrate that it was the only factor and is an area for future work. The best option was to increase the diameter of the beam pipe, as this best matched the output of the model to the physical measurements, resulting in only a difference between the model and the beam pipe drawings. It is unclear if this is because some change to the beamline had not been documented, or an error in TOPAS is responsible for this discrepancy. An error in TOPAS is not considered a likely cause as it has been verified by a wide range of groups for use in proton therapy [73, 75, 76, 79, 80]. Disassembling the entire beamline would be costly and time consuming, this is not feasible. Leaving the only practical course to change the model to match the measured results. We accept this solution is not ideal but, due to practicalities, we are unable to confirm whether our changes fully reflect the physical beamline. However, our simulation now matches measurements well and assumption moving forward is that our model is an accurate reflection of the true beamline geometry.

4.5. Conclusion

Through the application of Monte Carlo methods, a simulation in TOPAS was developed to closely match the University of Washington preclinical proton research beam platform. The model was based on dimensions provided by the University of Washington and, whilst most information was available, no accurate information was available for some sections of the beamline. The model developed matched the measured PDD well with some minor deviations. A novel beamline component analysis was carried out to gain an understanding and provide insight into what caused some initial mismatch between model and the physical beamline. Possible solutions were discussed, and it was decided to change the diameter of the large beampipe in the model. The depth of the Bragg peak in the Monte Carlo model agrees within experimental uncertainty of the depth measurements. The model depth was measured to be 18.1 mm, corresponding to a proton beam with an output energy of 44.95 MeV. This depth also agrees with the reference values for the depth of a 44.95 MeV beam [82].

The graphite degrader at the start of the beamline has been shown to lower the energy of the beam and drastically increases the divergence. The large beam pipe and the collimator have a large impact on increasing the surface dose. The ion chamber and graphite degrader decrease the energy of the beam with the final output energy being 44.95 MeV, this is a decrease from an initial energy of 50.5 MeV. The other components of the beam have minimal impact on the output beam. Further work should be carried out to identify the cause of the difference between the model and the beamline. Measurements could be taken with the ion chamber

removed to further verify the accuracy of the model. This would be difficult as delivering the correct dose without being able to measure the number of monitor units delivered could be problematic.

Chapter 5

Collimator Design

This chapter performs an investigation into design considerations when constructing minibeam collimators. The aims are to reduce the production of secondary particles from interactions with the collimator and the proton beam, as observed in Chapter 4, and to maximise the PVDR. To achieve these aims, three collimator variables were investigated: the total thickness of the collimator, the width of the slots used to produce minibeams, and the material of the collimator. The chapter starts with a brief introduction into the areas of collimator design investigated followed by a method section describing the design of each simulation performed and then a results section with important results from each method shown. The overall outcomes and findings are discussed in the discussion section and an overall summary is provided in the conclusion.

5.1. Introduction

As discussed previously in Chapter 2, a minibeam dose distribution is produced from a uniform beam by blocking sections of it with a collimator. A collimator is usually a block of metal with sections removed allowing the beam to travel through. Either a slot configuration where the dose distribution is only modulated in one direction or a grid of holes configuration can be used which provides modulation in two directions, theoretically offering advantages. However, this has yet to be

shown with biological testing. As slot collimators are easier to manufacture and consequently less costly than hole collimators, this section of work will focus on slot collimators. However, the results should also be applicable to hole collimator designs. One of the advantages of proton minibeams is the ability to produce a uniform dose for treatment at depth whilst maintaining a spatially modulated dose near the surface, potentially sparing normal tissues. Therefore, it is important to design a collimator which maximises this advantage.

A diagram of a collimator with the various terminology used in this section is shown in Figure 5.1 and the coordinate system is shown in Figure 5.2. Figure 5.1 shows that the septa thickness, CTC spacing, and the slot width are all interconnected in the x direction. The CTC spacing is dependent on the lateral spread of proton at the Bragg peak, which is a function of the initial energy of the proton beam, and thus for a particular beam energy a certain spacing is required to produce a level of uniformity at the Bragg peak.

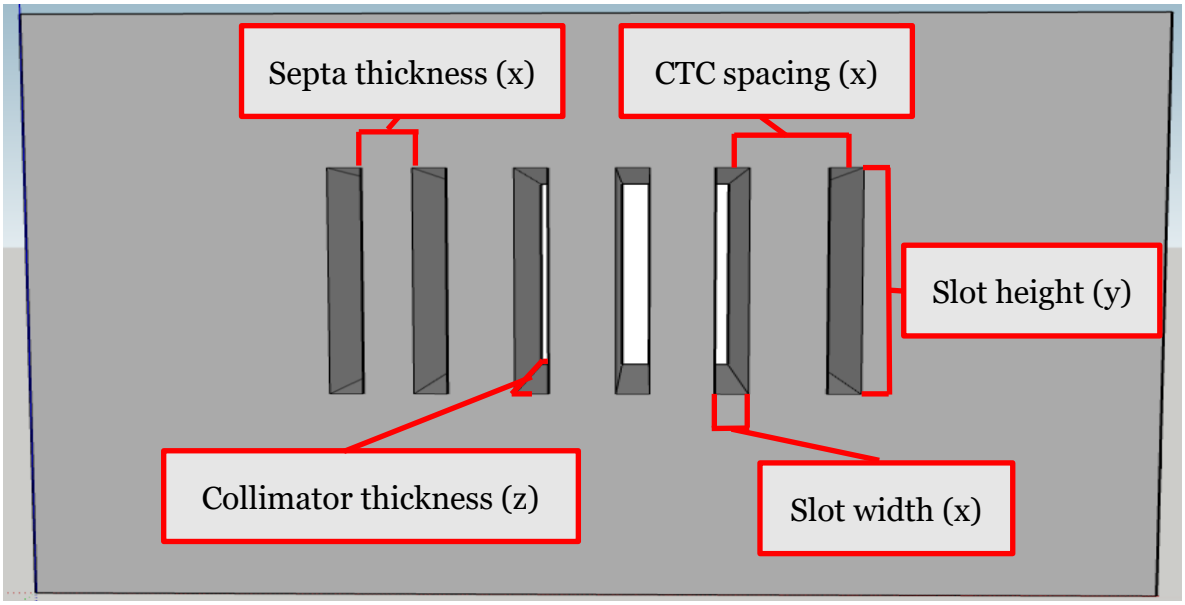

Figure 5.1: Beams eye view of collimator slots and variables used in TOPAS simulations.

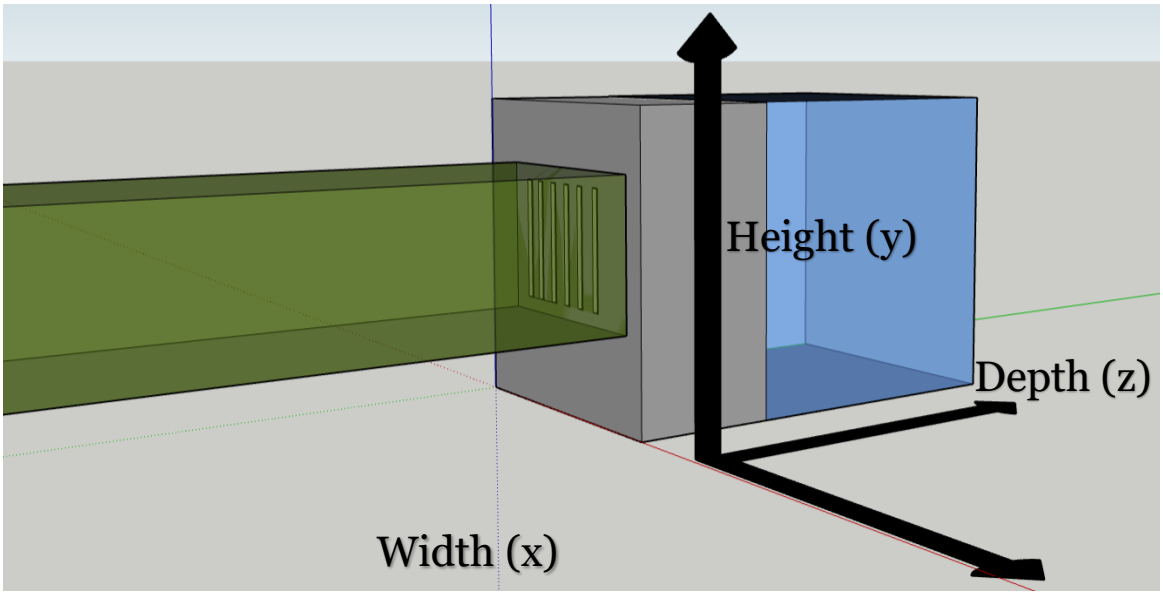

Figure 5.2: Diagram of simulation setup and directions. Showing the proton beam in green, the minibeam collimator with vertical slits (fewer are shown for clarity) in grey and the water phantom in blue

For the 50.5 MeV proton beam a 1 mm CTC spacing was used to produce a uniform dose distribution at the Bragg peak, which follows on from the discussion in Chapter 3. For higher energies, a larger CTC spacing can be used to produce a uniform Bragg peak. The CTC spacing also has a large impact on the spatial modulation close to the surface. Increasing the CTC spacing increases the distance between the minibeams and reduces the dose delivered to the valley, which comes at a cost of decreased uniformity at the Bragg peak. Reducing the uniformity of the dose delivered to the target to increase the PVDR could see an increase in sparing health tissue at the cost of local tumour control. This is not an area of research this section of work undertakes, as producing a uniform dose at the Bragg peak is a key design aspect for this thesis. This could be a potential area of research in the future. Leading to fixing the CTC at 1 mm distance, which results in the septa thickness and the slot width being inversely proportional.

The width of the minibeam exiting the collimator is determined by the width of the slots of the collimator. The width of this minibeam directly impacts the mini/micro beam sparing effect. This sparing effect has been observed for beams with widths between 0.02 - 0.67 mm [13, 50, 57]. Most of this research has historically been performed on photon beams and there is currently little research into this area for proton beams. Previous research by Eunsin Lee *et al* demonstrated that narrower slots and a thicker collimator does increase the PVDR at 5 mm and 10 mm depths [23]. This thesis aims to extend on this work and provide a more thorough investigation into this area, leading towards a better understanding of the collimator thickness and slot width for our 50.5 MeV beam.

For a particular material, a proton will on average travel through a material a fixed range before stopping. This range is primarily determined by the proton's initial energy and the attenuation properties of the material. It is important that a collimator is thick enough to block incoming protons that are travelling within the septa. A concern for minibeam collimators is the fact that they consist of many thin slots in the block of material. If the angle of incidence is sufficiently large, a proton with a large angular deviation has the potential to pass though the septa from one slot to another. This would result in scattered particles exiting the collimator and reducing the quality of the minibeams. Increasing the thickness of the collimator can reduce this effect but will also reduce the dose rate. Dose rate is reduced when the thickness of the collimator is increased removing particles with high angular spread, resulting in a less divergent mini beam [23].

The material of the collimator dictates the interactions between the beam and the collimator, and the subsequent secondary particles produced by the collimator. An ideal material would have a short path length of protons travelling through it, thus high attenuation, so protons are easily blocked. The ideal material would absorb all energy locally so that unwanted energy is not delivered as extra dose to valley regions, negatively impacting normal tissue. Although it may seem sensible that both the above criteria could be best met using a dense material, the type and energy of secondary particles produced is quite important as this can have a major impact on the final dose delivered. Previous research by Gustafsson on neutron production from collimators in proton therapy showed heavier materials produce more neutrons [21]. To reduce neutron production, lighter materials are preferred. However, as already mentioned, in order to produce clinically viable minibeams thicker collimators would be needed [21]. Gustafsson demonstrated that tungsten collimators produced a significantly higher neutron dose when compared to other materials e.g. Brass, Iron and Nickel, shown in Figure 5.3. Gustafsson's research guided the use of stainless steel as the collimator material in previous sections. This work expands on aspects of Gustafsson's research and investigates details on all secondary particles produced from the collimator, with a focus on how these materials impact proton mini/microbeams.

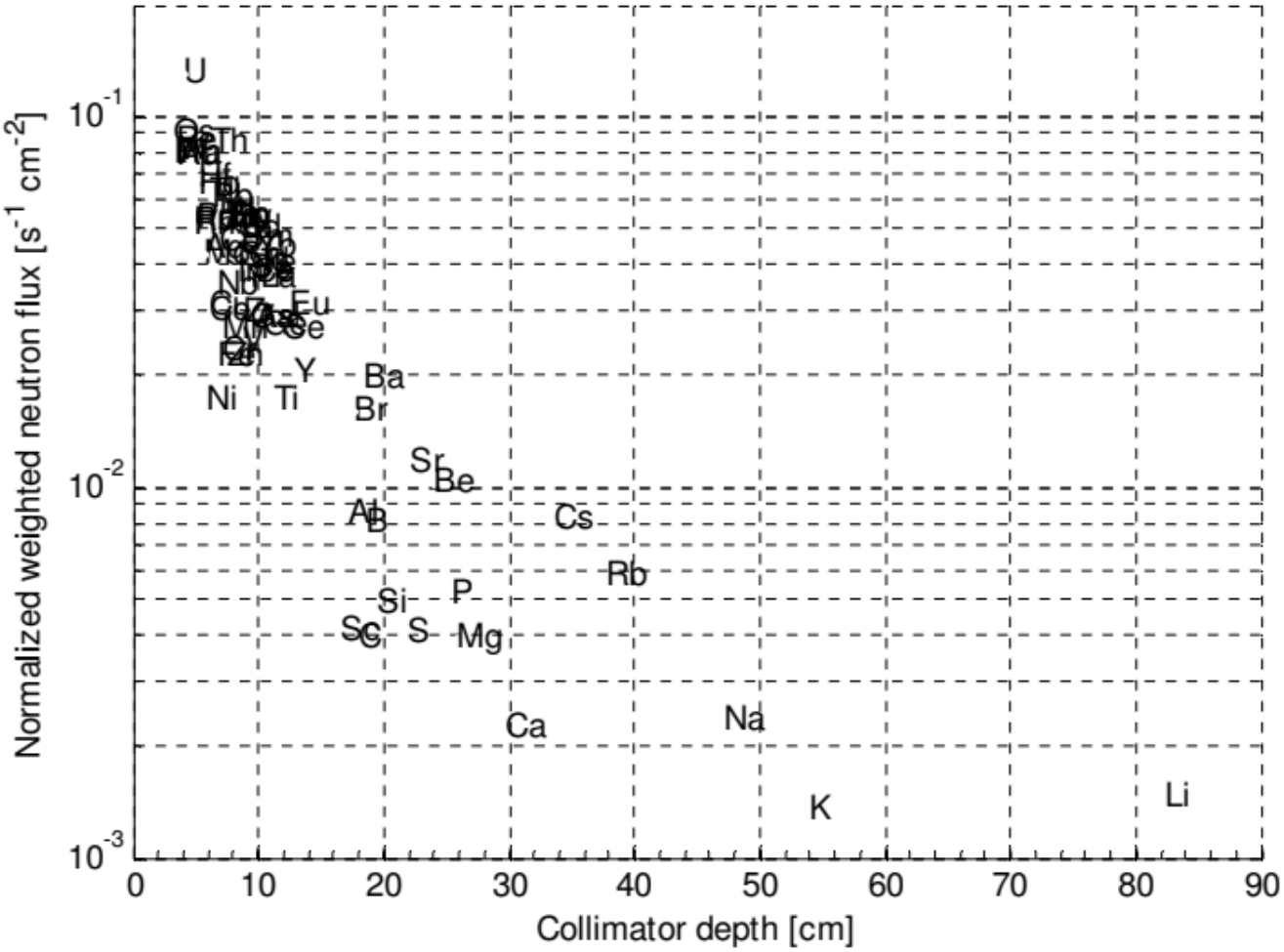

Figure 5.3: Normalised weighted neutron flux versus collimator thickness. Each element is marked with its chemical abbreviation. Reproduced from Gustafsson [20]

5.2. Methods

This section is divided into different simulations, each of which investigates a specific component of collimator design. TOPAS version 3.1.3 was used for this section of work and default physics lists were used as these are optimised for proton therapy. Each simulation uses a uniform flat 50.5 MeV monoenergetic beam in a vacuum world. In this section a monoenergetic beam was used in preference to the entire beamline to allow a more direct interpretation of how the individual collimator parameters impact the output minibeam. This also decreases “noise” and uncertainties from other components in the beamline and reduces simulation processing time. A stainless steel collimator and water phantom were placed adjacent to each other in the centre of the world, with the collimator placed between the beam source and a 25 mm cube water phantom. The width (x) and height (y) of the collimator were fixed at 60 mm to ensure only those particles which are able to get through the collimator were measured in the phantom, i.e. no contamination of measurement from particles transiting around the edge of the collimator. The collimator has a CTC spacing of 1 mm for reasons discussed in the introduction. Dose is measured in the water phantom with (x, y, z) voxel dimension of 0.075 x 5 x 0.075 mm, respectively, as this size has been previously determined to be most efficient for these simulations. Note, the coarse resolution in y-dimension is acceptable and actually advantageous as the collimator has the slots running vertically, thus producing a uniform beam in the vertical direction. This results in the water phantom being divided into 333 x 5 x 333 voxels. A phase space scorer was placed at the boundary between the collimator and the water phantom to record energy, position, direction, and particle type for all particles that pass through it. This scorer was not perceived by TOPAS as a component of the

simulation geometry and will not affect the particles passing through or the final dose deposited. The phase space scorer and dose data were then categorised as having either interacted with or NOT interacting with the collimator. This is to enable examination of the impact the collimator has on the scattered particles produced. In order to reduce processing time and decrease disk space usage, the phase space scorer only collected the first one million histories, as we are primarily interested in the number, type, and energy of particles, not the position distribution of these particles. This resulted in less than 2% uncertainties for the data displayed in the results section.

5.2.1. Impact of Collimator Thickness

Initial setup was performed as described in section 5.2 but with the following additions and modifications. The proton beam was defined to have a field size of 25 x 25 mm (x, y). The collimator had 21 vacuum filled 0.3 x 20 mm (x, y) slots spaced 1 mm apart, the length (z) of these slots was equal to the collimator thickness (z). The length (z) of the collimator thickness was varied with values of 5 mm, 10 mm, 15 mm, 20 mm, 25 mm, 30 mm, 35 mm, 40 mm, 50 mm, and 60 mm. These values were chosen based on the proton range in stainless steel. Proton range in stainless steel is 4.24 mm, thus the lengths of 5 mm multiples were chosen to ensure protons should be blocked from a range of incident angles. The minibeam field then impinges on a water phantom. Dose and phase space data are collected for each collimator thickness with each simulation consisting of 10^8 primary protons (histories).

5.2.2. Impact of Collimator Slot Width

The simulation was modelled with the method described in 5.2, with the following additions and modifications. The collimators thickness was set at 25 mm for this experiment. The collimator had again 21 vacuum filled slots with a fixed height of 20 mm. The width of each slot was varied between 0.1 – 0.7 mm with the septa width varied between 0.9 – 0.3 mm respectively, to maintain the 1 mm CTC spacing. This range of minibeam widths was chosen to represent a range of minibeam options. The minibeam sparing effect has been observed and reported for beams up to 0.68 mm. This gives an approximate upper limit on the width of the slots which we rounded to 0.7 mm [57]. Moving below 0.1 mm slot widths could potentially show improvements, this would however lead to technical difficulties building collimators with very thin slots and the differences between minibeams and microbeams is beyond the scope of this thesis. Dose and phase space data is collected for each collimator slot width with 10^8 histories.

5.2.3. Impact of Collimator Material

This simulation aims to determine the impact collimator material has on the resultant proton minibeam and subsequent dose distribution. For this a 12.5 x 12.5 mm flat beam was generated in a vacuum. The size of the beam was reduced to decrease processing time. The number of slots in the collimator was reduced to eleven 0.3 mm slots spaced 1 mm CTC. The length of the slots was also reduced to 10 mm reducing the minibeam field area from 20 x 20 mm to 10 x 10 mm. The water phantoms height and width were adjusted to 12.5 x 12.5 x 25 mm to match the beam size. The voxel size was kept consistent with previous sections in width

and depth directions resulting in 167 x 5 x 333 voxels. The collimator thickness was set to 100 mm to ensure that most materials regardless of density should be able to fully block a 50.5 MeV proton. The collimator material was varied with different elements from atomic number Z = 4 - 94, excluding gases. These elements were chosen to give a comprehensive investigation of elements that a collimator could potentially be built from. Dose and phase space data was collected for each collimator slot width with 10^7 histories. The number of histories was an order of magnitude less than previous simulations in this chapter in order to reduce processing time. However, this should not impact final results as the size of the beam and number of voxels were also reduced, resulting in a similar number of interactions events per voxel.

5.3. Results

The term “peak” as used in this section refers to the highest dose across central axis (as opposed to the Bragg peak along central axis) of each minibeam and the “valley” is the midpoint between two parallel minibeams. When referring to the Bragg peak this will always be called the ‘Bragg peak’. The minibeam peak profiles were collected in MATLAB for all 21 minibeams beamlets. Then 19 of these were averaged together to produce an average minibeam depth dose curve. The two minibeams on the outer edge are not included as these have reduced dose at the Bragg peak due to reduced in-scatter. The 20 valleys between the minibeams are also averaged together to produce an average valley depth dose curve. The ratio between these two averaged dose curves is the peak to valley dose ratio, hereafter simply referred to as the PVDR. The phase space files were processed in MATLAB only including particles travelling into the water phantom, as particles that are reflected were absorbed by the collimator. These particles were then grouped by particle type.

5.3.1. Collimator Thickness

The PDDs for different collimator thicknesses are shown in Figure 5.4 and normalised to the Bragg peak in Figure 5.5. The entrance peak dose for the 10 – 50 mm thick collimators was large relative large, about 70% of the Bragg peak, compared to that for a monoenergetic proton beam which as shown in Chapter 4 had an entrance dose of 16% of the Bragg peak. This is a consequence of protons that interact with the septa lose energy through Coulomb interactions, resulting in the beam being contaminated with lower energy protons. Per the Bethe equation, they will have subsequent shorter path lengths in water. The height of the Bragg peak is also decreased by a lack of in-scatter equilibrium in the beam at depth, resulting in a relative decrease in dose at the Bragg peak compared to surface dose [83]. This Bragg peak dose equilibrium effect is further investigated in the results section on collimator slot width. A small marginal peak is also observed at a depth of approximately 20 mm, resulting from scattered lower energy protons from the collimator.

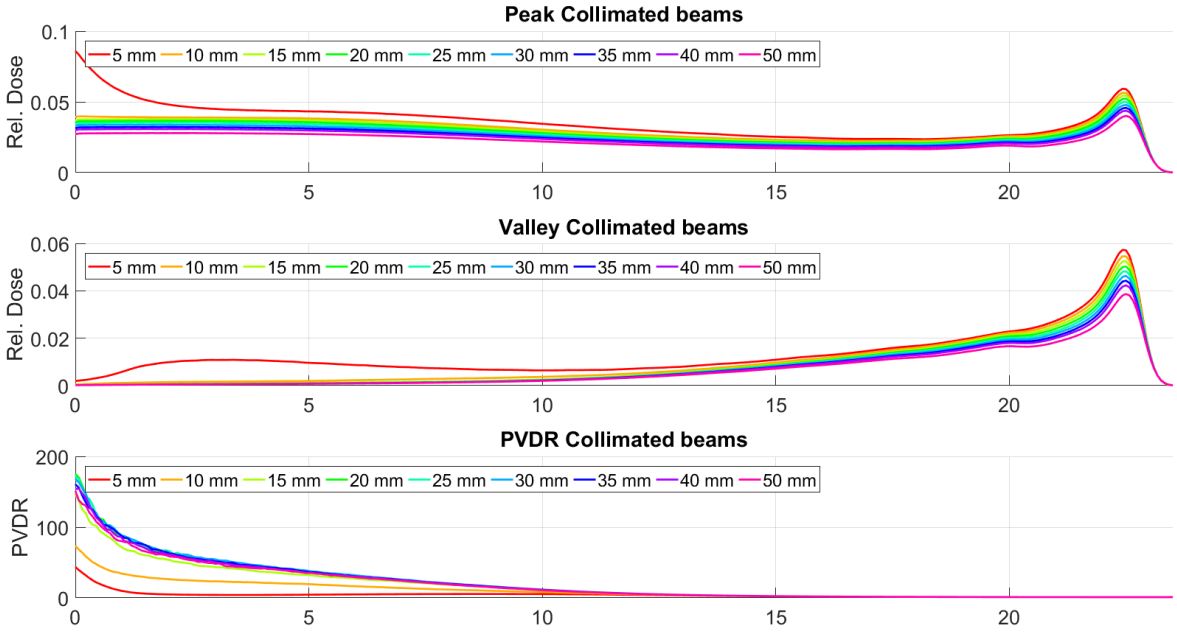

Figure 5.4: Average peak dose PDD, average valley dose PDD and averaged PVDR for various collimator thicknesses.

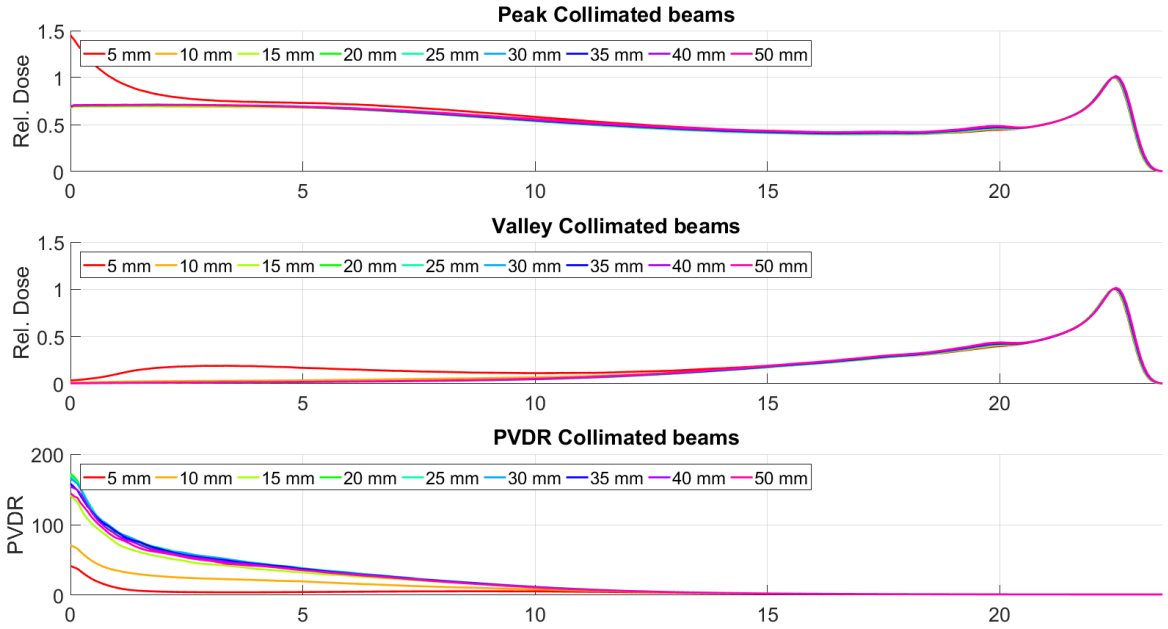

Figure 5.5: Average peak dose PDD, average valley dose PDD and averaged PVDR for various collimator lengths. Peak and valley PDDs are normalised to the Bragg peak.

The 5 mm and 10 mm collimator thickness results both have a high surface dose in the minibeam peaks and a higher valley dose between the surface and 15 mm depth. The PVDR for both the 5 mm and the 10 mm long collimators is notably lower than that of the rest of the collimators. This is due to the thickness of the collimator being less than 15 mm and therefore not sufficient to block all protons from the uniform beam. While it would be expected that a length of 4.24 mm would block a proton travelling in stainless steel, this only applies to protons with no angular divergence. Protons with sufficient angular divergence can pass horizontally between the minibeam slots, through the stainless steel and the gaps forming the minibeam slots. These protons would have an effective path length through the stainless steel which is less than 4.24 mm whilst travelling through the 5 – 10 mm collimators. Resulting in a minimum length for the collimator of 15 mm or slightly more than three times the path length of the material.

The results in Figure 5.4 show that increasing the collimator thickness decreases the dose at all depths therefore lowering dose rate. As the beam has some divergence some protons will impact the side of the slots when passing through. As the collimator's thickness increases, more particles are likely to be removed by this effect, the benefit being the angular divergence of protons with the produced minibeams is decreased when using longer collimators. The PVDR results show that there is not clear benefit to increasing the collimator thickness as there is no observable increase in the PVDR going beyond 20 mm. The reason for this result is shown in the next set of results, the phase space results: Figure 5.6 and Figure 5.7.

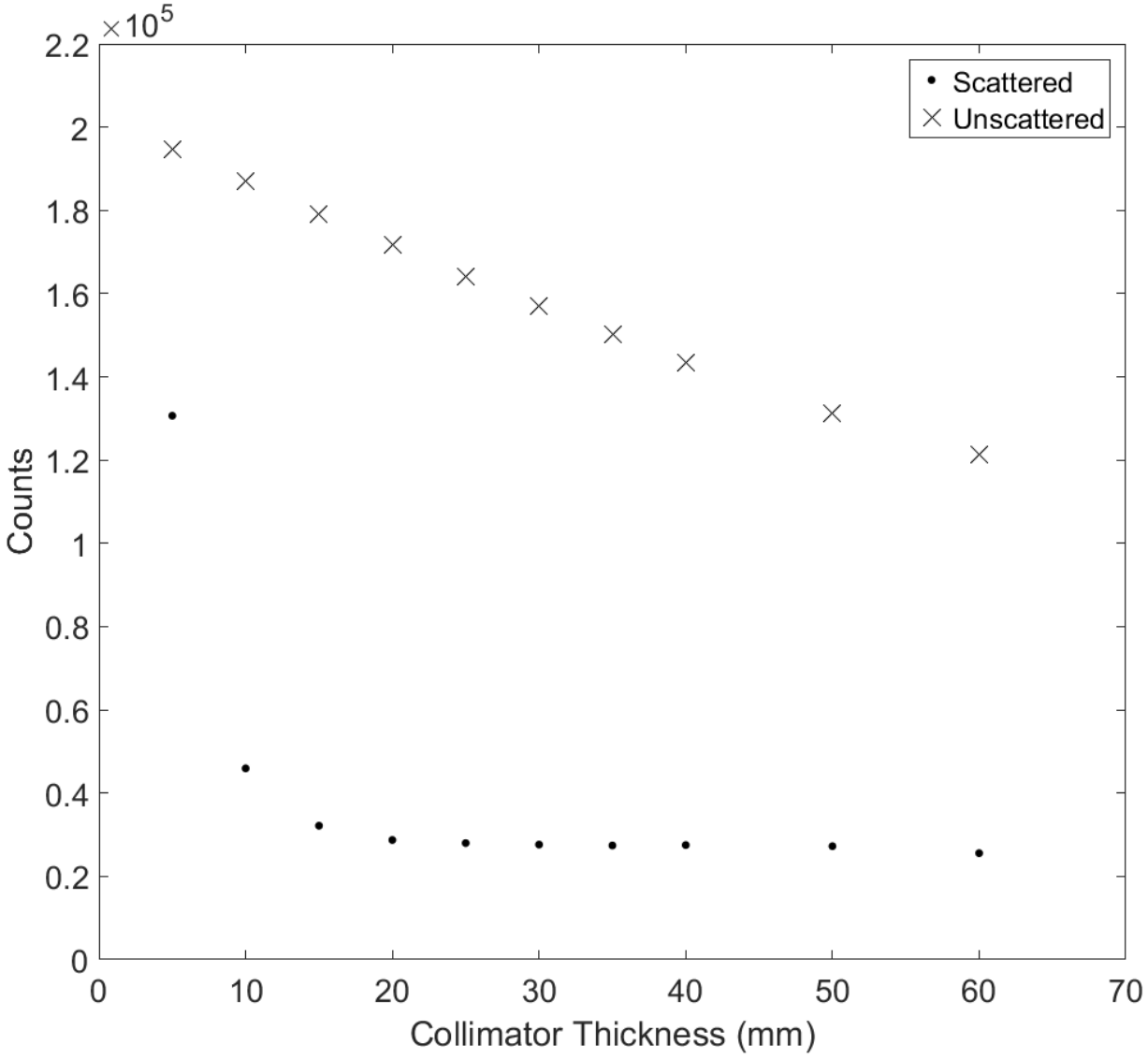

Figure 5.6: Number of protons entering the water phantom as a result of collimator thickness. Showing protons scattered off the collimator and protons that passes straight through.

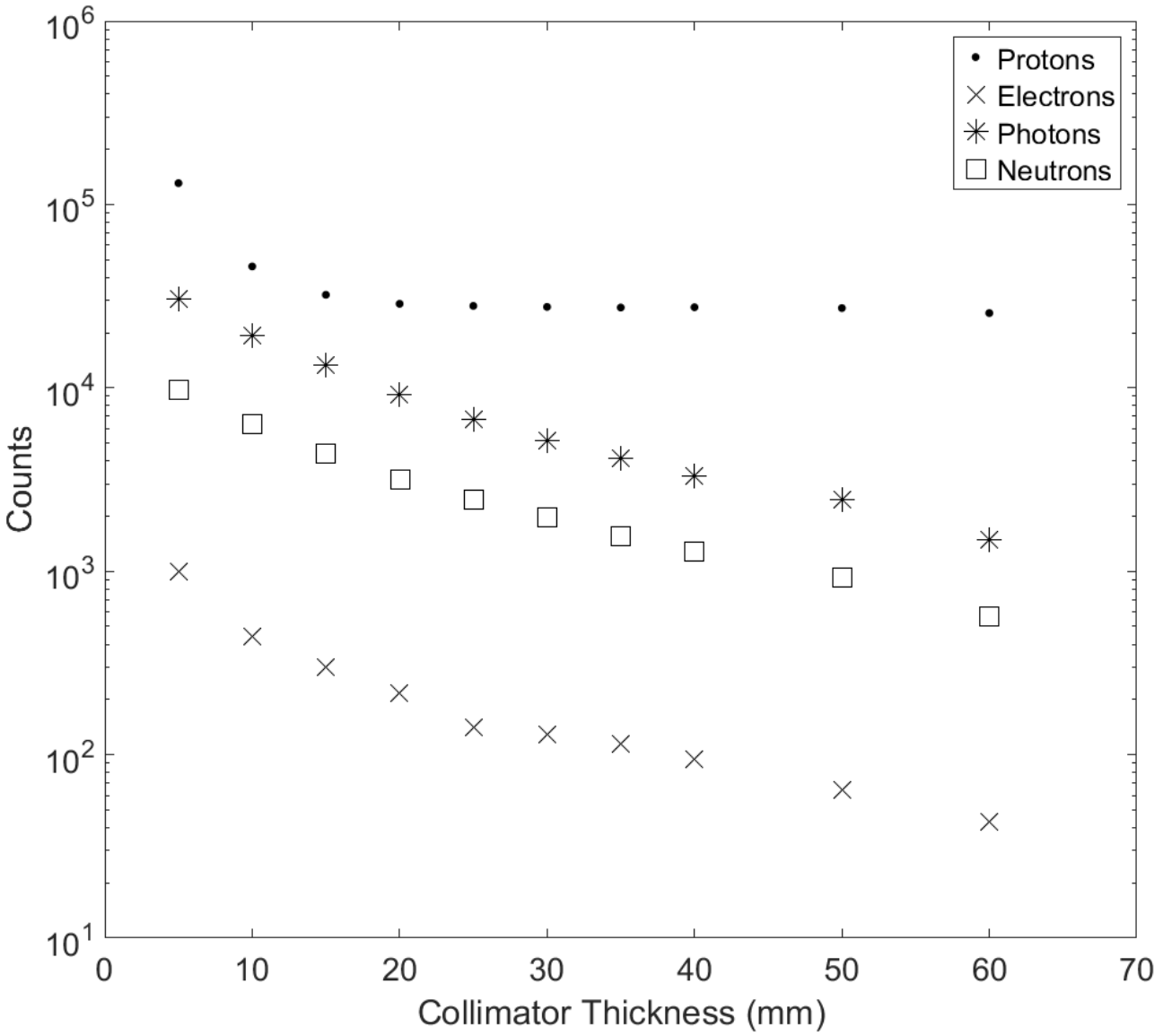

Figure 5.7: Number of particles entering the water phantom as a result of collimator thickness. Showing particles scattered off the collimator.

Between 98 – 89% of the particles measured in the phase space scorer were protons for the 10 – 60 mm collimators, respectively as shown in Figures 5.6 and 5.7.

Figure 5.6 compares numbers of protons exiting the collimator having passed directly though (crosses) or having interacted with the collimator septa (dots). As the thickness of the collimator increases the number of protons passing directly through the collimator decreases linearly. This matches the previous observations showing a decreasing dose with collimator thickness.

There are a large number of scattered protons for collimators thinner than 15 mm are due to these collimator's thickness being insufficient to block protons with angular divergence. For collimators with thicknesses beyond 15 mm, increasing the thickness has little impact on the number of scattered protons. This difference between scattered and non-scattered protons helps to explain the differences in the PVDR's previous dose results. With a range of between 15 - 20 mm for the collimator thickness producing a maximum in the PVDR with limited benefits beyond 25 mm thickness.

Figure 5.7 shows the results from all particles entering the water phantom that have interacted with the collimator septa. Note, this figure uses a log scale on the y-axis to display the data more clearly. Of the particles that have interacted with the collimator septa most are scattered protons. When the protons interact with the septa a small number of photons, neutrons, and electrons are produced. Other particles are not shown due to insignificant numbers present in the results. The number of photons, electrons and neutrons reaching the water phantom is reduced with increased collimator thickness. This decrease follows the trend of the total number of protons passing through the collimator and decreases with collimator thickness. However, these non-proton scattered particles have limited impact on the dose distribution as there are far fewer of them. It should also be noted that neutrons are not fully blocked by the small water phantom and are able to pass through without interactions. Neutrons have a high biological impact and have a high penetrating power though many materials, making them a radio-safety hazard so should not be fully disregarded. Further work around neutrons is covered in Chapter 6.

5.3.2. Collimator Slot Width

The collimator minibeam slot width results are shown in Figure 5.8 and Figure 5.9 unscaled and normalised to the Bragg peak, respectively. The peak results indicate that as the width of the minibeams decrease the relative ratio between the surface dose and the Bragg peak increases. In particular, the dose at the Bragg peak increases as shown in the Figure 5.8. The surface dose also displays a cut-off effect with all minibeams from 0.3 - 0.7 mm receiving the same surface dose but the 0.2 mm and 0.1 mm to a larger degree showing a large decrease in dose. The effect occurs at both the Bragg peak and the surface and is a result of the lack of in-scatter in the beam discussed in the previous section. While this effect has a large impact at the Bragg peak for all beams it also has an impact for the 0.1 mm and 0.2 mm wide minibeams.

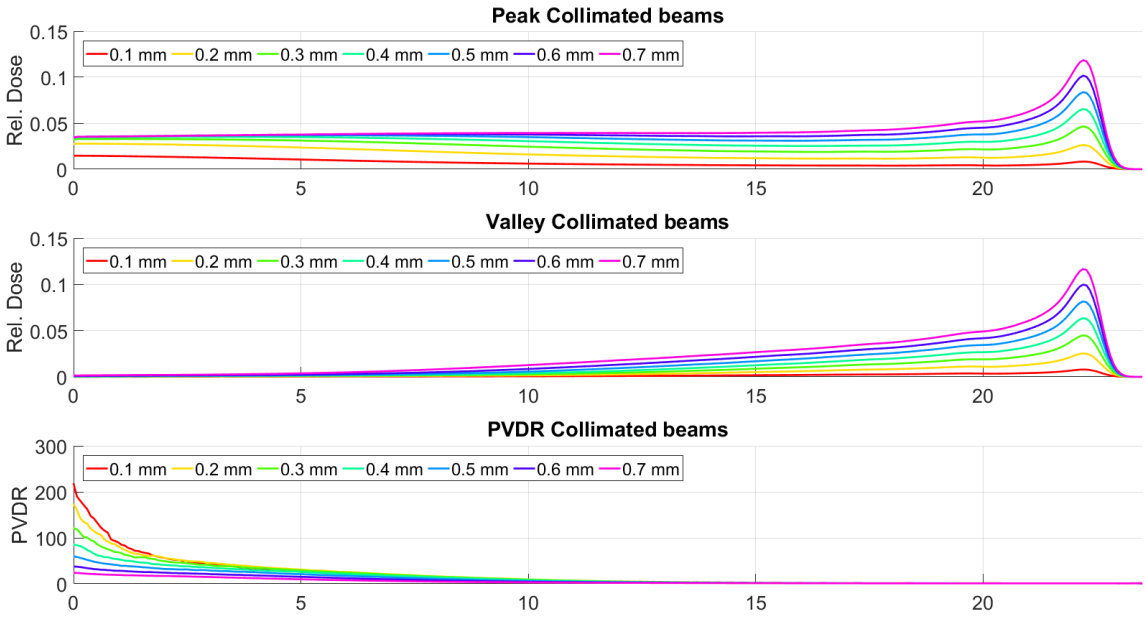

Figure 5.8: Peak dose, valley dose and PVDR for various collimator slot widths.

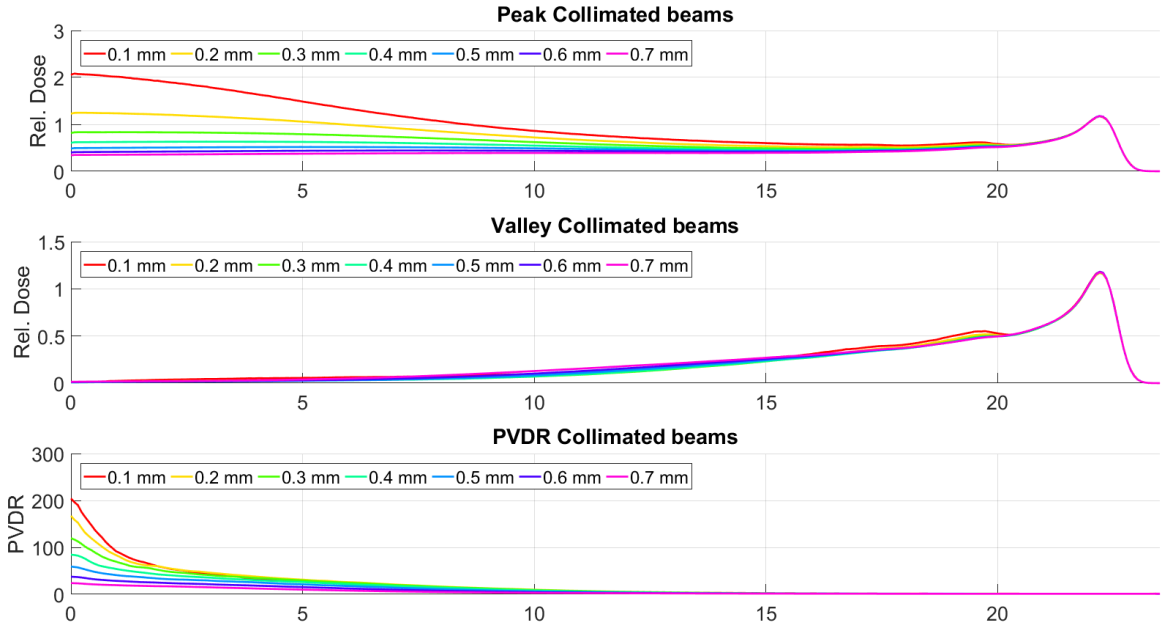

Figure 5.9: Peak dose, valley dose and PVDR for various collimator slot widths. Peak and valley dose are normalised to the Bragg peak.

Interestingly, a small peak at 19.5 mm depth can be observed in Figure 5.10 in both the peak and valley results. This peak is again a result of protons scattering off the collimator and depositing their energy at shallower depths in the water phantom. The scatter from the collimator is more clearly shown in the normalised results with the ratio between scattered dose to non-scattered dose increasing in the peaks and valleys as the width of the beam decreases. It can also be observed in Figure 5.10 that increasing the width of the minibeam increases the relative valley dose between 5 mm and 16 mm depths. This is a result of requiring a fixed CTC spacing between the minibeams, as discussed in Section 5.1. As the width of the minibeam increases the width of the septa decreases, resulting in less attenuating material for the wider minibeams, allowing some unwanted protons to propagate through the collimator. This is similar to decreasing the thickness of the overall collimator shown in the previous Section 5.3.1. This has a large impact on the 0.7 mm, a medium impact on 0.6 mm and a small impact on the 0.5 mm wide minibeams.

The 0.2 – 0.4 mm results show no noticeable differences between the 0 and 17 mm depths. This is a function of the thickness of the collimator and the width of material between minibeams. For no impact to be observed for a 25 mm thick collimator a minimum septa thickness between slots of 0.6 mm is required. Increasing the thickness of the collimator would allow this effect to be removed for wider minibeams. This effect is explored further in the phase space results section below. Decreasing the width of the minibeam is shown to increase the PVDR for all results, with large increases at the surface. This has the downside of a lower uniform dose distribution at the Bragg peak and a high surface dose in the minibeams.

Results from the phase space are shown in Figures 5.1 and Figure 5.11. It can be observed that the number of primary protons passing through the collimator increases linearly with slot width. This increase can be attributions to the linear increase in area as the slots have a fixed height. The number of scattered protons does increase with slot width but at a much slower rate. The narrower the slot the larger the PVDR. With narrower slots the ratio between un-scattered to scattered protons decreases, thus reducing the quality of the beam. The scattered protons have much lower mean energy of 36.7 MeV, resulting in a projected range in water of 12.5 mm, which is considerably less than the range of 22.3 mm for a 50.5 MeV proton. The scattered protons also increase the surface dose whilst not delivering dose to the Bragg peak. This produces a high PVDR at the surface, but reduces the overall quality of the treatment, as delivering dose to the Bragg peak is the main aim.

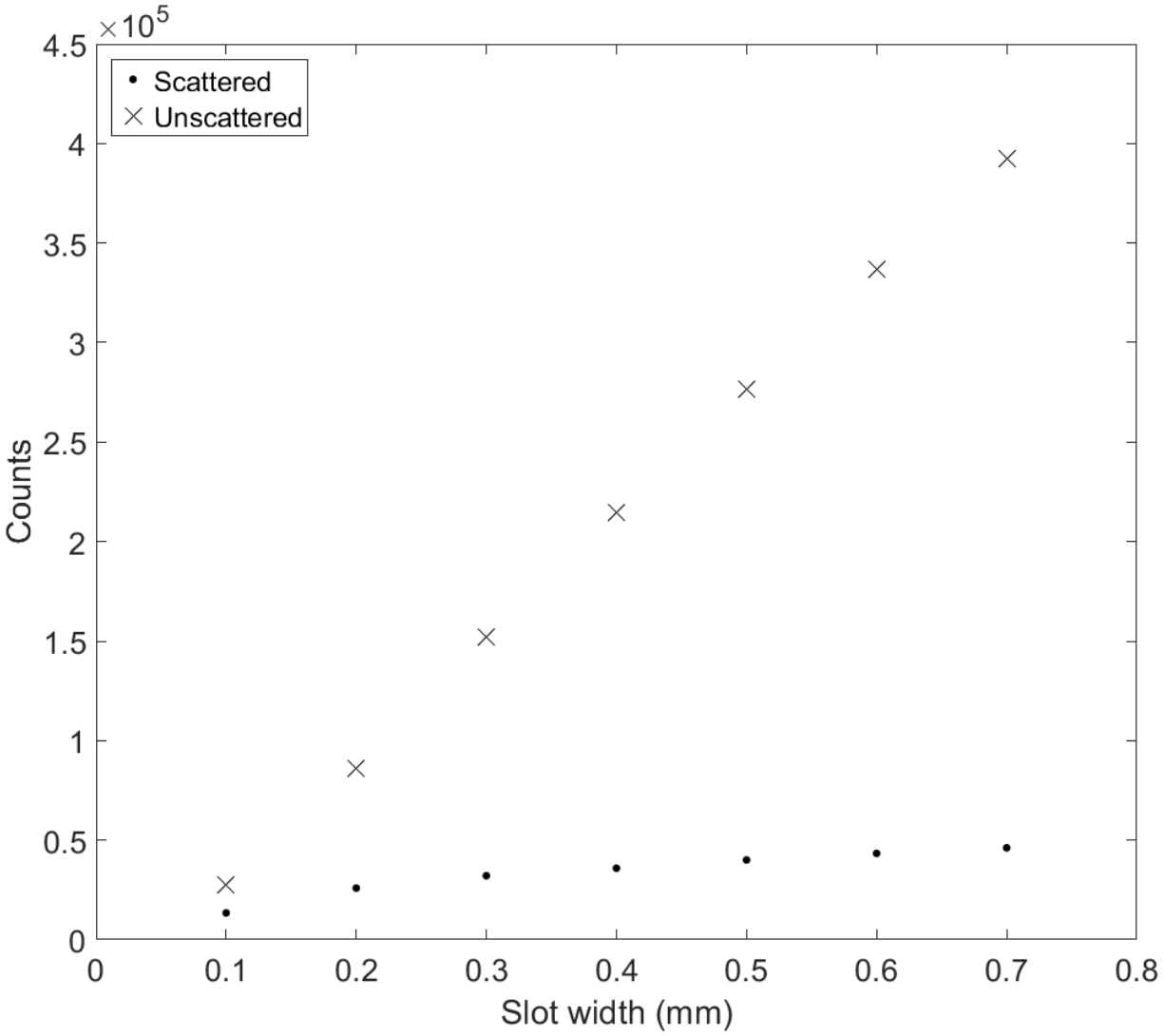

Figure 5.10: Number of protons entering the water phantom as a function of collimator slot width. Showing protons scattered off the collimator and protons un-scattered.

Figure 5.11 shows a breakdown of all scattered particles from the collimator. The number of neutrons, photons and electrons show no major trends as related to collimator slot width. This implies that these particles are produced by roughly the same number of protons impacting the sides of the collimator regardless of slot width. This indicates that it is a function of the internal area of the slots impacting the production of these particles, which remains roughly constant.

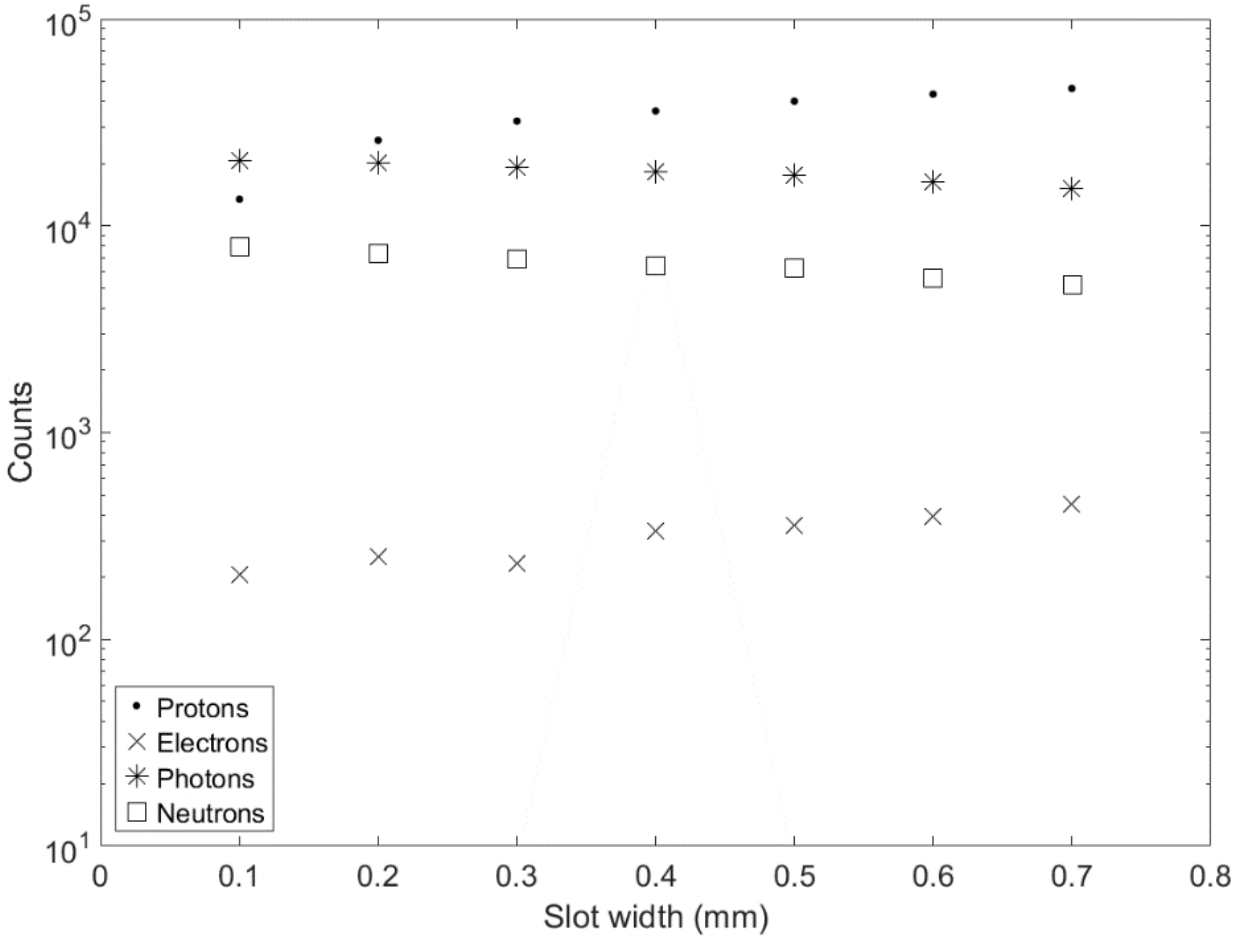

Figure 5.11: Number of particles entering the water phantom as a function of collimator slot width. Showing various particles scattered off the collimator.

5.3.3. Collimator Material

The collimator material results are shown in Figure 5.12 and Figure 5.13, displaying the mean peak dose and valley dose as a function of density at the surface for various collimator elements, respectively. The results only contain a component of the total dose from particles that have interacted with the collimator and then deposit dose in the water phantom.

Particles that have not interacted with the collimator have been omitted as these produce results which do not vary with material. It can be observed that use of material with increased density results in decreased scattered dose from the collimator. There is a negative approximate exponential relationship with density. It can also be observed in the surface peak data that not all elements sit on a single curve; some elements particularly between 5 and 15 g/cm^3 density show increased peak dose at the surface. The valley data also follow a similar trend. However, elements that have densities less than 5 g/cm^3 have a large spread, this is investigated further in the following results.

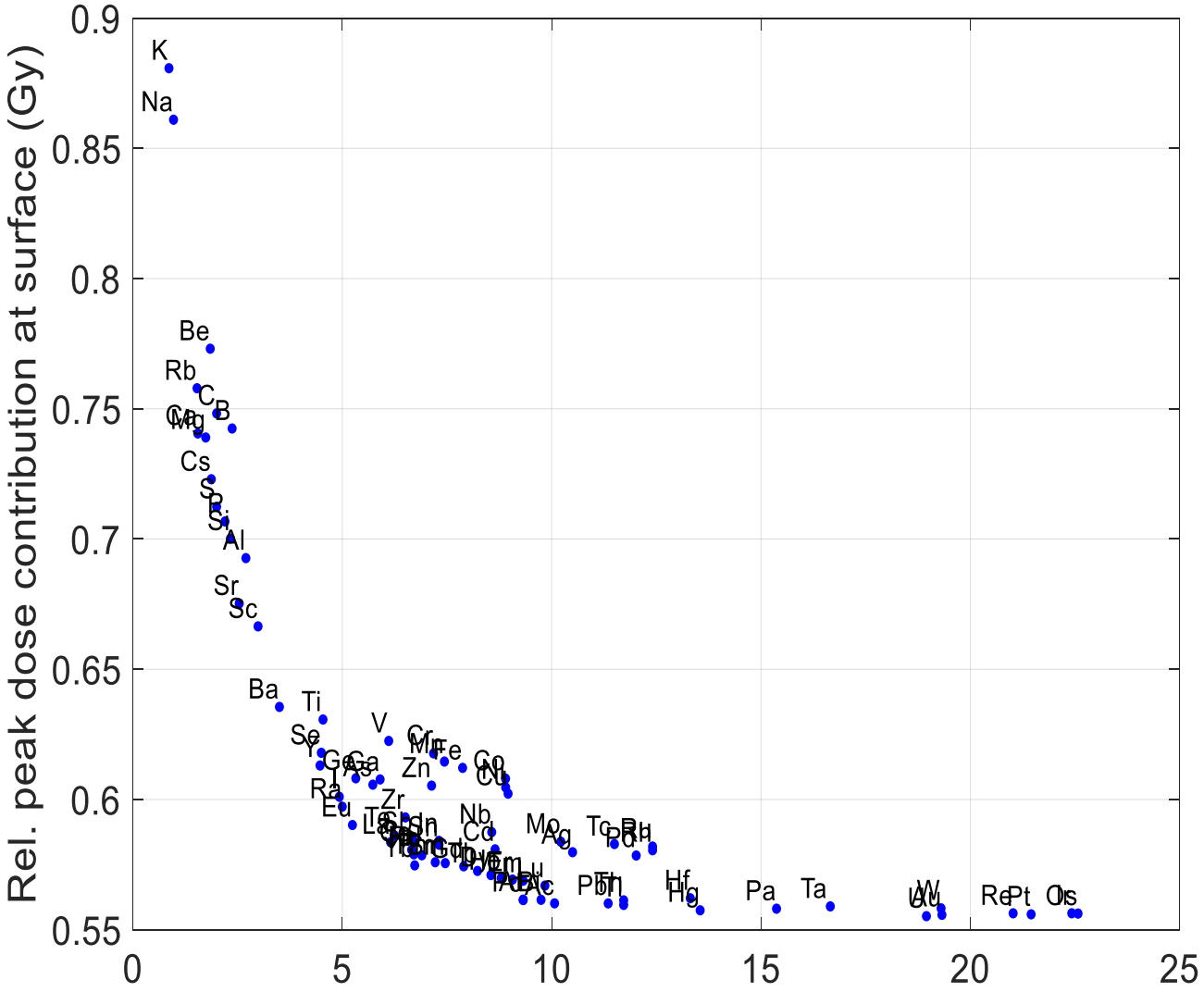

Figure 5.12: Impact of collimator material on scattered particles from the collimator, showing minibeam peak dose at the surface of the water phantom. Elements are labelled by their symbol Below is a zoomed in section of elements between 3 and 14 density for clarity.

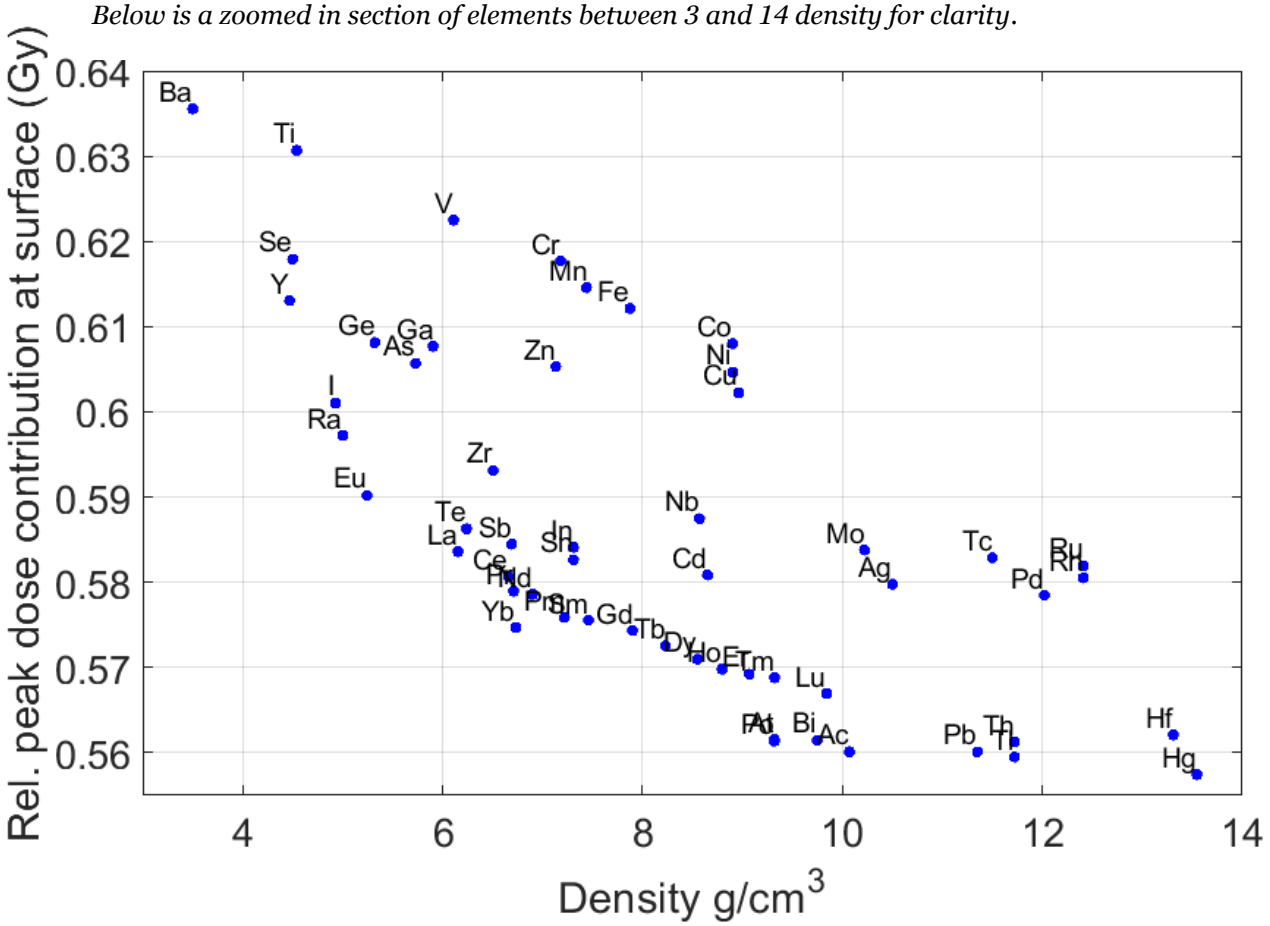

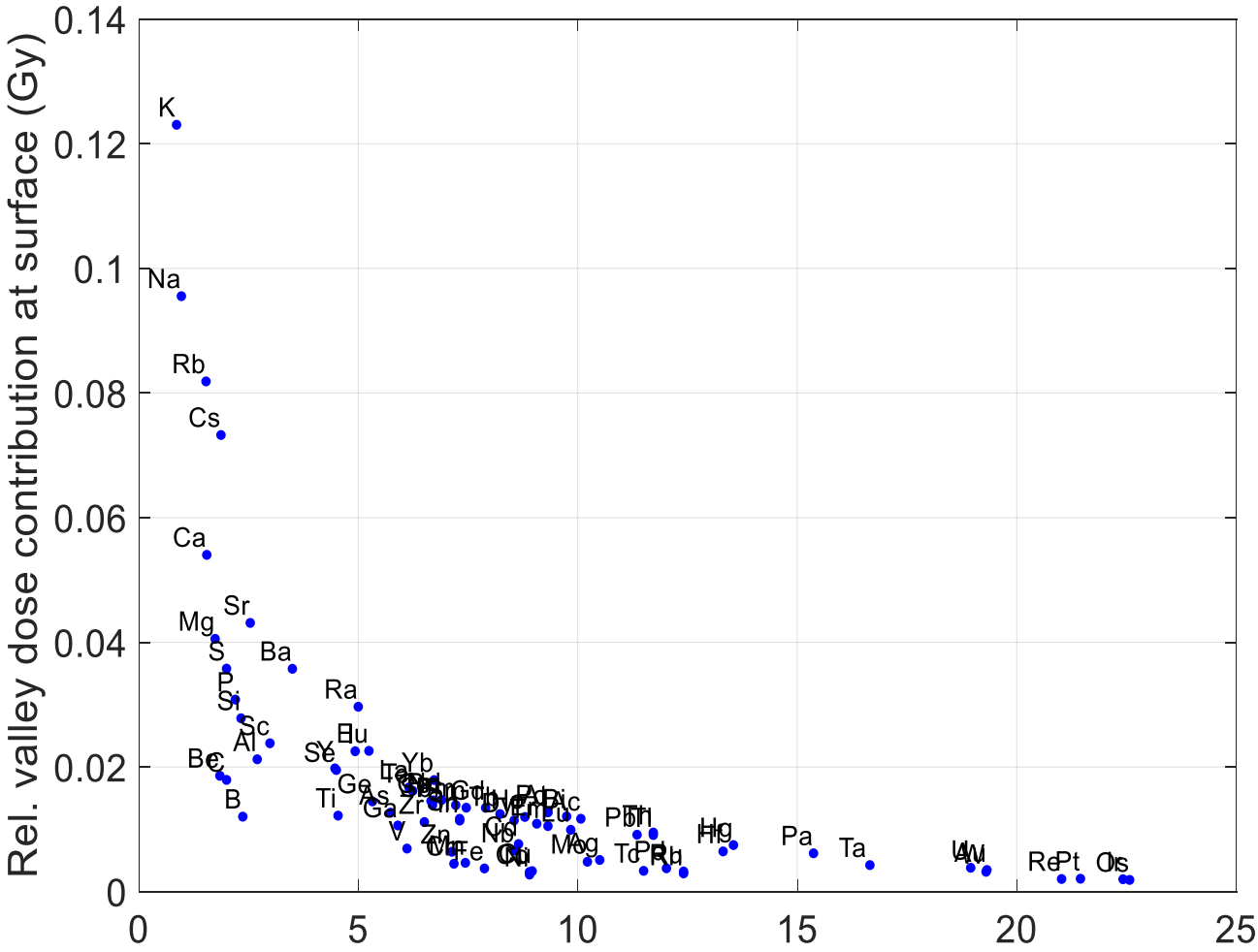

Figure 5.13: Impact of collimator material on scattered particles from the collimator, showing minibeam surface valley dose. Elements are labelled by their symbol. Above displayed with a linear scale and below displayed with a log scale for the elements with the lowest dose.

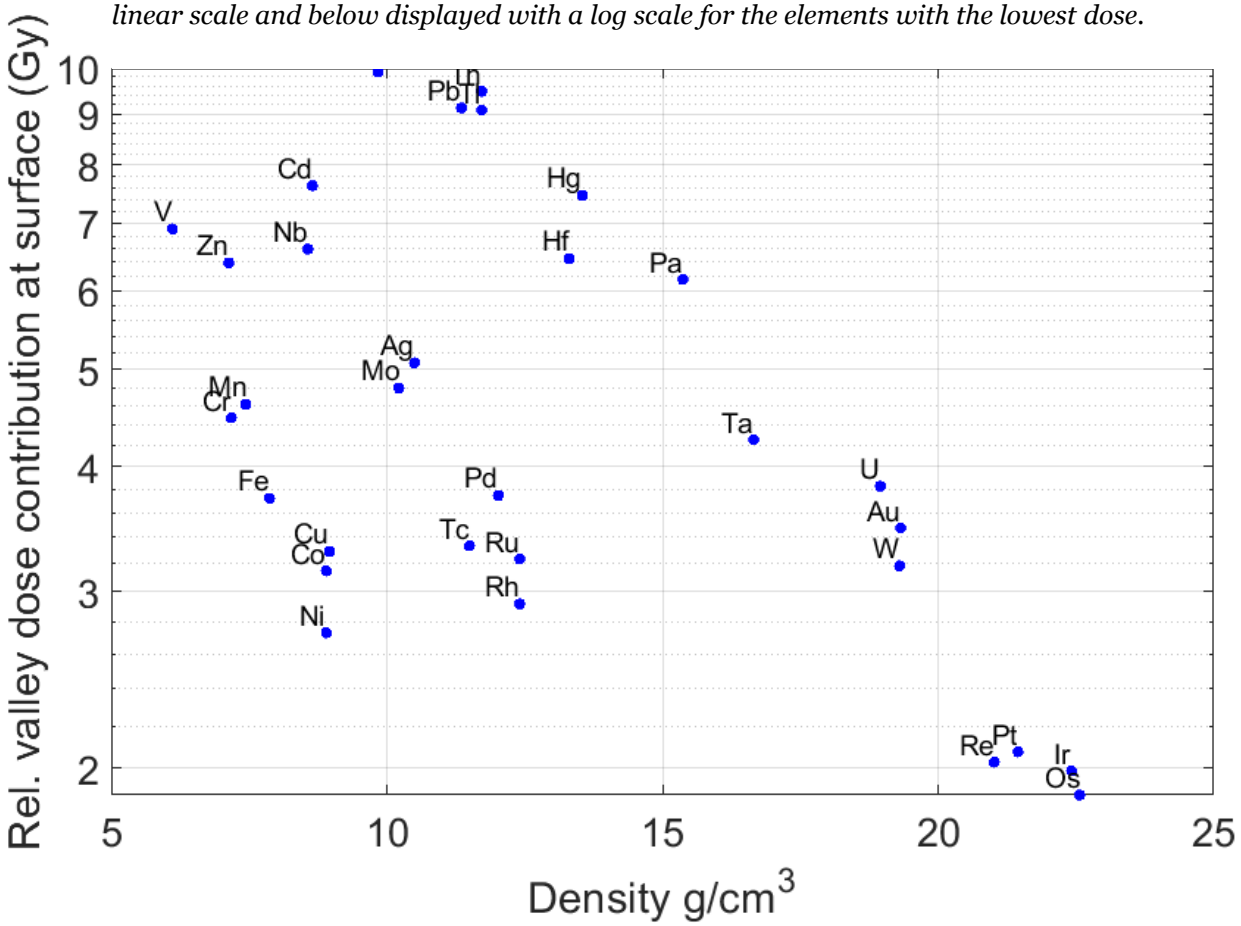

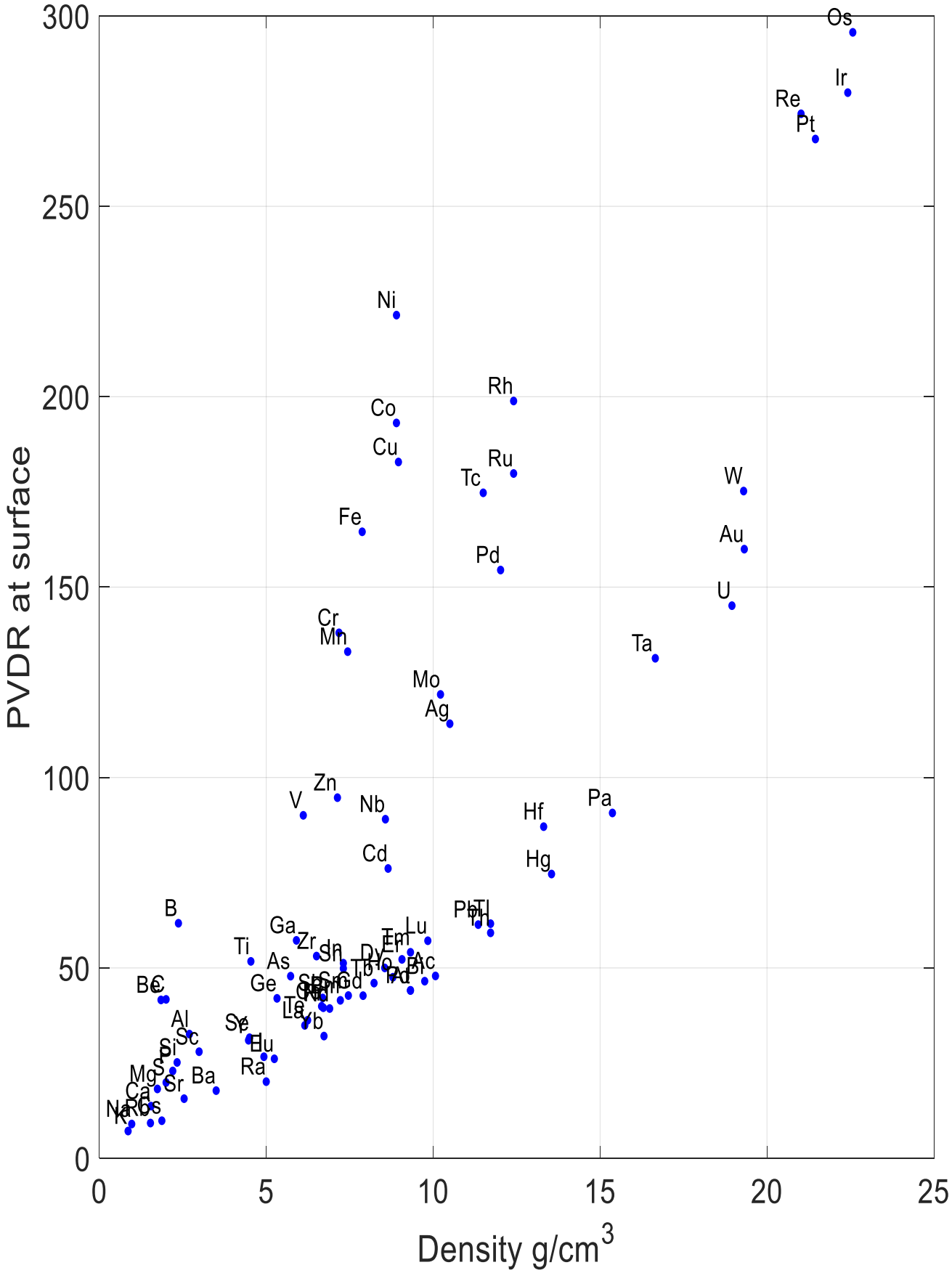

Figure 5.14: Impact of collimator material on scattered particles from the collimator, showing ratio between minibeam peak dose and valley dose at the surface.

The combined result of this becomes clear when looking at the ratio between the peak and valley at the surface in Figure 5.14, which shows an increasing trend where the PVDR increases with density up to a maximum of around 300 for osmium, the densest naturally occurring elements. Some other interesting results are also observed. There is a main curve from potassium through mercury to osmium, with two extra 'branches' coming off the main curve. Elements in these branches have significantly higher PVDRs than expected for their given densities. These are period 4 and 5 transition metals. The period 4 results are of particular interest as these elements obtain very high PVDR's at moderate densities particularly Ni, Co, Cu and Fe, with Ni producing a very high PVDR. The period 5 elements follow a similar trend. However, they produce a lower PVDR than that of the period 4 elements.

Figure 5.14 and Figure 5.15 show the PVDR at depths of 5 and 10 mm, respectively. The average PVDR decreases with depth due to proton beam divergence, producing a pseudo-uniform distribution at the Bragg peak. As the PVDR decreases with depth in the water phantom the range of differences in the PVDR caused by various elements decreases. At a depth of 10 mm these is a difference in PVDR of only seven between all elements, with most difference between elements clearly caused by the difference in density. This effect is less noticeable at 5 mm depth, where the transition metal 'branches' are still observable with Ni, Co, Fe and Cu producing excellent PVDR's. Clearly showing that element choice has a large effect on the surface dose distribution.

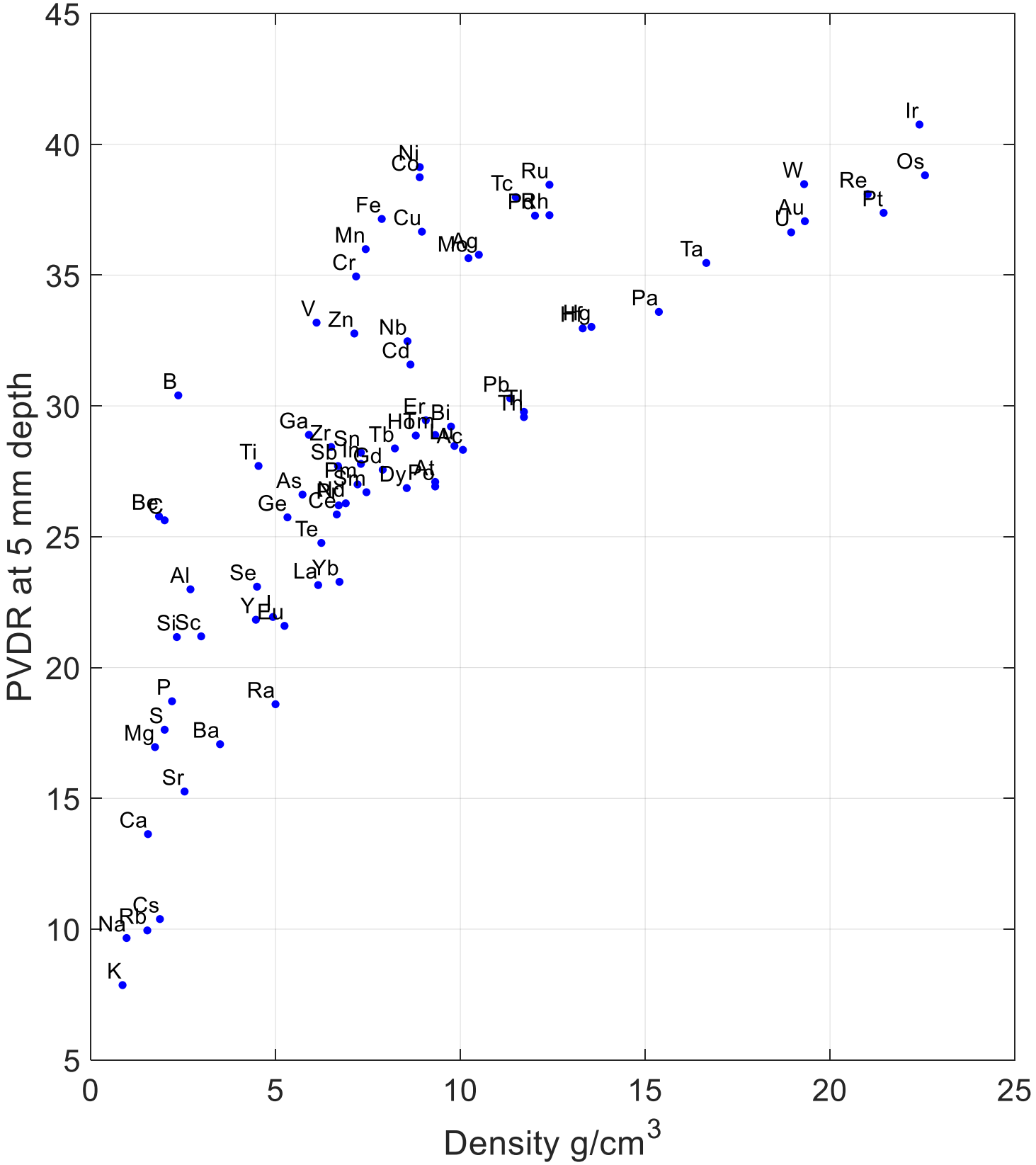

Figure 5.15: Impact of collimator material on scattered particles from the collimator, showing ratio between minibeam peak dose and valley dose at 5 mm depth. Elements are labelled by their symbol.

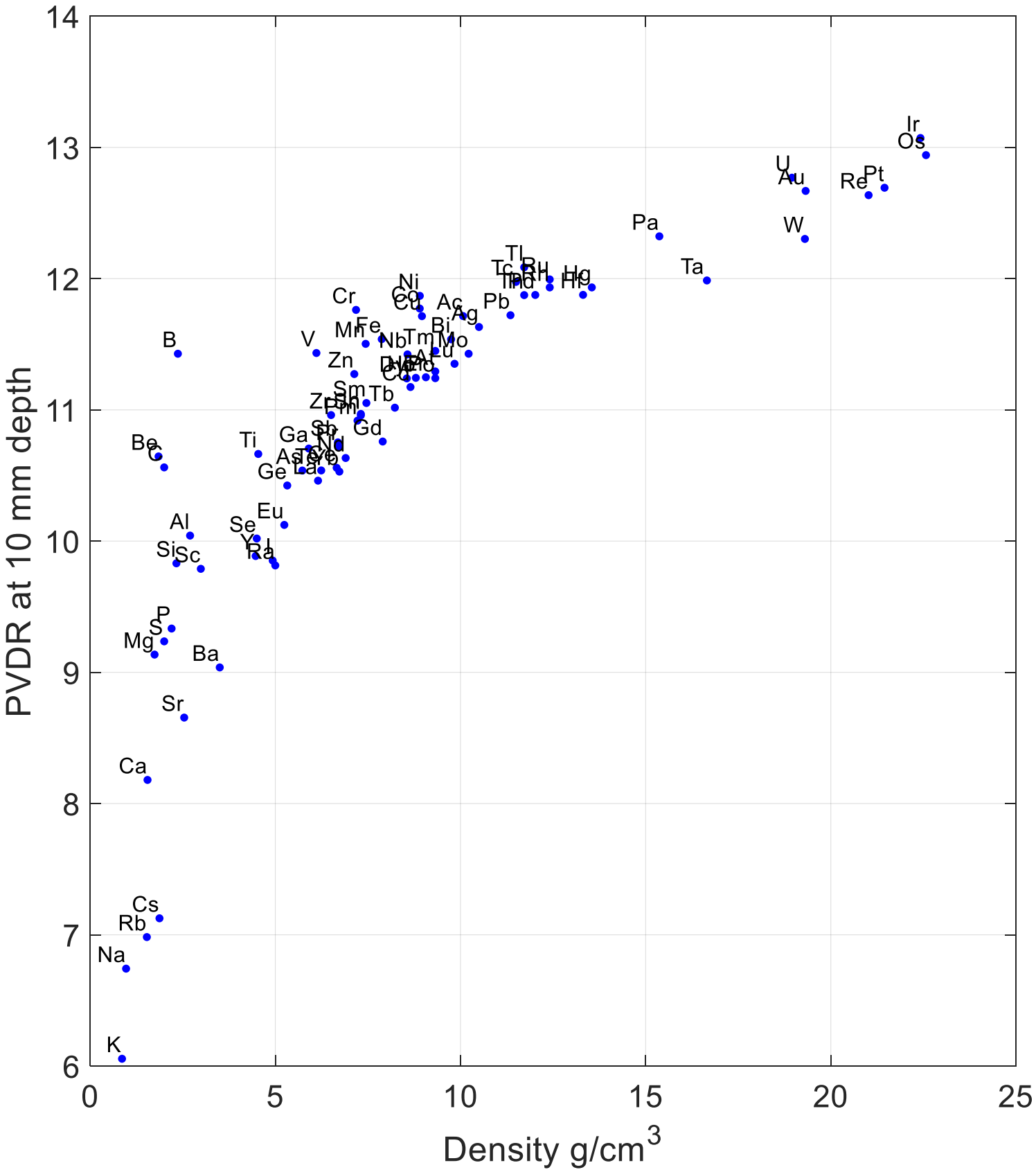

Figure 5.16: Impact of collimator material on scattered particles from the collimator, showing ratio between minibeam peak dose and valley dose at 10 mm depth. Elements are labelled by their symbol.

The results from the phase space data have been sorted in to proton, electrons, photons, and neutrons produced by each element in order to gain some insight into the cause of the differences between the different materials. Figures 5.16 - 5.19 shows the data from the total number of each particle produced by each material. Most elements scatter around 10 - 30 times more protons than any other particle. The number of protons scattered by the collimator exponentially decreases with density. Most elements follow this trend closely with only a small deviation for some of the transition metals. This trend agrees with results from the dose data in the previous section, showing that number of protons are the primary cause of this effect.

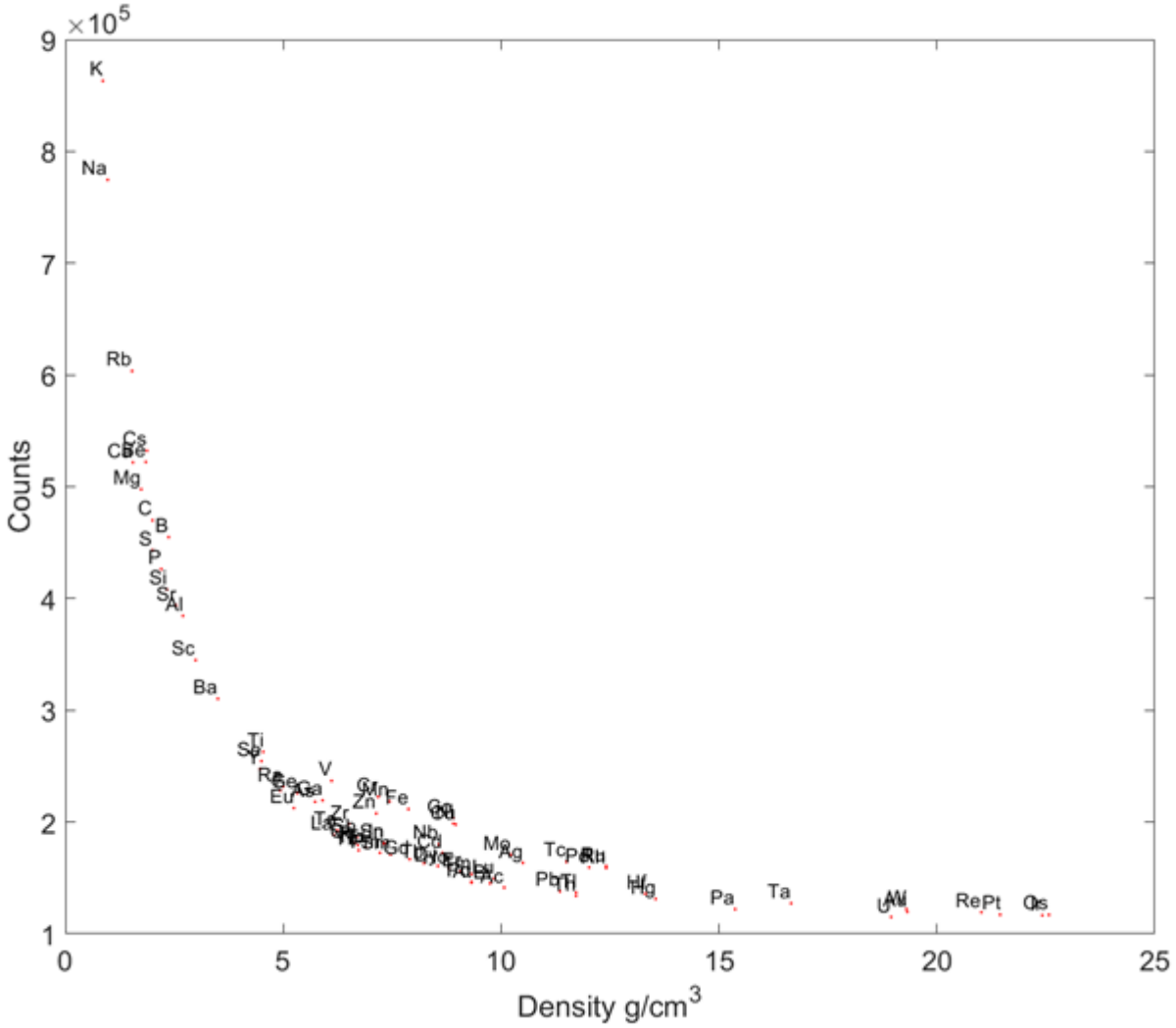

Figure 5.17: Effect of collimator material on the number of protons scattered by the collimator. Elements are labelled by their symbol.

The scatter results for the electrons, show that materials with a density between 0 g/cm^3 and 5 g/cm^3 increasing the density will decreases the number of electrons produced. Materials with densities higher than 5g/cm^3 have are no noticeable differences in the number of electrons produced. This indicates there is a cut-off effect based on density rather than elemental properties, and results in all elements with densities greater than 5g/cm^3 being approximately equal in electron production. The mean energy for all electrons for all elements is 0.84 MeV. Of all the particles considered in this work, secondary electrons are the particle least produced from the collimator.

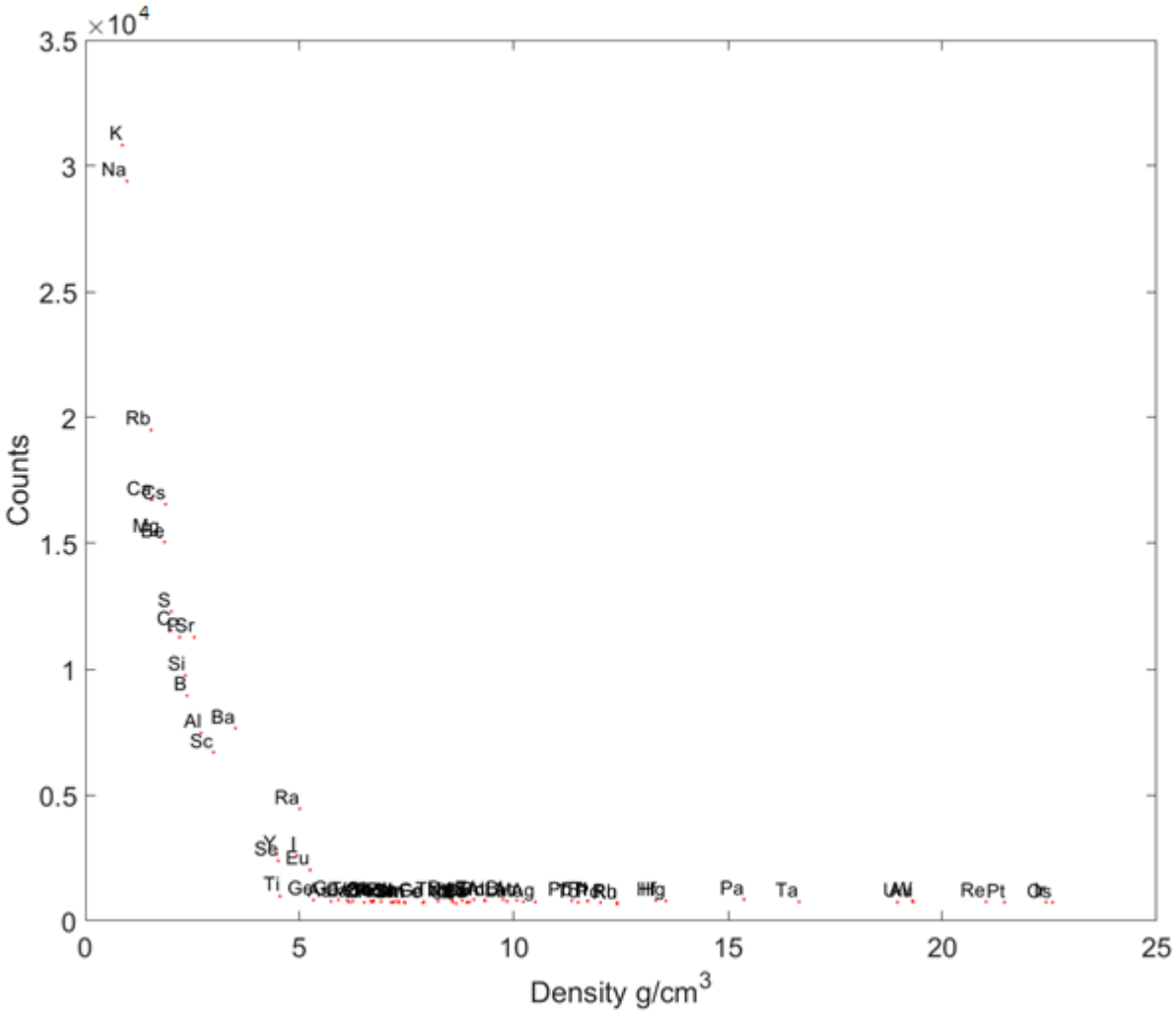

Figure 5.18: Effect of collimator material on the number of electrons scattered by the collimator. Elements are labelled by their symbol.

The number of photons produced by each element follows the same trend as scattered protons. Increasing the density of the collimator material decreases the number of photons produced. The photon results do have a much larger variance and do not lie directly on a particular curve. Elemental differences between each element are responsible for these differences. The number of photons produced by the collimator are between 3 – 16% of all secondary particles and have an energy range of between 1.4 – 4.9 MeV with an average energy of 1.98 MeV.

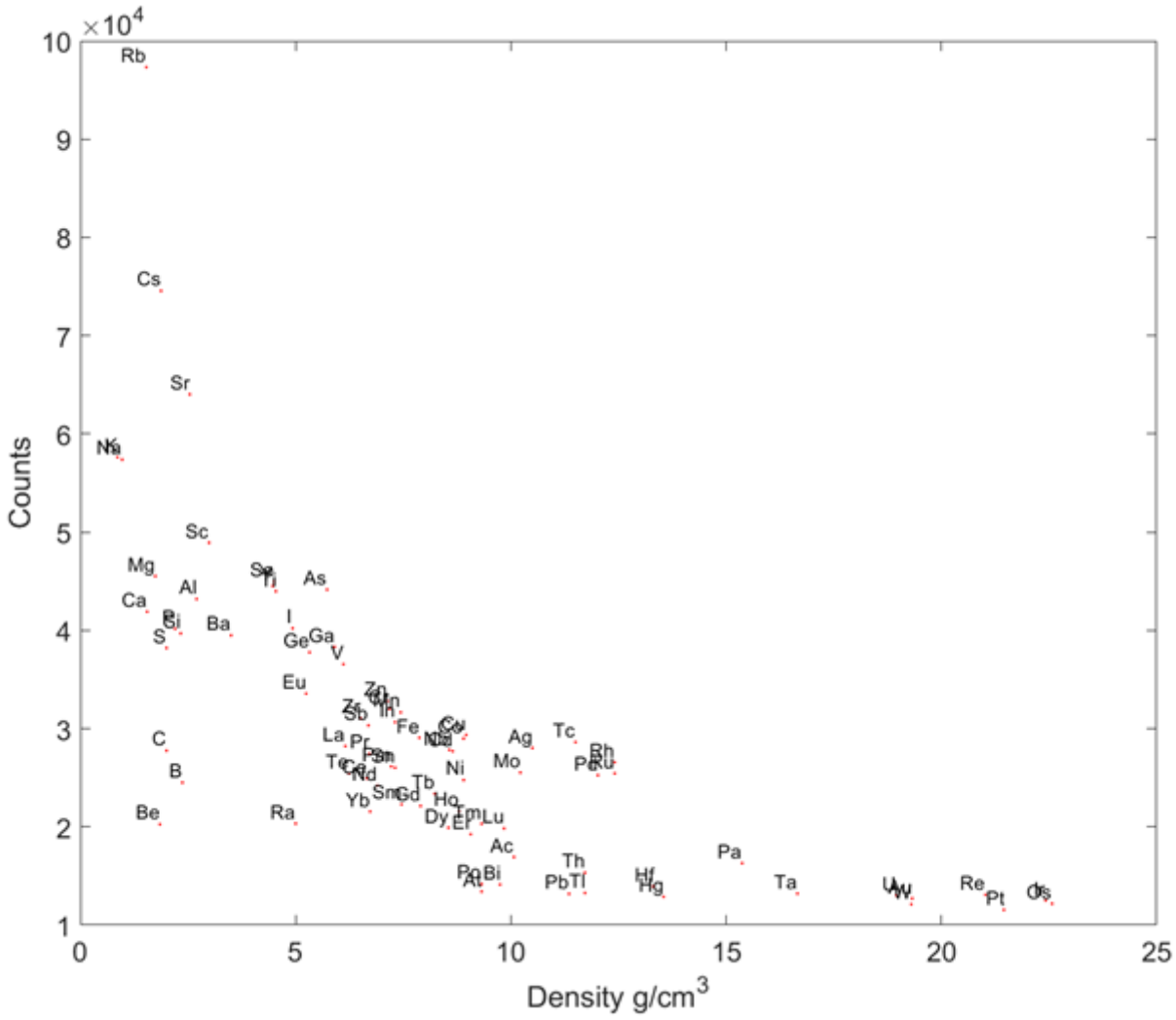

Figure 5.19: Effect of collimator material on the number of photons scattered by the collimator. Elements are labelled by their symbol.

The neutron results show no clear trend with density, showing neutron production depends mostly on elemental properties. Some of the low atomic number elements produce the lowest number of neutrons, particularly B, Be and C. Li was not simulated as its very low density resulted in it not being able to fully block protons, even with a 100 mm thick collimator. Period 3 and 4 elements also produce a considerably lower neutron yield than most other elements with Ca, C, S, Si, Mg and Ni standing out as particularly low neutron producers. While the number of neutrons produced by the collimator is drastically lower than the number of scattered and un-scattered protons, neutrons have a relatively high biological impact compared to protons, which is further investigated in the next chapter.

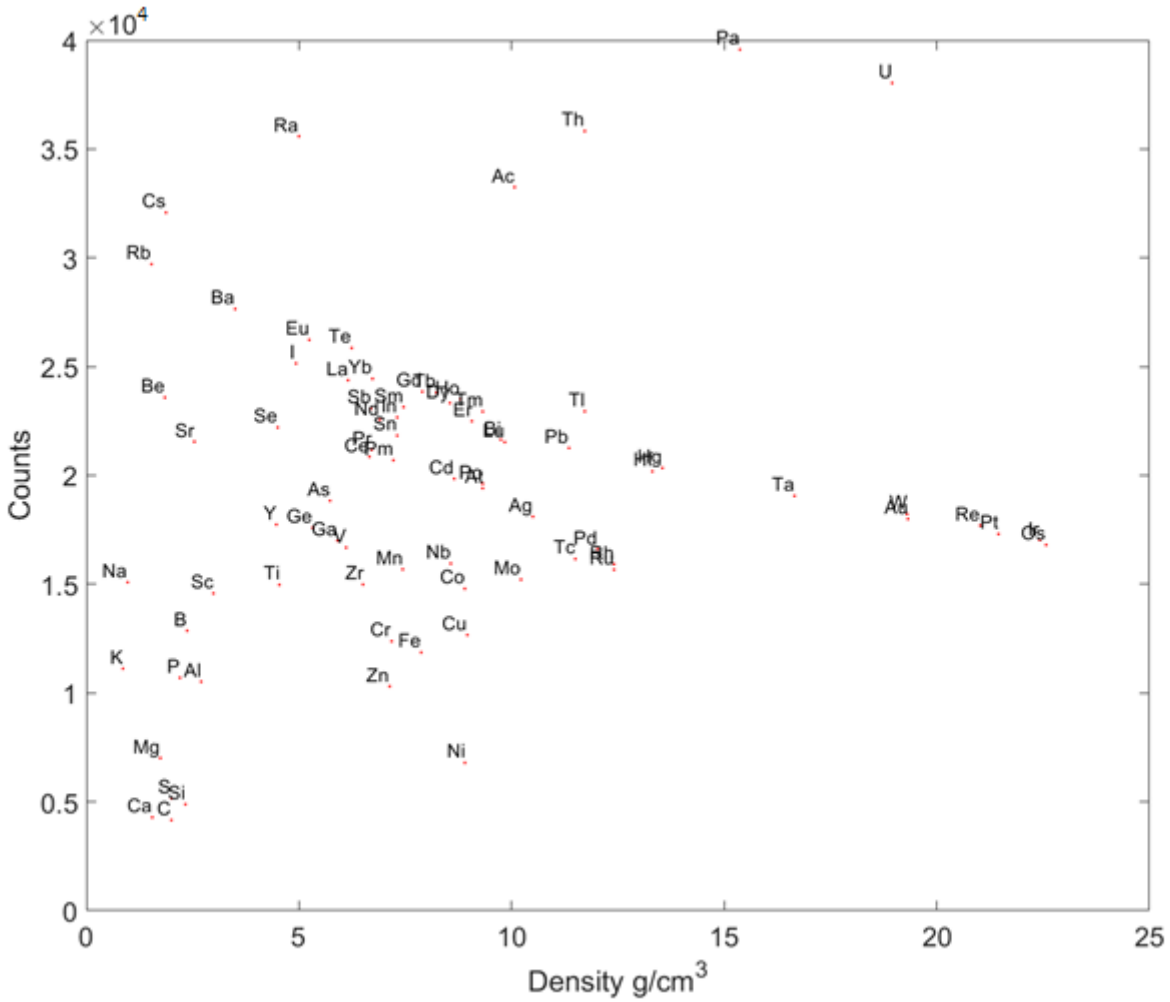

Figure 5.20: Effect of collimator material on the number of neutrons scattered by the collimator. Elements are labelled by their symbol.

5.4. Discussion

In this section consideration for development of a proton minibeam collimator is discussed. As a result of several Monte Carlo based investigations, it is clear that several factors need to be considered. Results from the collimator thickness simulations demonstrate that the thickness of the collimator should be at least 20 mm to ensure regions of low dose are clearly defined for a 50.5 MeV beam. The thickness of the septa between the collimator slots is also an important factor to consider as it is directly related to the collimator thickness. Increasing the thickness increases the PVDR up to a thickness of 25 mm. For thicknesses greater than this there is no noticeable improvement as the number of scattered protons from the collimator remains roughly constant and the total number of un-scattered protons decreases which decreases the dose rate.

Decreasing the collimator slot width was shown to increase the PVDR at the surface. This is primarily achieved by decreasing the valley dose. As the valley dose is thought to be primarily responsible for providing the ability for normal tissue repair, decreasing the valley dose should have significant benefits. This does come with the drawback of reducing the uniformity of the dose at the Bragg peak, thus decreasing dose delivered to cancerous tissue and potentially reducing local tumour control. With the various collimator slot widths, the 25 mm collimator has difficulty fully blocking the beam when the material between slots was less than or equal to 0.5 mm thickness, which works out to be 2% of the length of the collimator. Septa thickness between slots is based on the spacing between the slots (CTC). The appropriate CTC spacing depends on the energy of the beam and how uniform the distribution at the Bragg peak is desired to be. Overall, narrower minibeams should

be used to avoid this problem and have the advantage that narrower minibeams have increased PVDRs. Decreasing the width of the slots has the difficulty of increasing manufacturing complexity and therefore cost. The ideal micro/minibeam width/separation has also not been determined biologically. However, previous photon experiments have shown that smaller beams do produce a higher normal tissue sparing effect [12, 13]. A balance between these factors is required and based on the data here the use of 0.3 mm slots appears a convenient compromise to produce minibeams from a low cost collimator whilst still achieving reasonable dose at the Bragg peak and producing reasonable surface PVDR's.

Density of the collimator material has a large influence on the surface PVDR. The overall trend showed that increasing the density increased the PVDR at various depths. Increasing the density of the material has a similar impact as increasing the collimator thickness. As denser materials are more proficient at blocking lower energy protons and offer an advantage over increasing the collimator thickness as they will not reduce the dose rate by a similar factor. It was observed that some transition metals Ni, Co, Cu and Fe produce significantly higher PVDR's than other elements and therefore are better candidates for use in collimator manufacture. The differences in PVDR when using collimator of different elements decreases with depth, due to the divergence of protons. For example, the difference at 10 mm depth between an element with 9 g/cm^3 that produces a PVDR of 11 – 12 and an element with 20 g/cm^3 or more producing a PVDR of 12 – 13 is quite minimal, limiting the usefulness of very dense elements with depth.

The number of scattered protons, photons and electrons all show a dependency on density, with most particles scattered by the collimator being protons. As expected, neutrons show no discernible relationship to density, with results being dictated by elemental properties. Elements with low atomic number on the periodic table produce the lowest number of neutrons, in particular Ca, C, S, Si, Mg. However, Nickel is an outlier producing a very low number of neutrons compared to elements of similar density or atomic number. Neutrons are of particular concern due to their potential for high biological damage and hence radiation safety concerns [88]. The overall results for Ni, Fe, and Cu have excellent PVDR, low neutron production, low photon, electron, and scattered proton production due to their density making them excellent candidates for collimator material. This combined with the low cost of working and manufacturing these materials make them ideal choices for a collimator.

Based on these results combined, the ideal collimator thickness for a 50.5 MeV proton beam our setup, a stainless steel or nickel collimator with 0.3 mm minibeams with 1 mm CTC spacing, which is between 4.7 and 5.9 times the path length of the incoming protons, with the projected range of a 50.5 MeV proton in stainless steel being 4.24 mm. This justifies the use of the 25 mm collimator in previous experiments [18, 23]. However, based on the results in Chapter 4, the beam was discovered to be more realistically a 45 MeV proton beam. This results in the projected proton range of 3.5 mm, thus, a 20 mm thick collimator would also have been acceptable. The ideal collimator would be made out of nickel as it produced excellent PVDR's at both the surface and at depth and produced a low number of neutrons. Nickel an easy to manufacture material with the only downside is it being more expensive than stainless steel. The collimator that was

manufactured previously at part of this thesis was produced out of stainless steel. This was chosen due to its low cost, easy manufacturing and contains high percentages of both nickel and iron.

5.4.1. Manufacturing Limitations

A primary requirement of collimator design is that it is possible to produce a collimator with current technology, and that it is cost effective. This sets some primary limitations on available collimator design. A collimator with holes has been shown to have some advantages over one with slots in regard to the final dose distribution [89]. In particular it offers an “extra” direction of mini/micro beam sparing. Ideally a hole collimator should be used when producing mini/micro beams, however, the production of this type of collimator is technological challenging and costly. The slot collimator also does not block as much of the beam, which results in a higher dose rate throughput. This is important in limiting treatment times to a reasonable length or when motion is important as shown in Chapter 3.

This chapter investigated optimal collimator design from a physics point of view. However, practical limitations and constraints also need to be considered. Some materials are difficult to machine and can be very costly which rules out the use of them. They are still included in this section despite their limitations to provide a more complete picture.

5.5. Conclusion

This chapter investigated optimal collimator design for proton minibeams at a nominal beam energy of 50.5 MeV as is available at the University of Washington in Seattle. The minibeam specific approach and analysis is comprehensive and novel and systematically examined the most relevant parameters that influence the beam characteristics and dose deposition for proton minibeams. It was shown that increasing the thickness of the collimator beyond what is necessary to fully block protons was undesirable, as this reduced the number of primary protons whilst maintaining the same number of scattered protons. This resulted in a reduction of beam modulation and dose, which places an upper limit on the thickness of the collimator. For our setup, a collimator between 20 - 25mm thick was deemed ideal. The ideal width for minibeam beamlets was found to be between 0.3 – 0.4 mm as these widths have the highest PVDR whilst maintaining a reasonable dose delivered to the Bragg peak. These minibeam widths also have the lowest relative valley dose, thus reducing potential normal tissue damage and providing the possibility of tissue repair into the peak regions. In terms of collimator material, the collimator should be constructed from should be as dense a material as possible as this has been shown to maximise the PVDR. However, to reduce neutron production, this work has also shown the material should be ideally a group 4 transition metal. This is a novel finding that has previously not been shown before. Nickel is a particularly suitable candidate for collimator construction due to its low neutron production and remarkably high PVDR ratios at the surface and up to 10 mm depth.

One of the limitations in this chapter was that treating all particles equally in the results is problematic as the energy and type of particle can have a large impact on the resulting biological damage. This will be addressed in Chapter 6. Further work could investigate how higher energy proton beams are impacted by these collimator design parameters: expanding the scale from small animal energies at 50.5 MeV to human scale clinical energies of up to 230 MeV. This would require new CTC spacing to optimise dose delivered to the Bragg peak; a larger CTC spacing would also generate greater PVDR's at the surface enhancing the sparing effect when minibeams are used in a clinical situation. This chapter explored collimator design parameters and provided a novel insight into considerations for minibeam collimator optimisation, particularly for small animal beam energies.

Chapter 6

Relative Biological Effectiveness Considerations for Proton Minibeams

This chapter investigates the RBE of proton minibeams. In particular, how scattered particles from various collimator materials impact the biological dose distribution. As discussed previously in Chapter 2, protons and neutrons can deliver higher biological damage for the same quantity of absorbed dose. As physical collimators scatter protons and produce neutron, the dose from these need to be considered to build an overall picture of the impact collimator material has on proton minibeam dose distributions. This has been an area of hot debate with letters to the editor in the International Journal of Radiation Oncology, Biology and Physics by V. Sahadevan, and F. Dilmanian *et al.*, particularly the RBE of neutrons produced by proton minibeam collimators [90, 91].

When protons interact with the collimator, there is a small probability that neutrons are produced. These neutrons produce high biological damage and can potentially negatively impact regions of normal tissue. In a letter to the editor by

Sahadevan *et al.* concerns were raised over the production of neutrons when generating proton microbeams with a 109 MeV proton beam and a tungsten-copper alloy collimator [90]. Dilmanian *et al.* claimed that the RBE of these neutrons in their paper was 10 [91, 92]. The RBE of 1-2 MeV neutrons has been shown to be as high as 100, and for a typical proton therapy, a constant neutron RBE of 25 was also suggested by Sahadevan *et al.* In Dilmanian *et al.*'s reply they state that "Newhauser *et al.* found mean neutron weighting factors in the range of 6.7 to 9.2" and this was the basis for the RBE of 10 [91]. They also state that since the neutron dose was only 1% of the peak proton dose, it is insignificant. They did accept that further work on collimator material was required in order to minimise the biological neutron dose. Therefore, this chapter investigates in depth the biological damage caused by various collimator materials. With an emphasis on how each particle is produced by the collimator and how these particles affect the relative biological dose.

6.1. Introduction

RBE is the ratio of bio between two doses to reach the same level of effect, or endpoint, between various different types of ionising radiation and that of typically photons. RBE is the ratio of the biological effectiveness between two types of ionising radiation for the same amount of absorbed energy for a given biological endpoint. The reference radiation is generally an X-ray beam with 250 keV photons or cobalt-60 gamma rays. The primary interest of this chapter is in the RBE double-strand break endpoint. An equal dose of radiation from protons and photons has shown to have different resulting biological outcomes when delivered to a volume of cells. For example, a proton beam will cause more biological damage than a Co-60 source [93]. Traditionally for clinical use, RBE for cell survival for protons has been assigned a value of 1.1 [37]. However, RBE has been shown by Paganetti *et al.* to vary with e.g. depth, energy, and delivered dose, making this an approximation of the average of all these values [93]. A 50 MeV proton beam has been demonstrated to have a variable RBE DSB of between 1.05 at the surface and 1.4 post Bragg peak [18]. This can result in under- or overestimating the dose delivered to regions, creating unforeseen complications. The difference at the distal end of the Bragg peak is important, because there is variation in the range of an individual protons [94]. The problem is further exacerbated by an increase in RBE of the beam at this point [95]. This leads to the beam potentially overdosing unintended regions and can be particularly problematic when the beam stops just before critical structures. The RBE variability is greater for lower energy proton beams, for example the 50.5 MeV proton beam at the University of Washington. An accurate measurement of RBE can be determined with cell experiments measuring cell kill as a function of dose. By modelling various cell death endpoints

from the delivered dose, an estimation of RBE can be simulated in Monte Carlo. For this work we are using a double-strand break model by Stewart *et al.* [96]. This model works off the idea that DSBs and multiple damage sites, where DNA is damaged or broken in multiple places in close proximity, have been linked to be primary causes of radiation cell death [97]. Therefore, an estimation of the cell kill can be calculated by modelling the number of DSBs that occur. The model randomly distributes damage in a section of DNA based on the delivered dose in Gy. Then it checks if the distance between damage segments is below a threshold to determine if a double-strand break occurs. This data was then used to produce an RBE estimate for all light-ions up to Fe, based on the number of DSBs relative to ^{60}Co. This data was then fitted to an analytical formula for cells irradiated under anoxic and nonmonic conditions. This analytical formula is what is used in the model used in TOPAS. While this model aims to produce a reliable estimate of RBE, research by Rorvik *et al.* has demonstrated that not all RBE models produce the same results [98]. This work consisted of a single model being utilised to provide a quantifiable result. Due to the variation between the different approaches, the modelling results should always be verified, by cell experiments in the future. The LET, which is a physical parameter is also included in this chapter as a reference as some RBE models are based off LET [35].

6.2. Methods

The first simulation presented in this chapter is of a simplified setup consisting of a near monoenergetic beam in a vacuum, passing through a minibeam collimator and delivering dose into a water phantom. The use of this setup was to highlight the impact the collimator has on the beam, and to remove influence from other beamline components from the simulation. The first simulation used a monoenergetic 50.5 MeV proton beam, that was a flat 12.5 mm square source with a small angular spread of 0.0026 rad. The angular spread matches what was used in Chapter 5. The collimator was a 60 x 60 x 100 mm metal block with eleven vertical minibeam slots cut into it. The slots were 0.3 mm x 10 mm and spaced 1 mm apart to cover a 10 x 10 mm square field. This was the same collimator design as used in Chapter 5. The collimator was modelled with four materials: brass, nickel, stainless steel, and tungsten. These materials represent a wide range of materials presently used and have a low neutron production as discussed in Chapter 5.

After the beam exits the collimator, all particles were collected by a phase space scorer. Data collected by the phase space scorer were grouped based on particle types, protons, beta particles, photons, and neutrons. The protons were further categorised by whether they had interacted with the collimator. The grouping of these particles enables the evaluation of how each individual component impacted the dose deposited in the water phantom.

A second scorer was also placed along the internal left-hand side of the collimator's central slot, shown in Figure 6.3. This scorer allowed the collection of information on: 1) where in the collimator particles were produced, 2) what types of particles were produced, 3) the energy of these particles, and 4) the direction of these particles. From this information a detailed analysis was performed on how collimator geometry impacts the minibeam dose.

A second analysis was performed simulating how each group of particles from the phase space scorer deposited dose in a water phantom. LET was simulated in each voxel as a total average of energy given to the voxel using the TOPAS LET scorer [99]. RBE was also scored using dose with the double-strand break model developed by Stewart *et al.* [96]. RBE was based on V79 cells from Chinese hamsters and was based on a prescribed dose of two Gy [100].

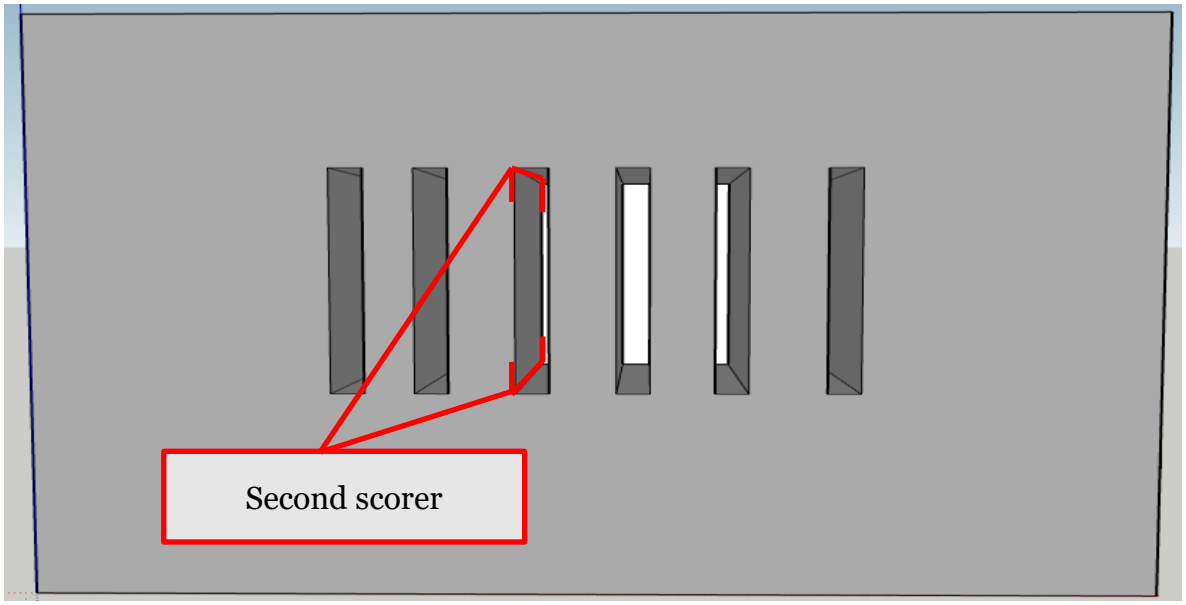

Figure 6.1: Diagram of phase space scorer location used in TOPAS simulations from a beams eye view.

An initial problem encountered was that the simulated dose from neutrons was low, even with more than a billion initial proton histories approximately 1% of particles exiting the collimator were neutrons. This resulted in poor dose statistics from neutrons, and consequently no useable data for neutron LET and RBE. The statistics could be improved by either running the phase space file multiple times or using variance reduction, however this would produce biased results. The solution decided upon was to first acquire the neutron spectrum for neutrons exiting the collimator made out of different materials by means of Monte Carlo simulations and then produce a neutron beam that was randomly sampled from this spectrum. The neutron beam could then be used to simulate dose to a water phantom. The spread of the beam was measured from the phase space file and used in the TOPAS simulation. The data from the phase space scorer is shown in Figure 6.2.

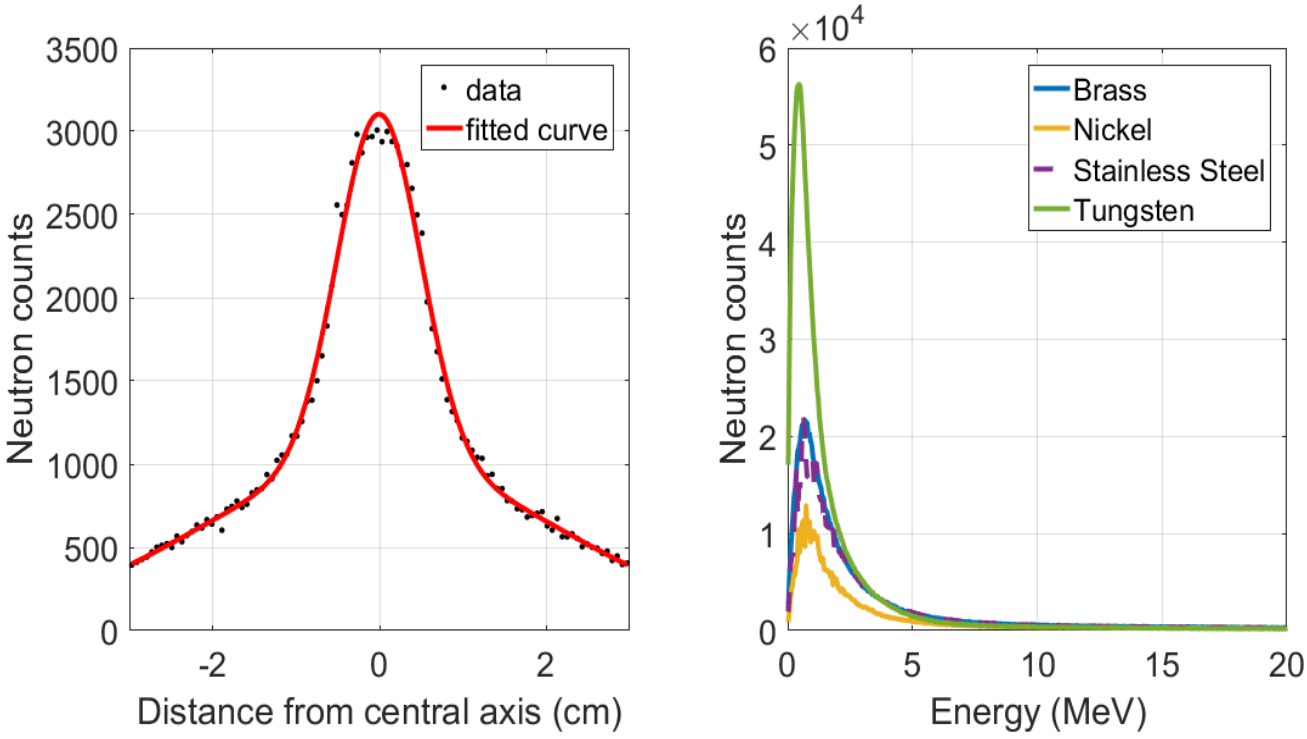

Figure 6.2(a): Neutron Flux from a Brass collimator showing the horizontal spread of neutrons exiting the collimator. (b): Energy of neutrons exiting various collimator materials.

Figure 6.2(a) shows the positional spread of neutrons exiting a brass collimator. It is interesting to note that the spread of neutrons shows no spatial correlation to the collimator minibeam slots and instead appears continuous. A fit was applied to this spread that could be used to produce the neutron beam within TOPAS for further simulations. The fit that most closely matched the collimator spread shown in Figure 6.2 (a) was a combination of two Gaussians. The same model fit approach was applied for each collimator material, details of the fit parameters are shown in Table 6.1. This shows the weighting of the Gaussian (height), the positional spread (standard deviation) and the angular spread angular deviation.

Figure 6.2(b) shows the energy spectra for neutrons generated by each collimator material. The neutron spectra have a peak at 0.5 MeV for tungsten and 0.7 MeV for brass, nickel, and stainless steel. The entire spectra were used in the TOPAS model to ensure the neutron beam matched the collimator output.

Table 6.1: Neutron beam fit data

		Brass	Nickel	Stainless Steel	Tungsten
1	Weighting Gaussian	75%	76%	72%	96%
	Position Spread	0.498 cm	0.505 cm	0.491 cm	0.450 cm
	Angular Spread	1.108 rad	1.110 rad	1.117 rad	1.071 rad
2	Weighting Gaussian	25%	24%	28%	4%
	Position Spread	1.826 cm	1.851 cm	1.844 cm	1.989 cm
	Angular Spread	1.108 rad	1.110 rad	1.117 rad	1.071 rad

Using the positional spread and neutron spectra, data each simulation was set up to produce a beam matching these characteristics. The output dose values were normalised to match the number of input neutrons to enable a fair comparison of neutron results with results of other particles.

A further simulation was performed to compare the difference between the monoenergetic beam described previously in this chapter, to that of a more detailed simulation, in this case the simulation of the whole small animal proton beamline at the University of Washington Medical Centre. This comparison allowed an investigation of the difference in RBE, caused by an idealised monoenergetic beam and a realistic poly-energetic beam, and how this impacts the overall dose delivered to the water phantom. The simulations parameters can be found in the Chapter 4 of this thesis where they were developed.

6.3. Results

An analysis of the different types of particles exiting the collimator are presented first. Dose results from these particles are then investigated and an analysis on the LET and RBE results is performed. Finally, a comparison between a monoenergetic and a realistic proton minibeam is performed comparing RWD.

6.3.1. Particle Energy and Distribution Results

For the monoenergetic beam, particles exiting the collimator were grouped into particle and interaction with the collimator. Using MATLAB, a histogram of all particles and energies was produced, shown in Figure 6.3. Note any particles that did not interact with the collimator are not shown.

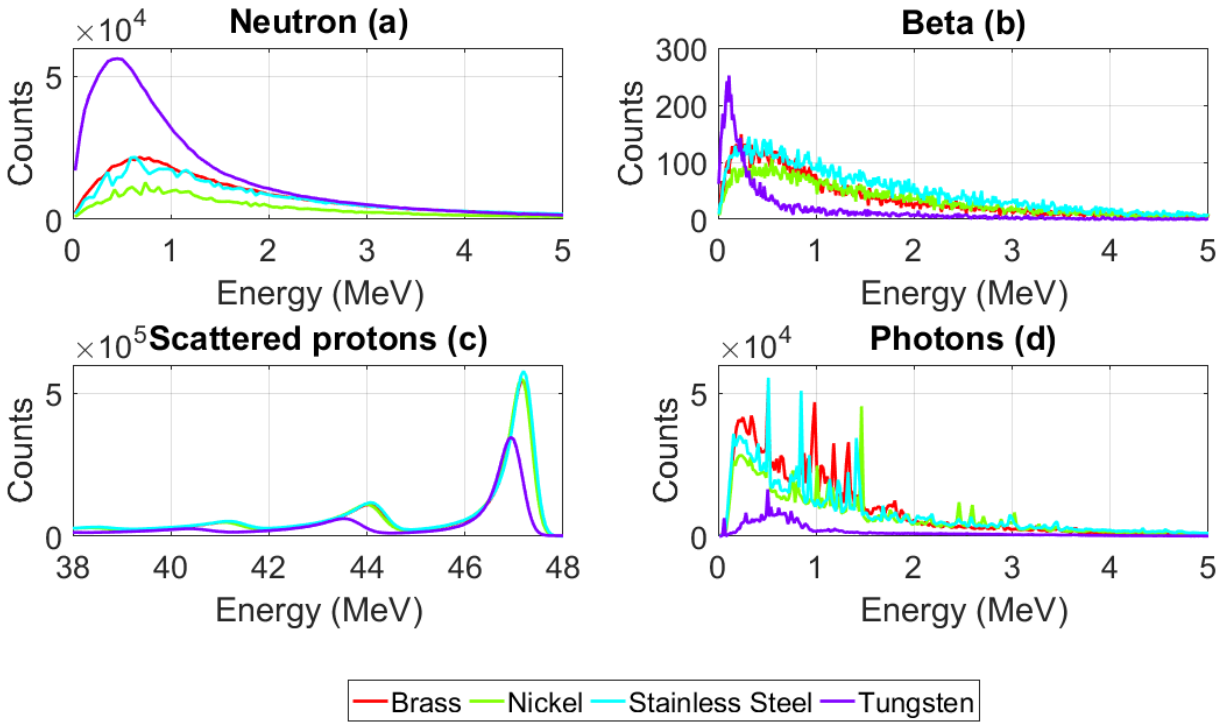

Figure 6.3: Energy distribution of particles that interacted with the collimator before exiting the collimator.

The neutron results, Figure 6.3 (a) match the findings recorded in Chapter 5 where the tungsten collimator produced a large number of neutrons, and nickel produced the least. Tungsten had peak number of counts approximately 2.67 times the other materials, with an energy peak of 0.46 MeV. Nickel, brass, and stainless steel energy had peaks of 0.46, 0.68, 0.68, and 0.74 MeV, respectively. The corresponding densities of tungsten, nickel, brass, and stainless steel energy are 19.3 g/cm^3, 8.91 g/cm^3, 8.55 g/cm^3, 7.99 g/cm^3, respectively. Reconfirming the results from Chapter 5 that material density is not the primary factor in neutron production. The differences in the total number of neutrons produced by a material is likely to be dependent on the nuclear cross-section between protons and a material's nucleus.

The beta particle results Figure 6.3 (b) include both positrons and electrons. It can be observed that the collimators only produce a relatively small number of beta particles and therefore, they will only have a minor impact on the final dose distribution. It is interesting to note that the results for tungsten were considerably different from the results of the other materials, with a higher peak of 250 counts at 110 KeV. Brass, nickel, and stainless steel peak at 130, 90 and 140, counts respectively, with a peak energy of 300, 400, and 380 KeV, respectively. These results demonstrate that tungsten produced the highest number of beta particles, followed by brass and stainless steel, with nickel producing the least.

Results for the scattered protons are shown in Figure 6.3 (c), displaying protons exiting the collimator having interacted with the collimator at some point. The interactions cause the protons to lose energy. It can be observed there are three main peaks for all materials, with smaller peaks at regular intervals. These results are shown in Table 6.2.

Table 6.2: Scattered proton energy peaks

Material	Peak Energy (MeV)				Average Energy Loss Between Peaks
	1	2	3	4	
Brass	47.2	44.0	41.1	38.4	6.6%
Nickel	47.1	44.0	41.1	38.4	6.6%
Stainless Steel	47.2	44.1	41.2	38.4	6.6%
Tungsten	46.9	43.5	40.4	37.4	7.2%

The average energy loss between each peak is also shown starting with the difference between the 50.5 MeV protons, then each subsequent peak. Brass, nickel, and stainless steel have an average energy drop of 6.6% between peaks, whilst tungsten has an average energy loss of 7.2%. Protons primarily interact via Coulomb interactions and, as a consequence, energy is lost. The differences in energy loss between materials, correlates with each material's density and number of electrons. The systematic differences between the peaks indicates that the particles are undergoing multiple scatter events and each peak represents a subsequent scatter. Each peak is not a sharp peak, indicating variability in the energy lost in each collision, resulting in energy spread of the resulting particles.

The photon results in Figure 6.3 (d) show that, amongst the materials simulated, tungsten produces the lowest number of photons, whilst the other three materials all produce a similar number of photons. The photons for brass, nickel, and stainless steel all peak at approximately 250 KeV. This does not include characteristic peaks, with a height of 5.3, 3.5 and 4.4 times that of tungsten, respectively. Tungsten peaks with an energy of 650 KeV. Minor secondary peaks in the photon's distribution are caused by characteristic photons. For example, the Ni 58 1454.3 KeV photon peak can be observed and a strong peak at 511 KeV from electron positron annihilation [101, 102]. These photons only make up a small component of the particles leaving the collimator and thus have a minimal impact on the dose delivered by the beam.

Overall, of the particles produced by interactions with the collimator, 85 – 89% are scattered protons. Tungsten has a smaller number of these scattered protons compared to the other materials which all show comparable results. The next largest group by number of particles is neutrons, between 3 – 12% and then photons between 3 – 9%. Out of all the materials tungsten has the highest number of neutrons and the fewest photons. The number of beta particles is negligible compared to the other particles producing less than 0.1% of the total number of particles for all materials.

The phase space scorer results are displayed in the next section. This scorer was placed on the internal septa of the collimator and collected all particles exiting the septa's internal surface. All these particles have either interacted with the collimator or have been produced in the septa. As each surface is geometrically

symmetrical, it can be assumed that the number of particles exiting one side of the internal septa of the collimator should be similar to the number exiting any other septa. The positional and energy information is of interest as this allows us to build an understanding of what is occurring in specific locations as the beam passes through the collimator.

The first set of these results is the combination of position and energy results for the four main particle types: neutron, beta, proton, and photons. This data was processed in MATLAB and plotted using a 3D histogram where the counts in each bin are indicated by colour. A logarithmic scale was used for the colour spectrum, enabling the large difference between particle flux to be observed. The phase space scorer lies along a central septum, making the scorer a plane with height (y) and length (z). This section of research is primary interested in the depth within the septa at which the particles are found. The height position is assumed to be less important as the beam should be homogenous in this direction, therefore it can be averaged, reducing noise. Data is grouped into 10,000 energy bins and position bins.

Figure 6.4 shows the results for all particles. The neutron graphic shows that most neutrons are generated near the entrance of the collimator, between 0 – 1.5 cm depth in the collimator. These neutrons peak at a depth of 0.05 - 0.35 cm with a range of energy between 0.7- 1.3 MeV. A small number of higher energy neutrons are also generated at this depth. These neutrons have energies up to 20 MeV and are produced when protons interact with the collimator from the uniform 50.5 MeV beam. For depths between 1.5 – 10 cm, neutrons of 0.1 – 3.0 MeV energy are produced throughout the thickness of the collimator.

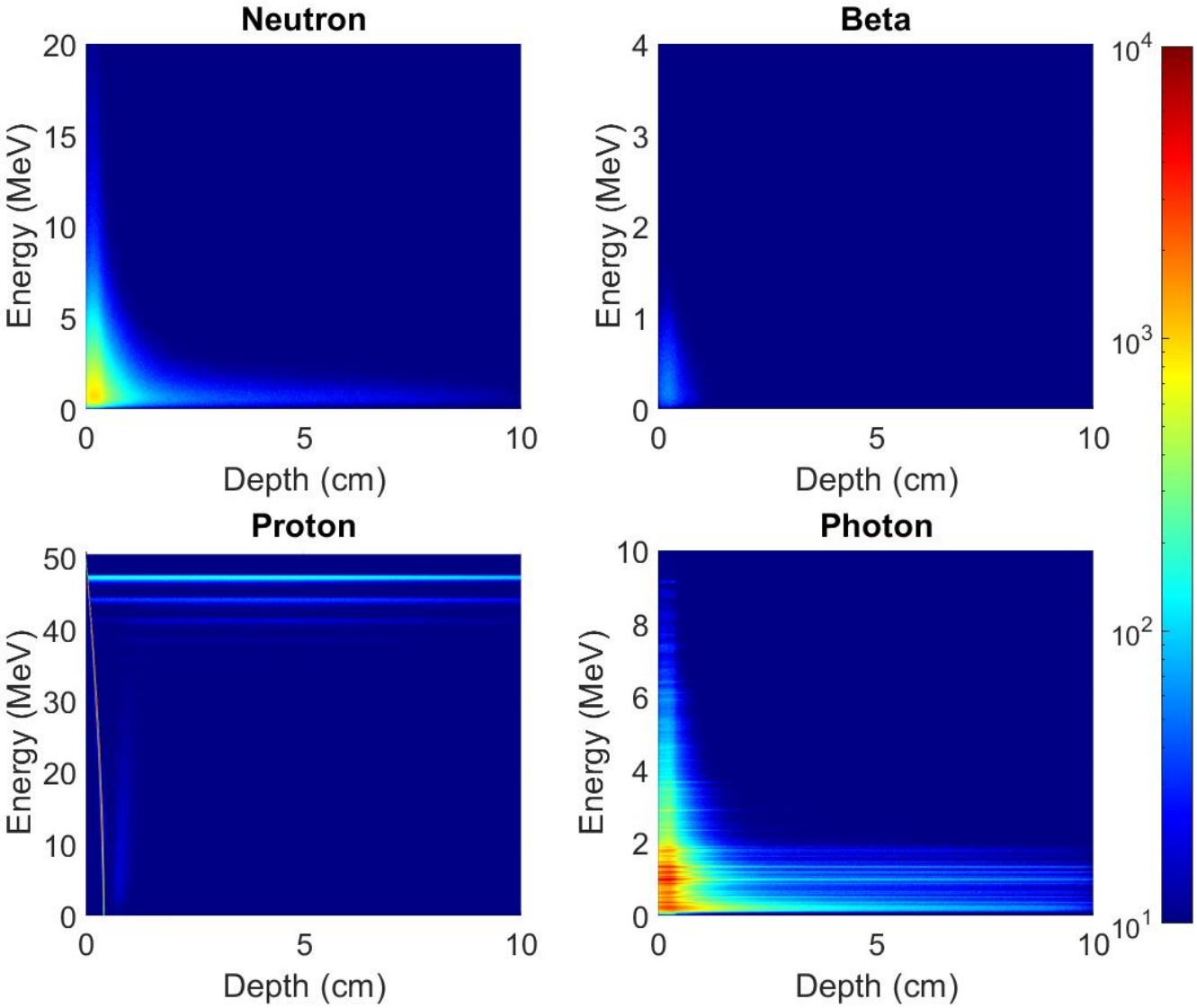

Figure 6.4: Position and energy distribution of particles exiting the surface of a septa in a Brass collimator. Colour scale represents number of particles.

These neutrons have an energy peak at 0.65 MeV. It can also be observed that the number of neutrons decreases with depth. This is a likely to be a function of the number of particles in the minibeam reducing with depth as the beam is collimated, thus absorbing primary protons.

Only a small number of beta particles are produced near the surface of the collimator at a depth between 0 – 1.5 cm with energy between 0 – 2.0 MeV. These particles are generated from proton interactions in the collimator as a result of the collimator stopping the main beam in the septa. Most of these beta particles do not exit the collimator and are absorbed back into the collimator material.

The results for protons can be divided into two sections: vertical curves and horizontal lines. The first section of results show a red near vertical curve starting at the surface at 50 MeV and decreasing energy with depth, until a depth of 0.43 cm. Corresponding to the projected range of a proton in brass and matches the calculated value from SRIM [82] and demonstrates that these protons are from the collimator blocking 50.5 MeV protons from the uniform beam. Showing the minimum thickness of a brass collimator required to fully block the main beam.

A second vertical band is also present at a depth of 0.6 – 1.2 cm. Starting with an energy of zero MeV and peaking at 34 MeV. The band results from scatter generated by the adjacent collimator septa. Protons from the initial red vertical curve on the opposite septa impact with these septa and some of the protons are reflected into the gap. Protons reflected form this ‘shadow’ of the initial curve. Most of these protons in the vertical curve and reflected ‘shadow’ have a large angular deviation from the main beam and therefore impact with the collimator septa, resulting in the protons being absorbed and not contributing to the final output of the collimator.

The second section of the proton results shows horizontal lines that can be observed running along the entire length of the collimator. The vertical lines begin at the same depth as the vertical curve. These lines reveal that protons are being scattered throughout the length of the collimator. The number of protons in each vertical line decreases as the energy level decreases. Each line represents a higher order scatter event in decreasing energy. The majority of the particles travelling down the collimator are 50.5 MeV protons. Therefore, it is most probable that the scatter that reduces the 50.5 MeV protons to 47.2 MeV. Each order scatter event after the first is less probable. The scatter events do not occur with discrete angles or energy. There is a range of energy lost in each collision and the peak is used as a comparison. As the number of protons travelling down the collimator decreases due to collimation, the number of scatted protons also decrease with depth. With the log scale this is difficult to observe but is present in the data. The protons that are scattered off the sides throughout the length of the collimator have low angular divergence from the beam, demonstrating that the protons only skim the surface of the collimator slot and exit the collimator into the water phantom. These results help explain the previous data from Chapter 4 in Section 4.3.2 where the proton energy peaks at uniform energy intervals.

The photon results can be split into two sections as previously described with the proton results. Firstly, a large peak of photons at the surface and second horizontal lines throughout the depth of the collimator. The greatest number of photons are generated near the surface, between 0 – 1.5 cm, with energy between 0 – 10 MeV. Of these photons the majority are between 0 – 2.0 MeV and at a depth between 0 – 0.46 cm. These photons are produced by stopping of the main beam. Many of these photons are absorbed by the collimator and do not contribute to the final

particle stream exiting the collimator. The horizontal lines throughout the depth of the collimator are caused by interaction of protons bouncing off the side of the collimator septa. These are at fixed energy intervals and are a function of the initial proton energy and the material properties. These photons have energies between 0 – 2.0 MeV. Most of these photons exit the collimator and contribute to the final dose.

6.3.2. Dose Contribution from Scattered Particles

In this subsection the magnitude of the dose resulting from scattered particles for different collimator materials is evaluated. The results are split into particle type showing the dose from neutrons, beta particles, scattered protons, and photons. All results are scaled based on the total number of particles exiting the collimator, allowing the simulations to be compared. The neutrons, beta particles, and photons show little, to no, spatial dose differences between the valley and peak regions. This observation indicates that the dose from neutrons, beta particles, and photons produce a uniform dose over the width of the phantom. An important note is the uniformity of these particles could have a larger impact in the valley regions. The lack of spatial variation is a result of two factors; first, the particle's ability to pass though the collimators septa without being fully absorbed and secondly, the high angular deviation of these particles exiting the collimator.

Figure 6.5 shows the depth dose for neutrons (a), beta (b), scattered protons(c), and photons (d), for different collimator materials. Dose was normalised to the Bragg peak, for protons that did not interact with the collimator. Starting with the neutron dose results, they all follow similar trends, starting low at the surface then peaking within the first 5 mm and decreasing with depth after the dose peak.

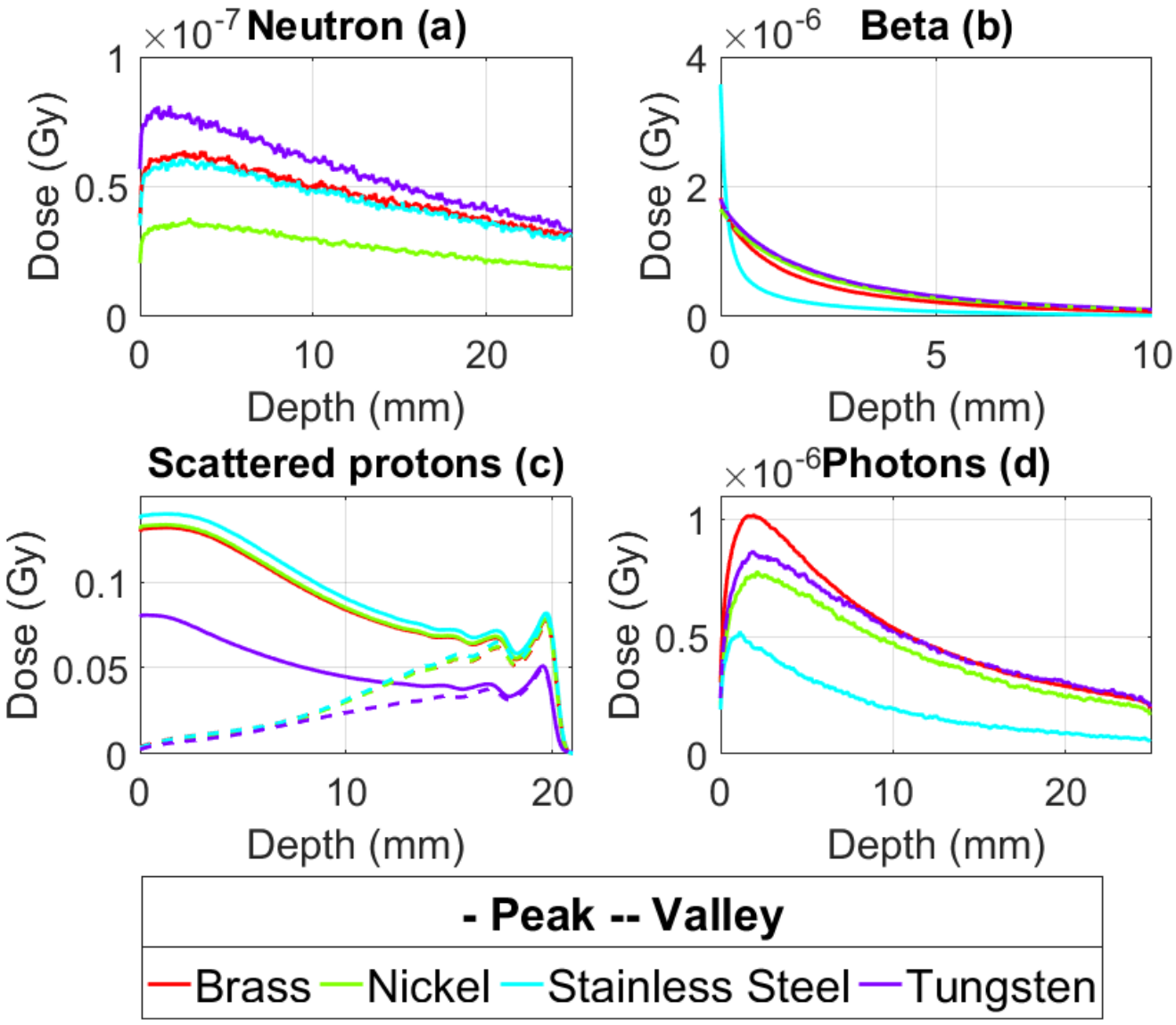

Figure 6.5: Dose of various particles that have interacted with or are produced by various collimators. Peak dose is shown as a solid line, valley dose is a dashed line.

Tungsten starts at 56 nGy and peaks at 81 nGy at a depth of 1.1 mm, which corresponds to 5.6x10^{-6}% and 8.1x10^{-6}% of the total dose in at the Bragg peak. Brass and stainless steel have a similar initial dose relative to the Bragg peak dose at 3.8x10^{-6}% and 3.5x10^{-6}% nGy, respectively, and both peak at a depth of 2.6 mm with a peak dose of 6.4x10^{-6}% and 6.0x10^{-6}%, respectively. Nickel has the lowest dose with a surface dose relative to the Bragg peak dose of 2.1x10^{-6}%, a peak of 3.8x^{-6}% at 2.9 mm depth. These results concur with Chapter 5 where tungsten had

the highest neutron output and thus, the highest neutron dose, which is 30% higher than the dose for brass and stainless steel. The relative scattered dose from nickel is low, 60% the dose from either brass or stainless steel. Agreeing with the results from Chapter 5 that nickel produces less neutrons and thus produces a low neutron dose.

The beta dose (b) has a general trend of a high surface dose which decreases with depth for all materials. Stainless steel has the highest surface dose of 3.6 μGy. This dose rapidly decreases with depth and by 0.15 mm, stainless steel has less dose than the other materials. Tungsten, nickel, and brass have a similar surface dose relative to the Bragg peak dose of $1.8x10^{-4}$%, $1.7x10^{-4}$% and $1.8x10^{-4}$%, respectively. Tungsten has the highest dose beyond 0.15 mm depth, followed by nickel, brass, and then stainless steel with the lowest dose.

Results for the scattered protons (c) can be split into the peak results and valley results. The peak dose results have a high surface dose which decreases with depth before peaking with multiple Bragg peaks. The surface dose relative to the Bragg peak dose for stainless steel, nickel, brass, and tungsten is 13.7%, 13.1%, 12.9%, and 8.0%, respectively. The main peak at 19.7 mm depth, has a height of 8.2%, 7.9% and 7.8% Gy for nickel, brass, and stainless steel, respectively. This peak corresponds to the 47.2 MeV scattered protons. The main peak for tungsten is at 19.5 mm depth with a dose of 5.1% Gy and this peak is a result of the 46.9 MeV first order scattered protons. A second peak can be observed at a depth of 17.3/16.9 mm and this corresponds to the 44.2/43.5 MeV second order scattered protons. A third peak is also present from the third order scattered protons. Further peaks are not visible above the dose curve. The large surface dose results from the lower

energy protons originating from the initial conversion of the uniform beam into minibeams. The dose from proton scattered off the tungsten collimator is 40% lower than that of the other materials due to tungsten's greater density, increasing the collimation of the beam, thus decreasing the number of particles exiting from the collimator. Stainless steel has the highest dose from scattered protons due to having the lowest density of the materials evaluated.

The valley dose results for the scattered protons (c) show a general trend where the dose increases with depth before peaking with multiple Bragg peaks. The surface dose for stainless steel, nickel, brass, and tungsten is 0.07%, 0.28%, 0.4%, and 0.26% mGy, respectively. The valley dose at the Bragg peak is 7.6%, 7.3%, 7.2%, and 4.7%, respectively. Stainless steel and nickel have similar high surface dose. While, nickel and tungsten have low surface dose. This impacts the ratio between the peaks and valley resulting in nickel producing the best peak to valley ratio of 45.4 at the surface, followed by stainless steel with a value of 35.6, brass and tungsten have similar values of 30.6 and 29.3, respectively.

Photon dose (d) is shown to peak near the surface and then decrease with depth for all materials. The peak occurs at a depth of approximately 1.7 mm for all materials apart from stainless steel which peaks at 1.1 mm. Brass has a peak of 1.01×10^{-4}%, followed by tungsten at 0.86×10^{-4}% which is 15% less. Nickel is next with a peak of 0.78×10^{-4}%, and stainless steel has the lowest photon dose with a peak of 0.52×10^{-4}%. This demonstrates the material of the collimator can reduce the photon dose by 50% depending on material used. Hence, stainless steel has a major advantage over tungsten when it comes to photon dose.

Comparing the total scattered dose from all particles signifies that scattered protons are the primary contributor of scattered dose, delivering more than 10^5 times that of any other particle. The neutron dose is extremely low being a factor of ten times less than both beta and photons. This is more clearly shown in Figure 6.6 which summarises the dose contribution for all secondary particles exiting a stainless steel collimator, including the primary protons that did not interact with the collimator for a comparison.

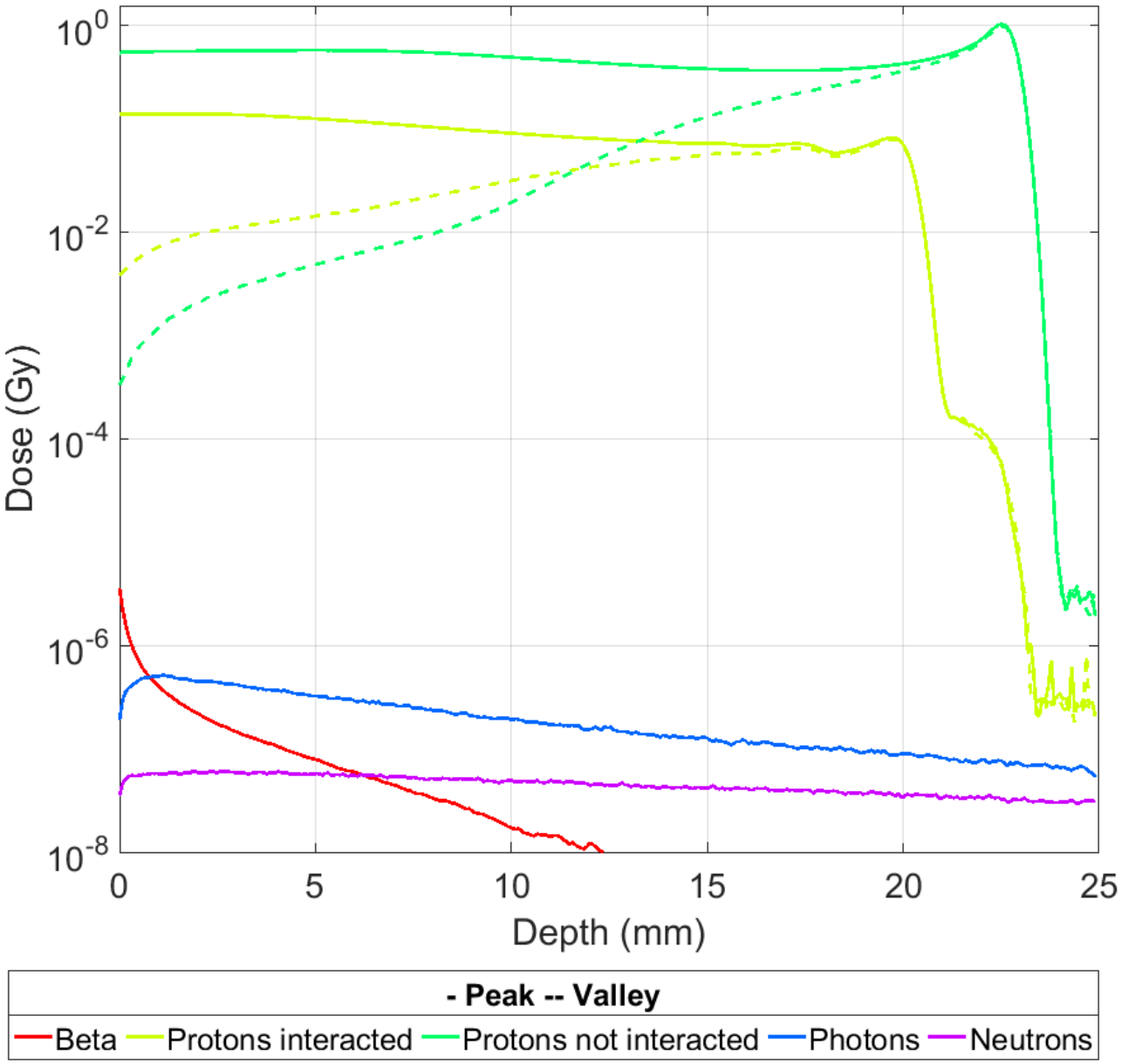

Figure 6.6: Depth dose curves of all particles exiting a stainless steel collimator. Peak dose is shown as a solid line, valley dose is a dashed line.

Stainless steel is shown for clarity and it should be noted that the graph uses a logarithmic scale for the y-axis to display the dose from all particles clearly. This data is mostly repeated from the previous results but aims to highlight the relative differences in greater detail. The dose from primary is also included for reference to give a more complete picture of the overall dose delivered to the water phantom.

The peak dose region for protons that have not interacted with the collimator has the highest dose at all depths. This dose peaks at the Bragg peak with a peak of 0.98 Gy before rapidly decreasing. The second highest dose is produced by the peak regions of protons that interacted with the collimator, from a depth of 0 – 13.5 mm, after which the valley dose of protons that did not interacted becomes the second highest source of dose. The valley dose for proton that not interacted is less than ones that that did interact. The difference between the two is a factor of ten at the surface which then decreases until a depth of 11.7 mm. The valley region for protons not interacted has a higher dose than protons that did interact with the collimator. All other particles contribute negligible dose at all depths.

These results show that approximately 80% of the peak dose is a result of un-scattered protons, and 20% of the peak dose is from scattered protons, with less than 0.001% of the dose from other particles. The valley dose is comprised of approximately 91% scattered protons and 9% un-scattered protons with less than 0.1% of the dose is from other particles. The decrease in the PVDR is therefore caused by these scattered protons as they dominate the valley dose. The peak dose is also increased by 25% due to the scattered protons at the surface, this percentage decreases with depth. It is important to note that the RBE of each particle has not

been considered in these results and does need to be before a final conclusion can be drawn. This analysis will be performed in following sections of this chapter.

6.3.3. LET Distribution

Using the TOPAS LET scorer, LET was measured for the protons and neutrons exiting brass, nickel, stainless steel and tungsten collimators. LET in TOPAS is measured per voxel and therefore is a measure of the total LET delivered to that voxel, rather than on a per track basis. Results were processed in MATLAB. For the neutron results, LET was averaged around the central axis in both the width (x) and height (y) directions in order to reduce noise. This is possibly due to the neutron distribution being semi-uniform. The proton LET results combine all peaks, except the two on the edge, to form an average. Voxels can also be averaged in the height direction around the central axis as there is no spatial variation in this direction.

Results from the neutron LET simulations are shown in Figure 6.7. The LET distribution of neutrons with depth generated by the tungsten collimator is higher than that from the other materials considered here. All materials have a high surface LET which decreases slightly with depth. Tungsten's LET peaks at 46 MeV/mm/g/cm^3, whilst all other materials peak at 42 MeV/mm/g/cm^3. Tungsten's high LET indicates that the dose from neutrons will be more biologically damaging especially at the surface. The neutron dose is semi-uniform over the width of the phantom and leads to a higher apparent impact in the minibeam valleys, decreasing the PVDR.

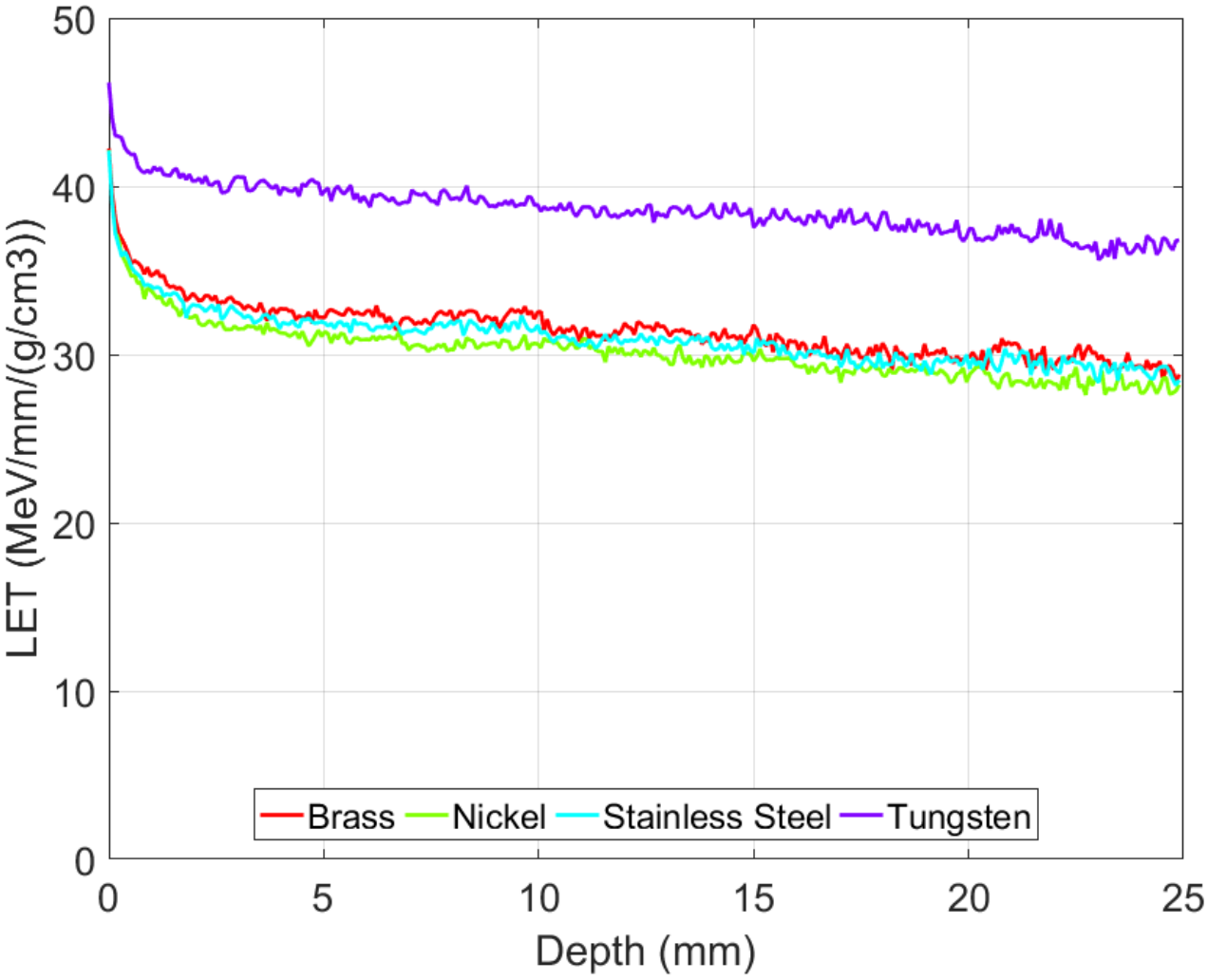

Figure 6.7: LET of neutrons from minibeam collimators of various materials.

Thus, reducing the normal tissue sparing from the micro/minibeam effect. Nickel produces the least neutrons, however this does not have a large impact on the LET, resulting in nickel's neutrons still having the same LET as brass and stainless steel. Results for the peak and valley LET of protons are shown in Figure 6.8. Starting with the peak dose it can be observed that all materials have an LET of 2.3 MeV/mm/(g/cm^3) for protons that interact with the collimator. For protons that did not interact with the collimator the LET in the peak regions is only 1.3 MeV/mm/(g/cm^3), which is 43% less. This will increase the surface dose in the peak region by a larger factor than would be expected compared to that of a monoenergetic beam.

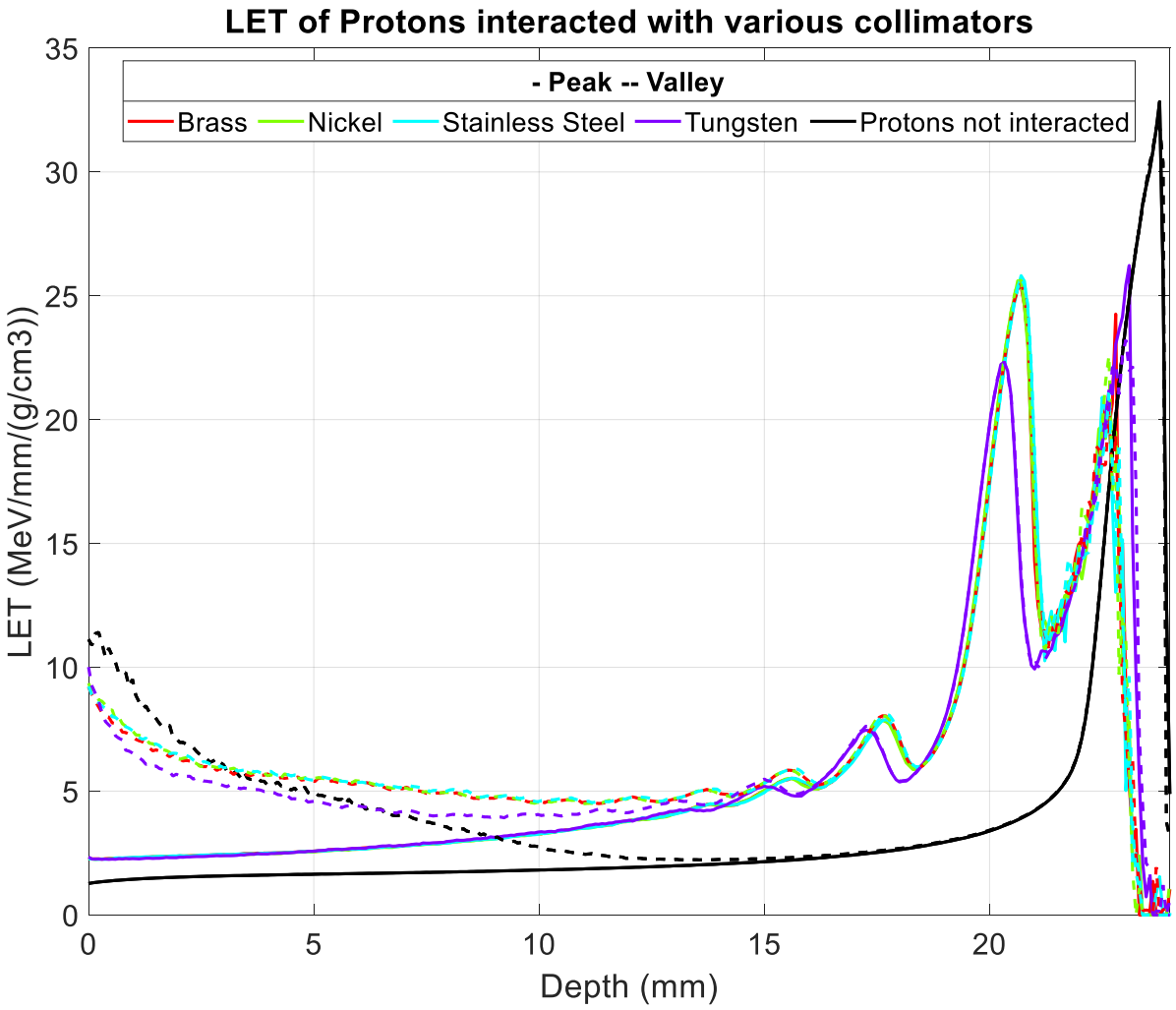

Figure 6.8: LET of Protons from various collimator materials. Peak dose is shown as a solid line, valley dose is a dashed line.

LET for the peak dose region slowly increases with depth and peak and valley LET become equal from a depth of 15 mm. This depth was shown in the previous dose results section as the point where the dose merges into a semi-uniform dose.

The valley regions have a high LET at the surface, which decreases with depth. The LET at the surface is particularly high at 11.0 MeV/mm/(g/cm^3) for the protons that did not interact with the collimator. Tungsten has the next highest LET at 9.9 MeV/mm/(g/cm^3), followed by nickel at 9.3 MeV/mm/(g/cm^3). Leaving brass and stainless steel with the lowest surface LET of 9.1 MeV/mm/(g/cm^3). A high surface LET is caused in part by a biasing effect where the valley region is a low dose region.

The few particles that do deliver dose have a higher LET on average as they have already been through interactions enabling the deposition of dose in this region. The relationship between the dose and LET is inversely proportional in this region. As dose increases with depth, the LET decreases until the dose is semi-uniform at a depth of 15 mm.

Three peaks can be observed in the LET at depths from 15 to 25 mm. The results for brass, nickel, and stainless steel are all very similar with peaks of 22.7 MeV/mm/(g/cm^3), 25.7 MeV/mm/(g/cm^3) and 8.0 MeV/mm/(g/cm^3) at 22.4 mm, 20.7 mm, and 17.7 mm depths respectively. These correspond to the dose peaks from 50.5 MeV, 47.2 MeV, and 44.0 MeV protons. It should be noted that the dose peaks occur at a depth of 22.5 mm, 19.7 mm, and 17.3 mm. The peak that corresponds to the 50.5 MeV protons in these three materials only contain a few protons that have lost a small amount of energy and therefore is not a complete peak and dose not match the results for the un-scattered protons. The two other LET scattered peaks occur 1.0 mm and 0.4 mm deeper than the dose peaks. For protons that did not interact with the collimator, they peak at 32.8 MeV/mm/(g/cm^3) at a depth of 23.8 mm, 1.3 mm deeper than the dose peak. This large peak both increases the effective dose at the Bragg peak and on the distal edge of the Bragg peak. The large LET on the distal edge of the Bragg peak is a major concern as it increases the dose uncertainty of the Bragg peak depth, limiting the ability for placement near critical structures. The results for tungsten is shifted as this material produces different scattered proton energy peaks tungsten has the following peaks 26.2 MeV/mm/(g/cm^3) at depth of 23.1 mm, 22.3 MeV/mm/(g/cm^3) at a depth of 20.3 mm, and 7.5 MeV/mm/(g/cm^3) at a depth of 17.3 mm. The two scattered peaks are 0.8 mm and 0.4 mm deeper than the dose

peaks. As dose past these peaks drops to near zero LET past the end of the peaks becomes influenced by individual particles with high LET producing noise past the main LET peaks.

6.3.4. RBE Distribution

RBE was scored with the RBE DSB scorer in TOPAS, modelling the DSB biological damage [96]. RBE was measured for protons and neutrons exiting brass, nickel, stainless steel, and tungsten collimators. RBE is measured per voxel and gives an average of RBE in each voxel based on all particles that have deposited dose in the water phantom. Results were processed in MATLAB with the same with described in Section 6.3.3.

Figure 6.9 illustrates the neutron RBE results, showing a similar trend to the results from LET. Demonstrating the close relationship between RBE for DSB and LET used in this model. The RBE for tungsten starts at 3.00 at the surface and decreases to 2.65 with depth. The three other materials have an RBE of 2.85 at the surface which decreases to 2.25 with depth. These results highlight the larger amount of biological damage that neutrons cause at the surface and throughout the phantom. The tungsten collimator has a higher neutron output, and this results in a higher LET and thus a higher RBE.

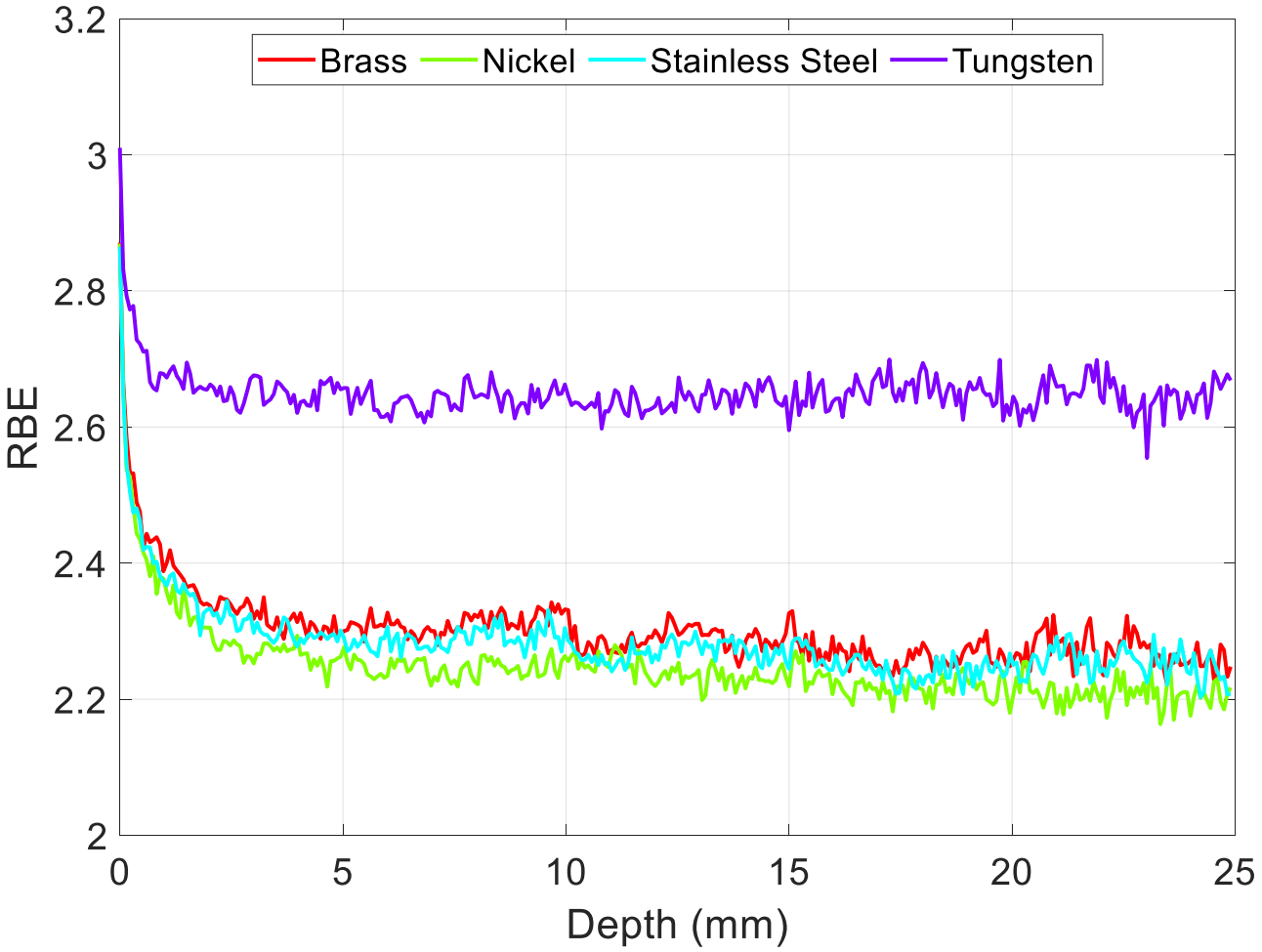

Figure 6.9: Neutron DSB RBE from various collimator materials

The high RBE of the neutrons increases the neutron dose to at least 2.25 at all depths. This is of particular importance in the valleys and post Bragg peak where the dose from protons drops, as the neutron dose can have a larger relative effect. The proton RBE results, shown in Figure 6.10 for RBE DSB follow similar trends to the LET results in the previous section. A high surface RBE can be observed for the valleys of 1.52, 1.42, 1.40, 1.39, and 1.38 for protons interacted, tungsten, nickel, stainless steel, and brass, respectively.

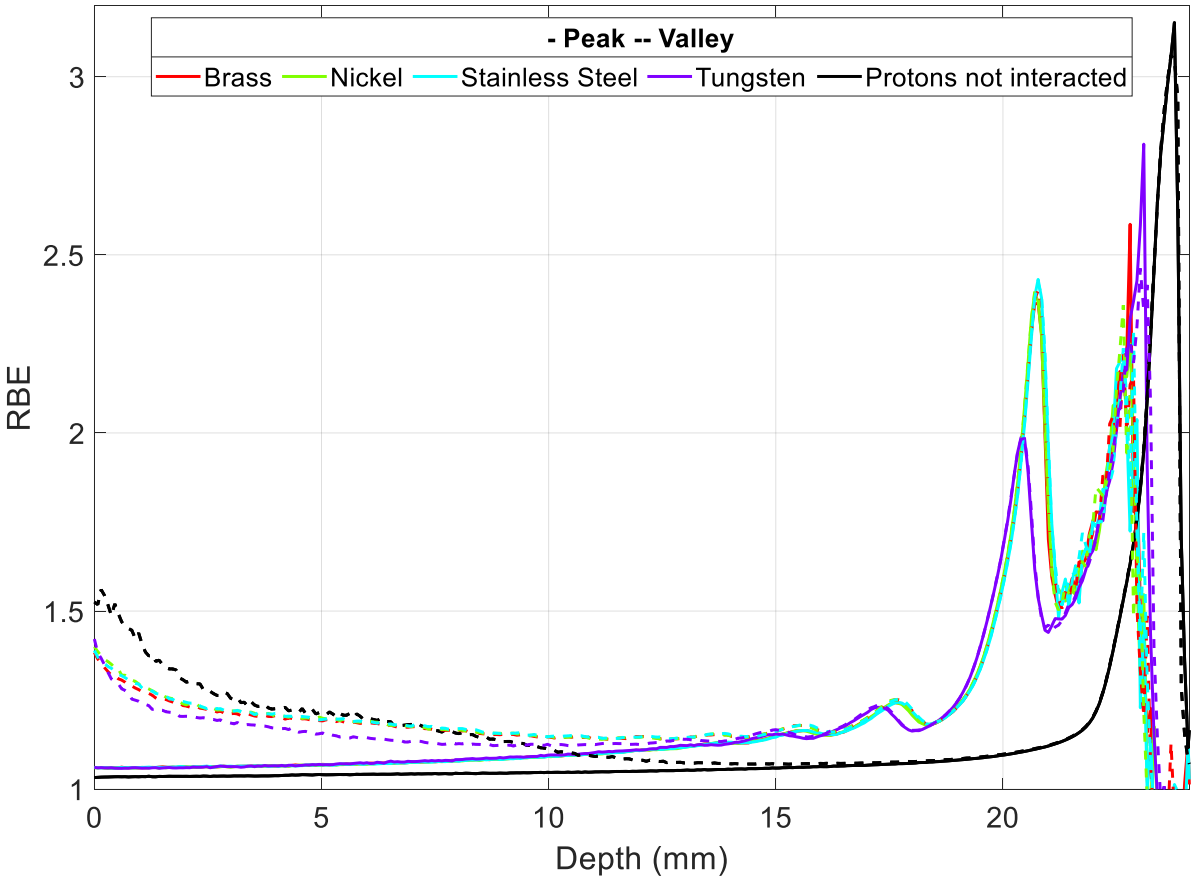

Figure 6.10: Proton DSB RBE from various collimator materials. Peak dose is shown as a solid line, valley dose is a dashed line.

The RBE in the peak regions at the surface is 1.03 for protons that have not interacted with the collimator, and 1.06 for protons that have interacted with collimators regardless of material. At a depth of 15 mm the RBE for peaks and valleys merge at 1.07 for protons not interacted and 1.16 for protons that did interact. Protons that did not interact with the collimator increase RBE until a peak of 3.15 at 23.8 mm depth. This peak is past the dose peak as discussed previously. There are three peaks for the brass, nickel, and stainless steel collimators. These peaks occur at 22.6 – 22.8 mm, 20.7 mm and 17.7 mm depths and have an RBE of 2.22 – 2.59, 2.43, and 1.25, respectively.

The differences in the 22.6 – 22.8 mm peak is caused by a low number of protons being present in this peak. Resulting in protons that do influence this peak having a larger impact on the average RBE making the peaks noisier. Tungsten has the following RBE peaks 2.81 at 23.1 mm depth, 1.99 at 20.5 mm depth, and 1.24 at 17.3 m depth. It is noted that RBE is significantly higher than that of a normal clinical beam due to two factors. Firstly, this model uses an idealistic monoenergetic beam, resulting in a large number of protons stopping at the same point which increases the RBE at this point. Secondly, lower energy protons have a higher LET and consequently RBE.

To gain an overall picture of the impact RBE has on the biological dose, both RBE and dose can be combined to the RBE weighted dose, RWD. RWD is simply the product of RBE and the physical dose. The RWD was calculated in MATLAB by multiplying corresponding voxels from the previous simulations. Figure 6.11 shows this combination with the stainless steel collimator for protons that have interacted with the collimator. Only stainless steel is shown here for clarity as this is the material a collimator was manufactured from for the University of Washington based on the results from this thesis. Figure 6.11 demonstrates the increased RWD over the whole dose curve, with a factor of 1.4 at the Bragg peak. While this is a large increase it is less the RBE maximum of 2.6. This is caused by the RBE peak not coinciding with the dose peak, but instead peaking after the dose peak. This increases the dose on the distal edge of the Bragg peak by a 47% and increases the depth of the peak from 19.6 mm to 19.7 mm for the RWD.

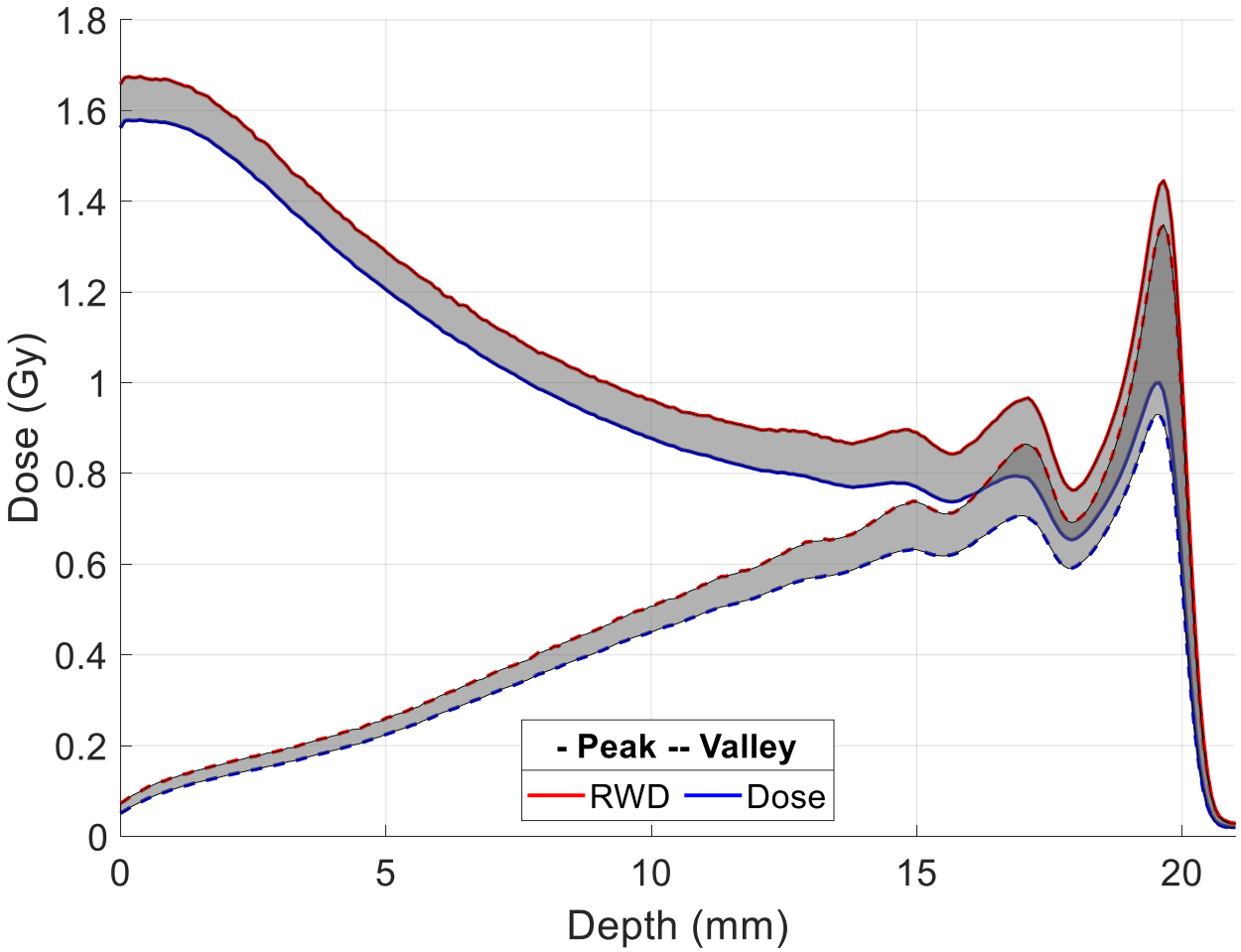

Figure 6.11: RBE weighted dose compared to dose for protons scattered off a stainless steel collimator, differences is shown in grey. Peak dose is shown as a solid line, valley dose is a dashed line.

The overall comparison between RWD and physical dose results shown in Figure 6.12 demonstrate that the increase in effective dose the neutrons and protons have in comparison to all components of the minibeam exiting the stainless steel collimator. Note, a log scale is used so a comparison between all particle contributions can be performed. An increase in the peak dose of the protons is quite visible at the Bragg peak and at the surface for the valley regions. The neutron dose has increased by a large amount, however, it does not contribute a large amount to the overall dose received by the water phantom and the overall dose is still dominated by protons. The peak regions are dominated by protons which have not

interacted with the collimator and the valley regions are dominated by protons that have interacted with the collimator.

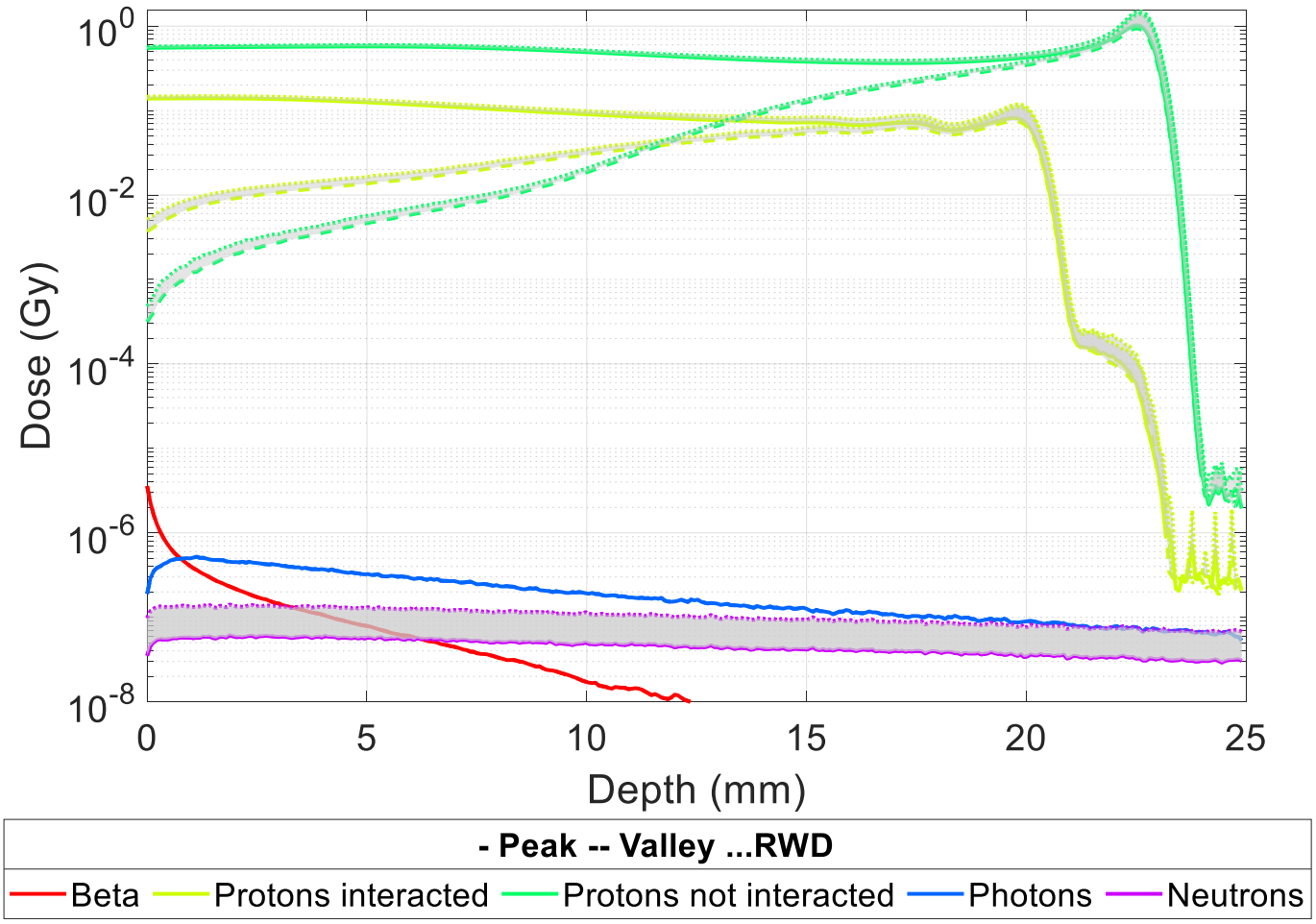

Figure 6.12: Comparison between dose and RBE weighted dose for all particles exiting a stainless steel collimator. Peak dose is shown as a solid line, valley dose is a dashed line and RBE weighted dose as a dotted line

6.3.5. Comparison Between Simplified Model and PPRP

The next section of results gives the difference between a simplified monoenergetic and a realistic beamline with a collimator. The realistic beamline uses the PPRP model as discussed previously in Chapter 4. The monoenergetic setup uses a nickel collimator as this represents an ideal material for producing minibeams with a collimator. Which has been shown in previous sections produces the least neutrons and delivering remarkably high PVDRs compared to other materials. Dose was normalised to the Bragg peak of the peak regions for both the peak and valley data, allowing a comparison between the two sets of results.

Figure 6.13 (a) illustrates the dose and RBE for the monoenergetic setup with a nickel collimator. Figure 6.13 (b) shows the dose and RBE for the whole beamline with a stainless steel collimator. The monoenergetic beam has a Bragg peak depth of 22.5 mm and the whole beam has a Bragg peak depth of 17.0 mm. The surface dose for the pure beam is 0.67 Gy for the peak regions and 0.003 Gy for the valley regions. The surface dose for the realistic beam is 1.45 Gy for peak regions and 0.020 Gy for the valley regions. Both beams have the secondary peak before the main Bragg peak in both the peak and valley dose, caused by scattered protons from the collimator.

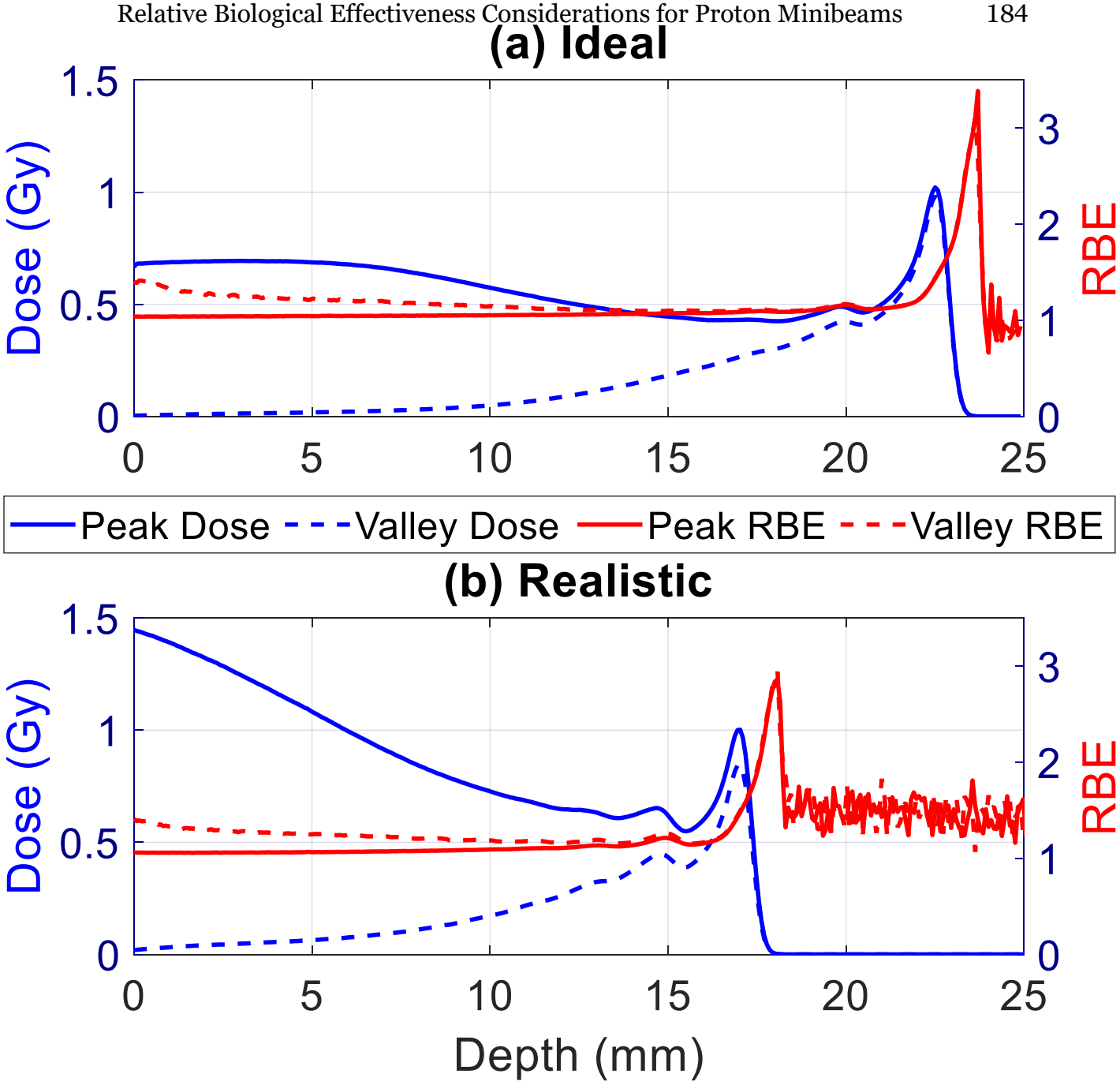

Figure 6.13: Comparison between and ideal (a) beam and realistic beam (b) for dose and RBE

There is a factor of two in the peak and 6.7 in the valley difference in dose between monoenergetic and realistic beams at the surface. This difference in surface dose between peak and valley results in a PVDR of 214 for the monoenergetic beam and 73 for the realistic beamline. These differences are caused by the number of scatter particles in the realistic beam produced by interaction with components upstream

of the water phantom. Many of these scattered particles are lower energy protons depositing energy at the surface, particularly in the valley regions. This also impacts the depth of the Bragg peak as protons in the realistic beam must pass through multiple components of the beamline resulting in energy loss and thus a lower energy beam than the monoenergetic beam. This observation has been shown in the previous chapter where the entire beamline was modelled.

The RBE for the monoenergetic beam starts at 1.03 and has a slight increase to 1.12 until it peaks at a depth of 23.7 mm with a peak of 3.39, 1.2 mm deeper than the dose Bragg peak. A small peak in RBE is also observed in the monoenergetic beam at a depth of 20.0 mm with a peak of 1.17, caused by scatter from the collimator. The dose past the Bragg peak falls to a near zero value, when this occurs the RBE becomes dominated by a few particles resulting in poor statistics. This is shown as the noise distal to the RBE peak at a depth of 23.7 mm. The RBE for realistic beamline starts at 1.06 and increases with depth to 1.15 before the main peak. The main peak is located at a depth of 18.1 mm with a peak of 2.94 and is 1.1 mm deeper than the dose peak. A small peak caused by collimator scatter at a depth of 14.9 mm with a peak height of 1.2 before the main peak. The higher dose of the whole beamline increases the surface dose and the respective RBE at the surface. This is primarily caused by scattered particles depositing dose in these regions. These particles are primarily low energy protons, which have a high LET at the end of their tracks.

The valley RBE is higher than that of the peak RBE at the surface and starts at 1.40 and 1.41 for the monoenergetic and realistic beam, respectively. RBE decreases with depth until at 15.0 mm depth it is equal to the peak RBE. This shows that even though the valley dose for the whole beam is 2.8 times higher than that of the monoenergetic beam the RBE in the valley dose is remarkably similar. The RBE is high at the surface possibly due to a biasing effect, where low energy protons more likely to be the particles that deposit dose in the valley at the surface, and these low energy protons have higher LET and RBE. As depth increases, most of these lower energy protons have already deposited all their dose, so the remaining protons will deposit dose in either the primary or secondary Bragg peaks, decreasing the LET and RBE at these peaks.

6.4. Discussion

In this section the various particles produced from minibeam collimators and their biological impact was discussed. The Monte Carlo modelling revealed that the first 15 mm of the collimator is particularly important in converting the beam from a uniform beam into a collimated beam. This starting region is also responsible for the generation of most of the neutrons and photons that exit the collimator. From 15 mm depth to the end of the collimator, protons are scattered which contributes to the lower energy Bragg peaks previously observed in the dose distribution. This is caused by protons impacting the side of the collimator and being scattered with a small angular deviation from the main beam. It is possible that the number of these scattered protons would increase with a beam of higher angular divergence than the near monoenergetic beam simulated.

The issue concerning the impact of neutrons generated by the collimator has been raised as an important consideration when generating proton minibeams with a collimator. This dose is uniform and therefore is of greatest concern in the valley dose regions any treated volume. However, the dose delivered to the water phantom by neutrons is exceedingly small compared to that of the dose delivered by protons. This results in the valley region dose being mainly dominated by scattered protons. Even when the high RBE of these neutrons is included they still deliver an exceedingly small dose, resulting in only minor impacts on final RWD. The only situation where it could be a concern if a collimator were made out of a material with a high neutron output and these neutrons had significantly higher RBE. A large number of neutrons with a high RBE may impact the valley dose, especially if the dose from protons is also exceptionally low. Therefore, it is

recommended that a tungsten collimator, or a high-density material with a high neutron production, is not used. The difference between nickel, brass and stainless steel is minimal for most results, however nickel does continue to show some benefits over the other materials. The choice of using stainless steel for a minibeam collimator remains justified in part due to low cost and ease of manufacture. In any future development, stainless steel material could be optimised further by using an alloy that has a higher nickel content.

Photons produced by the collimator deliver very little dose to the water phantom even though there is a large quantity, indicating that photon scatter should not be a major design constraint, as limiting this avenue of secondary dose will not have a major impact on the output of the collimator.

The majority of the dose delivered to the water phantom in the peak regions is from protons that have not interacted with the collimator. With a minor component particularly at the surface from protons that have interacted with the collimator and lost energy. The inverse of this is true for the valley regions with scattered protons dominating the dose. The RBE of protons has also been shown to be higher in the valley's regions than in the peak regions. Decreasing the PVDR of the overall minibeams and reduces the normal tissue sparing of the minibeams. Minimising dose to the valley regions is critical to reduce damage to normal tissue. These high RBE protons in the valleys and uniform dose from neutrons mean that collimator design is critical to reduce dose to the valleys.

The RBE was also shown to be high post Bragg peak. This is a major concern for the 50.5 MeV beam as this effect increases the effective depth of the beam, thereby increasing the effective dose past which the normal dose Bragg peak occurs. This result has been shown in previous research by Cuaron *et al.* where the RBE increases post Bragg peak increasing biological damage at the distal edge [95]. The relative dose when the RBE peaks is exceptionally low so it over all has a minor impact. This effect also occurs with the scattered proton Bragg peaks at shallower depths, increasing the impact the scatter has on the dose distribution. Compared to clinical proton beam for which an average RBE of 1.1 has been deemed sufficient, for the low energy PPRP it is highly recommended to include a variable RBE correction to consider the large variations in RWD across the spatial dose distribution.

6.5. Conclusion

A comprehensive and novel analysis of the physical and biological dose contributions for different minibeam collimator materials has been presented. New insights were obtained into the different components that contribute scattered dose to the various regions and this was investigated for different collimator materials that were identified in Chapter 5. Neutrons generated from a minibeam collimator, whilst having a high LET and RBE only have a minor impact on the final dose distribution as the majority of the dose in the peak regions is from protons that have not interacted with the collimator, and the majority of dose in the valley regions is from protons that have interacted with the collimator. The RBE of protons in the valley regions is extremely high, up to 1.5 at the surface. This reduced the PVDR and decreased the potential normal tissue sparing of the treatment and should be considered in designing future treatments with proton minibeams. This RBE is for a 50.5 MeV proton beam and raises questions on the RBE in the valley for higher energy proton beams. This RBE data is based off a double-strand break model and future work should perform biological experiments to verify the accuracy of these RBE values.

This chapter also demonstrated that the region of the collimator that blocks the uniform beam is critical in generation of secondary particles. Future work may involve designing a multi-material collimator that would be designed to reduce neutron production from this region and reduce scattered protons from remainder of the collimator, which would reduce the dose in the valley regions. This would help to increase the PVDR of the minibeam dose distribution and increase the normal tissue sparing.

Chapter 7

Concluding Remarks and Future Work

This chapter provides a summary of the work presented and the key findings of this thesis. A discussion on future work as an outcome off from this work then follows.

7.1. Summary

The overarching aim of this thesis was to characterise proton minibeams for use in radiation therapy via the Monte Carlo method. The first area investigated was to address the concern that spatially modulated dose distributions are susceptible to target motion. Work by Manchado de Sola *et al*. demonstrated that motion was a concern for X-ray microbeams even with high dose rate synchrotrons [19]. The work on motion presented in Chapter 3 of this thesis investigated and characterised the effects on the dose distribution for various proton minibeam collimator designs, providing insight into how the effect of motion can be reduced for proton minibeam therapy, enabling it to be used preclinically to treat small animals and potentially humans in the future. This work is novel and covers a wide range of motion relevant for small animal irradiation, however it also extends to clinical beams and as such is easily translatable to a range of proton minibeam geometries.

Results from using Monte Carlo and MATLAB modelling presented in this thesis demonstrated that motion has a detrimental impact on all proton minibeam dose distributions. Motions with a small amplitude such as cardiovascular brain pulsations, which are of the order of 60 μm and 300 μm for mice and humans, respectively, have only a minor impact on the peak dose and minibeam width, and no observable impact on the valley dose. For motions that are less than the width of the minibeam the peak dose maximum height remains roughly constant. Internal motion in humans is often much larger than the width of the proton minibeams and will decrease the peak dose and spread dose into the valleys. However, the valley dose was shown to depend on the spacing between the minibeams and the magnitude of motion. Proton energies typically used for human treatment allows for a larger CTC spacing; this helps to mitigate dose delivered to valley regions and indicating the potential of proton minibeams in treating cancers in regions of small motion i.e. brain.

The second research area of this thesis was to simulate and characterise the University of Washington's 50.5 MeV PPRP beamline. This characterisation is important for future proton minibeam biological experiments, and was published in part in Physics in Medicine & Biology [18]. A difference between simulations and measurement was initially observed in the shape of the PDD curve requiring a detailed analysis to gain an understanding of what was causing the differences. The depth of the Bragg peak in the Monte Carlo model agreed (within experimental uncertainty) with the depth measurements. The model depth was measured to be 18.1 mm. This is shallower than expected for a 50.5 MeV proton beam and actually corresponds to a proton beam with an output energy of 44.95 MeV. This depth also agrees with the reference values for a 44.95 MeV beam [82]. The decrease in energy

from 50.5 to 44.95 MeV was determined to be a result of interactions with the graphite degrader, Kapton exit window, and the ion chamber.

Uncertainties in the exact physical dimensions of some beam pipe components were identified, resulting in differences between the measurements and model in the shape of the PDD. An analysis of the scattering characteristic of the protons along the beam transport system revealed that by iteratively increasing the diameter of the large beam pipe the shape of the PDD curve could be matched. A small number of scattered protons were produced by the large beam pipe and this was also shown to lead to an increase in the surface dose within the water phantom. Other components were found to have a minimal impact on the proton beam.

The remaining sections of the thesis considered an optimal collimator design for proton minibeams at a nominal beam energy of 50.5 MeV as it is available at the University of Washington in Seattle. The minibeam specific approach is comprehensive and novel, and systematically examined the most relevant parameters influencing the beam characteristics and dose deposition. Results showed that increasing the thickness of the collimator beyond what is necessary to fully attenuate protons reduced the number of primary protons whilst maintaining the same number of scattered protons. This resulted in a reduction in beam modulation and dose and placed an upper limit on the thickness of the collimator. For our setup, a stainless steel collimator between 20 – 25 mm thick was deemed ideal. The first 5 mm, the proton range in a material, of the collimator was shown to be critical in converting the uniform beam into spatially modulated beams. This region is also where most neutrons, electrons, and photons that exit the collimator are generated. The ideal width for minibeam beamlets was found to be between 0.3

– 0.4 mm as these widths have the highest PVDR whilst maintaining reasonable dose delivery to the Bragg peak depth. These minibeam widths also have the lowest relative valley dose, thus reducing potential normal tissue damage and providing the possibility of tissue repair into the peak regions. In terms of collimator material, the collimator should be constructed from as dense a material as possible, as this has been shown to maximise the PVDR. However, to reduce neutron production, this work has also shown that the material should be ideally a group 4 transition metal. This is a novel finding that has previously not been shown before. Nickel is a particularly suitable candidate for collimator construction due to its low neutron production and remarkably high PVDR ratios from the surface to 10 mm depth.

The last area of research in this thesis was to explore any effect different collimator materials have on the RBE of particles exiting the collimator. This has been an area of debate and results presented in this work provided novel insight into this area. Results from Monte Carlo modelling showed that the LET and RBE of neutrons generated from various collimators was higher than previously understood. However, the overall RWD from neutrons was only a minor component of the dose distribution. In the valley regions where the neutron dose is relatively high, it is still only a minor component and should have minimal, if any, impact on the overall treatment. The LET and RBE results from protons did show RBE values of up to 1.5 in the valley regions increasing damage to normal tissue and reducing the PVDR of the dose distribution at the surface. At the distal end of the Bragg peak the simulated RBE values were up to three for the 50.5 MeV minibeam. This increases the effective depth of the Bragg peak somewhat and adds uncertainty to the depth at which maximum dose is delivered. This can be problematic when

placing the distal edge of the Bragg peak near critical structures and until better understood should be avoided with this low energy proton beam.

7.2. Limitations and Future Work

Modelling the impact of motion on dose distributions assumed that translational motion only occurred in a single direction (parallel to the direction of spatial modulation), and that this motion was regular and repeatable. For motions in any generic directions the component of the motion, which is parallel to the direction of modulation, could be used for an estimation on the results. However, this was beyond the scope of this work and a full analysis should be performed to verify this prediction. Ideally treatment planning should consider the impact of patient motion when utilising mini/microbeams. Research into the advancement of treatment planning systems would need to consider that microbeams require very high spatial resolution with a very fast acquisition time, which is not feasible in most clinical environments. Therefore, it is likely that a spread factor will be needed to estimate the reduction in spatial modulation of the minibeams.

Throughout this thesis the maximum dose in the centre of the peak and minimum dose in the centre of valley have been used to produce the PVDR. While this has been shown to vary with depth, there is no investigation of how dose varies within each peak and valley region. The variation of dose laterally in these regions potentially could have an impact on the biological damage delivered to the normal tissue, particularly at the peak/valley boundaries and particularly when motion is considered.

Output from simulations of the PPRP beamline modelled from supplied drawings disagree with measurement and hence adjustments to the simulation beamline were made. This limits somewhat the results from the model produced by this work. However, a large portion of this work used a monoenergetic beam to aid in understanding the physical processes and interactions, making the results more transferable to other beamlines and to overcome this limitation. Future work that uses this model should take this into account and, if possible, correctly identify or validate the reason suggested herein for the source of disagreement. This was considered beyond the requirements for this thesis due to likely the requirement of having to dismantle the current beamline.

While the main focus of this work has been on low energy (50.5 MeV) proton beams, the simulations, and results where generalised were appropriate to consider higher proton energies. Future work should verify that the collimator results are applicable to these higher energies necessary for human treatments. True understanding of tissue damage cannot yet be realised with models. The future of this work needs to involve collaboration with biologists who are able to do studies of actual tissue damage having been exposed to these proton beams. As proton minibeams diverge with depth, the width of the minibeam also increases. Which raises questions over how this increased width of the minibeam will impact normal tissue. Ideally future tissue studies should be performed to confirm the effect proton minibeam width has in normal tissue. Normal tissue sparing of photon microbeams has been shown to depend on the width of the beam [11]. It is therefore critical to determine if there is a maximum beamlet width where the sparing effect is no longer applicable. If this is the case, then proton minibeams will only maintain the sparing effect at the surface regions in treatments. This work

primarily uses monoenergetic, or a realistic near monoenergetic proton beam which only covers a limited volume with their Bragg peak. Future work could investigate how to produce a spread out Bragg peak, in depth, with proton minibeams and what implications this has for the conclusions found in this thesis.

The collimator geometry used in this thesis only uses slot collimators, which are spatially modulated in a single direction. Hole collimators can be spatially modulated in two orthogonal directions, potentially offering advantages. While this work should be applicable to hole collimators, future work should investigate the differences between them, as hole collimators have a larger internal surface area so possibly will produce a larger number of scattered particles. This thesis also aimed to deliver dose uniformity at the Bragg peak, with the minimum dose no less than 85% of the maximum dose. This level of uniformity was somewhat arbitrary, and was used to fix the CTC spacing between the minibeams. It is therefore important that that impact of level uniformity versus increased spacing for minibeams is investigated with tissue based studies to identify a requirement level of uniformity for successful tumour control.

This thesis also investigated single element materials for use in collimator construction to provide a better understanding of the influence material has on dose deposition for future work. In this thesis multi-material collimators were not considered, however there could be advantages in using such designs and this should be investigated. The first 15 mm of a minibeam collimator material was shown to be responsible for producing the majority of neutrons that exit the collimator. Changing this material to one more suitable at reducing the number of neutrons, could be beneficial. The remainder of the collimator could then be

designed to reduce proton scatter and maximise the PVDR. These collimators should be produced from a higher content nickel alloy for further improvements. A concern that was beyond the scope of this thesis, was the activation of certain materials from a proton beamline. It is possible that when a proton beam interacts with a material some of the protons can be absorbed by the materials nucleus creating unstable nuclei, which can pose a radio-safety concern. Care needs to be taken when using a material to ensure that people are not exposed unknowingly to a radioactive collimator and any research into this area needs to take this into account.

References

[1] G. Delaney, S. Jacob, C. Featherstone, and M. Barton, "The role of radiotherapy in cancer treatment: estimating optimal utilization from a review of evidence-based clinical guidelines," *Cancer,* vol. 104, no. 6, pp. 1129-37, Sep 15 2005, doi: 10.1002/cncr.21324.

[2] C. Garibaldi *et al.*, "Recent advances in radiation oncology," *Ecancermedicalscience,* vol. 11, p. 785, 2017, doi: 10.3332/ecancer.2017.785.

[3] T. Bortfeld, "IMRT: a review and preview," *Phys Med Biol,* vol. 51, no. 13, pp. R363-79, Jul 7 2006, doi: 10.1088/0031-9155/51/13/R21.

[4] D. Wolff *et al.*, "Volumetric modulated arc therapy (VMAT) vs. serial tomotherapy, step-and-shoot IMRT and 3D-conformal RT for treatment of prostate cancer," *Radiother Oncol,* vol. 93, no. 2, pp. 226-33, Nov 2009, doi: 10.1016/j.radonc.2009.08.011.

[5] C. G. Rusthoven, C. F. Lauro, B. D. Kavanagh, and T. E. Schefter, "Stereotactic body radiation therapy (SBRT) for liver metastases: a clinical review," in *Seminars in Colon and Rectal Surgery*, 2014, vol. 25, no. 1: Elsevier, pp. 48-52, doi: https://doi.org/10.1053/j.scrs.2013.09.009.

[6] M. Fuss *et al.*, "Proton radiation therapy (PRT) for pediatric optic pathway gliomas: comparison with 3D planned conventional photons and a standard photon technique," *Int J Radiat Oncol Biol Phys,* vol. 45, no. 5, pp. 1117-26, Dec 1 1999, doi: 10.1016/s0360-3016(99)00337-5.

[7] A. M. Allen *et al.*, "An evidence based review of proton beam therapy: the report of ASTRO's emerging technology committee," *Radiother Oncol,* vol. 103, no. 1, pp. 8-11, Apr 2012, doi: 10.1016/j.radonc.2012.02.001.

[8] Particle Therapy Co-Operative Group. "Particle therapy facilities in clinical operation." PTCOG. https://www.ptcog.ch/index.php/facilities-in-operation (accessed 12/05/2020, 2020).

[9] H. Paganetti, "Relative biological effectiveness (RBE) values for proton beam therapy. Variations as a function of biological endpoint, dose, and linear energy transfer," *Physics in Medicine & Biology,* vol. 59, no. 22, 2014.

[10] R. R. Wilson, "Radiological use of fast protons," *Radiology,* vol. 47, no. 5, pp. 487-91, Nov 1946, doi: 10.1148/47.5.487.

[11] H. J. Curtis, "The interpretation of microbeam experiments for manned space flight," *Radiat Res Suppl,* vol. 7, pp. 258-64, 1967, doi: 10.2307/3583719.

[12] H. J. Curtis, "The use of a deuteron microbeam for simulating the biological effects of heavy cosmic-ray particles," *Radiation Research Supplement,* vol. 7, pp. 250-257, 1967, doi: 10.2307/3583718

[13] D. N. Slatkin, P. Spanne, F. Dilmanian, and M. Sandborg, "Microbeam radiation therapy," *Medical physics,* vol. 19, no. 6, pp. 1395-1400, 1992, doi: https://doi.org/10.1118/1.596771.

[14] D. N. Slatkin, P. Spanne, F. A. Dilmanian, J. O. Gebbers, and J. A. Laissue, "Subacute neuropathological effects of microplanar beams of x-rays from a synchrotron wiggler," *Proc Natl Acad Sci U S A,* vol. 92, no. 19, pp. 8783-7, Sep 12 1995, doi: 10.1073/pnas.92.19.8783.

[15] J. A. Laissue *et al.*, "Weanling piglet cerebellum: a surrogate for tolerance to MRT (microbeam radiation therapy) in pediatric neuro-oncology," in *Penetrating Radiation Systems and Applications III*, 2001, vol. 4508: International Society for Optics and Photonics, pp. 65-73, doi: https://doi.org/10.1117/12.450774.

[16] Y. Prezado and G. R. Fois, "Proton-minibeam radiation therapy: a proof of concept," *Med Phys,* vol. 40, no. 3, p. 031712, Mar 2013, doi: 10.1118/1.4791648.

[17] E. Dorman and R. Emery, "The University of Washington clinical cyclotron a summary of current particles and energies used in therapy, isotope production, and clinical research," in *Proceedings of 20th International Conference On Cyclotrons and Their Applications 2013*, 2013. [Online]. Available: https://accelconf.web.cern.ch/CYCLOTRONS2013/papers/th2pb03.pdf. [Online]. Available: https://accelconf.web.cern.ch/CYCLOTRONS2013/papers/th2pb03.pdf

[18] J. Meyer *et al.*, "Biological and dosimetric characterisation of spatially fractionated proton minibeams," *Phys Med Biol,* vol. 62, no. 24, pp. 9260-9281, Nov 21 2017, doi: 10.1088/1361-6560/aa950c.

[19] F. Manchado de Sola, M. Vilches, Y. Prezado, and A. M. Lallena, "Impact of cardiosynchronous brain pulsations on Monte Carlo calculated doses for synchrotron micro- and minibeam radiation therapy," *Med Phys,* vol. 45, no. 7, pp. 3379-3390, Jul 2018, doi: 10.1002/mp.12973.

[20] D. Wang *et al.*, "Impact of spot size on plan quality of spot scanning proton radiosurgery for peripheral brain lesions," *Med Phys,* vol. 41, no. 12, p. 121705, Dec 2014, doi: 10.1118/1.4901260.

[21] B. Gustafsson, "Optimization of material in proton-therapy collimators with respect to neutron production," MSc, Uppsala University, Uppsala, Sweden, 2009. [Online]. Available: https://www.diva-portal.org/smash/get/diva2:460603/FULLTEXT01.pdf

[22] E. S. Diffenderfer, C. G. Ainsley, M. L. Kirk, J. E. McDonough, and R. L. Maughan, "Comparison of secondary neutron dose in proton therapy resulting

from the use of a tungsten alloy MLC or a brass collimator system," *Med Phys,* vol. 38, no. 11, pp. 6248-56, Nov 2011, doi: 10.1118/1.3656025.

[23] E. Lee, J. Meyer, and G. Sandison, "Collimator design for spatially-fractionated proton beams for radiobiology research," *Phys Med Biol,* vol. 61, no. 14, pp. 5378-89, Jul 21 2016, doi: 10.1088/0031-9155/61/14/5378.

[24] World Health Organization. "Cancer Fact Sheet." World Health Organization. https://www.who.int/en/news-room/fact-sheets/detail/cancer (accessed 18/05/20, 2020).

[25] E. J. Hall and A. J. Giaccia, *Radiobiology for the Radiologist*. Philadelphia, UNITED STATES: Wolters Kluwer Health, 2011.

[26] G. Iliakis, "The Biological Foundations of Risks from Ionizing Radiation Exposures: How an Understanding of Associated Effects Will Help Their Quantification and Mitigation," in *Sustainable Risk Management*, P. A. Wilderer, O. Renn, M. Grambow, M. Molls, and K. Mainzer Eds., (Strategies for Sustainability. Cham: Springer International Publishing, 2018, ch. Chapter 12, pp. 149-158.

[27] C. Tobias *et al.*, "Pituitary irradiation with high-energy proton beams a preliminary report," *Cancer research,* vol. 18, no. 2, pp. 121-134, 1958.

[28] S. Graffman, A. Brahme, and B. Larsson, "Proton radiotherapy with the Uppsala cyclotron. Experience and plans," *Strahlentherapie,* vol. 161, no. 12, pp. 764-770, 1985.

[29] W. D. Newhauser and R. Zhang, "The physics of proton therapy," *Phys Med Biol,* vol. 60, no. 8, pp. R155-209, Apr 21 2015, doi: 10.1088/0031-9155/60/8/R155.

[30] H. Bethe, "Bremsformel für elektronen relativistischer geschwindigkeit," *Zeitschrift für Physik,* vol. 76, no. 5-6, pp. 293-299, 1932.

[31] D. R. Olsen, O. S. Bruland, G. Frykholm, and I. N. Norderhaug, "Proton therapy - a systematic review of clinical effectiveness," *Radiother Oncol,* vol. 83, no. 2, pp. 123-32, May 2007, doi: 10.1016/j.radonc.2007.03.001.

[32] P. Sigmund, "Particle penetration and radiation effects volume 2," in *Springer series in solid-state sciences*, vol. 179: Springer, 2014.

[33] C. Grassberger, A. Trofimov, A. Lomax, and H. Paganetti, "Variations in linear energy transfer within clinical proton therapy fields and the potential for biological treatment planning," *Int J Radiat Oncol Biol Phys,* vol. 80, no. 5, pp. 1559-66, Aug 1 2011, doi: 10.1016/j.ijrobp.2010.10.027.

[34] A. L. McNamara, J. Schuemann, and H. Paganetti, "A phenomenological relative biological effectiveness (RBE) model for proton therapy based on all published in vitro cell survival data," *Phys Med Biol,* vol. 60, no. 21, pp. 8399-416, Nov 7 2015, doi: 10.1088/0031-9155/60/21/8399.

[35] Y. Chen and S. Ahmad, "Empirical model estimation of relative biological effectiveness for proton beam therapy," *Radiat Prot Dosimetry,* vol. 149, no. 2, pp. 116-23, Apr 2012, doi: 10.1093/rpd/ncr218.

[36] J. J. Cuaron *et al.*, "Exponential Increase in Relative Biological Effectiveness Along Distal Edge of a Proton Bragg Peak as Measured by Deoxyribonucleic Acid Double-Strand Breaks," *Int J Radiat Oncol Biol Phys,* vol. 95, no. 1, pp. 62-69, May 1 2016, doi: 10.1016/j.ijrobp.2016.02.018.

[37] H. Paganetti *et al.*, "Relative biological effectiveness (RBE) values for proton beam therapy," *Int J Radiat Oncol Biol Phys,* vol. 53, no. 2, pp. 407-21, Jun 1 2002, doi: 10.1016/s0360-3016(02)02754-2.

[38] K. Ando *et al.*, "Relative biological effectiveness of the 235 MeV proton beams at the National Cancer Center Hospital East," *J Radiat Res,* vol. 42, no. 1, pp. 79-89, Mar 2001, doi: 10.1269/jrr.42.79.

[39] J. T. Tang *et al.*, "Comparison of radiobiological effective depths in 65-MeV modulated proton beams," *Br J Cancer,* vol. 76, no. 2, pp. 220-5, 1997, doi: 10.1038/bjc.1997.365.

[40] International Commission on Radiological Protection, "ICRP publication 103," *Ann. ICRP,* vol. 37, no. 2.4, p. 2, 2007.

[41] G. Baiocco *et al.*, "The origin of neutron biological effectiveness as a function of energy," *Sci Rep,* vol. 6, p. 34033, Sep 22 2016, doi: 10.1038/srep34033.

[42] A. Köhler, "Zur Röntgentiefentherapie mit Massendosen," *Münch. med. Wochenschr,* vol. 45, pp. 2314-2316, 1909.

[43] F. Liberson, "The Value of a Multi-perforated Screen in Deep X-ray Therapy," *Radiology,* vol. 20, no. 3, pp. 186-195, 1933, doi: 10.1148/20.3.186.

[44] A. S. Meigooni *et al.*, "Dosimetric characteristics of a newly designed grid block for megavoltage photon radiation and its therapeutic advantage using a linear quadratic model," *Med Phys,* vol. 33, no. 9, pp. 3165-73, Sep 2006, doi: 10.1118/1.2241998.

[45] J. K. Ha, G. Zhang, S. A. Naqvi, W. F. Regine, and C. X. Yu, "Feasibility of delivering grid therapy using a multileaf collimator," *Med Phys,* vol. 33, no. 1, pp. 76-82, Jan 2006, doi: 10.1118/1.2140116.

[46] G. Narayanasamy *et al.*, "Therapeutic benefits in grid irradiation on Tomotherapy for bulky, radiation-resistant tumors," *Acta Oncol,* vol. 56, no. 8, pp. 1043-1047, Aug 2017, doi: 10.1080/0284186X.2017.1299219.

[47] V. Peng, N. Suchowerska, L. Rogers, E. Claridge Mackonis, S. Oakes, and D. R. McKenzie, "Grid therapy using high definition multileaf collimators: realizing benefits of the bystander effect," *Acta Oncologica,* pp. 1-12, 2017, doi: https://doi.org/10.1080/0284186X.2017.1299939.

[48] E. J. Hall, "The bystander effect," *Health Phys,* vol. 85, no. 1, pp. 31-5, Jul 2003, doi: 10.1097/00004032-200307000-00008.

[49] M. Gao, M. M. Mohiuddin, W. F. Hartsell, and M. Pankuch, "Spatially fractionated (GRID) radiation therapy using proton pencil beam scanning (PBS): Feasibility study and clinical implementation," *Med Phys,* vol. 45, no. 4, pp. 1645-1653, Apr 2018, doi: 10.1002/mp.12807.

[50] J. A. Laissue *et al.*, "Microbeam radiation therapy," in *SPIE's International Symposium on Optical Science, Engineering, and Instrumentation*, 1999: International Society for Optics and Photonics, pp. 38-45.

[51] F. A. Dilmanian *et al.*, "Response of rat intracranial 9L gliosarcoma to microbeam radiation therapy," *Neuro Oncol,* vol. 4, no. 1, pp. 26-38, Jan 2002, doi: 10.1093/neuonc/4.1.26.

[52] E. Brauer-Krisch *et al.*, "MOSFET dosimetry for microbeam radiation therapy at the European Synchrotron Radiation Facility," *Med Phys,* vol. 30, no. 4, pp. 583-9, Apr 2003, doi: 10.1118/1.1562169.

[53] J. A. Laissue, H. Blattmann, H. P. Wagner, M. A. Grotzer, and D. N. Slatkin, "Prospects for microbeam radiation therapy of brain tumours in children to reduce neurological sequelae," *Dev Med Child Neurol,* vol. 49, no. 8, pp. 577-81, Aug 2007, doi: 10.1111/j.1469-8749.2007.00577.x.

[54] E. A. Siegbahn, J. Stepanek, E. Brauer-Krisch, and A. Bravin, "Determination of dosimetrical quantities used in microbeam radiation therapy (MRT) with Monte Carlo simulations," *Med Phys,* vol. 33, no. 9, pp. 3248-59, Sep 2006, doi: 10.1118/1.2229422.

[55] J. A. Laissue *et al.*, "Neuropathology of ablation of rat gliosarcomas and contiguous brain tissues using a microplanar beam of synchrotron-wiggler-

generated X rays," *International Journal of Cancer,* vol. 78, no. 5, pp. 654-660, 1998, doi: 10.1002/(sici)1097-0215(19981123)78:5<654::Aid-ijc21>3.0.Co;2-l.

[56] H. M. Smilowitz *et al.*, "Synergy of gene-mediated immunoprophylaxis and microbeam radiation therapy for advanced intracerebral rat 9L gliosarcomas," *J Neurooncol,* vol. 78, no. 2, pp. 135-43, Jun 2006, doi: 10.1007/s11060-005-9094-9.

[57] F. A. Dilmanian *et al.*, "Interlaced x-ray microplanar beams: a radiosurgery approach with clinical potential," *Proc Natl Acad Sci U S A,* vol. 103, no. 25, pp. 9709-14, Jun 20 2006, doi: 10.1073/pnas.0603567103.

[58] F. A. Dilmanian *et al.*, "Microbeam radiation therapy: tissue dose penetration and BANG-gel dosimetry of thick-beams' array interlacing," *Eur J Radiol,* vol. 68, no. 3 Suppl, pp. S129-36, Dec 2008, doi: 10.1016/j.ejrad.2008.04.055.

[59] D. E. Hyer, P. M. Hill, D. Wang, B. R. Smith, and R. T. Flynn, "Effects of spot size and spot spacing on lateral penumbra reduction when using a dynamic collimation system for spot scanning proton therapy," *Phys Med Biol,* vol. 59, no. 22, pp. N187-96, Nov 21 2014, doi: 10.1088/0031-9155/59/22/N187.

[60] C. Grassberger *et al.*, "Motion interplay as a function of patient parameters and spot size in spot scanning proton therapy for lung cancer," *Int J Radiat Oncol Biol Phys,* vol. 86, no. 2, pp. 380-6, Jun 1 2013, doi: 10.1016/j.ijrobp.2013.01.024.

[61] L. Hong *et al.*, "A pencil beam algorithm for proton dose calculations," *Phys Med Biol,* vol. 41, no. 8, pp. 1305-30, Aug 1996, doi: 10.1088/0031-9155/41/8/005.

[62] N. Metropolis and S. Ulam, "The Monte Carlo method," *J Am Stat Assoc,* vol. 44, no. 247, pp. 335-41, Sep 1949, doi: 10.1080/01621459.1949.10483310.

[63] J. Meyer, J. Eley, T. E. Schmid, S. E. Combs, R. Dendale, and Y. Prezado, "Spatially fractionated proton minibeams," *Br J Radiol,* vol. 92, no. 1095, p. 20180466, Mar 2019, doi: 10.1259/bjr.20180466.

[64] P. J. Keall *et al.*, "The management of respiratory motion in radiation oncology report of AAPM Task Group 76," *Med Phys,* vol. 33, no. 10, pp. 3874-900, Oct 2006, doi: 10.1118/1.2349696.

[65] C. Bert and M. Durante, "Motion in radiotherapy: particle therapy," *Phys Med Biol,* vol. 56, no. 16, pp. R113-44, Aug 21 2011, doi: 10.1088/0031-9155/56/16/R01.

[66] S. Webb, "Motion effects in (intensity modulated) radiation therapy: a review," *Phys Med Biol,* vol. 51, no. 13, pp. R403-25, Jul 7 2006, doi: 10.1088/0031-9155/51/13/R23.

[67] Y. Seppenwoolde *et al.*, "Precise and real-time measurement of 3D tumor motion in lung due to breathing and heartbeat, measured during radiotherapy," *International Journal of Radiation Oncology*Biology*Physics,* vol. 53, no. 4, pp. 822-834, 2002, doi: 10.1016/s0360-3016(02)02803-1.

[68] J. Boda-Heggemann *et al.*, "Deep Inspiration Breath Hold-Based Radiation Therapy: A Clinical Review," *Int J Radiat Oncol Biol Phys,* vol. 94, no. 3, pp. 478-92, Mar 1 2016, doi: 10.1016/j.ijrobp.2015.11.049.

[69] X. Zhong *et al.*, "Tracking brain motion during the cardiac cycle using spiral cine-DENSE MRI," *Med Phys,* vol. 36, no. 8, pp. 3413-9, Aug 2009, doi: 10.1118/1.3157109.

[70] A. Gilletti and J. Muthuswamy, "Brain micromotion around implants in the rodent somatosensory cortex," *J Neural Eng,* vol. 3, no. 3, pp. 189-95, Sep 2006, doi: 10.1088/1741-2560/3/3/001.

[71] L. M. Smyth, S. Senthi, J. C. Crosbie, and P. A. Rogers, "The normal tissue effects of microbeam radiotherapy: What do we know, and what do we need to know to plan a human clinical trial?," *Int J Radiat Biol,* vol. 92, no. 6, pp. 302-11, Jun 2016, doi: 10.3109/09553002.2016.1154217.

[72] J. A. Laissue *et al.*, "Response of the rat spinal cord to X-ray microbeams," *Radiotherapy and oncology,* vol. 106, no. 1, pp. 106-111, 2013, doi: https://doi.org/10.1016/j.radonc.2012.12.007.

[73] J. Perl, J. Shin, J. Schumann, B. Faddegon, and H. Paganetti, "TOPAS: an innovative proton Monte Carlo platform for research and clinical applications," *Med Phys,* vol. 39, no. 11, pp. 6818-37, Nov 2012, doi: 10.1118/1.4758060.

[74] S. Agostinelli *et al.*, "Geant4—a simulation toolkit," *Nuclear Instruments and Methods in Physics Research Section A: Accelerators, Spectrometers, Detectors and Associated Equipment,* vol. 506, no. 3, pp. 250-303, 2003, doi: 10.1016/s0168-9002(03)01368-8.

[75] B. Faddegon *et al.*, "The TOPAS tool for particle simulation, a Monte Carlo simulation tool for physics, biology and clinical research," *Phys Med,* vol. 72, pp. 114-121, Apr 2020, doi: 10.1016/j.ejmp.2020.03.019.

[76] M. Testa *et al.*, "Experimental validation of the TOPAS Monte Carlo system for passive scattering proton therapy," *Med Phys,* vol. 40, no. 12, p. 121719, Dec 2013, doi: 10.1118/1.4828781.

[77] M. Testa, C. H. Min, J. M. Verburg, J. Schumann, H. M. Lu, and H. Paganetti, "Range verification of passively scattered proton beams based on prompt gamma time patterns," *Phys Med Biol,* vol. 59, no. 15, pp. 4181-95, Aug 7 2014, doi: 10.1088/0031-9155/59/15/4181.

[78] J. M. Verburg, M. Testa, and J. Seco, "Range verification of passively scattered proton beams using prompt gamma-ray detection," *Phys Med Biol,* vol. 60, no. 3, pp. 1019-29, Feb 7 2015, doi: 10.1088/0031-9155/60/3/1019.

[79] W. G. Shin *et al.*, "Independent dose verification system with Monte Carlo simulations using TOPAS for passive scattering proton therapy at the National Cancer Center in Korea," *Phys Med Biol,* vol. 62, no. 19, pp. 7598-7616, Sep 12 2017, doi: 10.1088/1361-6560/aa8663.

[80] H. Liu, Z. Li, R. Slopsema, L. Hong, X. Pei, and X. G. Xu, "TOPAS Monte Carlo simulation for double scattering proton therapy and dosimetric evaluation," *Phys Med,* vol. 62, pp. 53-62, Jun 2019, doi: 10.1016/j.ejmp.2019.05.001.

[81] M. Faßbender, Y. N. Shubin, V. P. Lunev, and S. M. Qaim, "Experimental studies and nuclear model calculations on the formation of radioactive products in interactions of medium energy protons with copper, zinc and brass: Estimation of collimator activation in proton therapy facilities," *Applied Radiation and Isotopes,* vol. 48, no. 9, pp. 1221-1230, 1997, doi: 10.1016/s0969-8043(97)00102-4.

[82] J. F. Ziegler, M. D. Ziegler, and J. P. Biersack, "SRIM – The stopping and range of ions in matter (2010)," *Nuclear Instruments and Methods in Physics Research Section B: Beam Interactions with Materials and Atoms,* vol. 268, no. 11-12, pp. 1818-1823, 2010, doi: 10.1016/j.nimb.2010.02.091.

[83] S. M. Vatnitsky *et al.*, "Dosimetry techniques for narrow proton beam radiosurgery," *Phys Med Biol,* vol. 44, no. 11, pp. 2789-801, Nov 1999, doi: 10.1088/0031-9155/44/11/308.

[84] R. Serduc *et al.*, "Brain tumor vessel response to synchrotron microbeam radiation therapy: a short-term in vivo study," *Phys Med Biol,* vol. 53, no. 13, pp. 3609-22, Jul 7 2008, doi: 10.1088/0031-9155/53/13/015.

[85] R. Serduc *et al.*, "In vivo two-photon microscopy study of short-term effects of microbeam irradiation on normal mouse brain microvasculature," *Int J Radiat Oncol Biol Phys,* vol. 64, no. 5, pp. 1519-27, Apr 1 2006, doi: 10.1016/j.ijrobp.2005.11.047.

[86] R. Risler, J. Eenmaa, J. Jacky, I. J. Kalet, P. Wootton, and S. Lindbaeck, "Installation of the cyclotron based clinical neutron therapy system in Seattle," in *Proceedings of the Tenth International Conference on Cyclotrons and their Applications*, 1984: IEEE East Lansing, MI, pp. 428-430.

[87] R. Zhang and W. D. Newhauser, "Calculation of water equivalent thickness of materials of arbitrary density, elemental composition and thickness in proton beam irradiation," *Phys Med Biol,* vol. 54, no. 6, pp. 1383-95, Mar 21 2009, doi: 10.1088/0031-9155/54/6/001.

[88] E. J. Hall, J. K. Novak, A. M. Kellerer, H. H. Rossi, S. Marino, and L. J. Goodman, "RBE as a Function of Neutron Energy: I. Experimental Observations," *Radiation Research,* vol. 64, no. 2, pp. 245-255, 1975, doi: 10.2307/3574262.

[89] M. Klodowska, P. Olko, and M. P. Waligorski, "Proton microbeam radiotherapy with scanned pencil-beams--Monte Carlo simulations," *Phys Med,* vol. 31, no. 6, pp. 621-6, Sep 2015, doi: 10.1016/j.ejmp.2015.04.006.

[90] V. Sahadevan, "In Regard to Dilmanian et al," *Int J Radiat Oncol Biol Phys,* vol. 93, no. 5, p. 1164, Dec 1 2015, doi: 10.1016/j.ijrobp.2015.08.052.

[91] F. A. Dilmanian, J. G. Eley, and S. Krishnan, "In Reply to Sahadevan," *Int J Radiat Oncol Biol Phys,* vol. 93, no. 5, pp. 1164-5, Dec 1 2015, doi: 10.1016/j.ijrobp.2015.08.051.

[92] F. A. Dilmanian, J. G. Eley, and S. Krishnan, "Minibeam therapy with protons and light ions: physical feasibility and potential to reduce radiation side

effects and to facilitate hypofractionation," *Int J Radiat Oncol Biol Phys,* vol. 92, no. 2, pp. 469-74, Jun 1 2015, doi: 10.1016/j.ijrobp.2015.01.018.

[93] H. Paganetti, "Relative biological effectiveness (RBE) values for proton beam therapy. Variations as a function of biological endpoint, dose, and linear energy transfer," *Phys Med Biol,* vol. 59, no. 22, pp. R419-72, Nov 21 2014, doi: 10.1088/0031-9155/59/22/R419.

[94] H. Paganetti, "Range uncertainties in proton therapy and the role of Monte Carlo simulations," *Phys Med Biol,* vol. 57, no. 11, pp. R99-117, Jun 7 2012, doi: 10.1088/0031-9155/57/11/R99.

[95] J. J. Cuaron *et al.*, "Exponential increase in relative biological effectiveness along distal edge of a proton Bragg peak as measured by deoxyribonucleic acid double-strand breaks," *International Journal of Radiation Oncology* Biology* Physics,* vol. 95, no. 1, pp. 62-69, 2016.

[96] R. D. Stewart *et al.*, "Rapid MCNP simulation of DNA double strand break (DSB) relative biological effectiveness (RBE) for photons, neutrons, and light ions," *Phys Med Biol,* vol. 60, no. 21, pp. 8249-74, Nov 7 2015, doi: 10.1088/0031-9155/60/21/8249.

[97] V. A. Semenenko and R. D. Stewart, "A fast Monte Carlo algorithm to simulate the spectrum of DNA damages formed by ionizing radiation," *Radiat Res,* vol. 161, no. 4, pp. 451-7, Apr 2004, doi: 10.1667/rr3140.

[98] E. Rorvik *et al.*, "Exploration and application of phenomenological RBE models for proton therapy," *Phys Med Biol,* vol. 63, no. 18, p. 185013, Sep 13 2018, doi: 10.1088/1361-6560/aad9db.

[99] J. Schuemann *et al.*, "TOPAS-nBio: An Extension to the TOPAS Simulation Toolkit for Cellular and Sub-cellular Radiobiology," *Radiat Res,* vol. 191, no. 2, pp. 125-138, Feb 2019, doi: 10.1667/RR15226.1.

[100] B. Marples and M. C. Joiner, "The response of Chinese hamster V79 cells to low radiation doses: evidence of enhanced sensitivity of the whole cell population," *Radiat Res,* vol. 133, no. 1, pp. 41-51, Jan 1993, doi: https://doi.org/10.2307/3578255.

[101] E. K. Johansson *et al.*, "Thoroughγ-ray and particle decay investigations ofNi58," *Physical Review C,* vol. 80, no. 1, p. 014321, 2009, doi: 10.1103/PhysRevC.80.014321.

[102] F. A. Berends and R. Kleiss, "Distributions for electron-positron annihilation into two and three photons," *Nuclear Physics B,* vol. 186, no. 1, pp. 22-34, 1981, doi: 10.1016/0550-3213(81)90090-0.